Polymer/Inorganic Interfaces II

EDITORS:

Lawrence T. Drzal
Robert L. Opila
Nicholas A. Peppas
Carol Schutte

DISCLAIMER NOTICE
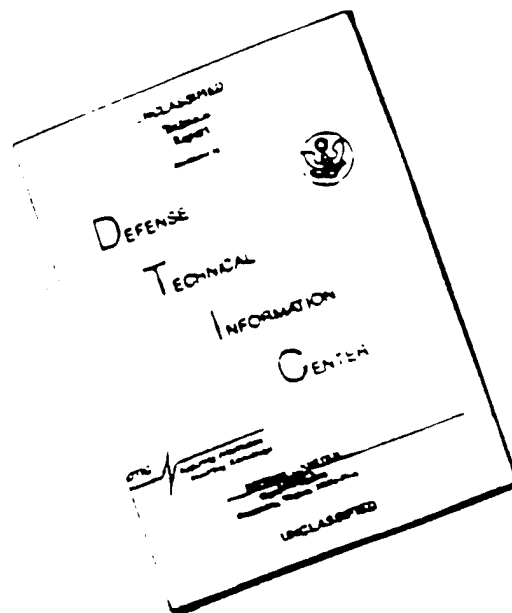
THIS DOCUMENT IS BEST QUALITY AVAILABLE. THE COPY FURNISHED TO DTIC CONTAINED A SIGNIFICANT NUMBER OF PAGES WHICH DO NOT REPRODUCE LEGIBLY.

Polymer/Inorganic Interfaces II

POLYMER/INORGANIC
INTERFACES II

Symposium held April 18-20, 1995, San Francisco, California, U.S.A.

EDITORS:

Lawrence T. Drzal
Michigan State University
East Lansing, Michigan, U.S.A.

Robert L. Opila
AT&T Bell Laboratories
Murray Hill, New Jersey, U.S.A.

Nicholas A. Peppas
Purdue University
West Lafayette, Indiana, U.S.A.

Carol Schutte
National Institute of Standards and Technology
Gaithersburg, Maryland, U.S.A.

19960627 085

DTIC QUALITY INSPECTED 1

CONTENTS

PART I: EXPERIMENTAL PROBES OF INTERFACES

PART II: BIOINTERACTIONS AND BIOINTERFACES

PART III: ADHESION AND INTERFACE DURABILITY

*Invited Paper

*Invited Paper

*Invited Paper

PREFACE

This volume contains contributions that were presented in the symposium on polymer/inorganic interfaces during the 1995 MRS Spring Meeting in San Francisco.

This volume addresses various aspects of polymer/inorganic interfaces, such as surface preparation and treatment, characterization, and performance of interfaces. In addition, it also discusses applications where the interface and its properties play a significant role, such as biointerfaces, microelectronics, polymer composites, and interpenetrating polymer networks. Tailoring surface properties of substrates, and hence interfaces, involves both the use of self-assembled monolayers and tethered copolymers (brushes) for controlling surface energy, lubricity, biocompatibility, adhesion, and topography. Polymeric brushes have the ability to modify their morphology as the solvent strength or pH changes. Primers influence adhesion of polymers to metals either by altering the chemical interactions which form reactive species that hasten chemical bonding or altering acid base interactions, or by altering the mechanical performance, such as tensile strength and viscoelastic properties of that primer coating.

Characterization techniques allow for the further understanding of properties at interfaces. For example, ellipsometric characterization of ultrathin polymeric films yields data on the swelling of these films on exposure to solvent compared to that in thicker films. The direct measurement of polymeric and interfacial energies allows for further understanding of adhesion and surface science of polymeric coatings. The use of transmission electron microscopy and differential scanning calorimetry enables the study of the fiber/matrix interfacial morphology and may contribute towards understanding of properties of composite interfaces. X-ray photoelectron spectroscopy measures the bond formation between metal-carbon as well as metal-oxygen-carbon interactions that yield information regarding the chemical characteristics of metal/polymer interfaces and may assist in optimization of their adhesion. Furthermore, near-edge x-ray absorption fine structure elucidates the orientation of bonds at buried polymer/metal interfaces. This nondestructive analysis allows for the measurement of interfacial chemical interactions between the polymer and metal, and may be useful in optimizing adhesion in these types of systems.

The contributions of this volume examine various inorganic material/polymer interfaces with emphasis on composites, epoxy resins, polyurethanes, poly(methyl methacrylate), polysiloxanes and various hydrophilic polymers. They have been arranged in seven units that identify major research efforts in specific fields. We hope that this volume will be a small, albeit important, addition to the already growing literature in this field.

Finally, the success of the symposium was due in large part to the financial support of the Office of Naval Research, the Army Research Office, the Automotive Composites Consortium, Physical Electronics Incorporated, and Surface/Interface, Inc.

<div style="text-align: right">

Lawrence Drzal
Robert L. Opila
Nicholas A. Peppas
Carol Schutte

May 1995

</div>

ix

MATERIALS RESEARCH SOCIETY SYMPOSIUM PROCEEDINGS

MATERIALS RESEARCH SOCIETY SYMPOSIUM PROCEEDINGS

Prior Materials Research Society Symposium Proceedings available by contacting Materials Research Society

Part I

Experimental Probes of Interfaces

PHOTOPOLYMERIZATION DYNAMICS STUDIES OF ACROLEIN ON Al, Ni, and Au SUBSTRATES USING SURFACE SECOND HARMONIC GENERATION

FANG CHEN, SUCHITRA SUBRAHMANYAN, HILARY S. LACKRITZ
School of Chemical Engineering, Purdue University, West Lafayette, IN 47907-1283

ABSTRACT

The dynamics of the gas phase photopolymerization of acrolein on aluminum (Al), nickel (Ni), and gold (Au) substrates were studied *in-situ* and in real time using surface second harmonic generation (SSHG) and monitoring vapor pressure decay. The Al and Ni substrates had a significant effect on the apparent rate of polymerization. A dark reaction after irradiation occurred in the absence of metal (Al or Ni) substrates, but no dark reaction was observed when the metal substrates were present. The significant differences in the metal/monomer interactions during photopolymerization are indicated by SEMs of the polyacrolein, as well as evidence from FTIR-ATR spectra. The SSHG intensities from the Au, Al, and polyacrolein surfaces were obtained.

INTRODUCTION

Solvent-free gas phase photopolymerization on metal substrates shows potential for creating defect-free thin films with excellent electrical and optical properties for commercial applications such as environmental protective coatings and electrical insulators. The photopolymerization-formed thin films are of particular interest in applications such as microlithography,[1] photoresists,[2] and semiconductor devices.[3] Understanding the photopolymerization kinetics is imperative for enhanced control of thin film growth and the determination of film mechanical and electrical properties. A second order nonlinear optical process, SSHG, has been developed to determine the surface dynamics *in-situ* .

Vinyl monomers such as acrolein[4] and methyl methacrylate[5] are reported as photoinitiable monomers near the ultraviolet (UV) region. Researchers[6,7] have studied the effects of physical parameters including monomer pressure, temperature, and light intensity on the physical properties of polymer films. However, little is known about the polymerization kinetics and their ability to be modified by processing methods.

The photopolymerization of vinyl monomers is a free radical reaction.[8] Radical production and polymerization in the gas phase can be spatially directed by laser-based processing techniques and light exposure procedures. Upon exposure to a suitable light source, photopolymerization of a monomer vapor in contact with a metal substrate produces a thin film with good uniformity and mechanical properties.[9] Free radical photopolymerization involves three main steps: initiation, propagation, and termination. In the presence of a metal substrate, photoinitiation can occur in the gas phase, on the metal substrate, or by a combination of both. The conventional method for studying gas phase reaction kinetics is to determine the apparent rate of polymerization by monitoring the time dependence of monomer vapor pressure as a function of light intensity. The surface dynamics during the photopolymerization are currently unclear because of the lack of surface probing tools with high sensitivity and good time resolution. In recent years, SSHG has been proven[10,11] in its ability to study surface dynamics with submonolayer sensitivity and high surface specificity.

We employed SSHG to study the dynamics of acrolein polymerization at Al and Au substrates with the polymer film growth characterized *in-situ* and in real time. SSHG is a laser-excited coherent optical process with advantages of high spectral and spatial resolution. Its good sensitivity and selectivity in the interfacial region facilitates the potential for examining the surface reaction dynamics by *in-situ* mapping of molecular composition of the

3

surface monolayer. By monitoring the surface second order nonlinear susceptibility, surface reaction rates can be determined *in-situ*.

A medium with inversion symmetry forbids a second order nonlinear optical process. SSHG is based on the principle[12] that such a symmetry will be broken at an interface, where the nonlinear processes are allowed. This indicates that the SSHG will be highly surface specific and without any contributions from the bulk materials. The nonlinear polarization induced by the incident laser field is given by:[13] $\bar{P}_s^{(2)}(2\omega) = \bar{\chi}_{s,eff}^{(2)} : \bar{E}(\omega)\bar{E}(\omega)$, where $E(\omega)$ is the electric field at frequency ω, and $\chi_{s,eff}^{(2)}$ is the effective surface second order nonlinear susceptibility. The surface second harmonic intensity, $I_{2\omega}$, in the reflected medium with nonlinear polarization $P^{(2)}(2\omega)$ as a source term, is proportional to the square of the fundamental light intensity and surface second order nonlinear susceptibility.

The surface photopolymerization kinetics is determined by monitoring the SHG intensity, I, from the surface as the reaction proceeds, i.e., I, is measured simultaneously along with the pressure change during the photopolymerization. The unreacted surface monomer concentration can be deduced by :[14] $I^{1/2} \propto \chi_{s,eff}^{(2)} = \chi_{ss}^{(2)} + \theta\chi_m^{(2)} + (1-\theta)\chi_p^{(2)}$, where $\chi_{ss}^{(2)}, \chi_m^{(2)}, \chi_p^{(2)}$ are the equilibrium second order nonlinear susceptibilies of metal, monomer, and polymer surfaces, respectively. θ is the unreacted monomer coverage on the surface.

By simultaneously studying the gas phase kinetics and surface dynamics during photopolymerization, the photoinitiation sites and reaction rate law can be determined. Furthermore, the relation between the polymer film properties and photopolymerization processing has been studied using various spectroscopy such as the Fourier transform infrared-attenuated total internal reflection (FTIR-ATR), X-ray photoelectron spectroscopy (XPS). Scanning electron microscopy (SEM) was used to characterize the polymer topography. Polymer glass transition was also determined.

EXPERIMENTAL SECTION

Prior to use, acrolein (ACR, Aldrich, structure $CH_2=CH-CHO$) was passed through an inhibitor removal column, then vacuum distilled and degassed via freeze-pump-thaw cycles 5 times. Au, Al, and Ni substrates (Johnson-Matthey) were polished with micropolish alumina (0.05CR) and degreased with acetone.

Purified monomer was introduced into the reaction cell by thermoequilibrium between a Schlenk tube and the reaction cell. Photopolymerization was carried out in a specially designed reaction cell (made of aniodized aluminum) which enabled the *in-situ* measurement of SSHG and gas phase pressure in real time. The photopolymerization was then initiated using the Hg-Xe arc lamp. A UG-11 filter which transmits 95% light between 250 nm and 400 nm was placed before the reaction tube to minimize thermal polymerization. The transmitted light intensity was measured with a coherent power meter. Pressure in the reaction cell was measured with a transducer which had a linear response from 0 to 1.034×10^5 N/cm^2.

SSHG was used to measure the surface decay of $\chi_{s,eff}^{(2)}$ during the reaction. A nanosecond pulsed laser (1064 nm) is the source of fundamental light. The filtered laser beam passes through a polarizer and a half wave plate. The incident light is focused onto the sample at 70° to the surface normal. The SSHG signal generated at the surface was detected by a photomultiplier.

XPS was used to determine the metal substrate elemental composition. FTIR-ATR was empolyed to identify the polymer structure. Differential Scanning Calorimetry (5°C/min.) was used to study the thermal stability of polymer films. SEM was utilized to characterize the film topography.

RESULTS AND DISCUSSION

Surface Characterization of Al, Ni, and Au

To understand the effects of Al, Au, and Ni substrates on the photopolymerization dynamics, their surface compositions have been studied using XPS. Fig. 1 shows the XPS spectrum of an Al surface. The atomic composition analysis indicates that : On the Al surface, the percentage of carbon (C), oxygen (O), and Al are 64.8%, 22.9%, and 12.3% respectively; On the Ni surface, the percentage of C, O, and Ni are 50.6%, 33.9%, and 15.6%, respectively; On the Au surface, the percentage of C, O, and Au are 54.3%, 11.9%, and 33.8%, respectively.
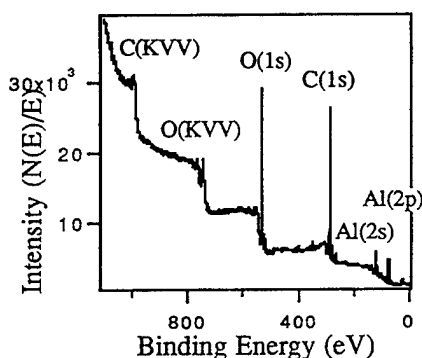
Fig.1. XPS spectrum of an Al substrate
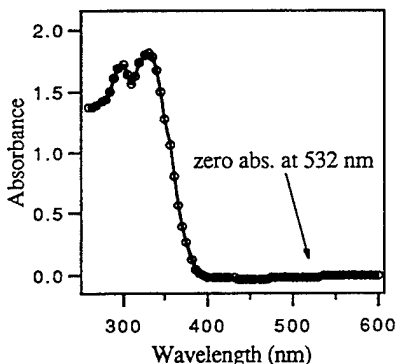
Fig.2 UV absorbance spectrum of acrolein

Pressure Decay During Photopolymerization

The rate of apparent polymerization in the gas phase was followed by measuring the monomer vapor pressure drop in the reaction cell. Fig. 3 shows the time dependence of monomer pressure in the gas phase during the photopolymerization of acrolein. An induction period, indicated by a delay in the onset of pressure decay, was observed in all samples. When an Al substrate was present, there was a 30 min induction period followed by an exponential decay of the monomer pressure, demonstrating first-order photopolymerization kinetics. After approximately 1.5 hours the pressure appears to decay linearly with time, which might be caused by the deposited layers of polymer on the Al substrate as the reaction proceeded. Similar induction period, first order kinetics, and subsequent linear pressure decay were observed in the case of Ni substrate. There was no possibility of a dark reaction being initiated by the irradiation as shown in Fig. 3 by the corresponding flat portions of the curves. A shorter induction period was found without a metal substrate. The reaction rate was found to be first-order in monomer concentration after a 15 min induction period. It is also interesting to note the existence of the possibility of a dark reaction being initiated by the irradiation which is in contrast to the case of Al and Ni substrates reactions. This is partially due to the fast quenching effect of the metal substrate on free radicals.

5
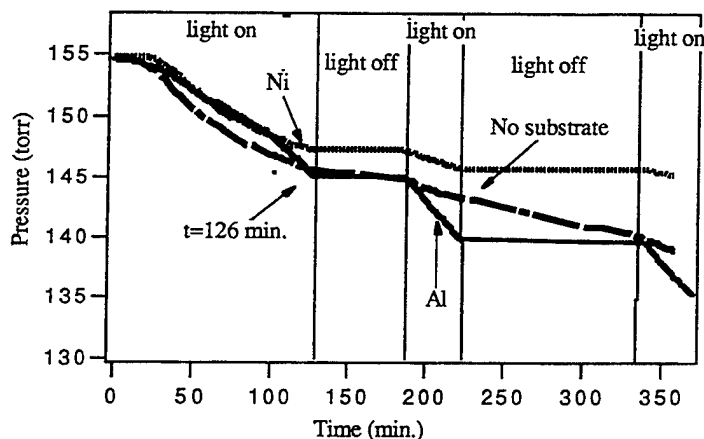
Fig. 3. Time dependence of pressure. The irradiation was turned on and off as indicated.

Steady State Surface Second Harmonic Generation Intensity:

The surface reaction rate law can be determined by monitoring the time dependence of surface monomer concentration decay during photopolymerization. SSHG from a metal surface arises from its free-electron-like polarizability. The adsorbates on metals reduce the free electron response due to the partial localization of the electrons upon adsorption. This means SSHG intensity can differentiate between the metal, metal/polymer, and metal/monomer surfaces. The SSHG intensities from Al, Au, and polyacrolein surfaces were obtained. Fig. 4 shows that the SSHG intensities from the Al and Au surfaces are larger than that from polyacrolein. The difference enables the surface unreacted monomer coverage to be monitored by following the SHG intensity decay during photopolymerization.

The SSHG measurement had no effect on the photopolymerization kinetics indicated by the UV-VIS absorbance spectrum of acrolein at the reaction temperature as shown in Fig. 2. Acrolein has zero absorbance at the fundamental light (1064 nm) and the SSHG (532 nm).
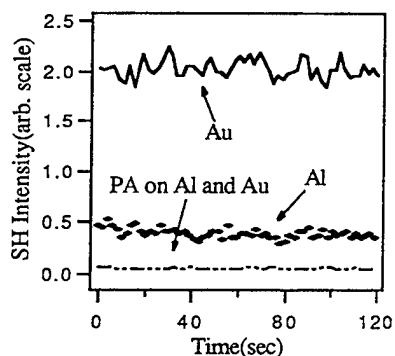
Fig. 4. SHG intensity from Au, Al and PA/Al, Au
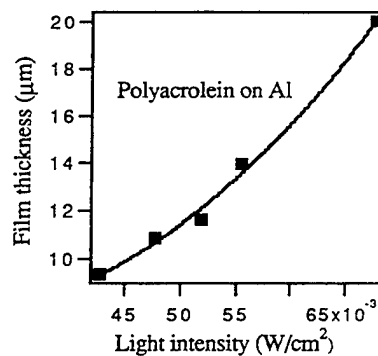
Fig.5. Film thickness vs. light intensity

6

<u>Light Intensity Dependence of Final Film Thickness</u>

Photopolymerization of acrolein onto an Al substrate was carried out for 30 min at room temperature (22°C) as a function of light intensity and the dependence of the final film thickness was obtained. It was reported[15] that thermopolymerization can be minimized by keeping the power/area less than 100 mW/cm^2. A UG-11 filter kept the light intensity below 100 mW/cm^2. The final film thickness was calculated from the film weight gain and surface area by assuming a constant density of the polymer film (polyacrolein density is 1320 kg/m^3)[16]. Fig. 5 shows that the polymer film thickness increases with the increase of light intensity.

<u>Structure of Polyacrolein Formed on Al, Ni, and Au</u>

The IR spectra of polyacrolein formed on Al, Ni, and Au are shown in Fig. 6. In all the spectra, polyacrolein chains contained bonds corresponding to ether, acetal, carbonyl, and unsaturated hydrocarbonyl groups in various amounts. The hydrocarbon, carbonyl, and -CO-H peaks from the spectrum of polyacrolein on Au were observed at different wavenumbers than those from polyacrolein formed on Al and Ni. The spectra of polyacrolein formed on Al and on Ni exhibited peaks at the same wavenumber with different intensities. It is not clear at this stage whether Al, Ni, and Au substrates have catalytic effects on the photo-polymerization. However, a metal surface does affect the polymer structure.

Polyacrolein has been reported as a complex, crosslinked polymer, often referred to as "disacryl', with cyclic acetal and hemiacetal (tetrahydropyran) structural units as well as free aldehyde.[17] The polymer formed on an Al substrate was insoluble in all common solvents and became swollen after extensive soaking in a base bath and acidic solution. The glass transition temperature of polyacrolein formed on an Al substrate was 118.7°C. It was observed that at temperature above 250°C the polymer charred instead of melting also indicating a crosslinked polymer structure.
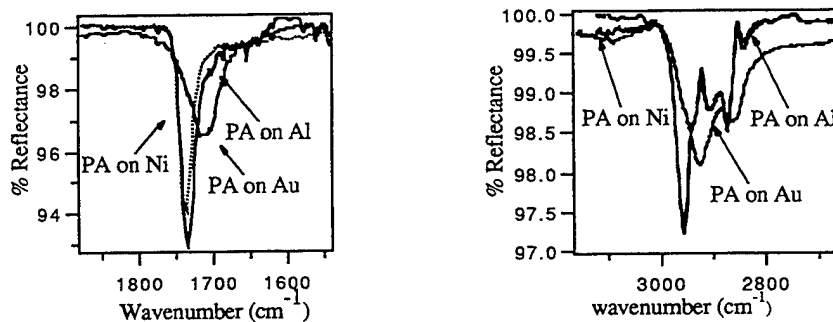
Fig. 6. IR specta of polyacrolein formed on Al, Ni, and Au substrates

<u>Microspherical Structure of Polyacrolein Formed on Al, Ni, and Au</u>

The SEMs of polyacrolein formed on Al, Ni, and Au substrates are shown in Fig. 7. An irregular array of ellipsoidal particles with size ranging from 1-5 µm were found from the polyacrolein formed on Al and Ni. However, the micrograph of polyacrolein formed on Au has uniformly distributed leaf-like particles. Evidence of particle aggregation was observed at

2000x magnification. In the gas phase photopolymerization, particle size and distribution were limited by the collision of radicals with other radicals, with a metal substrate, and with the wall of the reaction cell. The deposition of particles on all the surfaces in the reaction cell indicated that initiation occurred in the gas phase. However, the insoluble, continuous polyacrolein film demonstrated that the polymer growth occurred in the monomer adlayer on Al, Ni, and Au substrates as opposed to the film being formed from the deposition of polymer particle aggregates in the gas phase. The different types of micrographs observed in polyacrolein formed on Au and Al also confirmed the effect of substrate structure on the formation of polymer.

| (a) | (b) | (c) |
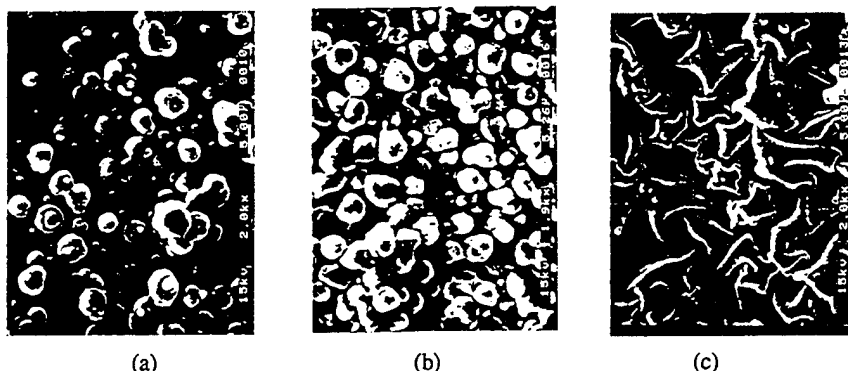
Fig. 7. SEMs of polyacrolein formed on (a) Al (x 2,000), (b) Ni (x 2000), and (c) Au (x 2,000)

CONCLUSIONS

The determination of photopolymerization dynamics is imperative to the enhanced control of thin film growth and film properties. A unique method was established here to study the photoinitiation and dynamics of photopolymerization on Al, Ni and Au substrates by monitoring the gas phase kinetics and surface dynamics *in-situ* and in real time. An induction period was observed in the gas phase of the acrolein photopolymerization. The Al and Ni substrate had a significant effect on the apparent rate of the reaction. No dark reaction was observed when Al and Ni substrates were present, but a dark reaction occurred in the absence of a metal surface. The effects of Al, Ni, and Au substrates on polymer film properties were studied using SEM and FTIR-ATR. The significant differences in the metal/monomer interaction during photopolymerization were illustrated by the SEM micrographs of polyacrolein formed Al and Au substrates, as well as that from FTIR-ATR spectra. These preliminary results demonstrated the importance in studying the surface photopolymerization dynamics. SSHG was developed here and provides an approach for studying the surface dynamics. The SHG intensities from Au, Al, polyacrolein on Al, and polyacrolein on Au were obtained. Future work will emphasize characterizing the surface dynamics of photopolymerization using SSHG.

REFERENCES

1. A. Barraud, C. Rosilio, A.R. Texier, Thin Solid Films **68**, 91 (1980)
2. H. Ringsdorf, Agrew Chem.Int. Ed. **15**, 764 (1976)
3. B. Maun and H. Kuhn, J. Appl. Phys. **42**, 4398 (1971)
4. F.E. Blacet, G.H. Fielding, J.G. Roof. J. Am. Soc. **59**, 2375 (1935)
5. H.W. Melville, Proc. Royal. Soc. A. **163**, 511 (1957)

6. F.D. Lewis, M.J. Nepras, H.L. Hampsch, Tetrahedron **43** (7), 1635 (1987)
7. A.N. White, in <u>Polymer surfaces</u>, edited by D.T. Clark and W.J. Feast (John Wiley & Sons, New York, 1978), p.155
8. G. Odian, <u>Principle of Polymerization Chemistry, ed.</u> (John Wiley and Sons, New York, 1981) p. 179
9. J.Y. Tsao and D.J. Enrlich, Appl. Phys. Lett. **42** (12), 997 (1983)
10. R.M. Corn and D.A. Higgins, Chem.. Rev. **94**, 107 (1994)
11. F.R. Aussenegg, A. Leitner, H. Gold, Appl. Phys. A **60**, 97 (1995)
12. Y.R. Shen, Annu. Rev. Phys. Chem. **40**, 327 (1989)
13. T.F. Heinz, Nonlinear Surface Elactromagnetic Phenomena, edited by H.F. Ponatch and G.I. Stegence (Elserier Science Publishers, 1991)
14. G. Berkovics, Th. Rasing, Y.R. Shen, J. Chem. Phys. **85** (12), 7374 (1986)
15. X.L. Zhuo, X.Y. Zhu, J.M. White, Surface Science Report **13**, 73 (1991)
16. R.F. Fishier, in <u>Acrolein,</u> edited by C.W. Smith (John Wiley & Sons, New York, 1962) p.211
17. A. Usanmaz and R.D. Dogan, Polymer J. **22** (3), 233 (1990)

BONDING AND PENETRATION AT METAL/SELF-ASSEMBLED ORGANIC MONOLAYER INTERFACES

D. R. JUNG, A. W. CZANDERNA, and G. C. HERDT
National Renewable Energy Laboratory, 1617 Cole Blvd., Golden, CO 80401

ABSTRACT

The purpose of research on metals (M) deposited onto self-assembled monolayers (SAMs) is to understand the interactions between the metal and eventually metal oxide overlayers on well-ordered organic substrates. Applications of M/SAM and inorganic/SAM research results to the understanding of real inorganic/organic interfaces in vacuum and under environmental conditions can potentially play a key role in the development of advanced devices with stable interfacial properties. The results of selected M/SAM studies to date are reviewed, and M/SAM combinations ranked according to reactivity and penetration. Specific examples of reactive interfaces (Cu/COOH, Cr/several groups) and nonreactive interfaces with penetration (Ag/CH$_3$, Ag/COOH) are used to illustrate the extremes.

INTRODUCTION

This review summarizes part of recent research[1-11] to identify metal/organic functional group interactions at metal/self-assembled monolayers (SAM) interfaces, primarily by means of X-ray photoelectron spectroscopy (XPS),[1-4,8-11] or to elucidate penetration rates of metal overlayers through the SAM using ion scattering spectroscopy (ISS).[5-7] As illustrated in Figure 1a, SAMs have fulfilled a need for model systems with highly ordered organic surfaces of uniform chemical composition for studying interactions at metal or metal oxide/organic interfaces.[1-11] Chemical bonding at metal/organic interfaces plays an important role in the reliability and durability of many technological devices.[12] Until recently, bonding at metal/organic interfaces was typically studied either by surface analysis of organic species adsorbed onto single crystal metal surfaces[13,14] or by surface analysis of metalized polymers.[15,16] The chemical environment studied in the first type of experiment bears little resemblance to that present at polymer/metal (oxide) interfaces. In contrast, the lack of structural and chemical order of polymer surfaces complicates the location and type of interactions with metal or oxide overlayers.

Reactive transition metals (e.g., Cr and Ti) are frequently used to promote adhesion at metal/polymer interfaces, and have been the subject of many studies.[17-20] Less reactive metals (e.g., Ag and Cu) are frequently used as metalization coatings of polymers for mirror applications or as grid lines in photovoltaic cells, which may contain polymer/metal interfaces. For studying the stability or reactivity of interfaces, SAMs are ideal because they form highly ordered, thermally stable arrays of close-packed aliphatic chains terminated by a surface of uniform chemical functionality as originally cited in the work of Allara and Nuzzo[21-22] and recently reviewed by others (Table 1).[23,24] SAMs with a variety of terminating functional groups are now available, making studies of the interaction between an organic surface of a known functionality and a known metal species possible. Progress in studying alkane thiol SAMs terminated with CH$_3$, OH, COOH, COOCH$_3$, and CN with Ti, Cr, Cu, Ni, Al, K, Na, Ag overlayers has been summarized and critically reviewed.[10]

Objectives of Recent Research

In support of the main goal of M/SAM research (understanding the interactions between M and MO overlayers on SAMs), the objectives of recent work have been to: (a) identify new chemical compounds or complexes, and intermediate stages in compound formation, if any; (b) measure as a function of the ratio of deposited metal atoms to SAM organic functional groups (OFGs), the three main configurations of metal that may be present, as illustrated in Figure 1b: S (smooth metal that is chemically bonded or complexed with the SAM and probably spread out on top of the SAM, C (clustered) nonbonded metal that is on top of the SAM and probably in the form of large clusters, and P (penetrating) nonbonded metal that significantly penetrates the SAM and whose morphology could take many forms; (c) compare quantities S, C, and P for deposition at different rates on surfaces at different temperatures, and thereby search for evidence of activated processes, metastable/nonequilibrium states, and results that depend on the degree of SAM ordering; (d) obtain images of clusters on the SAM (by scanning probe or electron microscopy), and use the distribution of cluster sizes, the rate of deposition, and the surface temperature as parameters to model the kinetics of cluster nucleation and growth; (e) characterize the degree of ordering and close packing of the SAM before and after metallization (are pinholes playing a role?); and (f) measure rates of penetration of metal through the SAM.

TABLE 1
Some Properties of Thiol/Au SAMs as
Summarized by Dubois and Nuzzo[24]

Strength of Au thiolate bond	~44 kcal/mol
Superlattice of S head groups on Au (111)	$(\sqrt{3}x\sqrt{3})R30°$
S-S nearest-neighbor spacing	4.99 Å
Tilt angle of methylene chain axis from surface normal	~25-30°
Twist angle of the C-C-C plane from the plane containing the chain axis and the surface normal	~52°
T at which significant chain disordering occurs	~380 K
T at which a C22 thiolate monolayer decomposes/desorbs	~500 K

Critical Questions in M/SAM Research

The lowest energy state of a M/SAM system is that for which all the deposited metal forms between the substrate and the SAM, because the surface free energies of metals are much higher than those of organics. Thus, two critical questions about M/SAM research are: are the configurations S and C of Fig. 1b stable at room temperature, and what factors determine that stability?

Chemical interactions (objective (a)) surely play a major role in the formation of a M/SAM interface. The scheme depicted in Fig. 1b, and our corresponding identification of species S with chemical bonding and species C and P with nonbonding, are intended as idealizations (e.g., we neglect the role of metal carbide formation which could occur along the entire chain). Studies that address objective (a) in combination with objectives (b), (d), or (f) can yield information on the correlation of the chemistry of the M/SAM system with the way that the metal is distributed in or on the SAM.

Objectives (c) and (e) are concerned with *how* a M/SAM system attains the observed chemical state and spatial distribution. The process of adlayer nucleation and growth, a competition that is kinetically dependent on surface temperature and deposition rate, may be considerably more complex than that found for two-dimensional systems if there is diffusion into (and not just over) the SAM. The mechanism of penetration may involve different possible rate-limiting steps, for example, lateral diffusion leading to penetration at defect sites vs. direct vertical diffusion that might be enabled by thermal motion (because of ambient

(a)

Metal of interest

Deposited metal

OFG of interest

SAM

Attachment to substrate

Substrate

(a) Vacuum

Overlayer

SAM

Substrate

(b)

S   C   P

(a)

z

z

y   x

α
27°

β
50°

X

H   H
H   H   LEED, He diffraction

Ellipsometry

IR, Raman, X-ray diffraction, NEXAFS

S   LEED, TEM electron diffraction, STM

(b)

X = CH₃   CO₂CH₃   CH₂OH   CO₂H
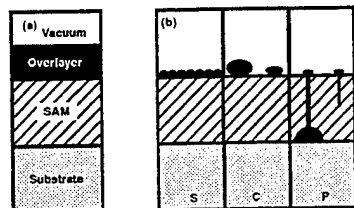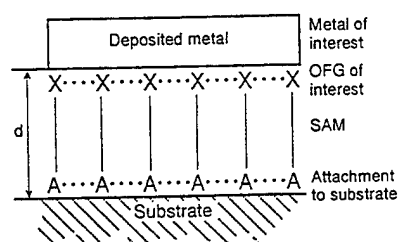
Fig. 1 (a) Idealized scheme for using an organized molecular assembly to form an interface between a metal overlayer and an organic functional group. The thickness of the SAM is d, and is the length of the molecule at perpendicular attachment. For an MUA SAM on gold, the attachment group is a thiolate and the methylene chain is 28° from the normal; (b) cross-sections of the principally observed results to date in which there is (S) strong metal-OFG interaction, (C) weak metal-OFG interaction, and (P) very weak metal-OFG interaction. The designations S, C, and P stand for smooth, clustered, and penetrating, respectively.
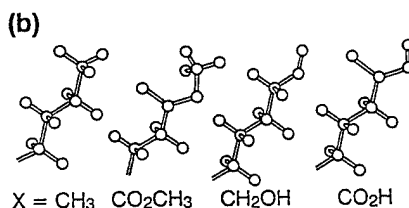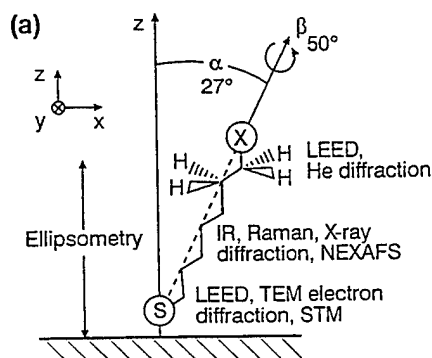
Fig. 2. (a) Schematic side-view of the orientation of a single, long-chain thiol molecule adsorbed on gold. The tilt angle (α) is with respect to the surface normal, whereas the twist angle (β) is with respect to a plane established by the chain axis and the surface normal vectors. The techniques listed to the right are those used to determine the structure of that portion of the molecule. (b) The surface projections of several representative group. (From Dubois, L. H. and Nuzzo, R. G. (1992), *Ann. Rev. Phys. Chem.*, 43, 437; With permission.)

13

thermal energy or transient thermal energy imparted by atom impact), chemical reaction with and saturation of the OFG, or disordering due to strong chemical effects.

The sorting of the various possibilities of chemical states and spatial distributions will require, in most cases, experimentation with both structural and spectroscopic probes under varying conditions of deposition rate and surface temperature. After this information is available, some general conclusions about processes at M/SAM interfaces may emerge that can be extended to predict processes at M/polymer interfaces. Detailed process information may result only from quantitative comparison with theoretical calculations and simulations of these systems.

Experimental Evidence for the Order and Structure of Alkane-Thiols on Gold

The properties of thiol monolayers on gold (Fig. 2) have been the subject of a recent review article[24] and are briefly summarized in Table 1. The characteristics of the ordered SAM include: (1) the presence of the desired OFG at the vacuum/SAM interface; (2) a low density of pinholes in the film; (3) uniform film thickness; (4) uniform average orientation of constituent molecules; (5) a low population of gauche bonds in the methylene chains; (6) lateral ordering (real-space Bravais lattice or translational symmetry vectors) and internal structure of the unit cell of the SAM monolayer; and (7) a domain size of coherent lateral order.

Of characteristics (1) through (7), (1) has been conveniently probed by measuring the contact angles of sessile drops of water and other liquids on the SAM surface; (2) has been probed by several techniques including STM, ISS, and cyclic voltammetry and show no (significant) evidence of pinholes; (3) has been shown by single-wavelength ellipsometry; (4) and (5) have been indicated from Fourier transform reflection absorption infrared spectroscopy (FT-RAIRS), surface Raman spectroscopy, and near-edge X-ray absorption fine structure (NEXAFS) spectroscopy; (6) has been deduced from diffraction patterns from the scattering of electrons, X-rays (XRD, or X-ray diffraction) and low-energy helium atoms (HAS, helium atom scattering); and (7) has been determined for the alkane thiolate SAM on Au to be approximately 60 Å by transmission electron diffraction (TEM), but results from XRD and HAS show 89 and 44 Å, respectively. Both STM and AFM studies have yielded images exhibiting $\sqrt{3}$ x $\sqrt{3}$ lattice patterns consistent with the diffraction results for these SAMs. The robust mechanical properties of SAMs, which have been deduced from interfacial force microscopy (IFM) studies, are particularly relevant for the potential uses of SAMs for surface modification as well as the question of damage or disordering that may occur in M/SAM studies. These and other film characteristics (e.g., their wettability by water and other liquids) are described further by Dubois and Nuzzo.[24]

Definitions Used In This Article

AFM atomic force microscopy; BE, binding energy; FT-RAIRS, Fourier transform reflection absorption infrared spectroscopy; HAS, helium atom scattering; IFM, interfacial force microscopy; ISS, ion scattering spectroscopy; M or MO, metal or metal oxide; M/SAM, metal/self-assembled monolayer; NEXAFS, near-edge X-ray absorption find structure; NREL, National Renewable Energy Laboratory; ODT, octadecanethiol, $HS(CH_2)_{17}CH_3$; OFG, organic functional group; RAIRS, reflection absorption infrared spectroscopy; SAM, self-assembled monolayer; SE, spectroscopic ellipsometry; (S)TEM, (scanning) transmission electron microscopy; STM, scanning tunneling microscopy; UV, ultraviolet; XPS, X-ray photoelectron spectroscopy; XRD, X-ray diffraction.

EXPERIMENTAL

A detailed list and critique of the experimental measurements used to characterize SAMs is available,[10] including all those identified in the preceding section. For the typical results presented in this article, the use of XPS and ISS will be described. The sample preparation methods described below are similar to those reported by other groups.

SAM Preparation

The SAMs were formed by immersing clean gold thin film samples in ethanolic solutions of $HS(CH_2)_{11}CN$, $HS(CH_2)_{17}CH_3$, $HS(CH_2)_{10}COOH$, or $HS(CH_2)_{15}COOH$, using the well-known self-assembly process for alkyl thiols.[21,24,25] Some of the gold films were prepared by evaporating 80 nm Au directly onto Ar^+ ion bombardment-cleaned Si wafer coupons,[26] while others were prepared by evaporating a 9 nm Cr adhesion layer followed by a 200 nm Au layer onto solvent-cleaned Si wafers. The hillock sizes of these two types of gold films have been measured by scanning tunneling microscopy (STM) and atomic force microscopy (AFM) to be 30-50 nm wide and 10 nm high for the Ar^+ ion sputtered substrates and about 100 nm wide and 10 nm high for the Cr-adhered Au films. In most cases, the Au surfaces were placed in a UV-ozone cleaner for 5 min to remove trace organic contaminants[27] prior to immersion in the thiol. Water contact angles of less than 10° were observed on the Au surface only if such a cleaning procedure was used. Following incubation times of 2-4 days at 295 K, a sample was removed, rinsed in ethanol, dried, and checked by water contact angle for the presence of the SAM. Contact angles of 10°-20°±2°, 64°±2°, and 112°±2° observed in this study for the COOH-, CN- and CH_3-terminated SAMs, respectively, are in good agreement with published results.[25]

Evaporative Deposition of the Metal

Evaporative deposition of the metal onto the SAMs and subsequent X-ray photoelectron spectroscopy (XPS) and ISS analysis were carried out using a Leybold-Heraeus LHS-10 surface analysis system. The LHS-10 is equipped with an analysis chamber and a sample preparation chamber through which a sample introduction rod can be translated without breaking vacuum. The sample preparation chamber is equipped with two vacuum feedthroughs that provide power to crucibles used for evaporative deposition. Deposition rates are measured with a quartz crystal oscillator using an IC 6000 deposition monitor. A negligible amount of sample heating occurs during deposition because the sample to source distance is approximately 38 cm. An X-ray source for XPS analysis, an ion gun for sputtering and for ISS, and a concentric hemispherical energy analyzer (CHA) are attached to the analysis chamber. The CHA is used to determine the energies of scattered ions in ISS. A complete description of this apparatus and its use for XPS and ISS have been presented previously.[28]

With the sample mounted onto a hot/cold transfer rod (initially at room temperature) and inserted into the LHS-10 chamber that is maintained at a base pressure of $2-5 \times 10^{-8}$ Pa, deposition of the metal took place in an attached preparation chamber that permits *in situ* transfer of the sample to and from the XPS (or ISS) analysis chamber at constant temperature. The sample was allowed to outgas at room temperature for 1 h prior to heating or exposure to X rays. In our standard procedure, the sample was: characterized by XPS at 295 K, heated or cooled as desired, recharacterized by XPS, exposed to the first incremental deposition of metal, and again characterized by XPS.[1,4-6] Repeated

deposition/characterization cycles were performed in some cases, resulting in total coverages of up to 20 Å. Typically, a time period of up to 2 h was required for each cycle of XPS characterization involving a survey spectrum and narrow scan spectra. In this paper, we refer to the amount of metal deposited as a uniform coverage, e.g., 1.0 nm Ag, as though it is uniformly covering the surface of the SAM. We are aware that clustering may occur, but must provide a frame of reference. In all experiments less than 3 min elapsed between the end of metal deposition and the beginning of the XPS or ISS analysis.

The photoelectron spectra were recorded using a non-monochromatic Mg $K\alpha$ X-ray source operated at 240 W. Narrow scans were taken using constant pass energies of 50 eV for C $1s$, O $1s$, Au $4f$, Cu $2p$, Ag $3d$, and Cr $2p$ (for coverages of 2 Å or more) and 200 eV for Cr $2p$ (for coverages below 2 Å) and N $1s$. Survey scans were taken in the constant transmission mode with a retardation ratio of 3. For determining XPS peak areas and binding energies, the C $1s$ narrow-scan line shapes were fit with a linear background and 85% Gaussian-15% Lorentzian (G/L) product functions of appropriate peak widths for each of the high resolution scans.

ISS compositional depth profiles were measured using 1 keV $^3He^+$ ions at a current density of 0.2 μA/cm^2 and temperatures from 113 to 293 K. The ion beam was rastered over a 2 mm x 2 mm area with the detected signal gated at a 70% aperture to minimize the signal from the etch-pit walls. During ISS analysis, He from the ion gun caused the chamber pressure to increase from a base pressure below $2x10^{-9}$ Torr to a carefully maintained pressure of $4x10^{-7}$ Torr. Each ISS spectrum was acquired over a period of approximately 40 s. Detection of C with $^3He^+$ is limited by the number of H atoms bonded to the C. Carbon in CH$_3$ or CH$_2$ is difficult to detect with ISS, but C or CH exposed to the ion beam are detectable. Consequently, we did not detect C in our compositional depth profiles. Sulfur from the thiol has been observed by ISS in previous work. Accordingly, data were taken over an energy range E/E_o of 0.850 to 1.0, to obtain depth profiles with good time resolution and good signal-to-noise.

RESULTS AND DISCUSSION

We present and discuss in this section a summary of the M/OFG combinations studied to date and rank them according to their relative reactivity and degree of penetration into the SAM.[10] We then present and discuss typical results for the reactivity of Cr/CN and Cu/COOH and the rate of penetration of Ag/CH$_3$ and Ag/COOH.

Ranking of M/OFG Combinations According to Reactivity and Penetration

In Table 2, based on the XPS and FT-RAIRS results, we have ranked the chemical reactivity of the various M/SAM systems according to the OFG of the SAM. Likewise, in Table 3, we have ranked the penetration of the M/SAM systems according to the XPS results reported for the different OFGs and different chain lengths of the SAMs. A dependence of the degree of penetration on the temperature of the sample, that is, lower penetration for lower temperatures, has been found for the systems of Cr/CN, Ni/CN, and Cu/CN (Reference 4; T = 173 K), Ag/CH$_3$ (References 5-7; T ≥ 90 K), and Ag/COOH (Reference 32). A dependence on the length of the thiolate molecule may also affect the XPS results shown in Table 3, that is, shorter molecules show evidence for permitting greater penetration.

We conclude from these rankings that the degree of penetration increases with decreasing reactivity. In order for the adsorbed metal atom or cluster to penetrate, it first must encounter the OFG. If there is a reaction there, then penetration is unlikely. If there is

TABLE 2. Ranking of the Reactivity of M/SAM Systems by Metal and OFG

Reactivity	Metal	Organic Functional Group	Type of Bonding	Ref.
Very high	Ti	COOH, COOCH$_3$, CH$_3$OH	Oxide and carbide	9
Very high	Cr	COOCH$_3$	Oxide and carbide	8
High	Ti, Cr	CH$_3$	Carbide	4, 8, 9
High	Cr	CN	Nitride and carbide	4, 8
Intermediate	Al	COOCH$_3$ (preheat-treatment)	Oxide	29
Intermediate	Al	COOCH$_3$ (postheat-treatment)	Metal-carboxylate	29
Intermediate	Cu	COOH, CH$_2$OH	Unidentate metal oxide	1, 2
Intermediate	K, Cu	COOCH$_3$	Metal-carboxylate	8, 29
Low	Ni, Cu	CN	Unspecified	3, 4, 8
No reaction	Ag, Al, Na	CH$_3$, COOH	---------	5, 7, 30, 31, 32

Notes: References are given to FT-RAIRS or XPS results, except for Na/CH$_3$. The degree of reactivity is based on the authors' interpretation of the results.

TABLE 3. XPS Evidence for Penetration in M/SAM Systems (All Au\S-(CH$_2$)$_n$-OFG) at Room Temperature (RT) and at Lower Temperatures (LT).

n	Metal	OFG	Metal Shift RT	Metal Shift LT	C 1s attenuation RT	C 1s attenuation LT	Penetration RT	Penetration LT	Ref.
15	Ti	COOH	HBE	?	?	?	Very low	?	9
15	Ti	COOCH$_3$	HBE	?	?	?	Very low	?	9
15	Ti	CH$_2$OH	HBE	-?	?	?	Very low	?	9
15	Cr	COOCH$_3$	HBE	?	?	?	Very low	?	8
15	Ti, Cr	CH3	HBE	?	?	?	Low	?	4,8,9
15	Cr	CN	HBE	?	?	?	Low	?	8
11	Cr	CN	HBE	HBE	Slightly	OK	Low	Low	4
15	Cu	COOCH$_3$	HBE	?	?	?	Low	?	8
10	Cu	COOH	Zero	?	?	?	Low	?	1
10	Cu	CH$_2$OH	LBE	?	Low	?	Moderate	?	2
11	Ni	CN	Zero	HBE	Low	Slightly low	Moderate	Low	4
15	Cu	CN	HBE	?	?	?	Low	?	8
11	Cu	CN	LBE	HBE	Quite low	?	Moderate	Low	3,4
17	Ag	CH$_3$	LBE	HBE	Zero	?	High	Low	5,6,7
10	Ag	COOH	HBE	?	?	?	Moderate	Low	32
15	Ag	COOH	HBE	?	?	?	Low	Low	32

Notes: The metal shift refers to whether a core level has been measured at low coverages to exhibit a high binding energy or low binding energy shift, HBE or LBE, respectively, with respect to the bulk metal core level. "C 1s attenuation" refers to the attenuation of the C 1s level compared to that expected for a uniform metal overlayer. References to the sources of these XPS results are given. Question marks (?) indicate that the information has not been reported. The degree of penetration is based on the authors' interpretation of the available XPS results, in which "very high" means the overlayer essentially resides in the same plane of the OFG and "high" means the overlayer penetrates to the Au/SAM interface.

17

no reaction, then penetration can proceed in some cases. Rates of penetration have only been measured in the cases of Ag[5-7] and Na[30,31] on CH$_3$-terminated SAMs and for Ag on COOH-SAMs.[32] Table 2 shows that the reactivity is highest for the oxygen-containing OFGs, (except for Ag/COOH) intermediate for the CN OFG, and lowest for the CH$_3$ OFG. For the metals, Ti is the most reactive, followed by Cr, Al, K, Ni, Cu, Na, and Ag, although the data for Al, K, Ni, and Na are scant. The decreasing reactivity within the transition metal series, Ti, Ni, and Cu, and the low reactivity of the noble metals, Cu and Ag, is in the same order as the filling of the d orbitals. The relative reactivity of trivalent Al and the monovalent alkali metals (Na, K) is not so clear at this point because so few of these M/SAM systems have been explored. Evaporating oxygen-free Al films has not been successful, as yet.[33] The M/SAM studies involving Al evaporation may have been affected by rapid oxidation of the deposit,[33] which would have had a severe effect on the chemical interactions at the interface.

There is some evidence that the reactivity of the SAM with the incoming M is also dependent on the SAM temperature.[4,11] Activation of M/SAM reactions may be because of electronic, steric, or structural factors and is not unexpected. Further temperature-dependent studies are warranted in order to learn more about activation energies in M/SAM reactions.

Reactive System: C 1s XPS Line Shapes for Cr/CN

The C 1s line shapes are shown in Figs. 3(a) and 3(b) for 0.6 and 6 Å Cr coverages, respectively, for deposition onto a series of different Au/S(CH$_2$)$_{11}$CN samples held at 173, 295, 323, and 373 K, along with the C 1s line shape for a bare SAM for comparison. The most striking difference in Fig. 3 is the steady increase from 295 to 373 K in the ~283 eV low binding energy (LBE) shoulder [Fig. 3(b)] that we assign to a Cr carbide species. A shift in the high binding energy (HBE) peak also is observed.

The HBE C 1s peak of the CN-terminated SAMs is found at 286.85±0.1 eV for zero Cr coverage, and is attributed to the end-most, nitrile carbon and its nearest (α) neighbor along the chain. At 6 Å Cr coverage the HBE peak shifts to 286.45±0.1 eV for lower temperatures (173-295 K) and to 286.25±0.15 eV for higher temperatures (323-373 K). The larger shift of this HBE C 1s component (about 0.2 eV) shows there is a slight increase in Cr(CN) reactivity in the higher temperature range. Similar results are found at lower Cr coverages, as shown in Fig. 3(a). The shift with Cr deposition probably results from a net charge transfer from Cr to CN molecular orbitals that increases the charge in the valence levels of the two endmost carbons. More detail about curve fitting of the C 1s line shapes, estimates of the chromium carbide stoichiometry (Cr$_3$C$_2$), and control experiments for assessing the influence of X-ray damage is available.[11]

Reactive System: Binding Energies of the XPS Cr 2p Levels

In Ref. 4, we discussed the correlation of metal penetration into or possibly through the SAM with the position of the Cr 2p BEs. The Cr 2p positions are shown in Fig. 4. They are shifted to HBE for Cr deposited at 295 and 173 K onto the CN SAM [Fig. 4(b)], consistent with little or no penetration. They are shifted to LBE for Cr deposited at 295 K onto Au [Fig. 4(a)], consistent with thin Cr deposits on a conducting substrate. They are not shifted, but are approximately at the bulk position, for Cr deposited at 323 and 373 K [Fig. 4(b)]. These results show smaller, negligible HBE shifts for 323 and 373 K compared to 295 K. In terms of the core hole lifetime/final state effect supported by Wertheim for the shifts of metal clusters on insulating substrates,[34] our result is consistent with some degree of penetration at 323 and 373 K.
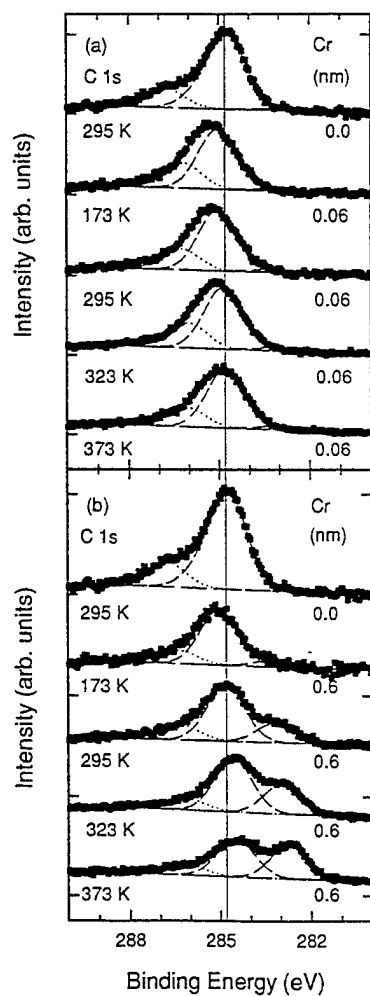
Fig. 3. C 1s XPS line shapes for the bare Au/S(CH$_2$)$_{11}$CN SAM at 295 K (top of a and b), and for (a) 0.6 Å Cr and (b) 6 Å Cr deposited on a series of Au/S(CH$_2$)$_{11}$CN SAMs at temperatures of 173, 295, 323, and 373 K, as labeled. The plots at 6 Å coverage have been increased in intensity by a factor of 1.5 for clarity. The position of the solid vertical line is 284.8 eV.
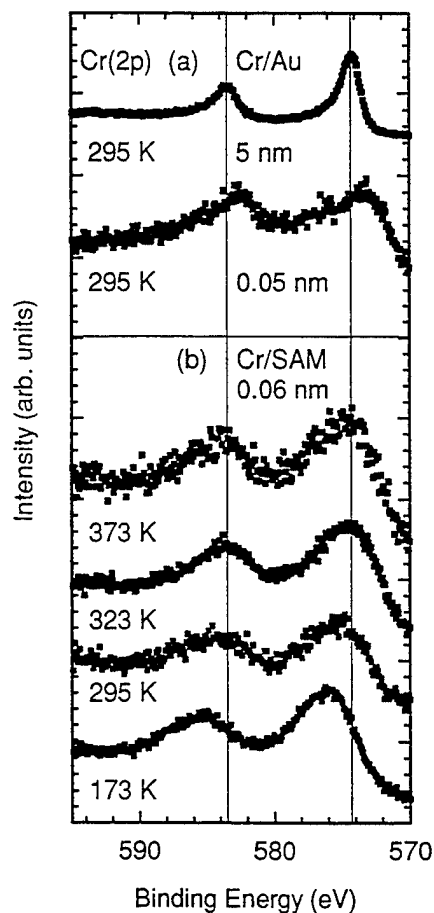
Fig. 4. Cr 2p XPS line shapes (a) for 0.5 and 50 Å Cr on Au at 295 K, and (b) for 0.6 Å Cr deposited onto a series of Au/S(CH$_2$)$_{11}$CN SAMs at 173, 295, 323, and 373 K, as labeled. The solid vertical lines at 583.45 and 574.25 eV mark the peak positions for bulk Cr 2p.

19

Reactive System: O 1s XPS Line Shapes for Cu/COOH

Czanderna et al. deposited Cu on the $HS(CH_2)_{10}COOH$ SAM and performed XPS as a function of coverage.[1] Changes were reported in the O 1s line shape (Fig. 5) that showed a constant component corresponding to the C=O oxygen, as well as a component due to the C-oxygen that shifted to lower BE with increasing Cu coverage. In addition, they observed a strong HBE shoulder on the low-coverage Cu 2p 3/2 peak (Fig. 6), no Cu 2p shake-up satellites due to Cu(II), and a Cu Auger peak consistent with a Cu(I) oxidation state. All of these data together were cited in support of the formation of a unidentate Cu(I)-O complex at the single-bonded O atom of the SAM. The leveling off of growth of the HBE Cu 2p component was interpreted as evidence that the Cu-COOH interaction was complete at a coverage of 0.2 to 0.6 nm Cu. This was the first M/SAM work published by the NREL group, although work with Cu on CH_3-, OH-, COOH-, and CN-terminated SAMs was begun in 1988 and yielded preliminary results that were reported in 1989. Further detailed discussion of these results is available.[1]

Penetrating Systems: ISS CDP of Ag/CH$_3$ and Ag/COOH from 113 K to 293 K

ISS compositional depth profiles were obtained from 113 to 293 K to study the penetration of Ag into ODT, MUA, and MDA, as a function of temperature. For all of these experiments, 1.0 nm Ag was deposited at a rate of approximately 0.01 nm/s onto the SAM prior to depth profiling. The elapsed time after starting metal deposition and completion of the first ISS spectrum was approximately 300 s (100 s, deposition; 160 s, sample transfer; and 40 s, first ISS spectrum). Thus, 5 min elapsed for time-dependent processes to proceed before our "initial" spectrum was taken during depth profiling. An ion beam current density of 0.2 $\mu A/cm^2$ was used for all ISS depth profiles. XPS and ISS measurements were carried out on several samples at 193 K and verified that no detectable oxygen signal could be obtained from the ODT samples. These data indicate that no ice formed on the samples during low temperature experiments.

The plots in Fig. 7 show the *fraction* of Ag (Ag intensity divided by Ag intensity plus Au intensity) in the ISS depth profiles as a function of erosion time at temperatures from 113 to 293 K. The data are consistent with an increasing rate of Ag penetration to the ODT/Au interface at progressively higher temperatures, which results in greater Au intensities that are detected concomitantly with Ag when the Ag is at the ODT/Au interface. The time to erode through a "bare" ODT SAM to the ODT/Au interface is about 1000 s at 0.2 $\mu A/cm^2$. The plots in Fig. 7 are consistent with a model of Ag residing on the methyl end group of ODT at liquid nitrogen temperatures and at the ODT/Au interface at 293 K.[7] The data also elucidate the temperature regime over which the rate of penetration increases rapidly. The residual Ag signal for erosion times greater than about 2000 s, which corresponds to the location of the ODT/Au interface, indicates the presence of Ag clusters at the ODT/Au interface.

The integrated initial ISS Ag peak intensity is shown as a function of temperature in Fig. 8 and provides a measure of the maximum ISS Ag signal obtainable with our apparatus for 1.0 nm Ag before extensive penetration into the SAM has occurred. In contrast to Fig. 7, the initial ISS Ag signal decreases above and below 153 K. The reproducibility of these data was carefully checked for coverages of 1.0 nm Ag. Two additional ISS compositional depth profiles were taken for a coverage of 5.0 nm Ag at 113 K to clarify the unexpected results below 153 K. The initial ISS signal intensity at 113 K and 5.0 nm Ag coverage is approximately the same magnitude as the data taken at 153 K with 1.0 nm Ag coverage. We have not determined if the Ag peak intensity is a maximum at 153 K (1.0 nm Ag) and 113 K (5.0 nm Ag).
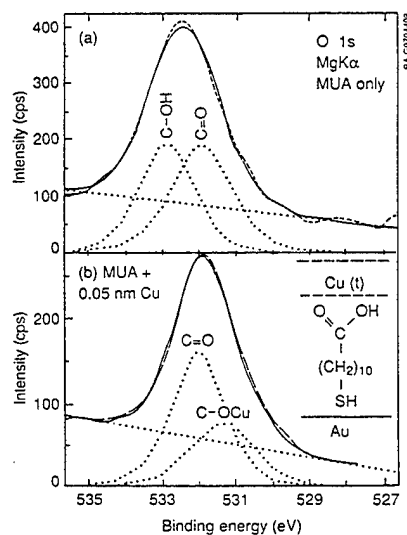
Fig. 5. Curve-resolved O 1s photoemission peaks for the $HS(CH_2)_{10}COOH$ SAM on gold before (a) and after (b) deposition of 0.05 nm of copper.
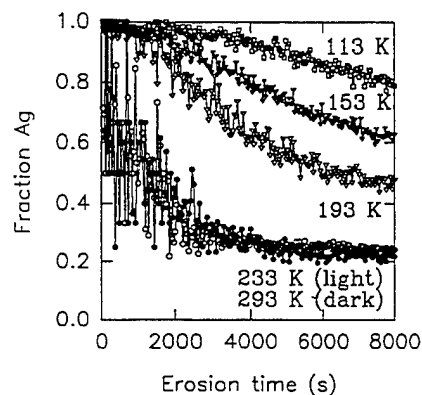
Fig. 7. Fraction of Ag signal (see the text) as a function of erosion time at 0.2 $\mu A/cm^2$ for 1.0 nm Ag on ODT/Au at temperatures of 113, 153, 193, 233, and 293 K.
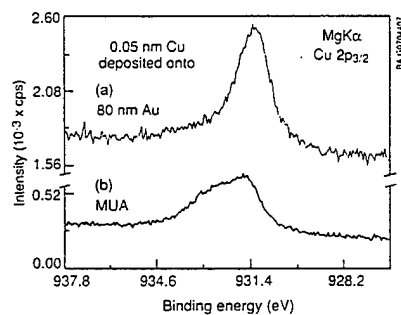
Fig. 6. Copper photoemission peaks for 0.05 nm of copper on (a) 80 nm of gold and (b) the $HS(CH_2)_{10}COOH$ SAM on gold.
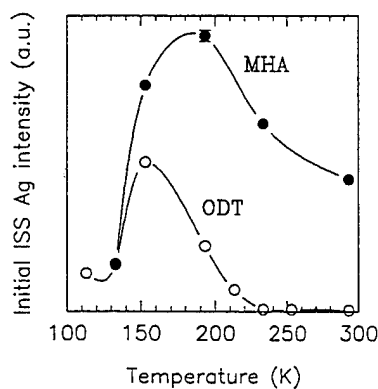
Fig. 8. Initial ISS peak intensities for 1.0 nm Ag on MHA and ODT after deposition at temperatures from 113 K.

21

The data for Ag/MUA and Ag/MHA in Fig. 8 also show a larger initial ISS signal is obtained. Data taken that is similar to that in Fig. 7 show the rate of Ag penetration is slower for MUA than for ODT, and even slower for MHA. For example, the ISS peak area was measured at four different positions on the same sample for 1.0 nm of Ag on MUA and MHA as a function of time after deposition at 295 K after waiting for about 5, 15, 35, and 65 min after deposition; a fifth ISS Ag peak intensity was measured after 900 min for both MUA and MHA. The data show that after deposition Ag remains on the surface of MUA for at least 5 min. and some Ag is on the MUA surface for more than 1 h. For MHA, Ag remains on the surface for more than 1 h (i.e., the Ag ISS intensity is unchanged), and the ISS intensity is only reduced to 68% of its initial value after 15 h, which shows that complete penetration to the SAM/Au interface is greatly retarded by the longer chain (C_{16} vs C_{11}) MHA.. By comparison, 1.0 nm of Ag penetrates ODT in less than 5 min at this temperature (Fig. 7). Ag on MUA is an intermediate case in which Ag remains on the surface for 5 to 15 min but then penetrates into the MUA, but 15% of the deposit is still on the surface after 1 h.

The time dependence of the slower Ag penetration through MUA and MHA compared with that for ODT at 295 K provides some indication of the mechanism of metal penetration through SAMs. First, weak interactions between Ag and the COOH group may retard the onset of Ag transport through MUA and MHA. We did not detect evidence for formation of a Ag unidentate complex with O, even though Ag-O interactions of 18 kcal/mol to 69 kcal/mol are known to exist.[39] Secondly, we speculate that hydrogen bonding between surface COOH groups results in a more tightly packed SAM and makes penetration of Ag through MUA and MHA more difficult. The CH_3 group on ODT, by comparison, is in free rotation at 295 K and does not retard transport of Ag to the ODT/Au interface. The increased rate of penetration of Ag through MUA relative to that for MHA is attributed to an enhanced defect density in the less tightly packed shorter chain alkanethiol. A third possibility is that the presence of the COOH group on MUA and MHA reduces the number of pinhole defects in the SAM, so that fewer transport pathways are available in these films, again with the MHA more defect free than for MUA.

In Fig. 8, the initial ISS Ag peak intensities from CDPs of 1.0 nm Ag on MHA and ODT are compared for temperatures from 113 K to 295 K. The decrease in intensity below 150 K for ODT was discussed in our previous paper.[6] As is seen in Fig. 8, a similar decrease occurs for MHA, though below 200 K, and we think the reasons for the decrease are the same as for the Ag on ODT.[6] The initial ISS Ag peak at 295 K for 1.0 nm Ag on MHA is more intense than the most intense initial ISS peak observed for 1.0 nm Ag on ODT. This result indicates that the Ag initially remains longer on the COOH surface of MHA, the ISS may be a maximum for any given temperature. Differences in Ag coverage on ODT and MHA probably result from differences in wetting behavior (and thus clustering) as well as penetration of Ag through the two SAMs. Even though SAMs are model systems for studying interactions at metal/organic interfaces, we emphasize that the systems being studied are complex when metal penetration occurs. Factors dictating the specific structure of metal overlayers on SAMs might include metal nucleation behavior, SAM defect density and domain size, the chemical functionality of the SAM, and the available free volume between alkanethiol chains.

Important Concerns about M/SAM Studies

Several important and crucial questions exist for M/SAM studies. These include: (a) are contaminants present in or on the film, (b) what kind of defects are in the SAM and at what density, (c) does the degree of penetration (Table 3) increase with increasing SAM defect density, (d) does the SAM disorder significantly even for low metal overlayer coverages, and (e) what problems are caused by X-ray and e-beam exposures? None of the questions (a) - (e) seem unmanageable based on a recent review by Jung and Czanderna.[10]

CONCLUDING REMARKS

In the research to date, the interactions of several M/SAM systems have been *identified*, along with *qualitative* relationships among the effects of chemical reactivity, temperature, and penetration of a metal/organic interface. With further research, the task remains to understand *quantitatively* how M/SAM interfaces are formed. This will require more complete characterization of the reactants, the structures, and the kinetics of the reactants and the structures of M/SAM systems.

The initial research on M/SAM systems has served as a test of their use as model systems, and of whether M/SAM research will have benefits in applied areas, for example, real M/polymer interfaces. The results described above are clearly more readily interpreted and more detailed than most of their counterparts in the metal/polymer interface literature. Based on the presence of similar reactants at a M/polymer interface, such as OFGs and metal atoms, this research approach succeeds in identifying factors that affect the initial bond between metal and polymer as the interface is formed in vacuum.

From the initial results, a continued broad effort is warranted for studying a matrix of 10 to 15 metals and metal oxides with about 10 different OFGs to evaluate the full potential of the approach and of this subfield of surface science. This should lead to the identification of submatrices targeted at specific classes of materials and applications.

Future characterization needs include obtaining (1) detailed, molecular orbital descriptions of new metal-organic bonds in a unique environment (because of the difference between bringing individual molecules to a metal surface compared with bringing individual metal atoms to an organic surface), (2) diffusion processes and rates for metals on organic surfaces, and (3) penetration processes and rates for metals into organic surfaces. These advances will be based on further work with valence band probes, lateral imaging probes, and probes that can measure rates of penetration, as discussed above. Control of defects and a capability for the characterization of defects will be necessary to understand the relative role of intrinsic vs. extrinsic effects in chemical and physical processes in M/SAM systems.

Finally, the results of M/SAM studies may be applied to the understanding of M/polymer interfaces, and for this reason, M/SAM interfaces are often described as "model" M/polymer interfaces. Studies of metal oxides, semiconductors, and other inorganics deposited onto SAM substrates should provide results than can be applied to the understanding of other types of inorganic/organic interfaces. Further relevance to inorganic/organic interfaces actually used in practice and to interfacial reaction mechanisms under ambient conditions can be gained by exposure of inorganic/SAM interfaces to different atmospheres, temperature extremes, radiation, and chemical reagents. Inorganic/organic interfaces with well-defined and stable properties are needed in advanced devices.[36-38] Research to identify and modify reactions at inorganic/SAM interfaces will provide the fundamental understanding to fill that need.

REFERENCES

1. A.W. Czanderna, D.E. King, and D. Spaulding, J. Vac Sci. Technol. **A 9**, 2607 (1991).

2. D.R. Jung, D.E. King, and A.W. Czanderna, Appl. Surf. Sci. **70/71**, 127 (1993).

3. D.R. Jung, D.E. King,, and A.W. Czanderna, J. Vac. Sci. Technol. **A 11**, 2382 (1993).

4. D.R. Jung and A.W. Czanderna, Mater. Res. Soc. Symp. Proc. **304**, 131 (1993).

5. G. Herdt and A.W. Czanderna, Surf. Sci. Lett. **297**, L109 (1993).

6. G. Herdt and A.W. Czanderna, J. Vac. Sci. Technol. **A 12**, 2410 (1994).

7. M.J. Tarlov, Langmuir **8**, 80 (1992).

8. P. Zhang, Ph.D. thesis, Department of Materials Science and Engineering, Pennsylvania State University, 1993.

9. R.L. Opila, K. Konstadinidis, D.L. Allara, and P. Zhang (private communication).

10. D.R. Jung and A.W. Czanderna, Crit. Rev. Solid State Mater. Sci. **19**, 1 (1994).

11. D.R. Jung and A.W. Czanderna, J. Vac. Sci. Technol. **A 12**, 2402 (1994).

12. E. Sacher, J.J. Pireaux, and S.P. Kowalczyk, (1990), in *Metallization of Polymers,* ACS Symposium Series, series editor, M. J. Comstock, (American Chemical Society, Washington, DC) and references.

13. F.P. Netzer and M.G. Ransey, Crit. Rev. Solid State Mater. Sci. **17**, 397 (1992).

14. M.R. Albert and J.T. Yates, *The Surface Scientist's Guide to Organometallic Chemistry* (American Chemical Society, Washington, DC, 1987).

15. J. M. Burkstrand, J. Vac. Sci. Technol. **20**, 440 (1982).

16. J.M. Burkstrand, J. Appl. Phys. **50**, 1152 (1978); **52**, 4795 (1982).

17. K. Kostanididis, R.L. Opila, J.A. Taylor, and A.C. Miller, in Ref. 4., 83-90.

18. S.G. Anderson, J. Leu, B.D. Silverman, and P.S. Ho, J. Vac. Sci. Technol. **A 11**, 368 (1993).

19. M.J. Goldberg, J.G. Clabes, and C.A. Kovac, J. Vac. Sci. Technol. **A 6**, 991 (1988).

20. J.L. Jordan, C.A. Kovac, J.F. Morar, and R.A. Pollack, Phys. Rev. **B 36**, 1369 (1987).

21. R.G. Nuzzo and D.L. Allara, J. Am. Chem. Soc. **105**, 4481 (1983).

22. D.L. Allara and R.G. Nuzzo, Langmuir, **1**, 45 (1985); 52 (1985).

23. A. Ulman, *An Introduction to Ultrathin Organic Films* (Academic, New York, 1991).

24. L.H. Dubois and R.G. Nuzzo, Annu. Rev. Phys. Chem. **43**, 437 (1992).

25. C.D. Bain, E.B. Troughton, Y.-T. Tao, J. Evall, G.M. Whitesides, and R.G. Nuzzo, J. Am. Chem. Soc. **111**, 321 (1989).

26. D.E. King and A.W. Czanderna, Surf. Sci. Lett. **235**, L329 (1990).

27. J.R. Vig, J. Vac. Sci. Technol. **A 3**, 1027 (1985).

28. J.R. Pitts, Ph.D. dissertation, Department of Physics, University of Denver, CO, 1985.

29. D.L. Allara, D.R. Jung, and P. Zhang, Metal atom reactions with self-assembled monolayers, paper presented at 39th Natl. Symp. American Vacuum Society, Chicago, November 9 to 13, 1992. (D.L. Allara, private communication.)

30. K. Bammel, J. Ellis, and H.-G. Rubahn, Chem. Phys. Lett. **201**, 101 (1993).

31. F. Balzer, K. Bammel, and H.-G. Rubahn, J. Chem. Phys. **98**, 7625 (1993).

32. G. Herdt and A.W. Czanderna, J. Vac. Sci. Technol. **A 13**, (1995) In Press.

33. Independent observations by D.L. Allara, et al. at Penn State U., R.L. Opila, et. al. at ATT-Bell Labs, and A.W. Czanderna, et. al. at NREL.

34. G.K. Wertheim, Z. Phys. **B 66**, 53 (1987).

35. D. Spaulding, M.S. thesis, Materials Science Dept., University of Denver, Denver, CO, 1989.

36. A.W. Czanderna and R.J. Gottschall, Eds., Mat. Sci. Engr. **53**, 1-168 (1982).

37. J.D. Swalen, D.L. Allara, J.D. Andrade, E.A. Chandross, S. Garoff, J. Israelachvili, T.J. McCarthy, R. Murray, R.F. Pease, J.F. Rabolt, K.J. Wynne, and H. Yu, Langmuir **3**, 932 (1987).

38. A.W. Czanderna and A.R. Landgrebe, Eds., Current Status, Research Needs and Opportunities in Applications of Surface Processing to Transportation and Utilities Technologies, Crit. Rev. Surf. Chem. **2** (Nos. 1-4) and **3** (No. 1), 1993.

39. A.W. Czanderna, J. Vac. Sci. Technol. **14**, 408 (1977).

IN SITU STUDY OF THE EXPOSURE
OF POLYCARBONATE TO AN ARGON PLASMA

S. VALLON*, B. DREVILLON*, F. PONCIN-EPAILLARD** AND J. C. ROSTAING***
*Laboratoire de Physique des Interfaces et des Couches Minces (CNRS UPR 258),
Ecole Polytechnique, 91128 Palaiseau, France
**Laboratoire de Chimie et Physicochimie Macromoléculaire (CNRS URA 509),
Université du Maine, Avenue Olivier Messiaen, 72017 Le Mans, France
***L'Air Liquide CRCD, BP 126, 78350 Les-Loges-en-Josas, France

ABSTRACT

The exposure of polycarbonate to an argon plasma is studied using *in situ* ellipsometry from the UV to the IR, nuclear magnetic resonance and light scattering measurements. An increase in the refractive index and the existence of two populations of different molecular weights show that structural changes occur in the polymer. They are correlated with modifications at the polymer unit scale, such as formation of new polar groups and decrease in dimethyl groups. Two simultaneous reaction mechanisms must be considered to account for these changes. The adhesion of a silica layer on treated polycarbonate is then discussed.

INTRODUCTION

Polycarbonate (PC) is a transparent polymer with good mechanical properties, but its use is limited by poor resistance to abrasion and to UV irradiation. This drawback could be overcome by using a hard protective coating acting as an anti-UV filter, such as a stack of plasma deposited silica and silicon nitride layers. However the adhesion of coatings is usually poor, because of the weak surface energy of polymers. For this reason a surface treatment is required before coating the polymer.

The effect of inert gas plasmas on polymers has been known for a long time[1,2]. Vacuum ultraviolet photons (λ<175 nm) can break C–H or C–C bonds, creating free radicals. Further reaction with other radicals or with other chains leads to recombination, unsaturation, branching and crosslinking. The last behavior may improve the bond strength of the surface by forming a very cohesive skin.

In the present paper we study the interaction of an argon plasma with PC, in order to improve the adhesion of a silica layer. Structural changes in the polymer are investigated by solubility, light scattering and *in situ* UV–visible ellipsometry measurements.The latter provide the refractive index of the material. The correlation is made with modifications at the polymer unit scale, which are studied by nuclear magnetic resonance (NMR) and *in situ* IR ellipsometry.

EXPERIMENTAL

The 3 mm thick PC samples are argon plasma treated in a dual mode microwave-radiofrequency plasma reactor of the surface wave type described elsewhere[3]. The microwave excitation generates a high concentration of active species in the gas phase, and the radiofrequency allows us to control the ion bombardment on the substrate. In this study the plasma conditions are as follows: pressure = 0.080 mbar; microwave power = 200 W; radiofrequency power = 0; treatment time = 10 s to 1 hr.

Proton NMR spectroscopy is run in CDCl$_3$ solution with TMS as reference on a 400 MHz Bruker apparatus.

<u>Spectroscopic ellipsometry</u>

Let us recall that the ellipsometric angles Ψ and Δ are defined by $\rho = r_p/r_s = \tan \Psi \, e^{i\Delta}$, where r_p and r_s are the complex reflexion coefficients for the parallel and perpendicular polarizations respectively. In the case of a homogeneous sample, Ψ and Δ are related to the complex refractive index $(n - i\,k)$ by

$$\varepsilon = (n - i\,k)^2 = \varepsilon_0 \sin^2\phi_0 \left\{ 1 + \tan^2\phi_0 \left(\frac{1 - \rho}{1 + \rho}\right)^2 \right\} \qquad (1)$$

where ε is the dielectric function of the material, n the real refractive index, k the extinction coefficient, ε_0 the dielectric function of the ambient medium ($\varepsilon_0 = 1$) and ϕ_0 the angle of incidence ($\phi_0 = 70°$). In the case of an inhomogeneous sample (one or more layer on a substrate), Ψ and Δ are still related to the complex refractive indices of the various materials.

In the infrared, the dielectric function is dominated by the vibrational contributions $\Delta\varepsilon$ of the chemical bonds, estimated from the lorentzian expression: $\Delta\varepsilon(\sigma) = F/(\sigma_0^2 - \sigma^2 + i\Gamma\sigma)$, where $\sigma = 1/\lambda$ is the wavenumber, and σ_0, Γ and F are the frequency, the width and the strength of the oscillator respectively. In the case of a thin film (thickness $d_f \ll \lambda/4\pi$) on a substrate, we present IR ellipsometry measurements in the form of the ellipsometric density $D = \ln (\rho_s/\rho)$, where ρ refers to the sample and ρ_s to the bare substrate[4]. D is directly related to the complex dielectric function ε_f of the film by

$$D = \frac{i\,4\pi\sigma\sqrt{\varepsilon_0}\,\tan\phi_0\,\sin\phi_0\,\varepsilon_s}{(\varepsilon_s - \varepsilon_0)(\varepsilon_s - \varepsilon_0\tan^2\phi_0)}\,d_f\,(1 - \varepsilon_0/\varepsilon_f)(\varepsilon_s - \varepsilon_f) \qquad (2)$$

where ε_s is the substrate dielectric function. Considering that D is roughly proportional to i d_f ($\varepsilon_s - \varepsilon_f$), and taking into account eqn. (2), a chemical bond in the film can be identified by a maximum of Re D together with a inflexion point (negative slope) in Im D, while a vibrational mode of the substrate results in the opposite behavior.

UV-visible ellipsometry measurements are performed in real time using a UVISEL Jobin-Yvon phase-modulated ellipsometer[5] in the 1.5-5 eV range. The FTIR ellipsometer is based on a double modulation system[6] and covers the range 900-4000 cm^{-1}.

RESULTS

Fig. 1 shows the effective refractive index n of PC measured by UV-visible ellipsometry. A progressive increase in n during the argon plasma treatment is observed. N is calculated for a homogeneous material (see eqn (1)), but actually the treated sample consists of a modified overlayer on an unchanged substrate, and n has to be considered as an average on the overlayer and the substrate. The progressive increase is probably related to an increase in the overlayer thickness. To estimate the thickness, an inhomogeneous layer model had to be used with *ex situ* multiple angle of incidence measurements (not shown). A first estimation gives a typical depth of variation of the refractive index of a few microns.

A possible interpretation for the increase in the refractive index is a densification: according to the effective medium theory[7], a given material has a smaller index if it contains inclusions of void; inversely a densification will result in a higher index. Moreover, densification would be in agreement with crosslinking, a well-known effect of inert gas plasmas on polymers[2].

Besides, the Δ spectra show a growing structure in the UV range (Fig. 2). Such a structure is related to the absorption of certain chemical groups (chromophores)[8], and the progressive increase in Δ indicates the emergence of new chromophores. Their origin will be discussed later.

In order to check whether the increase in the refractive index is related to crosslinking, the solubility of untreated and treated PC in THF has been measured (Table I). The increase in the insoluble fraction shows the appearance of an interchain bridging, already after a 10 s treatment.
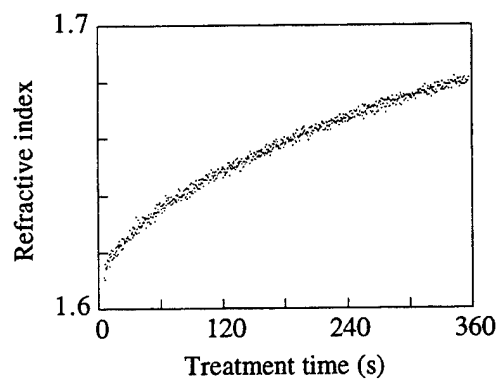
Fig. 1. Effective refractive index at 3.5 eV measured by ellipsometry in real time during the Ar plasma treatment.
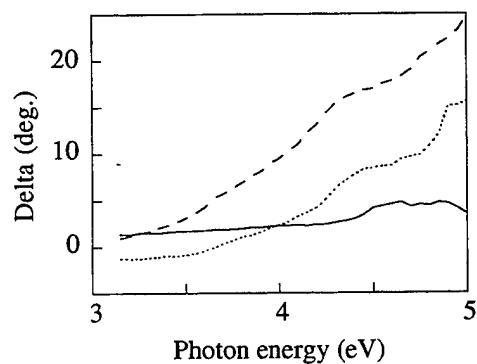
Fig. 2. Ellipsometric angle Δ in the UV range for untreated PC (solid line) and Ar plasma treated PC for 6 min (dotted line) and 1 hr (dashed line).

Table I. Insoluble fraction in THF, and integration of the two dimethyl singlets (NMR) referred to the untreated sample, for Ar treated PC.

Treatment time	Insoluble fraction(%)	$(CH_3)_2C$ (%)
untreated	56.8	100
10 s	60.1	99.5
6 min	65.8	98.2
1 hr	66.3	96.4

The insoluble fraction increases between 10 s and 6 min, and saturates after 6 min. Thus some crosslinking occurs in PC during the first 6 min of the Ar plasma treatment.

Light scattering measurements in dioxane have been performed to estimate the size of the coils: their size should increase in case of crosslinking. However it turns out that the treated samples contain two different populations: one of bigger size than the untreated sample, corresponding to the crosslinked fraction of the polymer; and the other one, in greater quantity, of smaller size than the untreated sample. The latter results from chain breakings in the polymer. This means that both the degradation and crosslinking reactions occur during the plasma treatment.

NMR measurements have been performed in order to elucidate the degradation and crosslinking mechanisms. The NMR spectra of the proton show for the untreated sample a multiplet at 7.2 ppm (aromatic protons) and two singlets at 1.7 and 1.6 ppm (dimethyl groups in the middle and at the end of a chain resp.) (Fig. 3). OH groups at the end of the chains have not been detected. The plasma treatment results in a progressive decrease in the integration of the dimethyl singlets (Table I), particularly at the chain ends. Thus methyl groups seem to be involved in the degradation and/or in the crosslinking reaction.

Further information about the chemical mechanisms is given by *in situ* IR ellipsometry. As explained in the experimental section, Ψ and Δ spectra of the treated samples are referred to the untreated sample spectra to form the ellipsometric density D. The major changes (i. e. D $\neq$ 0) are observed in the C=O stretching mode region (Fig. 4). The carbonate C=O mode (1771 cm^{-1}) appears as a negative peak in Re D and as an inflexion point with positive slope in Im D. Thus this mode, already present in PC, is in smaller quantity in the modified material (see eqn. (2)). On the contrary, new modes appear at 1690 and 1750 cm^{-1} as positive peaks in Re D and as inflexion points with negative slope in Im D. They correspond to new bonds in the modified material and can be attributed to less oxidised C=O groups than the carbonate group (carbonyl and ester groups). The three modes, hardly visible after 10 s treatment, become more and more intense after 6 min and 1 hr.

Moreover, XPS measurements show a decrease in the carbonate signal after a 10 s treatment, without any further evolution[9]. As XPS is only sensitive to the surface, while IR ellipsometry is also sensitive to the bulk, we can conclude that the reaction occurs first at the surface, and then propagates towards the bulk.
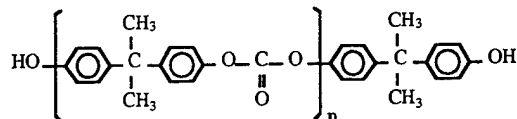
Fig. 3. PC chain.
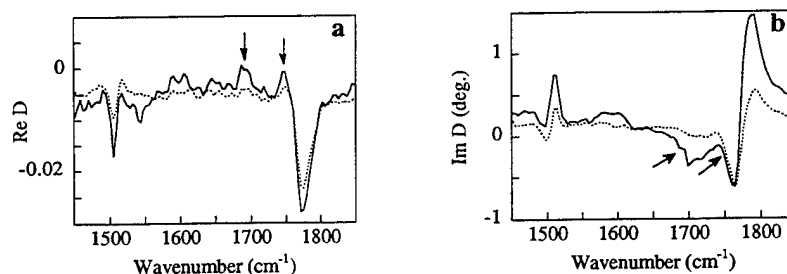
Fig. 4. Ellipsometric density D for 6 min (dashed lines) and 1 hr (solid lines) Ar treated PC. The arrows indicate vibrational modes appeared during the treatment.

30

DISCUSSION

Two reactions, degradation and crosslinking, seem to be in competition during the Ar plasma treatment. As we do not use any radiofrequency plasma in this study, and as the effect is not limited to the surface, we can infer that ion bombardment is not responsible for these reactions, but that their cause is UV light emitted by the plasma.

The literature concerning the photodegradation of PC mentions two photodegradation mechanisms: one through direct photochemistry, and the other through induced photochemistry[8]. The first one (Fig. 5) is due to the excitation of the polymer chromophores by short-wavelength photons, the absorption band of PC being centered at 265 nm. After breaking of the carbonate bond, two successive photo-Fries rearrangements occur. The phenylcarbonate units rearrange into phenylsalicylate units (L_1), which then rearrange into dihydroxybenzophenone groups (L_2). Concurrently the radicals coming from the carbonate breaking can recombine after decarbonyl-ation or a decarboxylation, generating various photoproducts (L_3). L_1, L_2 and L_3 are not stable in the combined presence of oxygen and UV light, but during the plasma treatment there is no oxygen. Hence the direct mechanism could be responsible for the decrease in the coil size, as chain breaking is one of the consequences of these reactions; for the new C=O modes (Fig. 4), from L_1 and L_2; and for the increased absorption in the UV range (Fig. 2), due particularly to L_2.

However crosslinking and the decrease in dimethyl groups are not accounted for by this mechanism. The second mechanism mentioned in the literature is induced by defects or impurities of the material. By absorption of long-wavelength photons, they produce R• radicals (Fig. 6). These radicals react with PC by removing a hydrogen atom from the methyl group, and this new radical isomerises into a tertiary macroradical R_3 to increase its stability. Then in the presence of oxygen, hydroperoxydes are formed and lead to degradation. In our case the macroradical could react with an other chain, leading to crosslinking.

The adhesion of a silica layer on PC has been measured using a microscratch test[10]. The 1 μm thick silica layer was plasma deposited, after an Ar treatment or directly on PC. Although an improvement is already obtained after 30 s, the best result is given by the 6 min treatment. Two reasons may be considered to account for the enhanced adhesion: crosslinking and creation of new polar groups (L_1 and L_2). As most changes in surface polar groups have occured after 10 s, the second mechanism is not prevailing. In spite of concurring degradation, crosslinking thus improves the adhesion of a silica layer on PC, probably through the formation of a cohesive skin.
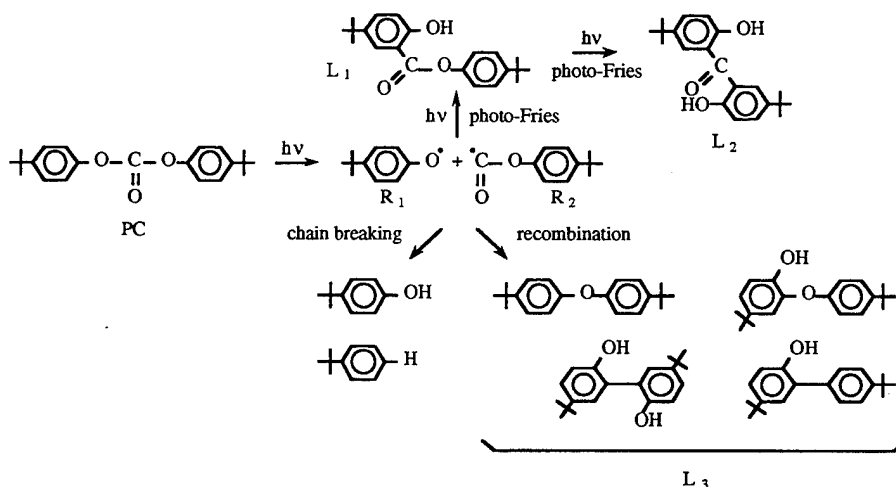
Fig. 5. Direct photodegradation mechanism of PC.
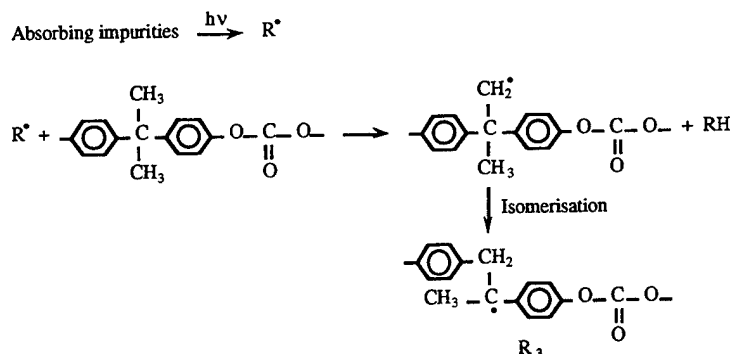
Fig. 6. Production of macroradicals (R$_3$) through the induced photodegradation mechanism of PC.

CONCLUSION

In this paper we have studied the interaction of an argon plasma with PC. Structural changes in the polymer have been investigated by light scattering measurements and by UV-visible ellipsometry, which provides the real-time refractive index of the material. The structural changes have been correlated with modifications at the polymer unit scale, which were studied by NMR and *in situ* IR ellipsometry. It appears that the exposure of PC to an argon plasma produces two simultaneous reactions: a degradation reaction, that results in chain breakings, formation of new polar groups (carbonyl and ester) and increased absorption in the UV range; and a crosslinking reaction that probably involves methyl groups. The later mechanism seems to be responsible for the enhanced adhesion of a silica layer on PC.

ACKNOWLEDGEMENTS

REFERENCES

1. R.H. Hansen and H. Schonhorn, J. Polym. Sci., Polym. Lett. Ed. **B4**, 203 (1966).
2. J.R. Hollahan and A.T. Bell, Techniques and Applications of Plasma Chemistry (Wiley, New York, 1974).
3. J.C. Rostaing, F. Coeuret, B. Drévillon, R. Etemadi, C. Godet, J. Huc, J.Y. Parey and V. Yakovlev, Thin Solid Films **236**, 58 (1993).
4. N. Blayo and B. Drévillon, Appl. Phys. Lett. **59**, 950 (1991); J. Non-Cryst. Solids **137-138**, 771 (1991).
5. B. Drévillon, Prog. in Cryst. Growth and Charact. of Mat. **27**, 1 (1993).
6. A. Canillas, E. Pascual et B. Drévillon, Rev. Sci. Instr. **64**, 2153 (1993).
7. D.E. Aspnes, Thin Solid Films **89**, 249 (1982).
8. A. Rivaton, D. Sallet and J. Lemaire, Polym. Photochem. **3**, 463 (1983).
9. A. Gheorghiu and C. Sénémaud (private communication).
10. L. Martinu and J.E. Klemberg-Sapieha (private communication).

NONDESTRUCTIVE CHARACTERIZATION OF FIBER-MATRIX ADHESION IN COMPOSITES BY VIBRATION DAMPING

WEIQUN GU[*], GUO-QUAN LU[*], H. FELIX WU[**], STEPHEN L. KAMPE[*],
P. ROSS LICHTENSTEIN[**], and DAVID W. DWIGHT[**]
[*]Department of Materials Science and Engineering, Virginia Polytechnic Institute and State University, Blacksburg, VA 24061
[**]Composites Innovation, Owens-Corning Science and Technology Center, Granville, OH 43023

ABSTRACT

Adhesion at fiber-matrix interface in fiber-reinforced composites plays an important role in controlling the mechanical properties and overall performance of composites. Among the many available tests applicable to the composite interfaces, vibration damping technique has the advantages of being nondestructive as well as highly sensitive. We set up an optical system to measure the damping tangent delta of a cantilever beam, and correlated the damping data in glass-fiber reinforced epoxy-resin composites with transverse tensile strength which is also a qualitative measurement of adhesion at fiber-matrix interface. Four different composite systems containing three different glass-fiber surface treatments were tested and compared. Our experimental results showed an inverse relationship between damping contributed by the interface and composite transverse tensile strength.

1. INTRODUCTION

It is well-known that the fiber-matrix interfacial adhesion has a major effect in achieving superior mechanical properties of a composite. The tensile strength of the composite is dependent on the ability of the composite to transfer the tensile load from the broken fibers to the surviving ones through shear in the matrix and at the interface. Thus, a method that is capable of determining the interfacial adhesion strength is needed to evaluate the mechanical performance of composite materials.

Numerous experimental techniques have been developed for measuring interfacial adhesion strength in fiber-reinforced composites. These methods include the single fiber pull-out test [1, 2], microbond test [3-5], the single fiber fragmentation test [6-9], the microindentation test [10, 11], and some nondestructive evaluation techniques, such as vibration damping [12]. Vibration damping is a promising nondestructive technique because it is simple and quite sensitive to the interfacial region. The method has a potential to be used by materials industry for *in situ* monitoring of the mechanical performance of composites.

According to the theory of energy dissipation [13], the quality of the interfacial adhesion in composites can be evaluated by measuring the part of energy dissipation contributed by the interfaces; the interface part can be obtained by separating the fiber and matrix from the total composites. Zorowski and Murayama [12] were the first to

develop a method for the quality of the interfacial adhesion in the reinforced rubber through energy dissipation measurements based upon the following relationship:

$$\tan\delta_{in} = \tan\delta_{comp} - \tan\delta_s \qquad (1a)$$

$$\tan\delta_s = \frac{\tan\delta_f E_f V_f + \tan\delta_m E_m V_m}{E_m V_m + E_f V_f} \qquad (1b)$$

where $\tan\delta_{in}$ is the internal energy dissipation due to poor adhesion from the interface, which can be used for evaluating the interfacial adhesion; $\tan\delta_s$ is the effective loss tangent for a composite with perfect interfacial adhesion, $\tan\delta_{comp}$ is the measured internal energy dissipation of the composite system. E is the Young's modulus and V represents volume fraction. Subscripts f and m refer to the fiber and matrix, respectively. By measuring the total system energy dissipation in terms of $\tan\delta$ and knowing $\tan\delta$ and the dynamic moduli of the components as well as the volume fraction of fibers, the dissipation due to the poor interfacial adhesion can be determined.

In this paper, we describe an optical setup for measuring vibration damping of cantilevers specimen. The setup was used to measure the damping of glass-fiber reinforced polymer composites, and the damping data were correlated with the transverse tensile strength of composites.

2. EXPERIMENTAL PROCEDURES

2.1 Composite Sample Preparation

Composite laminate specimens were fabricated at the Owens-Corning Science and Technology Center. D.E.R. 331 epoxy resin from Dow Chemicals Company and Lindride 66 curing agent from Lindau Chemicals Inc. were selected as the matrix material commonly used in filament winding process. The reinforcements were E-glass fibers with a diameter of 10 μm. Four fiber systems that contained different surface treatments were investigated in this study as listed in Table 1. To make a composite laminate, D.E.R. 331 epoxy (100 parts by weight) was mixed with Lindride 66, curing agent, (85 parts by weight). Composite laminates were fabricated through a filament winding machine and samples were cured for two hours at 120°C and two hours at 180°C under a hot press machine with a 1.43 MPa constant pressure. The composite laminates were then cut into 30 mm × 4 mm × 0.5 mm specimens. The actual length of the cantilever beam was 25 mm.

2.2 Optical Setup

A schematic of the optical setup designed to measure the deflection and vibration dynamics of a cantilever beam is shown in Figure 1. The construction consists of a 1 mW solid state laser (670 nm), a mirror, a beam splitter and a position sensitive photodetector. A sample is mounted by clamping it vertically between two plates such that the protruding part forms a cantilever beam. An electronically triggered pin is used

to generate an initial deflection on the sample; vibration of the sample is initiated by retracting the pin. Vibration curves are obtained by bouncing a laser beam off the sample to the photodetector.
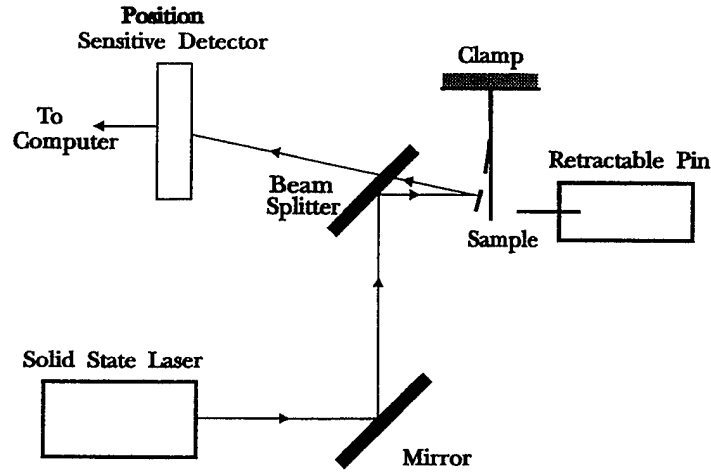
Figure 1. Schematic diagram of the optical system

The damping factor, $\tan\delta$, is calculated from decaying-oscillatory damping curve by the following [14]

$$\tan\delta = \frac{\ln(A_0 / A_n)}{n\pi} \qquad (2)$$

where n is the number of cycles of the vibration, A_0 is the amplitude of the first vibration, and A_n is amplitude of the nth vibration. The term $\frac{\ln(A_0 / A_n)}{n}$, also known as the logarithmic decrement Δ, can be obtained by fitting the experimental data to the following formula [14]

$$A(t) = B_0 \exp(-\zeta\omega_r t)\cos(\omega_d t - \phi) + B_1 \qquad (3)$$

where ω_r is the resonant frequency of vibration, $\zeta = \Delta / \sqrt{(2\pi)^2 + \Delta^2} \cong \Delta / 2\pi$ when damping is small, $\omega_d = (1 - \zeta^2)^{1/2}\omega_r$, B_0, B_1 and ϕ are constants.

Table 1. A List of the Samples Used in this Study

Specimen Type	Fiber Volume Fraction	Description of Surface Treatment
A	0.695	No.1 sizing with silane
B	0.610	Untreated fibers
C	0.677	No.1 sizing without silane
D	0.716	No. 2 sizing with silane

3. RESULTS AND DISCUSSION

Figure 2 is a typical example of the results that obtained from the optical system described above, in which a composite specimen without any fiber surface treatment (Type B specimen) was tested. The value of $\tan\delta$ was found to be 3.81×10^{-3}. This value is typical for this material system. Other experimental results are summarized in Table 2. The values presented here are the averages that obtained from at least five specimens.
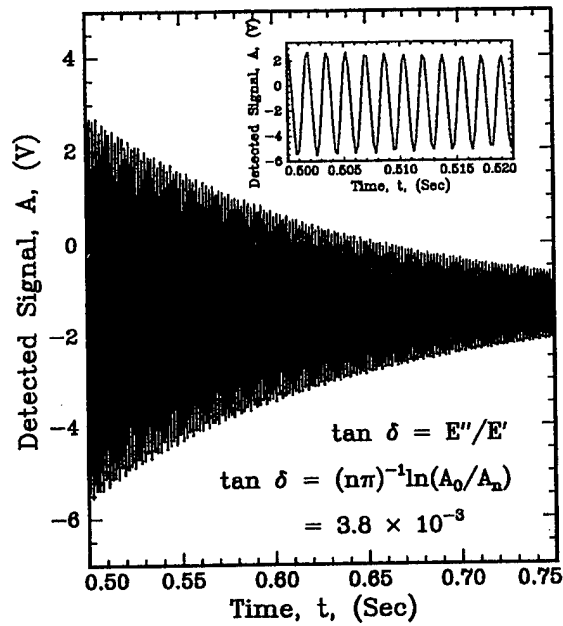
Figure 2. An example of the vibration damping curves from the optical system

Table 2. Measured Resonant Frequencies, Damping Factors, and Transverse Tensile Strength

Specimen Type	ω_r (s^{-1})	$\tan\delta_{comp}$ ($\times 10^{-3}$)	$\tan\delta_{in}$ ($\times 10^{-3}$)	σ_{tr} (MPa)
A	4061 (1.2%)*	2.46 (4.9%)	1.11	56 (8.8%)
B	3733 (2.0%)	3.74 (1.6%)	2.24	28 (14.7%)
C	3980 (2.7%)	2.75 (3.6%)	1.37	45 (8.5%)
D	4038 (1.2%)	2.73 (0.7%)	1.42	46 (9.3%)

*Numbers in parenthesis represent coefficient of variation.

From the Bernoulli-Euler beam equation [14-16], it can be shown that the Young's modulus, E, of the material is related to its frequency of vibration. The equation used for calculating E for a beam specimen is described as follows [14]:

$$E = \frac{12\rho\omega_r^2 L^4}{1.875^4 t^2}$$

(4)

where ω_r is the resonant frequency of the first mode of vibration, L and t are the length and the thickness of the beam, and ρ is the density. The density of the epoxy resin is 1.115 g/cm^3 [17].

It has been reported that the damping factor also varies with frequency [18, 19]. By changing the beam length, a resonant frequency of about 3900 s^{-1} was obtained, which is comparable to the frequencies of other composites that were tested. The measurements from our optical system show that $E_m = 2.4$ GPa and $\tan\delta_m = 25 \times 10^{-3}$. It is also known that $E_f = 72.3$ GPa and $\tan\delta_f = 1 \times 10^{-3}$ [20]. These data were used to calculate $\tan\delta_{in}$ which are also given in Table 2.

Equation (1) shows that with a higher value of $\tan\delta_{in}$ the poor adhesion exhibits in the system. Results show that Type B specimen appears to have the weakest fiber-matrix interfacial adhesion among the four composite systems. However, Type A specimen which contains No. 1 sizing and silane show the best interfacial adhesion. It is also interesting to note that the Type C specimen (having No. 1 sizing and no silane) and Type D specimen (having No. 2 sizing and different silane) seem to have an equal magnitude of interfacial adhesion.

It is known that the poor interfacial adhesion exhibits a low transverse tensile strength, σ_{tr}. The measured σ_{tr} from the same composite systems are also listed in Table 2. It can easily be seen that the observations from $\tan\delta_{in}$ are consistent with the results from σ_{tr}, and both show the same magnitude of the interfacial bonding. In other words, $\tan\delta_{in}$ and σ_{tr} are highly inversely correlated as shown in Fig. 3.
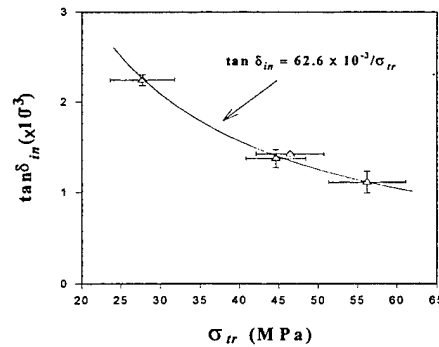
Figure 3. The relationship between $\tan\delta_{in}$ and σ_{tr}. Error bars represent ±1 standard deviation.

It is suggestive that a common process among the defect-related mechanisms involving a) transfer of kinetic energy of structural motion to potential energy of a defect and b) dissipation of the potential energy in the form of heat to its surroundings. Therefore, a sample contains more defects should have a higher damping factor; and also the more loosely configured a defect is, the higher its contribution to damping. At a strongly bonded interface, there are fewer loosely bonded defects or centers which can easily absorb kinetic energy; therefore, it should have smaller damping. At a weak interface, there are likely more loosely bonded defects or centers to absorb kinetic energy; thus, it should have higher damping.

4. CONCLUSIONS

An optical setup was constructed to measure the damping factor of a cantilever beam and used to characterize adhesion at fiber-matrix interfaces in glass-fiber reinforced polymer-resin composites. Tested samples had three different fiber-surface treatments and a controlling sample. The results show that the composite system having No. 1 sizing and silane exhibits the best fiber-matrix interfacial adhesion. The system having No. 1 sizing without silane turns out to be an equal magnitude of interfacial adhesion as the system having No. 2 sizing and different silane. Samples with untreated fibers have the weakest interfacial adhesion. The experimental results showed that a strong inverse relationship between damping characteristics of the fiber-matrix interface and transverse tensile strength of composites.

5. REFERENCES

1.   L. J. Broutman, Interfaces in Composites, STP 452, edited. by M. J. Salkind (American Society of Testing and Materials, Philadelphia, 1969), p. 27.
2.   P. S. Chua and M. R. Piggott, Composites Science and Technology, 22, 33 (1985).
3.   B. Miller, P. Muri, and L. Rebenfeld, Composites Science. and Technology, 28, 17 (1987).
4.   H. F. Wu and C. M. Claypool, Journal of Materials Science Letters, 10, 260 (1991).
5.   H. F. Wu and C. M. Claypool, Journal of Materials Science Letters, 10, 1072 (1991).
6.   H. F. Wu, G. Biresaw, and J. T. Laemmle, Polymer Composites, 12 (4), 281 (1991).
7.   A. N. Netravali, Z. -F. Li, W. Sachse, and H. F. Wu, Journal of Materials Science, 26, 6631 (1991).
8.   J. P. Favre and J. Perrin, Journal of Materials Science, 7, 1113 (1972).
9.   L. T. Drzal, M. J. Rich, M. F. Koenig, and P. F. Lloyd, Journal of Adhesion, 16, 1 (1982).
10.   J. F. Mandell, E. J. H. Chen and F. J. McGarry, Internat. J. Adhesion Adhesives, 1, 40 (1980).
11.   H. F. Wu and M. K. Ferber, Journal of Adhesion, 45, 89 (1994).
12.   C. F. Zorowski and T. Murayama, Proc. 1st Int. Conf. on Mech. Behav. of Mater., 5, Soc. of Mater. Sci., Kyoto, Japan, 28 (1972).
13.   L. E. Goodman, Structural Damping, ASME, 36 (1959).

14. L. Meirovitch, <u>Elements of Vibration Analysis</u>, edited by B. J. Clark and M. E. Margolies, McGraw-Hill, 1975.

15. E. Volterra and E. C. Zachmanoglou, <u>Dynamics of Vibrations</u>, Charles E. Merrill, Columbus, OH, 321 (1965).

16. K. Clark, <u>Dynamics of Continuous Elements</u>, Prentice-Hall, Englewood Cliffs, NJ, 75 (1972).

17. M. Weller and Hassel Ledbetter, J. Mater. Res., **5** (5), 913 (1990).

18. L. B. Crema, A. Caastellani and A. Serra, Journal of Composite Materials, **23**, 978 (1989).

19. R. F. Gibson and R. Plunkett, Journal of Composite Materials, **10**, 325 (1976).

Part II

Biointeractions and Biointerfaces

INTEGRATING CELL TRANSPLANTATION AND CONTROLLED DRUG DELIVERY TECHNOLOGIES TO ENGINEER LIVER TISSUE

D. J. MOONEY*#, K. SANO#, P.M. KAUFMANN#, K. McNAMARA*,
J.P. VACANTI#, R. LANGER*
*Dept. Chemical Engineering, Massachusetts Institute of Technology, Cambridge MA 02139
#Dept. Surgery, Harvard Medical School and Children's Hospital, Boston MA 02115

ABSTRACT

Engineering liver tissue using hepatocyte transplantation may provide a new approach for treating a variety of liver diseases. However, techniques to transplant hepatocytes and promote their survival must be developed. We have developed systems to transplant hepatocytes on highly porous (95%), biodegradable sponges, and to regulate the survival of cultured hepatocytes by releasing specific growth factors in the cellular environment. Sponges were fabricated from poly (L, lactic acid) (PLLA) and polyvinyl alcohol using a particulate leaching technique. Epidermal growth factor and insulin, critical factors for hepatocyte growth and survival in culture, were incorporated into microspheres fabricated from poly (lactic-co-glycolic acid) (PLGA) utilizing a double emulsion technique. The incorporated factors were released in a controlled manner over one month in vitro, and the released factors maintained their biological activity, as measured by their ability to promote hepatocyte growth and survival in culture. The growth factor-containing microspheres could be transplanted with hepatocytes using the porous sponges, and the localized, sustained release of these factors improved hepatocyte engraftment 2-fold. These studies suggest that hepatocyte-containing tissues can be engineered using cell transplantation, and that regulating the microenvironment of transplanted cells can control their engraftment.

INTRODUCTION

Whole liver transplantation is currently the established therapy for end-stage liver disease but it suffers from a great limitation in donor organs. Approximately 30,000 people still die each year in the United States of liver disease (1), and a large number of these people could be treated if there was an available supply of liver tissue. Transplantation of hepatocytes, the major liver-cell type, may replace liver function in patients suffering from liver failure, and provide an alternative to whole liver transplantation (2). The challenges in engineering liver tissue with hepatocyte transplantation include the necessity of delivering a large number of cells to a specific anatomic location, and providing a suitable environment for long-term hepatocyte engraftment.

Highly porous sponges fabricated from biodegradable polymers of the lactic and glycolic acid family may be ideal cell delivery devices (3). Large numbers of hepatocytes can be seeded in a highly porous device, and transplanted to the desired location. The pores provide a route for fibrovascular tissue ingrowth from the surrounding host tissue (4), and the ingrown blood vessels may provide for the metabolic needs of the implanted cells as they develop into a new tissue. Highly porous sponges have been previously fabricated from poly-L-lactic acid utilizing a particulate leaching technique, and coated with polyvinyl alcohol to enable even and reproducible seeding with hepatocytes (3). These devices have been utilized to tranpslant hepatocytes into experimental animals, where a number of the transplanted hepatocytes engrafted (histologically appeared healthy) and survived for the limited time of the experiment (1 week). However, it will be critical to provide the proper environment if these cells are to engraft over long time frames.

A variety of growth factors have been identified that regulate the survival and proliferation of hepatocytes. These include epidermal growth factor (EGF) and insulin (5). A critical role for insulin is suggested by the finding that trophic factors from islet cells improve the survival of transplanted hepatocytes (6), as does co-transplantation of islets with hepatocytes (7). However, it is difficult to attribute these effects to the presence of specific factors such as insulin due to the number of factors secreted by islets, and the potential role of islet-hepatocyte communication in this process. If techniques to reproducibly deliver specific factors were developed it would allow one

to investigate the role of various factors, alone and in combination, in the survival and growth of transplanted hepatocytes. This may allow one to define an optimal environment for the survival of transplanted cells, and move hepatocyte transplantation closer to a clinically relevant therapy.

In this report we describe a technique to deliver biologically active factors such as EGF and insulin over extended periods to hepatocytes transplanted into heterotopic sites using biodegradable polymer sponges. This approach modulates the microenvironment of transplanted hepatocytes to improve engraftment.

MATERIALS AND METHODS

Microspheres containing insulin and EGF were prepared by a modification of a previously described double-emulsion technique (8). In brief, a 75/25 copolymer of poly-(D,L-lactic-co-glycolic) acid (Resomer RG 75R, intrinsic viscosity 0.2 dl/g; Henley Chem. Inc, Montvale, NJ) was dissolved in ethyl acetate (Fisher Scientific) to yield a 5% solution (w:v). Mouse EGF (Collaborative Research; Bedford, MA) and recombinant human insulin (Sigma) was dissolved in water to yield a solution of 2 mg/ml (EGF) and 1 mg/ml (insulin), and 50 μl of the solution was added to 1 ml of the polymer solution. The resulting solution was sonicated continuously at 10 watts (Vibracell; Sonics and Materials, Danbury, CT) for 15 sec to yield a single emulsion. An equal volume of an aqueous solution containing 1% polyvinyl alcohol (MW 25,000, 88% hydrolyzed; Polysciences Inc., Warrington, PA) and 7% ethyl acetate was added to the single emulsion, and the resulting solution was vortexed (Vortex Mixer; VWR) for 15 sec at the high setting to yield the double emulsion. This double emulsion was transferred to a rapidly stirring 250 ml beaker containing 150 ml of an aqueous solution of 0.3% polyvinyl alcohol/7% ethyl acetate. The ethyl acetate was allowed to evaporate over the ensuing 3 hr to yield polymer microspheres with entrapped EGF. The microspheres were then filtered, washed with water, and microspheres with a size between 32 and 0.4 mm were collected. The microspheres were lyophilized (Labconco Freeze Dryer, Kansas City, MO), and stored at -20°C until use. Control beads were prepared with the same procedure, but the aqueous solution used to form the first, single emulsion (water in organic) contained no insulin or EGF.

To determine the efficiency of factor incorporation, and the kinetics of release from the microspheres, ^{125}I-labeled mouse EGF (260 mCi/mg; Biomedical Tech. Inc., Stoughton, MA) and ^{125}I-labeled insulin (New England Nuclear, Boston MA; 110 mCi/mg) were utilized as tracers. Approximately 1 μCi of labeled drug was added to the aqueous drug solution before formation of the single emulsion, and the beads were prepared as described above. After bead fabrication, a known mass of beads was counted in a LKB CliniGamma 1272 (Wallac, Gaithesburg, MD), and the incorporated cpm was compared to that of the initial aqueous solution to calculate the drug incorporation. Drug release was quantitated by placing a known mass of beads in a known volume of phosphate buffered saline (PBS) solution containing 0.1% Tween 20 (Sigma Chem. Co.), and incubating at 37°C. At set times, the solution was centrifuged to concentrate the beads at the bottom of the vial, and samples were removed and counted in a gamma counter. Sink conditions were maintained during the release study.

For scanning electron microscopic examination, samples were first gold coated using a Sputter Coater (Desk II, Denton Vacuum, Cherry Hill, NJ), and imaged using an environmental scanning electron microscope (ElectroScan; Wilmington, MA). Photomicrographs were taken with Polaroid 55 film.

Cultured hepatocytes were utilized to determine whether the drugs incorporated into and released from microspheres had retained their biological function. Hepatocytes were isolated from Lewis rats using a two-step collagenase perfusion, and purified using a Percoll gradient as previously described (9). Hepatocytes were plated at a density of 10, 000 cells/cm^2 on 24 well tissue culture dishes coated with 1 mg/cm^2 of type I collagen (Collagen Corp., Palo Alto, CA) using a carbonate buffer coating technique (9). Serum-free William's E medium (Gibco, Grand Island, NY) containing insulin (20 mU/ml; Sigma), dexamethasone (5 nM; Sigma), sodium pyruvate (20 mM; Gibco), a mixture of penicillin and streptomycin (100 U/ml; Irvine Scientific,

Santa Ana, CA), and ascorbic acid (50 mg/ml, fresh daily; Gibco) was used for all experiments. For conditions in which drug released from microspheres was utilized, medium with no drug was incubated with drug containing microspheres for 24-96 hr to allow release of known amounts of drug (calculated using the known release kinetics), the solution was centrifuged, and the medium containing the released drug was removed and used in subsequent experiments. To analyze cell entry into S phase of the cell cycle, tritiated thymidine autoradiography was utilized. Cultured hepatocytes were refed 48 hr after plating with medium containing 1 mCi/ml ^{3}H-thymidine (NEN; Boston, MA). At 72 hr cells were twice washed with PBS to wash out any non-incorporated ^{3}H-thymidine, fixed with glutaraldehyde, and dehydrated with 100% methanol. Culture wells were overlaid with NTB-2 emulsion (Kodak; Rochester NY), and the dishes were allowed to expose for 7 days in complete darkness. Dishes were developed with D-19 developer (Kodak).

Isolated and purified hepatocytes were mixed with EGF-containing or control microspheres, and seeded onto 95% porous cylindrical sponges (diameter=2.15 cm, thickness=1 mm) in a petri dish. The sponges were fabricated from poly-(L, lactic) acid (Medisorb; Cincinnati, OH), and coated with polyvinyl alcohol as previously described (3). Each sponge received 0.4 ml x 50x10^6 hepatocytes/ml + 10 mg of microspheres. Cell-polymer devices were implanted into the mesentery of laboratory rats as previously described (10). Implants were removed after 14 days, fixed in formalin, and processed for sectioning. Sections of implants were stained with hematoxylin and eosin, and engrafted hepatocytes were identified by their large size, large and spherical nuclei, and distinct cytoplasmic staining. All animals were housed in the Animal Research Facility of Children's Hospital, and NIH guidelines for the care and use of laboratory animals (NIH Publication #85-23 Rev. 1985) have been observed.

RESULTS

Microspheres fabricated with the double-emulsion technique had diameters ranging from 10 to 30 μm (the approximate size of suspended hepatocytes) (Fig. 1). The average diameter was 19±12 μm. The efficiency of insulin and EGF incorporation into microspheres was 42±10% and 53±11%, respectively. Insulin was released from the microspheres in a large initial burst, followed by a steady release over the ensuing 10 days. EGF release also had an initial burst, although not as large as insulin, and a steady release was again noted after this time (Fig. 2).
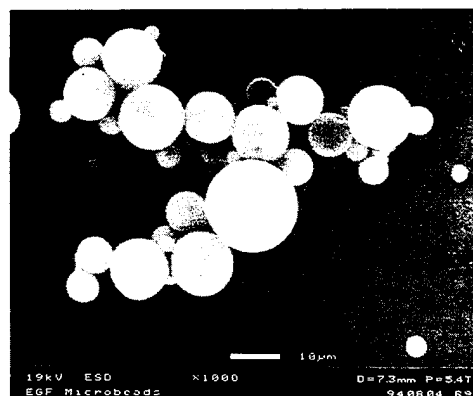
Figure 1. Photomicrograph of polymer microspheres. A scanning electron microscope was utilized to image microspheres. A size bar is shown on the photomicrograph.

A   B
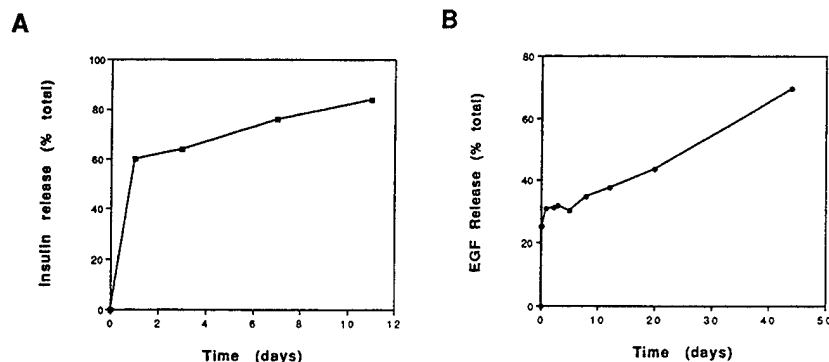
Figure 2. Release kinetics of ^{125}I-labelled insulin (A) and EGF (B) from polymer microspheres. The amount of protein released was normalized to the total radiolabelled protein incorporated into the mass of microspheres utilized in the release study. Results from a representative experiment are shown.

Studies with cultured hepatocytes were subsequently performed to determine whether the released factors retained their biological activity. EGF and insulin released from microspheres stimulated hepatocyte entry into the synthetic (S) phase of the cell cycle, indicating that they retained their biological activity. Both insulin and EGF normally stimulate hepatocyte growth in a dose-dependent manner (Fig. 3). Quantitation of the number of hepatocytes entering S phase revealed that insulin released from the microspheres still had retained significant activity, although less than control insulin (Fig. 3A). In contrast, the same dose of EGF either released from microspheres or control EGF showed a similar stimulation (Fig. 3B). EGF released from microspheres was also shown to promote the long-term survival of cultured hepatocytes (11).

To determine whether EGF released from microspheres could positively influence the engraftment of hepatocytes transplanted to a heterotopic site, hepatocytes ($2x10^7$ cells/sponge) and microspheres (10 mg/sponge) were mixed together and seeded onto porous, biodegradable sponges fabricated from poly-(L-lactic) acid (Fig. 4). The ratio of polymer/salt used in the sponge fabrication process was set at 0.03 to achieve a device porosity of $95\pm2\%$. Cell/microsphere-seeded devices were implanted into the mesentery of laboratory rats. Retrieval of implants after two weeks, followed by histological preparation and observation, revealed that animals which received EGF containing microspheres had a large number of engrafted hepatocytes (not shown). Quantitation of the number of engrafted hepatocytes revealed that animals which received EGF-containing microspheres contained a statistically significant greater number of engrafted hepatocytes than animals which received control microspheres (11).

DISCUSSION

A system has been developed to both deliver large numbers of hepatocytes to specific anatomic locations, and to release growth factors at the site of hepatocyte transplantation from polymer microspheres. Specific hepatotrophic factors (insulin and EGF) can be incorporated into polymer microspheres. These factors are released over extended time periods when the
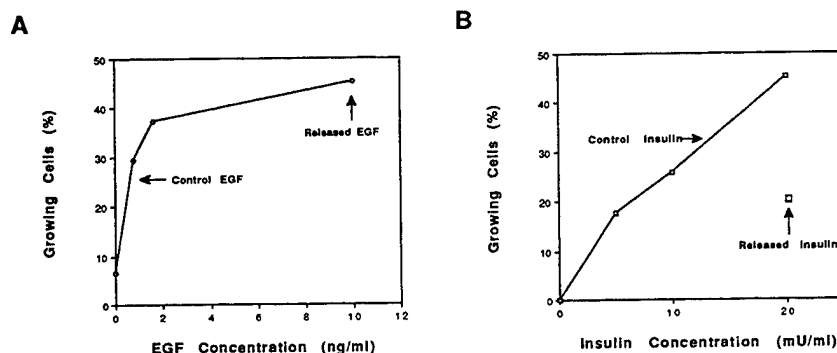
Figure 3. Stimulation of hepatocyte growth by EGF (A) and insulin (B). Hepatocytes were cultured in medium containing varying concentrations of EGF or insulin that was not incorporated into microspheres (Control), or a known amount of EGF or insulin released from polymer microspheres (Released). Released EGF stimulated hepatocyte growth to the same extent as control EGF, while released insulin had a lower stimulatory effect than control insulin. The growth of cells was analyzed using ^{3}H-thymidine autoradiography. Cells in S phase of the cell cycle (Growing cells) incorporate the radiolabelled thymidine and can be identified by their black nuclei following autoradiography.
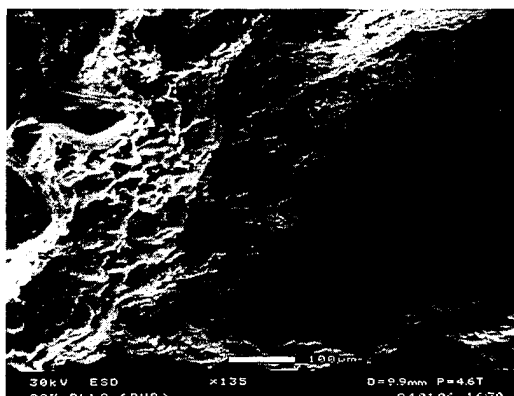
Figure 4. Photomicrograph of a biodegradable sponge seeded with hepatocytes prior to implantation. The sponge was visualized using scanning electron microscopy, and a size bar is shown on the photomicrograph.

47

microspheres are placed in an aqueous environment, and the released factors maintain their biological activity.

Hepatocytes can be transplanted in a variety of manners (reviewed in 12). The PLA sponges utilized in this study allow large numbers of hepatocytes to be efficiently transplanted into experimental rats at a desired anatomic location. Significant numbers of transplanted hepatocytes survive and form a new tissue with the ingrowing fibrovascular tissue and the polymer device (3). Fibrovascular tissue invasion leads to the formation of a vascular network which supplies the metabolic needs of the developing tissue.

Delivery of hepatotrophic factors via sustained release from microspheres may prove a valuable and flexible technique to control the local environment of transplanted cells. A known dose of a factor can be delivered with this approach, and the time over which a drug is released from a polymer matrix can typically be regulated by the drug loading, the type of polymer utilized, and the exact processing conditions (13). A critical feature is that the released protein(s) must retain its biological activity for this approach to be useful. The biological activity of proteins such as insulin can be compromised by the processing conditions, due to aggregation and denaturation of the drug (14). This may account for the decreased activity of insulin released from the microspheres in this study. The biological activity of the EGF incorporated into and released from microspheres in this study did not appear to be adversely affected, but additional studies will be necessary to confirm that this does not occur at later stages of the release. The large burst release of protein at the beginning of the release studies is likely related to surface-associated protein. It is unclear, however, why the initial burst was much greater for insulin than EGF.

In summary, we have developed a system to transplant hepatocytes and control the presence of specific growth factors in the local environment of the transplanted cells. This system may greatly improve the engraftment of transplanged hepatocytes, and other cell types, and move cell transplantation closer to a clinically relevant therapy.

ACKNOWLEDGMENTS

REFERENCES

1. American Liver Foundation, Vital Statistics of the United States, 1988:Vol.2 (A).
2. R. Langer and J.P. Vacanti, Tissue engineering, Science, **260**, 920 (1993).
3. D.J. Mooney, S. Park, P.M. Kaufmann et al, J. Biomed. Mat. Res., in press.
4. A.G. Mikos, G. Sarakinos, M.D. Lyman, D.E. Inger, J.P. Vacanti, and R. Langer, Biotech. Bioeng., **42**, 716 (1993).
5. N. Fausto, Prog. Growth Factor Res. **3**, 219 (1991).
6. V. Jaffe, H. Darby, A. Bishop, H.J. Hodgson, Int. J. Exp. Path. **72**, 289 (1991).
7. P.M. Kaufmann, K. Sano, S. Uyama, and J.P. Vacanti, Transplantation Proc. **26** (1994).
8. S. Cohen, T. Yoshioka, M. Lucarelli, L.H. Hwang, and R. Langer, Pharm. Res. **8**, 713 (1991).
9. D. Mooney, L. Hansen, J.P. Vacanti, R. Langer, S. Farmer, and D. Ingber, J. Cell Phys. **151**, 497 (1991).
10. S. Uyama, P.M. Kaufmann, T. Takeda, and J.P. Vacanti, Transplantation **55**, 932 (1993).
11. D.J. Mooney P.M. Kaufmann, K. Sano, et at., submitted.
12. L.K. Hansen, and J.P. Vacanti in Current controversies in biliary atresia. edited by M.A. Hoffman (R. G. Landes, Austin, TX 1993), p. 96.
13. R. Langer, Science **249**, 1527 (1990).
14. V. Sluzky, J.A. Tamada, A.M. Klibanov, and R. Langer, Proc. Natl. Acad. Sci. **88**, 9377 (1991).

This article also appears in Mat. Res. Soc. Symp. Proc. Vol 394

NATURAL POLY(HYDROXYBUTYRATE-HYDROXYVALERATE) POLYMERS AS DEGRADABLE BIOMATERIALS.

CYRIL CHAPUT*, L'HOCINE YAHIA*, AMINE SELMANI** AND CHARLES-HILAIRE RIVARD***.
*Biomedical Engineering Institute, Ecole Polytechnique, Montréal, Qc, CANADA;
**Chemical Engineering Department, Ecole Polytechnique, Montréal, Qc, CANADA;
***Department of Surgery, Ste-Justine Hospital, Montréal, Qc, CANADA.

ABSTRACT

Poly(ß-hydroxybutyrate-co-ß-hydroxyvalerate) have been recently proposed as degradable biomaterials for drug delivery systems, sutures, bone plates and short-term implants. Three PHB\HV (7, 14 & 22 % HV) films were analyzed for *in vitro* cytotoxicity and aqueous accelerated degradation, *in vivo* degradation and tissue reactions. The PHB/HV materials and extracts elicit few or mild toxic responses, do not lead *in vivo* to tissue necrosis or abscess formation, but provoke acute inflammatory reactions slightly decreasing with the time. The degradation of PHB/HV polymers present low rates *in vitro* as well as *in vivo*. The weight loss rate generally increases with the copolymer composition (HV content) and ranges from 0.15-0.30 (*in vitro*) to 0.25 %/day (*in vivo*). Compositional and physico-chemical changes in PHB/HV materials were rapidly detected during the accelerated hydrolysis, but were much slower to appear *in vivo*. The structural and mechanical integrity of PHB/HV materials tend to disappear early *in vitro* as well as *in vivo*. After 90 wks in dorsal muscular tissues of adult sheep, there was no significant dissolution of the PHB/HV polymer, 50-60% of the initial weight still remaining. PHB/HV polymers are biodegradable materials, either by hydrolysis or implantation, but with extremely low dissolution or degradation rates.

INTRODUCTION

Poly(ß-hydroxybutyrate-ß-hydroxyvalerate) materials [PHB/HV] are members of the Polyhydroxyalkanoate [PHA] family, a group of new polymeric materials based on bacterial polyesters. PHA materials are intra-membranarly produced by prokaryotic cells as carbon and/or energy reserves. PHB and polypropylene have been often compared in terms of physico-chemical (melting point, crystallinity level) and tensile properties, however PHB/HV polymers are reported as environmentally-and/or-bio-degradable materials [1]. These biotechnological thermoplastics are of extreme interest as 100% compostable and ecologic plastics for packaging materials.

Bacterial PHB and PHB/HV polyesters have been introduced and evaluated as biodegradable, biocompatible and natural thermoplastics for medical or surgical devices. Drug delivery systems, sutures, bone plates and restorative absorbable devices have been proposed with PHB homopolymer [2,3]. PHB membranes have been equally applied for guided gingival tissue regeneration and studied *in vivo* for thoraco-abdominal tissue reconstruction in animals [2,3,4]. The PHB/HV copolymers have been reported as presenting improved processibility, tactility and accelerated biodegradation properties over the PHB homopolymer. They have been recently preferred for evaluations of biomedical implantable systems such as orthopaedic resorbable composites or tissue engineering substrates. In orthopaedic surgery, PHB/HV biopolymers have been considered for their piezo-

electrical properties, low and progressive rate of hydrolysis in comparison to other synthetic resorbable polymers and potential bioactivity in regard to the depolymerization into β-hydroxybutyric acid (HB), a natural constituent of the human blood.

MATERIALS & METHODS

Three commercial PHB/HV (HV 7, 14 & 22 %) copolymers were processed by dissolution in chloroform solutions (10 % w/v) and casting on the glass surface of petri dishes. The solvent was allowed to evaporate for at least 96 hrs, and all PHB/HV films were stored under anhydrous conditions at room temperature. The cytotoxic responses of the PHB/HV films were controlled according to the direct contact and agar diffusion cell culture tests [ASTM F813-83(88) and F895-84(90)].

In vitro degradation studies

The accelerated degradation studies were performed in Phosphate Buffered Solutions (PBS), pH 7.4, at 70°C. The PHB/HV films were cut in rectangular-shaped specimens (70°C), and the sample size was measured using a micrometric caliper. The film specimens were then sealed in glass bottles with 50 ml of PBS solution. The accelerated hydrolysis of the PHB/HV samples was carried out in an oven (70°C), and the PBS solutions were checked daily to avoid excessive medium evaporation. To analyze the hydrolytic degradation effects, samples of the PHB/HV specimens were taken at 0, 5, 10, 20, 40, 60, 80, 110, 140, 160 and 220 days (70°C). Once removed from the aqueous medium, the PBS excess was eliminated on absorbent paper, the specimens were washed in distilled water and 70% ethanol, air-dried at 40°C, and then stored under anhydrous conditions at room temperature.

In vivo Implantations.

The PHB/HV materials for implantations were sampled in rectangular film specimens. The specimen sizes (width x length x thickness) were measured using a digimatic micrometric caliper. The PHB/HV specimens were sterilized by Ethylene Oxide (EtO). The PHB/HV films were implanted in dorsal muscular tissues of adult sheep for 1, 5, 8, 11, 15, 20, 25, 30, 52, 66, 70 and 90 weeks. The animals were anesthezied using Acepromazine[R] and Thiopenthal[R] 5.0%, and maintained during surgery by Halothane[R] 1.5%. The dorsal region was incised on each side of the spine, three independant pouches were created in the muscular bundles along and beside the spine. The PHB/HV film was disposed in the pouch and attached to the muscles using non-resorbable Prolene[R] sutures. The muscular pounches and dorsal incisions were closed with absorbable Dexon[R] sutures. The sheep were admisnistrated analgesics and antibiotics (Demerol[R]/Permlong[R]) for a two-day post-op period. All animals were sacrificed by Euthanyl[R] overdose and the muscular tissues surrounding the PHB/HV specimens were excised and freshly maintained in saline solutions. The muscular tissues were immediately dissected to extract the PHB/HV samples. Samples of the muscular tissues and fibrous capsules around the polymeric films were excised and fixed in 10% formalin solutions. The membranes were histologically analyzed for the 1, 5, 11, 20, 66, 70 and 90 week periods by paraffin embedding, thin slides (2-4 mm) and Hematoxylin & Eosin (HE) staining. The muscular tissues remaining around the PHB/HV specimens were enzymatically digested using collagenase (37°C, 1 week), then separated from the PHB/HV materials in a density gradient column with distilled water.

All PHB/HV specimens were washed using distilled water and ethanol, air-dried at 40°C, then stored at room temperature.

Biodegradation of PHB/HV polymers

After being washed and dried, the degraded PHB/HV film samples were weighed precisely using an analytical balance (weight variation < 0.01%) and the weight loss was calculated as being $(m_o-m)/m_o$ (m_o: initial weight, m: weight of the film at the period t). The linear correlation of the weight loss data with the degradation time was analyzed using a Pearson Product-Moment Correlation analysis with a 95% confidence level. The degradation effects on the degraded PHB/HV specimens were monitored using Gel Permeation Chromatography (GPC, Refractive Index), Nuclear Magnetic Resonance (^{13}C-NMR), and Differential Scanning Calorimetry (DSC). The PHB/HV surfaces were also studied by Scanning Electron Microscopy (SEM).

RESULTS AND DISCUSSION.

The cytotoxic responses to PHB/HV solid materials were quoted as mild reactions with few cell lysis and no lysis propagation outside the surface area beneath the solid samples. The preliminary toxicity tests suggest that the solid PHB/HV materials as processed in the laboratory elicit mild to moderate cellular reactions *in vitro*, however the potential cytotoxicity of PHB/HV extracts vary with the medium, weight or surface/volume ratio, time or temperature.

Table I: The weight loss rates of PHB/HV polymers during the *in vitro* and *in vivo* degradations.

PHB/HV (Initial dry weight)	PHB/7%HV (100 g)	PHB/14%HV (100g)	PHB/22%HV (100g)
K_{wl} (*in vitro*, 70°C) (milligrams per day)	170.2	263.8	283.1
K_{wl} (*in vivo*) (milligrams per day)	38.7	39.7	44.1

Table II: The number-average molecular weight (M_n) and M_w/M_n ratio verus the hydrolysis time.

PHB/22%HV	t (days)	M_n ($\times 10^3$)	M_w/M_n
in vitro (70°C)	0	63	3.79
	60	48	2.18
	140	11.5	2.27
	220	12.8	2.15
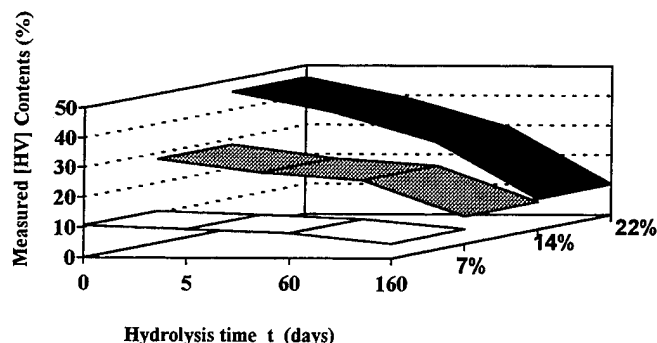
Figure 1: The mole HV content (%) of the PHB/HV polymers versus the hydrolysis time.

Table III: The thermal parameters of the PHB/22%HV polymer versus the hydrolysis time.

PHB/22%HV	t (days)	T_m (°C)	ΔH_m (J/g)
in vitro (70°C)	0	157.8	41.4
	10	154.2	63.6
	40	152.6	78.1
	80	153.4	80.2
	220	137.6	99.8

In vitro:

The mean weights of the PHB/HV materials are 103.5 (HV7%), 88.7 (HV14%) and 101.9 mg (HV22%). These materials were sampled in 40mm x 15mm rectangularly-shaped specimens.

Whatever the copolymer composition, all PHB/HV films clearly show pronounced signs of degradation by aqueous hydrolysis at high temperature. The weight loss rates [K_{wl} (in vitro, 70°C)] were calculated from the correlation analysis (Pearson's correlation coefficients > 0.92), and vary from 170.2 (HV7%) to 283.1 mg/day (HV22%) [**Table I**]. Undoubtedly, they tend to increase during the in vitro accelerated hydrolysis with the [HV] content in the copolymers.

The number-average molecular weights, M_n, (R.I.), and M_n/M_w ratio rapidly decrease with the hydrolysis time [**Table II**]. The k_d hydrolysis rate was calculated, as previously defined by Doi et al. (1990) for PHB/HV polymers, from the hydrolysis time, the number-average degree of polymerization at time zero [$DP_n(0)$] and the ratio of the number-average molecular weights at time zero and time t [$M_n(0)/M_n(t)$] [5]. The molecular weight-based degradation rate k_d was equal to 3.58×10^{-5} day^{-1} for aqueous hydrolysis of the PHB/22%HV polymer at 70°C (Pearson's Moment correlation coefficient: 0.90). The mole HV contents, defined as being the ratio of the NMR band intensities of the Methyl groups of the HB and HV units, clearly decrease at 70°C with the hydrolysis time. These drops in HV content seem not to be linearly correlated with the time, but were dependant upon the initial HV content (nominal) [**Figure 1**]. The crystallinity level of PHB/22%HV materials clearly increases during the hydrolytic degradation ranging from 28.3% (t=0) to 68.4% (220 days), when calculated with using a heat of melting for the crystalline region

about 146 J/g (pure PHB) [Table III]. Those results demonstrate that PHB/HV polymers chemically degrade *in vitro* by accelerated aqueous hydrolysis. The attacks take place in all polymer molecules, however the M_w molecular weights decreased slightly faster than the M_n molecular weights. The molecular weight distribution was still unimodal and tend to progressively narrow with the hydrolysis time (M_w/M_n). The quite linear relationship between the average number of bond cleavages per original polymer molecule and the hydrolysis time supports the fact that the decrease in M_n can be associated with randon chain scissions [5].

In vivo

The mean weight of the PHB/HV samples was about 284+/-1405 g and the mean surface area about 2715+/-591 mm^2 (N=30). The specimens rapidly broke up *in vivo* at the suture attachments and started to fold up on themselves and to be infiltrated by tissues.

No abscess formation and tissue necrosis was observed in the vicinity of the PHB/HV specimens. Acute inflammatory reactions with numerous macrophages, neutrophils, lymphocytes and fibrocytes were observed at 1 week in the capsule at the interface between the muscular tissues and implants. These reactions were quite less intense at 11 weeks for all implants and the density of inflammatory cells was much lower, but inflammatory cells (lymphocytes) still remain in the capsule and muscular tissues. The fibrous capsules were dense and well-vascularized, organized early with crimped oriented fibers and fibroblastic cells. Those connective tissue cells were aligned in parallel with the implant surface, especially at the interfaces with the PHB/HV films. Some muscular bundles were detached from the adjacent muscular tissues, and surrounded by the fibrous tissues. The fibrous tissues, which represented the interface between the dorsal muscles and the PHB/HV film, were subdivided into secondary fibrous membranes going deeply through the dense muscular bundles. A great number of isolated or grouped fatty cells were observed in the capsule, at the interface between the capsule and muscular tissues, and in the adjacent muscles for long-term implantation periods (70 and 90 wks). There were few differences in terms of capsules and tissue characteristics or cellular activity between the three PHB/HV polymers.

During the implantations, the PHB/HV specimens have presented irregular and weak values in term of dry weight loss, and most of the PHB/HV materials were still present at 70 and 90 wks, suggesting very low degradation and dissolution rates *in vivo*. The data analysis showed that the weight loss rates [K_{wl} (*in vivo*)] vary from 38.7 to 44.1 mg/day, increasing slightly with the HV content. Some compositional and physico-chemical changes were detected, more particularly on the PHB/22%HV materials which appear to be the most sensitive to the *in vivo* degradation: the number-average molecular weight (decreasing M_n), polydispersity (increasing M_w/M_n), mole HV content (decreasing [HV]) and heat of fusion (increasing ΔH_m) were clearly affected *in vivo*, and showed either increasing or decreasing tendencies with the implantation time. However, the degradation rates *in vivo* were much slower than those associated with the *in vitro* accelerated hydrolysis. The degradation rate k_d was determined as previously described for the hydrolytic degradation and found to be about 8.98×10^{-7} day^{-1} for the PHB/22%HV polymer (Pearson's Moment correlation coefficient: 0.99). There were not clear signs of surface degradation activity on the implanted polymeric films, and systematic examinations demonstrated that there was no clear difference in terms of texture or microporosity between the virgin and degraded surfaces.

Bacterial PHB/HV polyesters chemically degrade when submitted to hydrolytic attacks in physiological media, however they provide few significant signs of degradation at the physiological temperature. On the other hand, the use of high medium temperatures (50, 60 70°C and up) improves the ability to screen the hydrolytic degradation effects of such materials. At 70°C, the PHB/HV polymers undergo clear physico-chemical or compositional changes in terms of number-

53

and weight-average molecular weights, mole [HV] fraction, melting point and heat of fusion. The nominal copolymer composition and initial average molecular weights have a strong effect on the degradation kinetics. *In vivo*, those physico-chemical and compositional changes are not detected (HV 7 & 14%) or are very weak (HV 22%). At 70 and 90 wks implantation, no clear changes in terms of [HV] content, melting temperature or heat of fusion are observed. However, if the apparent mechanical performances rapidly change during the hydrolysis, the weight loss or dissolution rate appears to be extremely limited *in vitro* as well as *in vivo*. The hydrolysis rate k_d of a PHB/22%HV polymer is about 3.6×10^{-5} day^{-1} *in vitro* in PBS solutions at 70°C, and about 9.0×10^{-7} day^{-1} *in vivo* in muscular tissues of sheep. The hydrolytic degradation of the PHB/HV films may be associated with random chain scissions throughout the whole polymer matrix.

CONCLUSION.

The PHB/HV copolymers are chemically sensitive to aqueous hydrolysis, but provide low degradation rates *in vitro*, even at high temperatures (accelerated conditions). At 70°C, the degradation of PHB/HV films in PBS solutions, pH 7.4, were quantified by weight loss rates of about 0.15-0.30 mg/day. The hydrolyzed PHB/HV materials rapidly show significant changes in terms of number-average molecular weights and M_w/M_n ratio, mole HV content and thermal parameters (melting points, heat of fusion and crystallinity levels). Our observations suggest that PHB/HV materials also degrade *in vivo*, but present very low dissolution rates, approximately seven times slower than those observed for the accelerated hydrolysis. The *in vivo* degradation effects on PHB/HV polymers probably require very long implantation periods (years). The cytotoxic responses toward PHB/HV solid materials or extracts in MEM (Minimum Essential Medium), saline or DMSO media generally were quoted as mild to moderate. *In vivo*, all short-term (1-11 wks) tissue reactions were characterized by the presence of acute inflammation with the presence of numerous inflammatory cells. For implantations of 11 weeks and up, the fibrous capsules were variable in thickness, but were dense well-vascularized tissues with oriented crimped collagen fibers and fibroblasts.

REFERENCES

1. H. Brandl, R. A. Gross, R. W. Lenz, R. C. Fuller. In: Advances in Biochemical Engineering. Biotechnology. Vol. 41, edited by A. Fiechter (Springer-Verlag Berlin Heidelberg, 1990) pp77-93.
2. T. Malm, S. Bowald, S. Karacagil, A. Bylock, C. Busch. Scand. J. Thor. Cardiovasc. Surg. 26, 9 (1992).
3. T. Malm, S. Bowald, A. Bylock, T. Saldeen, C. Busch. Scand. J. Thor. Cardiovasc. Surg. 26, 15 (1992).
4. N.R. Boeree, J. Dove, J.J. Cooper, J. Knowles, G.W. Hastings. Biomaterials 14, 793 (1992)
5. Y. Doi, Y. Kanesawa, M. Kunioka, T. Saito. Macromolecules 23, 26 (1990).
6. S. Gogolewski, M. Jovanovic, S.M. Perren, J.G. Dillon, M.K. Hughes. J. of Biomedical Materials Research, 27, 1135 (1993).

This article also appears in Mat. Res. Soc. Symp. Proc. Vol 394

54

Part III

Adhesion and Interface Durability

INTERFACIAL WATER AND ADHESION LOSS OF POLYMER COATINGS ON A SILICEOUS SUBSTRATE

T. NGUYEN, E. BYRD, D. ALSHEH, W. McDONOUGH, and J. SEILER
National Institute of Standards and Technology, Gaithersburg, MD 20899

ABSTRACT

Water is often the main cause of adhesion loss of a polymer coating/substrate system. The buildup of the interfacial water layer and the loss of adhesion of polymer-coated siliceous substrates exposed to liquid water has been investigated. The thickness of the interfacial water layer was measured on epoxy-coated SiO_2-Si prisms using FTIR-multiple internal reflection (FTIR-MIR) spectroscopy. Adhesion loss on flat siliceous substrates was determined by a wet peel test on epoxy-coated SiO_2-Si wafers and adhesion loss of composites was obtained by measuring the interlaminar shear strengths of epoxy/E-glass fiber composites. Both untreated and 0.1% silane-treated substrates were used. Little water was observed at the interface of the silane-treated samples but about 10 monolayers of water have accumulated at the interface of the untreated samples after 100 h of exposure to 24 °C water. Untreated, flat substrates lost most of their bonding strengths within 75 h of exposure but silane-treated specimens retained 80% of their adhesion after 600 h of exposure to 24 °C water. Adhesion loss of untreated composites immersed in 60 °C water was greater than that of treated samples; however, the rate of loss of both silane-treated and untreated composites was much lower than that of flat substrates. Adhesion loss was found to follow the same trend as interfacial water buildup.

INTRODUCTION

The detrimental effects of water and water vapor on the adhesion of polymer-coated metals[1], adhesive bondings[2], polymer/fiber composites[3] and asphalt pavements[4] are well documented. However, there has not been a study that examined the relationship between the water layer at a polymer coating/substrate interface and the adhesion loss. The main reason for this is the lack of quantitative information on the interfacial water layer. A recent development of a technique to quantify the water layer at the polymer coating/substrate interface[5] has made it possible to study the linkage between these two phenomena. In the present study, the thickness of the interfacial water layer and the loss of adhesion of polymer coating/siliceous substrate systems as a function of time of exposure to water has been investigated. The interfacial water layer was measured on specimens of coatings applied on flat substrates, while adhesion loss was determined on both flat substrates and unidirectional polymer/E-glass fiber composites.

EXPERIMENTAL SECTION

Materials and Specimen Preparations

For measuring water at the polymer coating/siliceous substrate interface, specimens of an epoxy coating applied on untreated and silane-treated, 50x10x3 mm spectroscopic grade, Si parallelogram prisms were prepared. For adhesion loss measurements on flat siliceous substrates,

specimens of coatings on untreated and silane-treated, 100-mm diameter Si wafers were used. Adhesion loss of the composites was determined from unsized, untreated and silane-treated 16 ± 2 μm diameter E-glass fibers impregnated with an epoxy resin.

The polymer coating was a stoichiometric mixture of a low molecular weight, diglycidyl ether of bisphenol A (epoxide equivalent weight = 189 g) and a polyethertriamine (amine equivalent = 83 g) curing agent. This epoxy coating was used for both flat substrates and composites. Si prisms and wafers were cleaned with acetone followed by methanol and dried with hot air before use. The surfaces of these substrates had a native SiO_2 layer of about 2.5 nm thick, as determined by an ellipsometer. Under ambient conditions (24 °C and 45% relative humidity), they should be covered with silanol groups (SiOH) and adsorb water[6]. The hydroxylated, SiO_2-covered Si (SiO_2-Si) prisms and wafers, and E-glass fibers are designated as the siliceous substrates in this study. Silane-treated surfaces were prepared by immersing cleaned Si prisms, Si wafers, and E-glass fibers for 30 minutes in an acidified (pH=4) water solution containing 0.1% aminoethylaminopropyltrimethoxysilane. The treated substrates were dried for 10 minutes at 110 °C before use. After mixing thoroughly the two components and letting them stand for 30 minutes at ambient conditions, the coating was applied on the prisms and wafers using the drawdown technique, similar to that described in Reference 5. All coated samples were cured at 80 °C for four hours followed by two weeks at ambient conditions. The thicknesses of the coatings on the prisms and wafers (determined at the conclusion of the experiment) were in the 130-150 μm range. The quality of all coated specimens was good and no visible pinholes or air bubbles were observed (with a naked eye) on the sample surfaces. Tg of the cured epoxy films was 83 °C (by differential scanning calorimetry, DSC).

Unidirectional composites were prepared by impregnating E-glass fibers with the same epoxy in between two transparent polyethylene (PE) sheets. Unsized, untreated and silane-treated fibers approximately 250 mm long were carefully laid unidirectionally on one PE sheet. After fixing one end of the fibers onto the PE sheet (by an adhesive tape), the epoxy was poured liberally on the fixed end of the fibers. After placing the other PE sheet over the resin-soaked fibers, the resin was spread by a glass plate placed on the PE sheet. The resin was spread along the fiber direction repeatedly until the fibers and the resin formed a transparent mat. The impregnated fibers were cut to size and placed in open-ended, aluminum molds having an inside dimension of 200x8x6.5 mm. The molds were placed in an autoclave for three hours at 80 °C and under a pressure of 1.4 MPa above atmospheric pressure, followed by post curing at 100 °C for 12 h. After removing the composites from the molds and conditioning them at ambient conditions for two weeks, they were polished and cut to a specimen size of 38x7.9x6.35 mm for exposures and testings. All specimens were transparent and there was no evidence of visible air voids, as observed by the naked eye. The fiber fraction of the composites was 40 % (determined by thermogravimetric analysis) and Tg of the epoxy in the composites was 84 °C (by DSC).

Measurement of Water at the Polymer Coating/Siliceous Substrate Interface

. Specimen configuration and Fourier transform infrared-multiple internal reflection (FTIR-MIR) procedure used for the measurement of water at the polymer coating/siliceous substrate interface are similar to those described in Reference 5. Briefly, a water chamber was attached to each cured, coated prism. The specimen with the water chamber attached was placed vertically in an attenuated total reflection (ATR) accessory holder and measurement of water at the interface was carried out using an FTIR spectrometer with a variable ATR accessory. After filling the chamber with distilled water at 24 °C, FTIR-MIR spectra were taken automatically every 15 minutes without disturbance to the specimens or the spectrometer. For the specimen

configuration employed in this study, the only pathway for water migration from the environment to the interface is through the coating film thickness. All spectra were the co-additions of 32 scans and taken at a resolution of 4 cm^{-1}. Unpolarized light at a 45° incident angle and purged dry air were used.

The thickness of the water layer, l, at the polymer coating/siliceous substrate interface was determined using the following expression[5]:

$$l = \frac{d_{pw}}{2} \left[-\ln \frac{1 - \frac{A}{A_\infty}}{1 - c_w \frac{d_{pc}}{d_{pw}}} \right] \qquad (1)$$

where A is the FTIR-MIR absorbance; A_∞ is the maximum infrared absorbance of water (provided by FTIR-MIR analysis of water on a coating-free siliceous substrate); c_w is the fraction of water sorbed in the coating within the FTIR-MIR probing depth (extrapolated from water uptake in coating); d_{pw} and d_{pc} are the penetration depths of the evanescent wave (calculated from internal reflection theory) in water and coating, respectively. For a Si substrate, d_{pw} is 0.22 μm and d_{pc} is 0.24 μm. Equation 1 is still valid for the case where the water layer at the coating/substrate interface is not continuous, e.g., discrete droplets.

Assuming water is uniformly distributed over the entire surface area of the specimen, the amount of water at the coating/substrate interface is given by

$$Q_i = l \, a \, \rho \qquad (2)$$

where a is the area in contact with water and ρ is the density of water at the interface.

Measurement of Adhesion Loss

The adhesion loss of epoxy-coated SiO_2-Si wafers as a function of exposure to water at 24 °C was measured using an improved version of a wet, 90° peel adhesion tester described in Reference 7. The apparatus consists of a linear bearing slider fixed to a computer controlled universal testing machine fitted with a 2.0 kg load cell. The improvement arose from lighter materials used and a low-friction moving slider. This resulted in a friction reduction from 200 g to 120 g. At each pre-specified exposure time, epoxy-coated wafers were removed from the test chamber and each wafer was immediately incised with a razor into five 12x65-mm specimens. Each specimen was carefully peeled from the substrate, leaving a 35-mm length of the specimen unpeeled. The wafers were then positioned in the test apparatus and peeled at a rate of 20 mm/min. All peel tests were conducted at room temperature and took approximately 30 minutes for each wafer from the moment it was taken out from the test solution. Ten specimens on two wafers were tested and the results averaged.

Adhesion loss of the composites was determined from the interlaminar shear strengths (ILSS), which is a measure of the adhesion between the resin and the fiber. ILSS values were calculated from the peak load of the short-beam, three-point bending test (ASTM D2344):

$$ILSS = 3F/4bd \qquad (3)$$

59

where F is the peak load in kN, and b and d are the width and thickness of the specimen in m. Specimens of 38x7.9x6.35 mm immersed in distilled water at 60 °C were removed from the container and tested at pre-specified time intervals. The specimen was supported by a 25-mm span and tested at a displacement rate of 0.5 mm/min. To ensure accuracy, the calibration of testing machine was verified at each testing period. Except for two cases where only two specimens were used, the results were the average of three or four specimens.

RESULTS AND DISCUSSION

In order to provide quantitative information on water at the coating/substrate interface, FTIR-MIR difference spectra were acquired. This was done by subtracting spectra taken before exposure from those collected at different exposure times. Figures 1a and 1b display difference spectra in the 2800-3800 cm^{-1} region (water OH stretching) of epoxy-coated untreated and 0.1 % silane-treated SiO_2-Si prims exposed to water for several representative times. The high signal-to-noise ratio of these spectra is due to the low concentration of detected water in these samples. The bands in the 3000-3650 cm^{-1} region are due to OH stretching mode of water, as verified previously[8]. The band peaking near 3400 cm^{-1} was chosen for the analysis, and its intensity changes as a function of exposure time are presented in Figure 2 for untreated and silane-treated specimens. The intensity of the water bands of both untreated and silane-treated samples increased with exposure time up to approximately 100 h then leveled off. These changes are the result of water entering the coating/substrate interfacial region and interacting with the evanescent wave[8]. Further, it can also be seen that the intensity of water detected for the untreated specimen is higher than that for the silane-treated one.
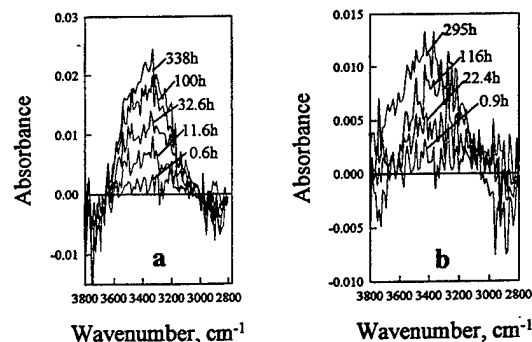
Figure 1.   FTIR-MIR difference spectra of epoxy-coated untreated (a) and 0.1% silane-treated (b) SiO_2-Si prisms exposed to 24°C water for several time intervals.

Substituting FTIR-MIR absorbance data (A) given in Figure 2, and c_w, A_∞, d_{pc} and d_{pw} values, which are taken from Reference 5, into Equations 1 and 2, thickness and amount of the water layer at the interface for epoxy coated untreated and 0.1% silane-treated SiO_2-Si substrate are determined. The results are given in Figure 3, which shows that essentially no or little water had entered the interface of the silane-treated specimens, but about 10 monolayers (one monolayer of water is about 0.3 nm) had built up at the interface of the untreated samples after 100 h exposure. The results on water at the interface for the silane-treated specimens suggest that the bond strengths between the treated surface and epoxy resin were stronger than those between the treated surface and water. Therefore, water molecules could not displace these bonds and thus

no or little water entered the interface. This result, which has been confirmed by a duplicate specimen, is supported by the adhesion loss data given in Figure 4. It is also consistent with the chemical bonding theory, which has been proposed as an explanation for the interfacial reinforcement mechanism and enhanced hydrolytic stability of composites made with silane-treated fibers[9]. It is noted that water is a weakly-sorbed species: the magnitude of water-oxide bonds are in the 40-65 kJ/mol range[10] and thus incapable of replacing stronger chemical bonds between the silane and the siliceous surface or between the silane and the epoxy resin.

It is important to point out here that the results of Figure 3 provide the first evidence that Equation 1 is valid for calculating water at the polymer/substrate interface. This equation, which was derived from the internal reflection theory, was based on a two-layer model consisting of the water layer at the interface and water sorbed in the coating film within the FTIR-MIR probing depth. If no water was at the interface, the total water detected (e.g. FTIR-MIR absorbance given in Figure 2) is due to only water in the polymer layer near the interface. This is the case for the coated, silane-treated specimens. These specimens had a hydrolytically stable interface, as evidenced by the small reduction in the adhesion after prolonged exposure (Figure 4) and corroborated by the well-established mechanism of silane coupling agents on glass fibers. Such an interface should allow little or no water entering this region. This is consistent with the results calculated from Equation 1 (Figure 3).
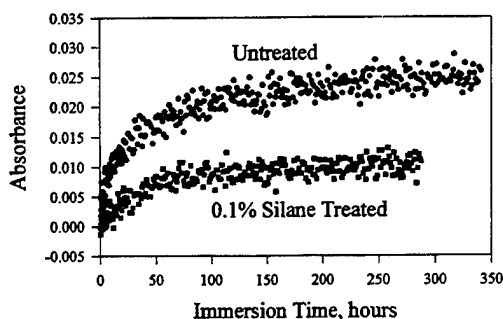
Figure 2. Intensity change of water band with time exposed to 24°C water for epoxy coated, untreated and 0.1% silane-treated SiO₂-Si prisms (each dot represents a data point).
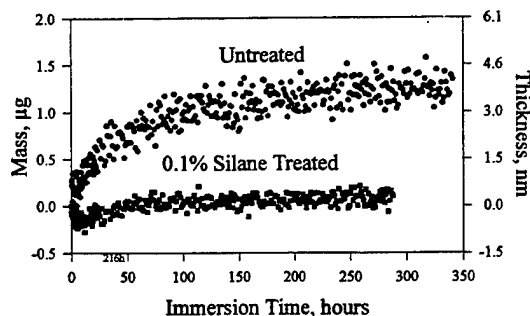
Figure 3. Thickness and amount of the interfacial water layer of epoxy-coated untreated and 0.1% silane-treated SiO₂-Si prisms exposed to 24°C water (each dot represents a data point).
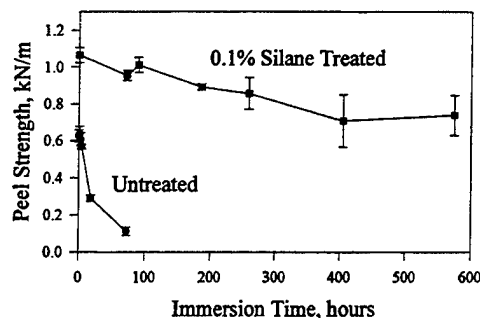
Figure 4. Peel adhesion of epoxy-coated untreated and 0.1% silane-treated SiO₂-Si wafers exposed to 24 °C water (bars on curves indicate one standard deviation).

Figure 4 presents adhesion changes as a function of time exposed to 24 °C water for epoxy-coated untreated and 0.1% silane-treated SiO_2-Si wafers. Untreated specimens lost most of their adhesion within 75 h of exposure, while silane-treated samples retained 80% of their adhesion even after 600 h immersion. These results, which are in good agreement with interfacial water data given in Figure 3, provide the first experimental evidence to show that the gradual buildup of a water layer at the interface is the main cause of adhesion loss of polymer coatings on an untreated siliceous substrate. The results of Figures 3 and 4 again illustrate the great affinity of untreated siliceous surfaces for water and that these surfaces must be modified to improve the durability of a polymer/siliceous substrate system.

Figure 5 displays ILSS data of composites prepared with untreated and silane-treated E-glass fibers immersed in distilled water at 60 °C for different times. Although at a lesser extent, the results follow the same trend with the adhesion loss of flat SiO_2-Si substrates; that is, composites of untreated fibers lost more of their shear strengths and at a faster rate than the composites of treated fibers did. Untreated and treated composites lost 55 and 23%, respectively, of their original shear strengths after three-month immersion. This compares with 83% adhesion loss after 75 h and 25 % loss after 600 h exposed to water at 24 °C for untreated and treated flat substrates, respectively. The results also show that the larger amounts of water at the polymer/substrate interface corresponded to the greater ILSS losses of the composites, suggesting that water at the resin/fiber interface may also play a role in the adhesion loss of composites.
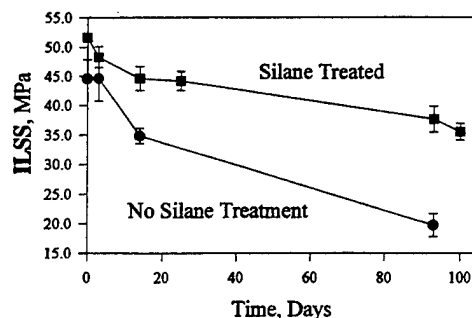
Figure 5. ILSS as a function of time in 60 °C water of untreated and 0.1 % silane-treated epoxy/E-glass fiber composites (bars on curves indicate one standard deviation).

The results of this study and other data for solvent-free organic coatings on siliceous substrates[11] indicate that larger amounts of water at the coating/substrate interface generally correspond with greater loss of adhesion. Additional data are needed to determine more precisely the range of the interfacial water layer corresponding with the range of the adhesion loss. If a relationship between adhesion loss and interfacial water layer exists, FTIR-MIR technique could be useful for estimating the adhesion loss at the molecular level and for predicting the durability of polymer/siliceous substrate systems.

SUMMARY AND CONCLUSIONS

Water is often the main cause of adhesion loss of a polymer coating/substrate system. This study investigated the accumulation of water at the interface, and adhesion loss of epoxy coatings on flat siliceous substrates and of epoxy/E-glass fiber composites. Both untreated and 0.1 % silane-treated flat substrates and fibers were included. Silane treatment effectively prevented water from entering the interface but a water layer of about 3 nm thick has built up at the interface of the untreated SiO_2-Si specimens after 100 h exposure to 24 °C water. Untreated, flat substrates lost most of their bonding strengths within 75 h exposure but silane-treated specimens retained 80% of their adhesion after 600 h exposure. Adhesion loss of untreated composites immersed in 60 °C water was greater than that of treated samples; however, the rate of loss of both silane-treated and untreated composites was much lower than that of flat substrates. Adhesion loss of both flat siliceous substrates and composites was found to follow the same trend with interfacial water buildup. If further analysis confirms that a relationship between the adhesion loss and the interfacial water layer exists, the FTIR-MIR technique could be useful for estimating the adhesion loss at the molecular level and for predicting the durability of polymer coating/siliceous substrate systems.

ACKNOWLEDGEMENTS

REFERENCES

1. H. Leidheiser, Jr. and W. Funke, J. Oil & Colour Chemists' Assoc. **70**, 121 (1987).
2 A.J. Kinloch (ed.) Durability of Structural Adhesives, (Applied Sci., N.Y., 1983).
3. C.L. Schutte, Materials Sci. and Eng. **R13**, 265 (1994).
4. M.A. Taylor and N.P. Khosla, Transportation Research Record **911**, 150 (1983).
5. T. Nguyen, D. Bentz, and W.E. Byrd, J. Coatings Technol. **66**, no. 834, 39 (1994).
6. T. Nguyen, E. Byrd, and D. Bentz, J. Adhesion **48**, 169 (1995).
7. D. Alsheh, T. Nguyen, and J.W. Martin, Proc. Adhesion Society Conference, February, 1994, p. 209.
8 T. Nguyen, W.E. Byrd, and C. Lin, J. Adhesion Sci. Technol. **5**, 697 (1991).
9. For brief reviews on this subject, see Reference 3 and J.L. Koenig and H. Emadipour, Polymer Composites **6**, 142 (1985).
10. P.A. Thiel and T.E. Madey, Surface Sci. Rep. **7**, 211 (1987).
11. T. Nguyen, D. Alsheh, D. Bentz, and W.E. Byrd, Proc. Adhesion Society Conference, February, 1995, p. 252.

ON THE MICROSTRUCTURE OF THE EPOXY/ADHEREND INTERPHASE

M. Libera,* W. Zukas,** S. Wentworth,** and A. Patel*
* Stevens Institute of Technology, Hoboken, NJ 07030
** U.S. Army Materials Tech. Laboratory, Watertown, MA 02172

ABSTRACT

It is now recognized that there is a region at the epoxy/adherend interface known as the interphase whose chemistry and structure are different from those of bulk epoxy. There is, however, no adequate understanding of its microstructure. This paper describes differential scanning calorimetry (DSC) and transmission electron microscopy (TEM) studies of the interphase between an aromatic amine cured epoxy and alumina/oxidized-aluminum surfaces. DSC results show dramatic differences in resin-cure behavior in the presence of particulate alumina. TEM results on microtomed cross-sectional specimens of anodized aluminum wire embedded in epoxy show regions of incomplete epoxy infiltration and interfacial stress. RuO_4 staining combined with high-angle annular-dark-field STEM imaging indicates that there are structural variations within the bulk epoxy at lengths of ~10-30nm. The magnitude of these fluctuations decreases in the near the adherend interface, and there is a simultaneous variation in the average epoxy structure. A plausible interpretation of these observations is that the interphase region suffers a variation in curing-agent concentration of unknown magnitude and there is a higher concentration of homopolymerized epoxy there relative to the bulk.

I. INTRODUCTION

Epoxies are particularly important as the matrix in fiber-reinforced composites, as durable coatings for inorganic materials, and as adhesives. These applications involve one or more interfaces between the epoxy and an adherend. Several researchers (1-4) have shown that there is a region at the epoxy/adherend interface known as the interphase whose chemistry and structure are different from that of bulk epoxy. This interphase can be critically significant. The ability of an epoxy matrix to transfer stress to a strong adherend in, for example, a fiber-reinforced composite is ultimately controlled by the interphase. The interphase has been studied by various optical spectroscopies (5-9), TEM (10), and XPS(11). Previous calorimetric studies by Zukas, Wentworth, et al. (12) using particulate alumina as a model adherend surface has shown that reactions involving only the epoxy become significant in the interphase for stoichiometric formulations of resins cured with aromatic amines. Further work (13) indicated that the alumina clearly leads to an interphase structure that is different from the bulk and also dependent on the cure history and water content of the system. Despite this progress, however, there is not yet an understanding of the interphase microstructure. This work presents first results using transmission electron-optical techniques coupled with DSC to address what specific microstructural features might be found in the interphase.

II. EXPERIMENTAL PROCEDURE

This research used epoxy resins based on diglycidyl ether of bisphenol A (DGEBA) including DER (Dow) and Epon (Shell) resins. Several primary aromatic amine curing agents were investigated including: diaminodiphenyl methane (DDM); 3,3'-diaminodiphenyl sulfone (33DDS); 4,4'-diaminodiphenyl sulfone (44DDS); and meta-phenylene diamine (mPDA).

65

DSC analyses were performed with a Perkin-Elmer DSC-2C calorimeter using 5-50mg samples encapsulated in stainless steel pans. Cure exotherms were obtained using dynamic scans at constant heating rates between 0.5 to 40°C/min. Neat resin formulations were prepared by mixing the epoxy resin with curing agent at various stoichiometries at room temperature. Similar samples which were filled with alumina particulate used Brockmann I activity neutral aluminum oxide (Aldrich, surface area =155m²/g, pore size = 5.8nm at 150mesh). Filled samples were prepared by first dissolving the curing agent in the neat resin at elevated temperature, cooling to room temperature, then adding the alumina. Pre-reaction of the formulation before the calorimetry experiments was minimized.

Transmission electron microscopy was done using a Philips CM20 FEG TEM/STEM in both traditional bright-field TEM mode and high-angle annular-dark-field (HAADF) STEM mode (14). Thin specimens were prepared by ultramicrotomy, supported on copper TEM grids with or without holey-carbon films, and stained. Two different staining procedures were used: (i) a several-step uranyl-acetate protocol developed by Di Filippo et al (15) ; and (ii) exposure to RuO_4 vapor (room temperature, 15min). Specimens were cut from tensile bars prepared by Prof. L.T. Drzal. These consisted of a single 125μm diameter anodized Al wire embedded in epoxy. The wire was anodized using phosphoric acid in general accordance with SAE Aerospace Recommended Practice 1524 REV A. The treated wire was dried and then encapsulated in Epon 828 cured with mPDA. This procedure produced a single wire axially aligned in a dogbone tensile coupon having a gauge section of 3mm x 1.5mm x 25mm (fig. 1).
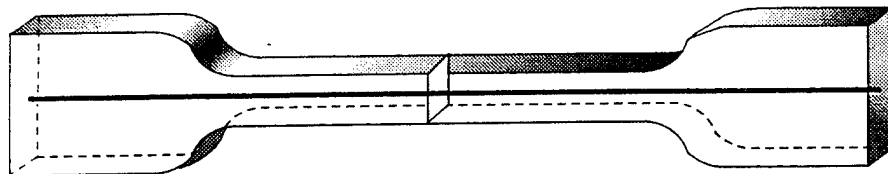
Figure 1 - Schematic illustration of the tensile specimen with a single axial anodized Al wire from which thin sections were cut for TEM characterization of the Al/epoxy interphase region.

III.1 RESULTS OF DSC STUDIES

The general cure exotherm observed for a dynamic DSC scan of a neat resin mixture is a single exotherm (12, 13) proportional to the amount of amine present. This indicates that epoxy/amine reactions take place during dynamic cures of these resins. Measured experimental features such as the fact that there is only a single isotherm, the exotherm peak temperature, and the enthalpy of reaction are consistent with other observations reported in the literature on similar epoxy systems (16-19). Figure 2a shows a typical result.

Filling the epoxy samples with activated alumina particulate has a significant effect on the DSC exotherms (figure 2b). Whereas the unfilled (neat) resin shows only a single exotherm, the filled resin shows three: two low-temperature exotherms and an exotherm somewhat lower in temperature than the unfilled exotherm. The two additional low-temperature peaks are

attributed to the action of the activated alumina. It appears to be acting as a catalyst for amine-epoxy reactions and as an initiator for epoxy-epoxy homo-polymerization reactions. The highest temperature exotherm in the unfilled neat resin is shifted to lower temperatures in the filled samples. This exotherm has been attributed to reactions involving excess epoxy (12,13).

III.2 RESULTS OF TEM & STEM IMAGING

Bright-field TEM images of uranyl acetate stained cross sections of the dogbone specimens are shown in figure 3. In addition to the fine-scale roughness induced by the anodized layer, there are burrs and other Al protuberances. There is also evidence of stress-induced wrinkling of the specimen near the interface (A), thickness striations from the microtomy (B), and incomplete infiltration of the epoxy (C). Staining using the Di Filippo uranyl-acetate protocol failed to show significant contrast within the epoxy both in bright-field TEM and HAADF STEM modes.
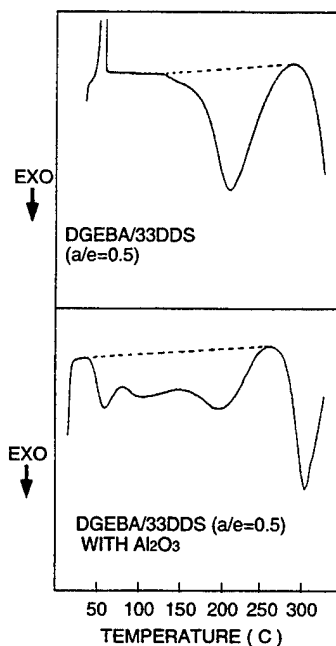
Figure 2 - DSC scans for neat (upper) and alumina-filled (lower) epoxies cure exotherms.
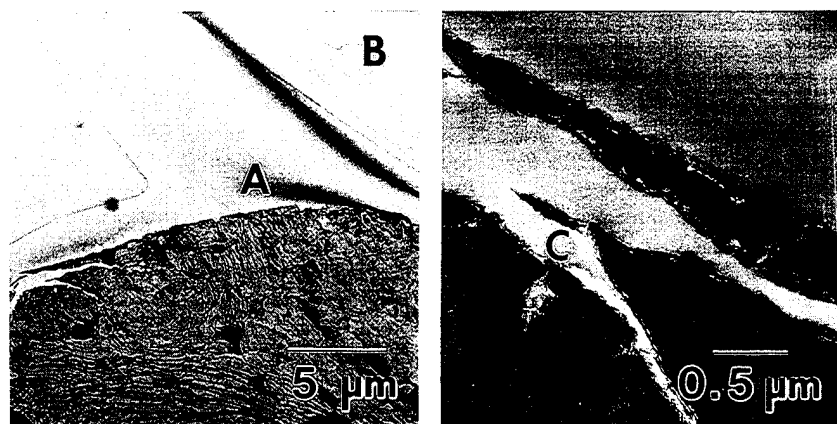
Figure 3 - Bright-field TEM images of the interface region between epoxy and an anodized aluminum wire. Uranyl acetate staining provides no electron-optical contrast within the epoxy.

Ru-stained specimens display substantial contrast within the epoxy when imaged via HAADF STEM. This imaging method is very effective at resolving variations in average atomic number. Regions rich in Ru (atomic number 44) appear bright in HAADF images. Representative results characterizing the bulk epoxy well away from the Al wire are presented in fig. 4. The contrast and brightness of the image are optimized to show the structure of the epoxy lying above one of the holes in the carbon support film. This image shows regions of light and dark contrast with fluctuations on a ~10-30nm length scale. There do not appear to be any obvious variations in the average HAADF signal scattered from the bulk epoxy. A similar microstructure was observed in several different areas of the bulk epoxy film.

50 nm
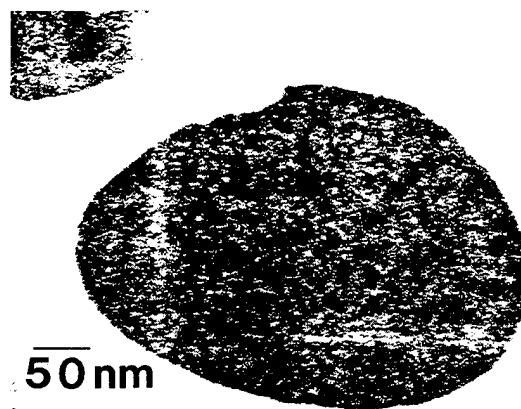
Figure 4 - HAADF STEM image of a RuO_4-stained bulk epoxy section on a holey-C support film.

HAADF STEM images characterizing the Al/epoxy interface are different than those from the bulk. Fig. 5a is a low-magnification image where the contrast and brightness are optimized to show the general structure. The darker circles correspond to areas where the electron beam passes only through epoxy. Fig. 5b shows a high-magnification image collected from one such region in the interphase. Here the contrast is optimized to show the structure of the epoxy. These conditions necessarily wash out the image where there is aluminum or carbon film. As in fig. 4, the epoxy shows regions of modulated contrast on a length scale of ~10-30nm. There is also a general variation in the average contrast perpendicular to the oxide/epoxy interface. The HAADF signal was recorded using a storage oscilloscope interfaced to the annular-dark-field detector as described in reference (20). Figure 5c plots this signal as a function of distance from the oxide/epoxy interface. The interface is not sharp. The epoxy region begins in the vicinity of x=60-80nm. Beyond that the signal rises from a minimum to a maximum at approximately x=170nm. The average signal is then roughly constant. The magnitude of the fluctuations about the average signal also appear smaller in the near-interface region than in the region beyond x~170nm. Similar behavior was observed at other locations in this same film.

IV. DISCUSSION AND CONCLUSION

The calorimetric data show clear evidence that activated alumina particulate has a significant effect on the epoxy cure behavior. At least two additional low-temperature exotherms appear in particulate-filled specimens which are absent in identical but unfilled specimens. The activated alumina appears to catalyze both the epoxy homopolymerization and the amine-epoxy

68
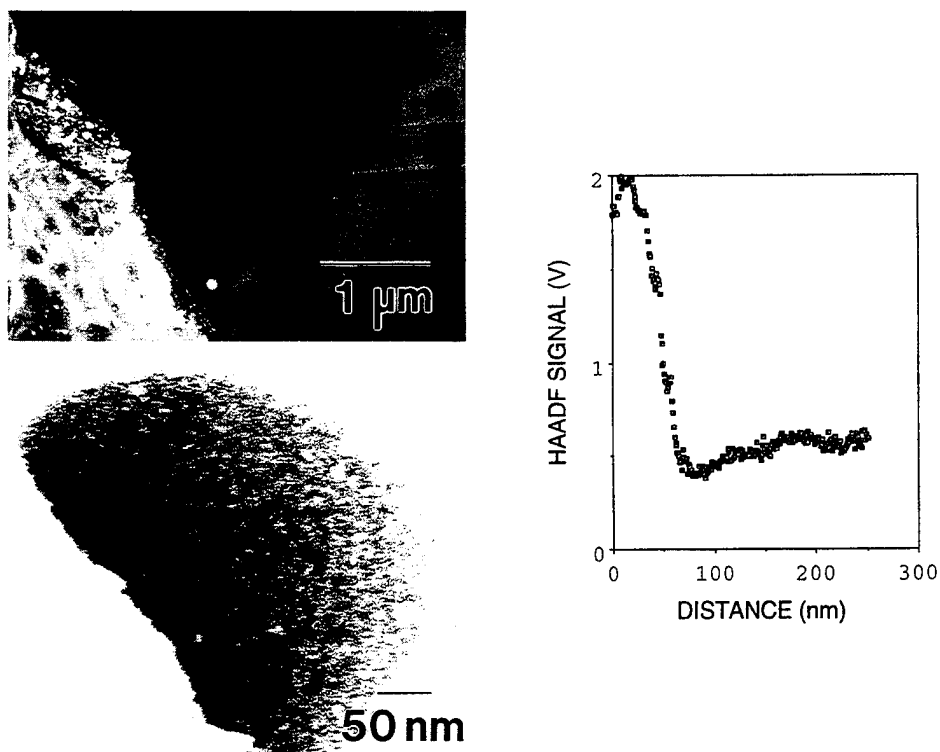
Fig 5 - HAADF STEM images of the RuO_4-stained wire/epoxy interface region: (a) contrast and brightness optimized to show general structure; (b) optimized to show epoxy structure; (c) HAADF detector amplified voltage as function of distance from the wire/epoxy interface.

reactions. Intuitively, one would expect any variations in the epoxy microstructure due to homopolymerization and other catalytic effects to occur in the vicinity of the adherend surface. The HAADF STEM images of Ru-stained epoxies, in fact, indicate that there is a Ru depletion close to the interface with anodize Al wire and that the average Ru concentration increases to some relatively constant value approximately 100nm away from the interface. These measurements also suggest that the rather uniform 10-30nm modulation of Ru concentration observed in bulk epoxy well away from the Al wire have a smaller amplitude near the interface. The important issue yet to resolve concerns what chemical or structural feature characteristic of the epoxy is manifested by the measured Ru distribution.

Ru staining involves covalent bonding where RuO_4 oxidizes particular chemical moieties in the polymer (21). It is particularly reactive with aromatic groups. These are contained by both the DGEBA resin and the mPDA curing agent used in the Al-wire dogbone specimens. Whether or not RuO_4 is more reactive with the epoxy or the curing agent due to the influence of other species in proximity to the aromatic rings in each case is not known. These variations, if present, are

likely to be small and may be compensated for if sufficient staining time is provided to saturate all reactive sites. Concluding that the Ru concentration and, hence, the HAADF STEM intensity is proportional to the concentration of aromatic rings thus appears reasonable. The number of aromatic rings per unit volume is different for the epoxy resin and the aromatic amine curing agent. A spatial variation in the concentration of aromatic rings could be caused by a variation in the concentration of curing agent. If so, the observation of a Ru/aromatic-ring depletion within the interphase would be consistent with the conclusion from the DSC work that the adherend surface catalyzes the homopolymerization reaction for which a curing agent is not needed. The curing agent would naturally segregate away from the interface to some distance where the interface no longer exerts a catalytic influence on the cure. This argument that spatial variations in curing agent concentration occur in the interphase region is weakened by the fact the RuO_4 staining procedure does not distinguish effectively between the epoxy rein or the curing agent. Future work will concentrate on similar electron optical analysis using epoxy systems were greater staining selectivity can be had or by using holographic imaging which may enable direct imaging of the unstained microstructure.

ACKNOWLEDGEMENTS

REFERENCES

1. L. H. Sharpe, J. Adhesion 4, 51-64 (1972).
2. L.H. Sharpe, *The Science and Technology of Adhesive Bonding*, Proc. 35th Sagamore Army Materials Conf., ed. L. Sharpe and S. Wentworth, Gordon and Breach, NY (1990).
3. L.T. Drzal, in *Epoxy Resins and Composites II*, Springer-Verlag, Berlin (1986).
4. J. Miller and H. Ishida, in Fundamentals of Adhesion, ed. L. Lee, Plenum, NY (1991).
5. A. Garton et al., J. Poly. Sci. Tech. A26, 1377 (1988).
6. A. Garton, J. Poly. Sci: Poly. Chem. Ed. 22, 1495 (1984).
7. J. Nigro and H. Ishida, J. Appl. Poly. Sci. 38, 2191 (1989).
8. D. Ondrus, F.J. Boerio, and K. Grannen, in ref 2.
9. S.L. Tidrick and J.L. Koenig, ibid.
10. J.S. Crompton, J. Materials Science 24, 1575-1581 (1989).
11. R. Dillingham and F.J. Boerio, J. Adhesion 24, 315 (1987).
12. W. Zukas, K. Craven, and S. Wentworth, J. Adhesion 33, 89 (1990).
13. W. Zukas, M. Sennett, and S. Wentworth, Proc.16th Ann. Mtg. Adhesion Soc. 187 (1993).
14. S.J. Pennycook, Ultramicroscopy 30, 58-69 (1989).
15. G. Di Filippo, J. Vander Sande, and D. Uhlmann, J. Appl. Poly. Sci. 35, 485-505 (1988).
16. C.C. Ricciardi and R.J.J. Williams, J. Appl. Poly. Sci. 32, 3445 (1986).
17. J. Galy, A. Sabra, and J. Pascault, Poly. Engr. Sci. 26, 1514 (1986).
18. A.C. Grillet, J. Galy, J. Pascault, and J. Bardin, Polymer 30, 2094 (1989).
19. J.M. Barton, J. Macromolecular Sci. Chem. A8, 25 (1974).
20. M. Libera, J. Ott, and K. Siangchaew, submitted to Ultramicroscopy.
21. J.S. Treat, J.I. Scheinbeim, and P.R. Couchman, Macromolecules 16, 589-598 (1983).

ADHESION AND THERMAL DEFORMATION OF CERAMIC/ POLYMER HETEROSTRUCTURES

CYNTHIA MADRAS , PETER Y. WONG, AND IOANNIS N. MIAOULIS*
Thermal Analysis of Materials Processing Laboratory, Mechanical Engineering Department, Tufts University, Medford, MA

ABSTRACT

The adhesion and thermal properties of optical ceramic structures bonded by a polymer interlayer are explored. The mechanical, adhesion and optical properties of the heterostructure are dependent on the thickness of the bond and on the residual thermal stresses developed during the bonding process. The thermomechanical properties of a bonded structure over a range of temperatures are investigated, focusing on the thermal expansion and operating temperature limits of the polymer bond. The temperature and stress histories during manufacturing are determined through both numerical modeling and experimental analysis. The effect of stress relaxation and initial stresses on the behavior of the bonding material are examined for different processing conditions. The bond material relaxation time constant, activation energy, viscosity, and shear modulus are approximated from observation of the temperature-dependent behavior of the structure.

INTRODUCTION

When fabricating complex layered devices for the optical or microelectronics industry, predicting existing thermal strains in the structure at every point during production and use is crucial. Thermal strains in layered devices bonded together by an organic layer, polymer or wax, are manifested as curvature changes in the structure similar to the curvature changes thin films cause when deposited on a substrate. If thermal stresses due to the actual bonding cause significant curvature changes, the optics, performance, and adhesion of the device may be compromised. These stresses are significant even at low bonding temperatures if the bonded materials have large differences in thermal expansion coefficients. Predicting thermal strains must involve complete characterization of the bonded materials and the bonding agent at its operation temperatures and through any thermal cycles the structure may undergo during use. With organic bonding layers, it is likely that inelastic deformation will occur at elevated temperatures if the bond layer is under thermal strain.

In order to fully understand and predict the strain and curvature of a structure, the elastic and inelastic temperature- and time-dependent behavior of the structure must be characterized. This study combines an elastic deformation model with a viscoelastic behavior model to fit observed behavior of an optical structure bonded with an organic material. Heat treatments involving prolonged holds at elevated operation temperatures were performed in order to obtain a wide characterization of the bond material and the behavior of the structure. All of the heat treatments were done at temperatures between room temperature and the bonding temperature of the structure. The thermal strains resulting from the temperature changes are considerable enough to cause observable curvature changes and inelastic effects caused by the bonding layer. The structure is a polished diamond disk bonded to a zinc sulfide (ZnS) disk by an optically-transparent high temperature wax. The melt temperature of the wax is 100°C and the materials were bonded at this temperature. These materials have applications in the infrared optics industry as durable high temperature coatings. However, diamond and ZnS have very different thermal expansion coefficients, and significant stresses result due to slight temperature changes. Because of the low melting temperature of the wax and the relatively high thermal stresses involved, the elastic and inelastic response to temperature changes are readily characterizable in this structure.

When a bonded structure is heated to a service temperature that is a significant fraction of the melting point of the adhesive material, the curvature of the entire structure will change over a period of time due to stress relaxation in the adhesive layer. Often the stresses will relax at room temperature. If the initial thermal stress in the bond is known when the sample is heated to its service temperature and the curvature change is observed, then significant properties of the system may be characterized. These properties are the relaxation time constant for the adhesive material, the activation energy for inelastic deformation, and the viscosity. There are several theoretical models that were used to characterize the behavior of this structure and estimate the properties as a function of time and temperature. The stress at a given temperature was estimated using an elastic strain model for layered structures developed by Townsend, et.al. [1]. This model uses the thermal expansion coefficients and elastic moduli of each of the layers to calculate the curvature, or thermal strain, and the thermal stresses throughout any layered structure. Thermal elastic stresses are predicted between the bonding temperature of the material, (in which the stresses are zero), and the service temperature at which the curvature change, or stress relaxation, is measured. The actual stress in the adhesive layer changes with time as it relaxes; however the initial stress is approximated to be elastic prior to the relaxation if the temperature is changed rapidly enough. If no inelastic deformation occurs in the bonded layer throughout all heat treatments, then the stress and curvature of the structure should be completely elastic and predictable by this model.

Since the wax adhesive material is a relatively small and simple molecule compared to long-chained or thermoset bonds, the stress relaxation may be modeled according to Maxwell's model of viscoelastic behavior. This model applies to a range of materials from glycerin to thermoplastics that are single relaxation mode polymers [2]. Maxwell's model describes the system as a spring and dashpot in series, where the displacement is the strain, the dashpot constant is the viscosity of the material, and the spring constant is the modulus of elasticity [3]:

$$\frac{\sigma}{\eta} + \frac{1}{G}\frac{d\sigma}{dt} = 0 \qquad (1)$$

where σ is the instantaneous stress, η is the viscosity of the bond layer, and G is the shear modulus of the wax bond. η, σ, and G are all temperature-dependent, making the shape of the solution vary with temperature. The stress at any time as it relaxes at a constant temperature may be determined from the solution to Equation 1 and the initial stress [3]:

$$\sigma = \sigma_0 e^{-t/\lambda} \qquad (2)$$

where σ is the time-dependent stress, σ_0 is the initial stress, t is the time, and λ is the time constant. σ_0 and λ are also temperature dependent, so Equation (2) must be fitted to the material behavior over a range of temperatures. The time constant may be measured by observing the curvature relax from an initial value to a value close to zero as a function of time since stress and curvature are directly related. If σ_0 and λ are known, then the stress in the bond may be known at any time for a given temperature and the change in curvature of the structure may be predicted as a function of time.

Another property inherent to each material is the relaxation activation energy, $\Delta\mu$, describing the free energy activation barrier for molecular motion [2]. Molecular motion is the relaxation mechanism. The relaxation time constant is related to the activation energy, temperature, initial viscosity, and shear modulus [2]:

$$\lambda(T) = \frac{\eta_0(T)}{G(T)} e^{\left(\Delta\mu^* / kT \right)} \qquad (3)$$

where λ is the time constant, η_0 is the initial viscosity, G is the shear modulus, $\Delta\mu^*$ is the Vogel-Fulcher activation energy for stress relaxation, k is Boltzmann's constant, and T is the temperature. The activation energy is ideally constant for a given material. However, $\Delta\mu$ in reality changes with temperature as the material expands and the free volume increases, but a constant $\Delta\mu$ is a reasonable approximation [2].

If the initial stress is known and the curvature change is observed as a function of time and temperature, then the other properties may be determined from this model and applied to predicting further curvature changes and stress relaxation in other layered structures.

EXPERIMENTAL

Samples of ZnS and diamond 2.54 mm (1 inch) in diameter were bonded together using a wax polymer bond with melting temperature of 100°C. Both disks had optically polished surfaces on both sides. The ZnS thickness was 880 μm and the diamond layer thickness was 210 μm. A high melting temperature wax of polyethylene structure was used as the bonding agent between the two optical disks. Several beads of wax were placed on the ZnS surface and melted on a hot plate. The temperature was measured by a thermocouple positioned at the edge of the ZnS piece. Once the wax was fully melted and evenly spread across the surface, the diamond disk was pressed on top of the melted wax surface and the structure was removed and placed on a cool (room temperature) surface in order to rapidly solidify the wax. The thickness of the adhesive layer was ~3 μm.

After the samples were bonded and cooled to room temperature, they were heated rapidly to final temperatures of 45°, 55°, and 65° and held at those temperatures while the curvature of the structure was measured as a function of time.

The structure curvature was measured by the laser-beam deflection method. Since both optical disks had initial non-zero curvatures, the absolute curvature values measured reflect the sum of both the initial and the thermal-stress induced curvatures of both bonded materials. Because of this, all of the results are stated in terms of *change* of curvature as a function of time and temperature rather than absolute curvature values.

RESULTS AND DISCUSSION

Time Dependent Stress Relaxation

Figure 1a), b), and c) show the measured curvature change of the bonded sample at 45°C, 55°C, and 65°C respectively as a function of time. The curvature change is fitted to an exponential function reflecting the viscoelastic stress relaxation that is occurring at these temperatures. There is scatter in the measured data due to sample and temperature control variations. The time constant for relaxation at each temperature, $\lambda(T)$, is apparent from the exponential decay of the relaxation curves. Physically, this represents the time at which 64% of the stress has been relaxed. The curvature is shown to decrease as the samples flatten out to a less stressed state.
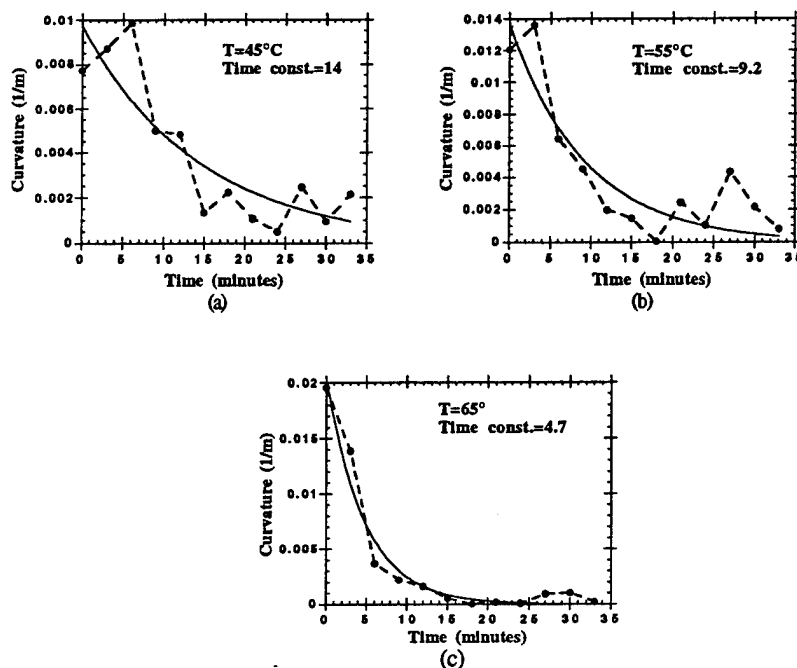
Figure 1. Measured change in curvature of the bonded structure as a function of time at (a) 45°C, (b) 55°C, and (c) 65°C. The exponential relaxation curve fit is shown with the time constants.

The relaxation time constants decrease with increasing temperature as expected from Equation 3. As the temperature approaches the melting temperature of the wax, stress relaxation is more rapid. Figure 2 shows the measured relaxation time constants, in seconds, as functions of temperature. Although difficult to detect, because the temperatures are so close and the noise in the curvature measurements, the time constants are decreasing along a slight exponential curve as would be expected.
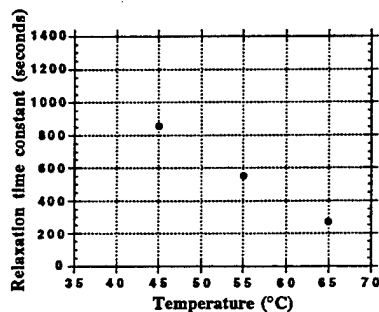
Figure 2. Time constants determined from curvature change measurements as a function of temperature.

The initial actual thermal stresses, σ_o's, in the wax bond at each temperature were not known explicitly, but were approximated at each temperature using the elastic strain model and an approximate modulus of elasticity. These approximate σ_o's, for a bond temperature of 75°, (where the curvature was measured to begin changing), were 7.4 MPa, 4 MPa, and 2.5 MPa at 45°, 55°, and 65° respectively. Figure 3 shows the time dependent stress relaxation at the three temperatures using the approximate values for the initial stresses.
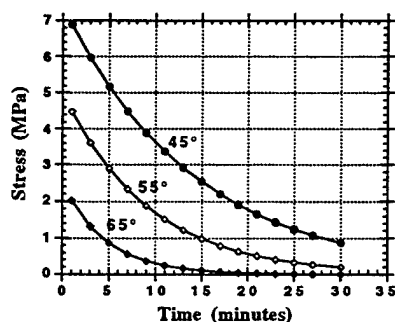
Figure 3. Approximate viscoelastic stress relaxation at 45°C, 55°C, and 65°C based on assumed initial stress and measured time constants.
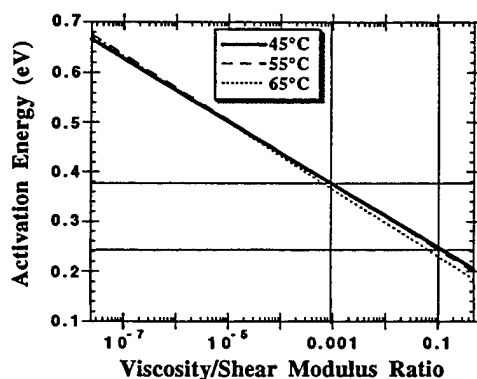
Figure 4. Range of bond material activation energy (Ea) determined from the time constants and the approximate viscosity/shear modulus ratio.

75

Activation Energy Prediction

The Vogel-Fulcher activation energy for inelastic deformation, a value not given for this material in the literature, was predicted by using Equation 3, solving for the activation energy as a function of η_o/G ratio. The η_o/G ratio of the bond material was approximated using appropriate ranges for this ratio. Figure 4 shows the activation energy as a function of η_o/G ratio using the experimentally measured time constants at each temperature. The region highlighted between the solid lines shows the appropriate range of activation energies. The range of initial viscosity expected for this material within the temperature regions investigated: 85% to 91% of the melting point of the bond material, is 10^5 to 10^6 kg/m·s [4]. The shear modulus is on the order of 10^4 Pa [5], giving a viscosity/modulus ratio of 0.01 to 0.1 as a best approximation. The material activation energy is in the range of 0.25 and 0.3 eV, or 5.8 to 6.9 kcal/mol.

CONCLUSION

A combination of elastic and inelastic stress theories were used to characterize time and temperature dependent behavior of an individual optical structure. The goal of this work was to use a predictive model to determine the curvature at any given temperature and time. The net curvature of the structure is a combination of elastic thermal stresses and stress relaxation in the organic bond layer. The wax bond behaves according to viscoelastic stress relaxation theory in which the structure curvature is dependent on the relaxation rate and temperature and properties of the wax bond. From observation of the curvature change as a function of time and temperature, key properties of the wax may be extracted, such as the Voger-Fulcher activation energy and the temperature dependent relaxation time constant. Knowing these properties enables prediction of the curvature of the structure at temperatures times other than what was observed in this study. In addition, the models employed here may be adapted for determining change in shape over time of a range of systems in which single relaxation mode thermoplastic polymers are used to bond different materials.

REFERENCES

1. P.H. Townsend, D.M. Barnett, and T.A Brunner, J. Appl. Phys. 62 (11), 4438-4444 (1987).

2. Shiro Matsuoka, Relaxation Phenomena in Polymers, (Oxford University Press, New York, 1992), p.9, pp. 45-49.

3. N.G. McCrum, C.P. Buckley, and C.B. Bucknall, Principles of Polymer Engineering, (Oxford University Press, Oxford, 1988), pp. 101-166.

4. R. Byron Bird, Warren E. Stewart, and Edwin N. Lightfoot, Transport Phenomena, (John Wiley & Sons, New York, 1960), pp. 14-18.

5. M.F. Ashby and D.R.H. Jones, Engineering Materials I, (Pergamon Press, Oxford, 1980), p. 31.

Part IV

Interface Characterization

XPS STUDY OF BURIED METAL/POLYMER AND POLYMER/METAL INTERFACE

P.K. WU
Department of Physics, Southern Oregon State College, Ashland, OR 97520.

ABSTRACT

Metal/Polymer systems have potential applications as interconnect materials in integrated circuits. Polymers with low dielectric constants, if used as interlayer dielectric, can reduce the RC time constant. Device speed can be doubled if a polymer can replace the present dielectric material, SiO_2. However, the problem of weak metal/polymer adhesion must be understood and resolved. *In situ* deposition and analysis are the most controlled means to study an interface formation process. However, for practical reasons, i.e., application, time, cost, and flexibility, it is critical to study metal/polymer interface *ex situ*. X-ray Photoelectron Spectroscopy (XPS), can be used to determine the composition and bonding structures of buried interfaces. This is achieved by examining peeled surfaces, thin overlayer, and low-energy-ion sputtered surfaces. The possible adhesion mechanism or failure mode is determined by correlating XPS results with adhesion strength. Based on these results, adhesion enhancement methods, such as substrate surface treatments, can be formulated. The product of these treatments can be evaluated using the same analysis. These techniques for studying buried interfaces using XPS are reviewed and results of their applications to the metal/Teflon AF 1600 interface is presented.

INTRODUCTION

Dielectric materials in interconnect technology are important to consider when electronics device operation frequency enters the GHz regime. The RC time constant of the interconnect ultimately limits the device speed. Just as important is the cross-talk between interconnect lines which will reach unacceptable levels as device dimensions decrease to submicron levels. These problems can be eliminated by using materials with low dielectric constants. Polymers are the most practical candidate for the proposed application. The present dielectric material, SiO_2 has a dielectric constant of 3.9. Teflon, for example, has a dielectric constant of 2.1. Polyimides and fluorocarbon polymer, with dielectric constants below 2.5, are being examined as potential insulators.[1-4]

For a material to be suitable as a new dielectric, it should have a low dielectric constant and be able to withstand 450°C, the highest currently used processing temperature, while in contact with the metal. For devices to function reliably, polymers used in interconnects must have good adhesion with metal. However, polymers such as fluorocarbon polymers, because of their low surface energy, show only weak polymer/metal adhesion. It is thus crucial to understand the adhesion mechanism as well as to develop means of improving metal/polymer adhesion.[5-14]

The ultimate adhesion strength between a polymer and metal depends on several mechanisms]:

79

1. Mechanical Anchoring - Adhesion improves with a rough interface which provides a large surface area for bonding as well as sufficient mechanical interlocking.[16, 17]

2. Chemical Bonding - Chemical bond formation at an interface improves the adhesion between the two materials.[18]

3. Electric Double Layer - When a polymer comes in contact with a metal, charge transfer between the two surfaces can result in the formation of a double electric layer, i.e., a capacitor, at the interface.[19] Because of electrostatic forces, energy is required to separate such an interface.[20]

4. Weak Boundary Layer - Any contamination, reaction or diffusion between two materials in contact may result in the formation of multiple interfaces with different compositions as a function of distance from the interface. Adhesion failure at such an region will occur at the layer with the weakest adhesion strength.[21, 22]

One or more of these mechanisms can be operative at any one time. All adhesion mechanisms operate at or near the interfacial region between the two materials. Establishing the relative importance of the adhesion mechanism can shed light on the choice of adhesion enhancement method. Adhesion can be enhanced by altering the interfacial region, for example, by increasing surface roughness and introducing bonding sites [16, 17], by enhancing interdiffusion or forced mixing [5], or by eliminating weak boundary layers. Surface modification of fluoropolymers is of great importance to improve adhesion and a review can be found in reference [23].

To understand the contribution from various mechanisms to the ultimate adhesion strength, one needs to determine the composition as a function of distance from the interface and the chemical state of the elements which contain information on the bonding structure and bonding sites. The latter is especially important in the case of polymers. Metal can preferentially bond to certain functional groups. If these groups can be identified, special copolymers can be synthesized to promote adhesion without compromising other beneficial properties of the polymer. Copolymers of fluoropolymers have shown to have good adhesion with some metals.[24]

X-ray Photoelectron Spectroscopy (XPS) is best suited for such measurements because of its ability to determine relative elemental concentrations as well as chemical bonding information. XPS application to polymer is well understood and chemical shifts are well documented.[25,26] The escape depth of photoelectron used in XPS is 1 to 4 nm and composition can be determined with good depth resolution. Unfortunately, some polymers will decompose on prolonged exposure to X-rays and care must be taken to ensure correct interpretation of XPS results.[27]

The most controlled means of studying interfacial formation is by *in situ* deposition and examination of the process under ideal conditions, i.e., in Ultra-High Vacuum. The chemistry and morphology of the interface as a function of film thickness can be determined as the film develops.[28] Such studies are important in revealing the basic mechanism of adsorption, nucleation and growth of overlayers. The results of these studies, however, are not directly applicable to device technology. Fabrication usually occurs under less than ideal conditions, i.e., lower vacuum or higher contamination, higher temperature because of higher deposition rate, and stress can result from subsequent processing conditions. In addition, some adhesion enhancement techniques are performed after the interface is formed, i.e., ion beam "stitching" of the buried interface [5]. Furthermore, weak boundary layers can form during subsequent processing. It is thus important to be able to study buried interfaces.

The common technique for exposing a buried interface is by ion sputtering using noble gas. Sputtering polymers however can result in many problems. In addition to differential sputtering, ion bombardment can induce mixing, i.e., as a result of momentum transfer, and in the case of polymers, can cause decomposition. Very useful information, however, can be determined from sputtered surfaces by careful interpretation of the results.

In this article, some of the techniques in applying XPS and ion sputtering to determine bonding structures at buried interfaces are illustrated using the sample system, Teflon AF 1600 and metals, i.e., Ag, Al, Au, and Cu. Teflon AF 1600 is an amorphous fluoropolymer synthesized by Resnick at Du Pont Corporation.[29] It is a copolymer of tetrafluoroethylene or Teflon and 2,2-bis(trifluoromethyl)-4,5-difluoro-1,3-dioxiole, see Figure 1. The bulk dielectric constant of AF 1600 is determined to be 1.9 at room temperature, the lowest of all polymers, including Teflon.[30] Deposition of amorphous AF 1600 films was recently reported by Nason et. al.[31] and R. Chow et. al [32] using vacuum pyrolysis and by Blanchet using a laser ablation method.[33] The amorphous nature of these films is potentially superior to Teflon in mechanical properties, i.e. reduced creep, as well as optical properties, i.e. reduced scattering.[34,35] AF 1600 is thus potentially useful as a dielectric layer in integrated circuit packaging and as a thin film waveguiding material. To realize such applications, some practical problems have to be addressed. Chief among these is the metallization of AF 1600.

Figure 1. The structure of AF 1600, $x:y = 1:2$

We deposited metal on AF 1600 films and measured the peel strength. We found that the AF 1600 peel strength is less than 5 gm/mm with metals such as Ag, Au, and Cu. But the peel strength between Al and AF 1600 is much higher, ~ 15 gm/mm. Our goal is to determine the adhesion mechanism in Al/AF 1600 and the Al bonding structure with AF 1600.[37]

EXPERIMENTAL

AF 1600 films are deposited using either the spin-on or vapor deposition techniques. Vapor depositions were done in a chamber with a base pressure of 4.0×10^{-4} Pa. Details of the vapor deposition procedure are described in Reference 31. Spin-on films are made from a solution consisting of AF 1600 in FC-75, a perfluorated solvent from 3M. Spin-on films are annealed at 110°C for 15 min to remove any solvent. In the present work, the thickness of the AF 1600 film is 50-100 Å in the case of AF 1600/metal/Si samples and 3000 Å in the case of metal/AF 1600/Si samples.

Metals are e-beam deposited in a system with a base pressure of 7.0×10^{-6} Pa. The deposition rate and film thickness used are 5 Å/sec and 3000 Å respectively for deposition on Si and 1 Å/sec and 30 - 100 Å respectively for deposition on AF 1600. The as-deposited metal films are found to be contamination free within the detection limit of XPS. All high resolution characteristic XPS spectra are identical to that from the pure metals. An oxide

layer is found on Al and Cu films as a result of exposure to atmosphere. The oxide layer can usually be removed by less than 30 sec sputtering with 5 keV Ar depending on the amount of exposure.

XPS is done using a Perkin-Elmer 5500 multitechnique system. Mg-kα X-ray is used in all spectra shown here. Sputtering is done using either 5 keV or 300 eV Ar ions at a pressure of 7.0 x10⁻³ Pa.

RESULT AND DISCUSSION

Atomic Concentration and Chemical Shifts

The relative composition of the AF 1600 can be determined from an XPS broad scan
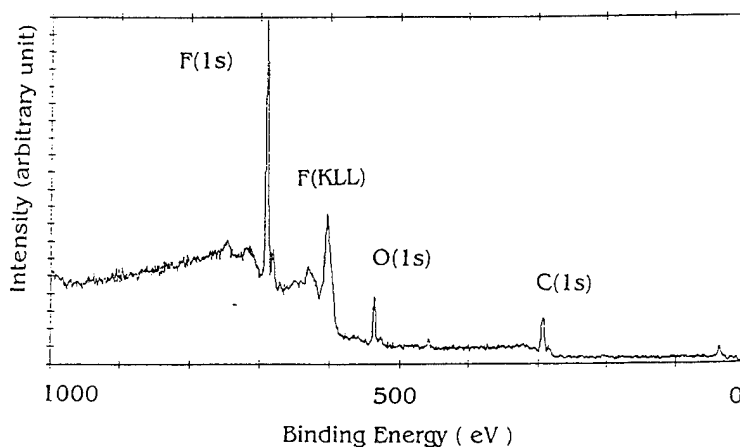
Figure 2 XPS broadscan of a spin-on AF 1600 film. C, O, and F are identified.

spectrum using peak area analysis.[25, 36] Figure 2 shows a typical broad scan spectrum from a spin-on AF 1600 film and Table 1 compares the measured relative atomic concentration of C, O, and F, in at. %, in the AF 1600 thin films determined from Figure 2 with the theoretical value calculated from the structure shown in Figure 1. The experimental result agrees closely with the theoretical values. Although the oxygen concentrations are slightly higher, they can be the result of contamination due to exposure to atmosphere.

Figure 3 shows the C(1s) spectrum taken

AF 1600	C	O	F
Theoretical	33	11	55
Measured	30	14	55

Table 1: Comparison of the theoretical atomic concentration, at. %, of different elements in AF 1600 to that determined by XPS, see Figure 2.
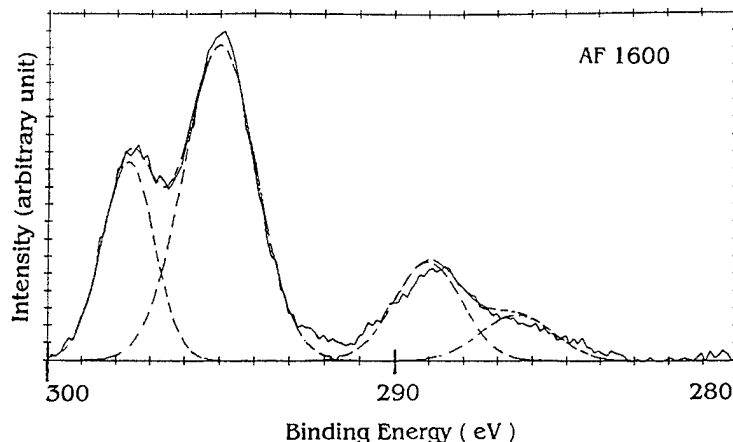
Figure 3. C(1s) spectrum from a AF 1600 film. Solid lines are measured intensity and broken lines are fitted spectra. Four peaks are identified, see text for detail.

from a spin-on AF 1600 film. The spectrum is composed of 4 peaks. The two most prominent peaks at 297.7 and 295 eV can be assigned to the -CF$_2$ and -CF$_3$ functional group respectively, see Figure 1. The peak at 288 eV is composed of two peaks from the F-C-O and the O-C-O functional group, see Figure 1. Figure 3 demonstrates the ability of XPS to identify bonding structure by determining the binding energy shift of the photoelectrons. Because the relative concentration of each functional group is proportional to the integrated area under their respective peaks, their relative concentration can be determined. The relative concentration of C associated with different functional group as determined from Figure 3 agrees well with the calculated value using the structure shown in Figure 1.

Effects of Sputtering

The effects of sputtering on an evaporated AF 1600 film are shown in Figure 4. Figure 4 shows C(1s) spectra
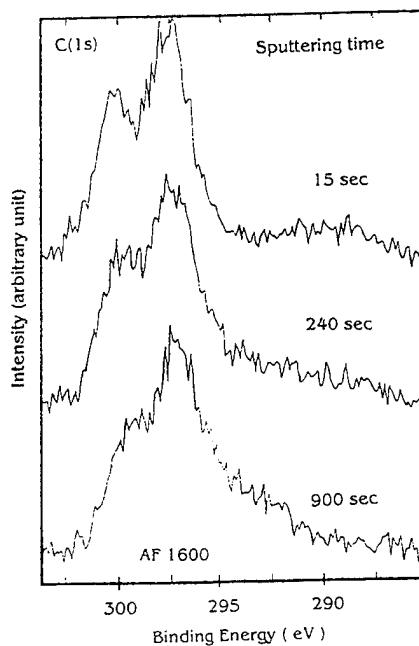
Figure 4. C(1s) spectra of AF 1600 after sputtering for 15, 240, and 900 sec.

after sputtering with 300 eV Ar ion for 15, 240, and 900 sec. Comparing these spectra with that from the as deposited spectrum, Figure 3, the integrated intensity of the two peaks at the lower binding energy is reduced after just 15 sec of sputtering and continues to decrease as a function of sputtering time. The bonding structure of the carbon associated with the F-C-O and the O-C-O functional group, see Figure 1, represented by these two peaks is thus changed as a result of sputtering. The integrated intensity of the highest energy peak corresponding to the -CF₃ group is reduced. At the same time, a broad peak developed at around 293 eV. These results indicate that the sputtering process altered the structure of AF 1600 and specifically the 2,2-bis(trifluoromethyl)-4,5-difluoro-1,3-dioxiole in the copolymer. A new bonding structure is formed with some of the carbon which have a binding energy shift to 293 eV. Figure 4 demonstrates the problem associated with a sputtered surface in which bonding structure can be destroyed and created.

Depth Profiling

Depth profiling is performed on spin-on AF 1600/metal/Si samples. Figure 5 shows the F atomic concentration as a function of sputtering time for spin-on AF 1600/metal/Si. Four metals, Ag, Al, Au, and Cu were used. Differences in F concentrations before sputtering are results of variations in film morphology, i.e. continuous versus patchy. Patchy films indicate the AF 1600 does not "wet" the substrate or a high interfacial energy. XPS measurements of the as-deposited spin-on AF 1600/Al/Si(100) show results similar to that from pure AF 1600. No Al can be identified from the as-deposited film indicating a continuous film without bare patches.

Figure 5 Depth-profiling of F on samples with structures AF 1600/metal/Si.

In all cases, most of the AF 1600 is removed after 10 sec of sputtering as indicated by the concentration of C, < 5 at. %, and F, < 15 at. %. The AF 1600 is completely removed after 30 sec of sputtering as indicated by the absence of C on the sputtered surface.

In the case of Ag, Au, and Cu, F is completely removed after 30 sec of sputtering, Figure 5. Thus any F and metal reaction product or sputtering induced F mixing occurring between AF 1600 and metals are limited within this sputtered depth.

In the case of AF 1600/Al, F, < 3 at. %, is present up to 150 sec of sputtering, see Figure 5. The extent of F mixing in the Al/Al₂O₃ matrix is much larger than in the previous cases and the depth is estimated to be > 150 Å.

Because the deposition and sputtering conditions are identical in all cases, we believe the F in the Al/Al₂O₃ matrix is a result of F diffusion and/or chemical reactions with Al rather than sputtering induced mixing. F is detached from the AF 1600 and diffuses into the Al/Al₂O₃ matrix. This result is confirmed by measurements on peel off surfaces, see below.

Figure 6. Al(2p) spectra from an AF 1600
film on Al sputtered for 10, 30, 120 sec.
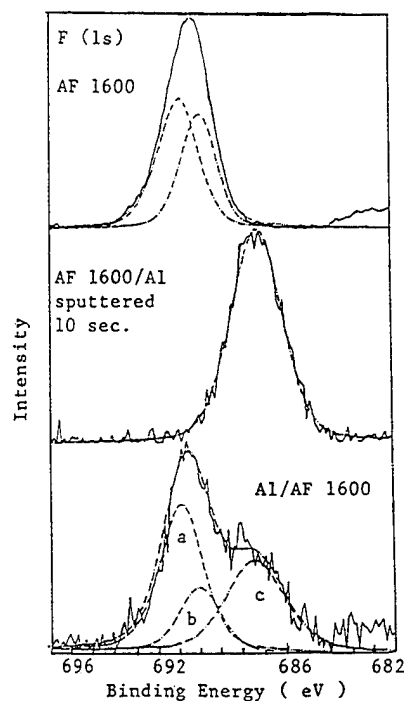
Figure 7. F(1s) spectra from an AF 1600
film, top; AF 1600/Al sputtered for 10 sec.
middle; and a thin layer of Al on AF 1600,
bottom.

Al and AF 1600 Interaction

Figure 6 shows the Al (2p) spectra from a spin-on AF 1600/Al/Si(100) sample at 10, 30,
and 120 sec of sputtering. The corresponding spectrum before sputtering is just the
background noise spectrum, i.e. no Al present, and is not shown. The bottom spectrum is
measured after 10 sec sputtering with contribution mainly from the interface. This spectrum
requires 3 peaks to fit, indicating three chemical states for the Al. Peak (a) is associated with
metallic Al, (b) with Al_2O_3, and (c) has the correct energy shift for AlF_3.[36] The presence of
Al_2O_3 is expected because the Al film is exposed to air before AF 1600 is deposited. The
integrated intensity of peak (c) decreases while that of peak (a) increases as a function of
sputtering time indicating that the AlF_3 concentration decreases as a function of depth from
the surface. After 120 sec of sputtering, the Al (2p) spectrum is similar to that from a metallic
Al sample, top spectrum in Figure 6. The presence of AlF_3 in the Al/Al_2O_3 matrix can be a
result of decomposition of the AF 1600 by ion bombardment and subsequent reaction with Al.
Direct chemical reactions between Al and F must be confirmed in samples without sputtering.
Peak (c) in Figure 6 shows the correct energy shifts for AlF_3, this does not mean that only

AlF_3 is present. Other species such as AlOF can also contribute to peak (c) in Figure 7. But the peak position of the peak indicates a substantial amount of AlF_3 is present.

F (1s) spectra from three samples are shown in Figure 7. The top spectrum is measured from a pure AF 1600. This spectrum has a single broad peak which can be fitted by two peaks. The lower binding energy peak is associated with the -CF_3 functional group and the other peak is associated with the -COF- and -CF_2- functional groups in the AF 1600.

The middle spectrum in Figure 7 is measured from a sample of AF 1600/Al after 10 sec sputtering. This spectrum shows a broad peak with a binding energy 3 eV lower than that from pure AF 1600, top spectrum. Because most of the AF1600 is removed after 10 sec of sputtering no charging effect is observed as indicated by the Al peak position, not shown, from the same surface. This peak has the correct energy shift as AlF_3. This spectrum is in agreement with the previous result. F in the Al/Al_2O_3 matrix is mainly in the form of AlF_3.

The bottom curve in Figure 7 is measured from a sample with a 30 Å thick Al film on AF 1600. The thickness of this film is less than the escape depth of the F(1s) electron. Photoelectrons from the interface contribute to this spectrum. The curve can be fitted with three peaks. Peaks (a) and (b) are associated with the -CF_2- and -CF_3 respectively and peak (c) is associated with AlF_3. Because no sputtering is performed on this sample, the reaction between AF1600 and the Al/Al_2O_3 matrix is spontaneous and not a result of ion bombardment. This reaction occurs as low as 110°C, the spin-on processing temperature and one of the product of this reaction is AlF_3.

Reaction Site on the Polymer

To determine the origin of the F in the AlF_3, one can compare the F(1s) spectra taken from a pure AF 1600 film and that from the interface of Al/AF 1600. In Figure 7, the relative integrated intensity of peak (b) with respect to peak (a) of the bottom spectrum, from the Al/AF1600, is smaller than that from pure AF 1600, top spectrum, indicating that the relative concentration of the -CF_3 group is reduced in the AF1600 in the Al/AF1600 sample. Thus F in the AlF_3 should originate from the -CF_3 functional group.

We have calculated the Gibbs free energy reduction in forming AlF_3 using F atoms from the CF, CF_2 and the CF_3 groups to be -15.9, -58.1 and -135.4 kcal/mole respectively. These calculations are based on thermodynamic data for gas phase compounds and the results should be used for rough comparison only. According to this calculation, it is energetically most favorable to form AlF_3 using F from a -CF_3 functional group. This calculation agrees with our assertion that the F in AlF_3 originates from the -CF_3 functional group. Our free energy calculation also shows that Al_2O_3 is more stable than AlF_3. This might be the reason for the deep penetration of F in the Al matrix. If the surface of the substrate is mainly Al_2O_3, F has to be dispersed in the matrix to find the suitable Al. The copolymer, 2,2-bis(trifluoromethyl)-4,5-difluoro-1,3-dioxiole, provides the necessary side chain with the -CF_3 functional groups which are vital to the reaction between AF 1600 and Al.

Peel off Film

The previous results show that Al will react with AF 1600 forming AlF_3 and other

compounds. We have not however determined the role of this reaction with adhesion strength. One way of looking at this problem is to peel the overlayer off the substrate and examine the composition and chemical structure of the separated surfaces.
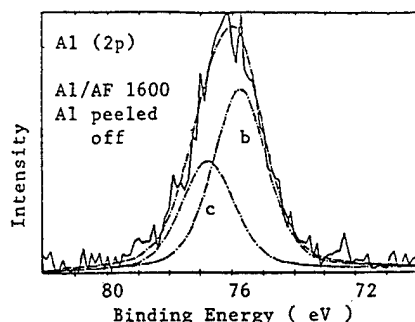
Figure 8. Al(2p) spectra from a Al/AF 1600 sample with the Al peeled off.

We deposited Al on AF 1600. The Al film is then mechanically peeled off. The surface of the remaining AF 1600 is then examined using XPS. The Al (2p) spectrum from such a surface is shown in Figure 8. Two peaks are required to fit the spectrum. These peaks correspond to peaks (b) and (c) in Figure 6. These two peaks are associated with Al_2O_3 and AlF_3 respectively. Thus AlF_3 formed at the interface adhered to AF 1600 as the Al is peeled off. The oxide, as represented by peak (b), can either be formed during deposition from reaction with AF 1600 or

Figure 9. O(1s) spectra from a sample of 30 Å Al/AF 1600, top curve, and from a sample of Al/AF1600 with the Al peeled off, bottom curve.

oxidation of residual Al after the peel test with ambient oxygen. Al_2O_3 and AlF_3 are also found on the peeled off film. Fracture thus occurs in the $Al/Al_2O_3/AlF_3$ layer. Throughout the rest of this paper, we will use $Al/Al_2O_3/AlF_3$ to describe this layer even though other Al, O, F compound may be present. This result seems to indicate that the $Al/Al_2O_3/AlF_3$ region is a weak boundary layer.

The previous result indicates that fracture occurs at the $Al/Al_2O_3/AlF_3$ interfacial region. Therefore some mechanisms, with larger adhesion strength, must be responsible for the adhesion between the AF 1600 and this interfacial region. A possible bonding structure which resulted in the observed adhesion strength can be identified from the O(1s) spectra shown in Figure 9. The top spectrum in Figure 9 is taken from a sample of 30 Å Al/AF 1600. The thickness of the Al is less than the escape depth of the photoelectron from the interface. Three peaks are identified. Peak (a) is associated with the Al_2O_3 and peak (b) is associated with the AF 1600. Peak (c) is a state associated with neither pure Al_2O_3 nor pure AF 1600.

The bottom curve in Figure 9 is taken from a sample of Al/AF 1600 with the Al peeled off. Again peak (c) is identified. The origin of this bond is not certain but it is possible that this bond is responsible for the adhesion between AF 1600 and the Al/Al$_2$O$_3$/AlF$_3$ region. More work however are required to determine the origin and the effect of this bond on adhesion.

SUMMARY

When 100 Å thick films of AF 1600 is deposited, spin-on or evaporated, on metal surfaces, continuous films were formed on Au and Al surfaces, while patchy films exposing the substrate metal are formed on Cu and Ag surfaces indicating large surface energy or weak adhesion. In the case of AF 1600/Al, chemical reactions between Al and AF 1600 is observed at the interface. The principle mechanism is the reaction between F, from the -CF$_3$ functional group in the AF 1600, and Al forming AlF$_3$. F detached from the -CF$_3$ functional group of the AF 1600, diffused into the Al/Al$_2$O$_3$ matrix and formed AlF$_3$. The diffusion depth of F is estimated to be > 150 Å. An Al film was evaporated onto an AF 1600 film. The Al film was then mechanically peeled off and the remaining polymer surface examined. AlF$_3$ was again found. This result seems to indicate that the Al/Al$_2$O$_3$/AlF$_3$ region is a weak boundary layer where fracture develops. An O bonding state associated with neither Al$_2$O$_3$ nor AF 1600 is identified at the interfacial region.

CONCLUSION

Composition and bonding information can be determined using XPS which are crucial in understanding the adhesion mechanism of buried polymer/metal and metal/polymer interface. When ion sputtering is required to exposed the interfacial region, it is found to alter the chemical structure of AF 1600. Useful information, however, can be obtained from sputtered surfaces by comparative analysis. Overlayer film of thickness less than the electron escape depth can be use to evaluate the extent of sputtered induced effects and identified chemical structure in close proximity to the interface. The fracture site and its local bonding structure is examined by peeling off the overlayer and exposing the fracture surface. Such information are critical to the understanding and identifying relative importance of the various adhesion mechanism. Our result shows that AF1600 alone without other treatment is not suitable as an interlayer dielectric for Al metallization both in terms of adhesion and F contamination.

REFERENCES

1. P. Singer, Semiconductor International, **11**, 50 (October 1993).
2. J.G. McDonald, J.T. Lin, H.J. Greub, R.A. Philhower and S. Dabral, IEEE Trans. Comp. Hybrids. Manuf. Technol. **12**, 195 (1989).
3. D.S. Soane and Z. Martynenko, Polymers in Microelectronics- Fundamentals and Applications, (Elsevier, New York, 1989).
4. L. You, G.-R. Yang, C.-I. Lang, J. A. Moore, J.F.P. McDonald, and T.-M. Lu, J. Vac. Sci. Technol. A, **11** (6), 3047 (1993).
5. J.E.E. Baglin, IBM J. Res. Develop. **38** (4), 413 (July 1994)
6. Y.-K. Kim, C.-A. Chang, and A.G. Schrott, J. Appl. Phys. **67** (1), 251 (January 1990)
7. F.D. Egitto and L.J. Matienzo, IBM J. Res. Develop. **38** (4), 423 (July 1994)
8. B.J. Love and P.F. Packman, J. Adhesion, **40**, 139 (1993)
9. A. Buchman, H. Dodiuk, M. Rotel and J. Zahavi, J. Adhesion Sci. Technol. **8** (10), 1211 (1994).
10. M. Collaud, P. Groening, S. Nowak, and L. Schlapbach, J. Adhesion Sci. Technol. **8** (10), 115 (1994).
11. K.-W. Lee and A. Viehbeck, IBM J. Res. Develop. **38** (4), 457 (July 1994)
12. L.M. Siperko and R.R. Thomas, J. Adhesion Sci. Technol. **3** (3), 157 (1989)
13. H.M. Clearfield, D.K. McNamara, and Guy D. Davis, in Adhesive Bonding, edited by L.-H. Lee, (Plenum Press, New York, 1991), pp. 203.
14. M-K. Shi, B. Lamontagne, l. Martinu, and A. Selmani, J. Appl. Phys. **74** (3), 1744 (August 1993)
15. W.J. van Ooij, in Physiochemical Aspects of Polymer Surface, edited by K.L. Mittal, (Plenum Press, New York, 1983) pp. 1035.
16. C.-A. Chang, J.E.E. Baglin, A.G. Schrott, and K.C. Lin, Appl. Phys. Lett. **51** (2), 103 (July 1987).
17. C.-A. Chang, Appl. Phys. Lett. **51** (16), 1236 (October 1987).
18. A.J. Kinloch, J. Mater. Sci., **15**, 211 (1980).
19. A.R. Akande and J. Lowell, J. Phys. D: Appl. Phys. **20**, 565 (1978).
20. B.V. Derjaguin and Y.P. Toporov, in Physiochemical Aspects of Polymer Surfaces, (Plenum Press, New York, 1983) pp. 605.
21. W.J. van Ooij, Rubber Chem. Technol. **52**, 605 (1979).
22. W.J. van Ooij, W.E. Weening, and P.F. Murray, Rubber Chem. Technol. **54**, 227 (1981).
23. L.M. Siperko and R.R. Thomas, J. Adhesion Sci. Technol. **3**, 157 (1989).
24. J.M. Park, L.J. Matienzo and D.F. Spencer, J. Adhesion Sci. Technol. **5**, no. 2, 153 (1991).
25. Practical Surface Analysis, edited by D. Briggs and M.P. Seah, (John Wiley & Sons Ltd, New York, 1990).
26. D. Briggs and G. Beamson, Analytical Chemistry, **84** (15), 1729 (August 1992).
27. F.-M. Pan, Y.-L. Lin, and S.R. Horng, Appl. Sur. Sci. **47**, 9 (1991).
28. L. Atanasoska and S.G. Anderson, J.M. Meyer III, and J.H. Weaver, Vacuum, **40** (1/2), 85 (1990).
29. P.R. Resnick, Polym. Prepr. **31**, 312 (1990).
30. A brochure detailing the technical properties of the Teflon AF 1600 product can be obtained from the Du Pont corporation, Wilmington, DE; for safety information

specify "Teflon AF: Safety in Handling and Use," No. HO7805.

31. T.C. Nason, J.A. Moore, and T.-M. Lu, Appl. Phys. Lett. **60** (15), 1866 (1992).

32. R.Chow, M.K. Spragge, G.E. Loomis, F. Rainer, R. Ward, I.M. Thomas, and M.R. Kozlwski, preprint, submitted for Materials Research Society Symposium Proceeding, Fall 1993.

33. G. B. Blanchet, Appl. Phys. Lett. **62** (5), 479, (1993).

34. W.E. Hanford and R.M. Joyce, J. Amer. Chem. Soc. **68**, 2081 (1946).

35. L. Holland, J. Vac. Sci. Technol. **14**, 15 (1977).

36. see for example, C.D. Wagner, W.M. Riggs, L.E. Davis, and J.F. Moulder, "Handbook of X-ray Photoelectron Spectroscopy". Perkin-Elmer Corp., Eden Prarie, MN.

37. P.K. Wu, G.-R. Yang, X.-F. Ma, and T.-M. Lu, Appl. Phys. Lett. **65** (4), 508 (1994).

ADHESION BETWEEN POLYIMIDE FILMS AND Al_2O_3 SUBSTRATE

Y. Nakamura, Y. Suzuki, Y. Watanabe and S. Hirayama
Department of Materials Science and Engineering, National Defense Academy
1-10-20 Hashirimizu, Yokosuka, Kanagawa 239, Japan

ABSTRACT

The adhesive strength of polyimide thin films on an alumina substrate has been studied by the pull test. Polyimide thin films were cured at various temperatures from 300 to 400 ℃, followed by etching in an oxygen plasma for 3 min. After metallization with chromium and copper, the pull test was carried out. It is found that the adhesive strength increases with an increase of the cure temperature. However the strength deteriorates noticeably at the cure temperature of 400 ℃. A possible reason for this is the variation of chemical states in the polyimide thin films.

INTRODUCTION

Multi-Chip Modules(MCMs) have been classified as either C, D, or L or a combination of these three types. However, there are only two types of MCM from this point of view: one case is where the circuit is deposited onto a substrate, the other uses lamination of individual layers without a substrate.[1] Advanced MCMs are a merge of chip, wire and substrate. MCM-D/C is a promising combination technology among the advanced MCMs technology. therefore the adhesion issue between different materials is a very important technical topic.

The reliability of any complex structure such as an MCM-D/C depends on its ability to resist the detachment of component materials, thus a knowledge of adhesion is essential for the fabrication of MCM structures. Polyimide has outstanding thermal stability and is relatively easy to fabricate onto silicon, but it is difficult to deposit onto ceramics such as alumina.[2-4] The wok presented in this paper investigates and characterizes the adhesion between polyimide thin films and an alumina substrate, focusing on the effect of the cure temperature of the polyimide thin films on the adhesive strength at ambient temperature.

91

EXPERIMENTAL

The polyimide precursor(RN812, Nissan Chemical Industries) for polyimide thin films was used as the raw material. Polyimide precursor solutions were spun coated onto an alumina substrate. The substrate was spun at 2000 rpm for 60 sec and cured. This resulted in a film thickness of about 2 μm . This process was repeated to make the desired thickness of films. The films were dried at 80 ℃ for 30 min on a hot plate in air and then cured at 300～400℃ for 30 min in air.

The surface of the polyimide thin films was etched in an oxygen plasma for 3 min, followed by sputtering with chromium and copper. The final thickness of 4 μm of copper was deposited by electroless plating. The 0.8 mm tin coated wire was soldered on the 2 mm square patterned copper surface, then the pull tests were carried out at a speed of 10 mm/min.

X ray photoelectron spectroscopy(XPS), Infrared absorption spectroscopy(IR) and scanning electron microscopy(SEM) were used for evaluation of the materials.

RESULTS AND DISCUSSION

The relation between the heating and cooling rates and the adhesive strength of the polyimide samples of 4 μm in thickness cured at 300 ℃ for 30 min is shown in Fig. 1. The adhesive strength was not affected by the heating and cooling rates and remained at the level of 1.3 kg/mm^2. It is found by the SEM examination that all fractures occurred at the interface between the polyimide thin films and the ceramic substrate.
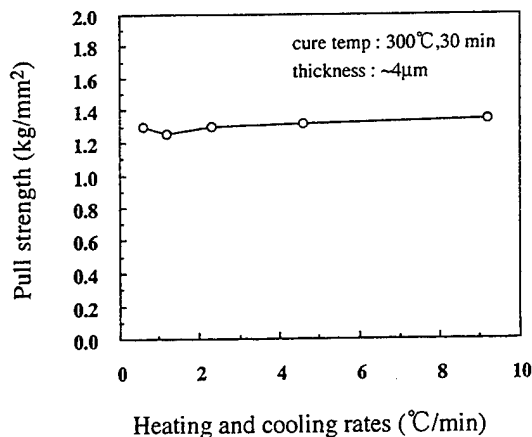
Fig. 1 Relation between heating and cooling rates and adhesive strength of samples cured at 300℃ for 30 min. Polyimide films thickness is about 4 μm.

The relation between the thickness of polyimide thin films and the adhesive strength

of samples cured at 300 ℃ for 30 min is shown in Fig.2. The adhesion was drastically decreased at the film thickness of 7 and 15 μm with the samples treated at the rates of 4.6 and 2.3 ℃/min, respectively. This abrupt decrease in strength may be explained by the existing cracks that were created by the thermal treatment due to the different coefficients of thermal expansion of polyimide and alumina. However constant strength was obtained by the samples at slower treated rates. Therefore, the rates of 1.2 ℃/min were adopted for the following experiments.
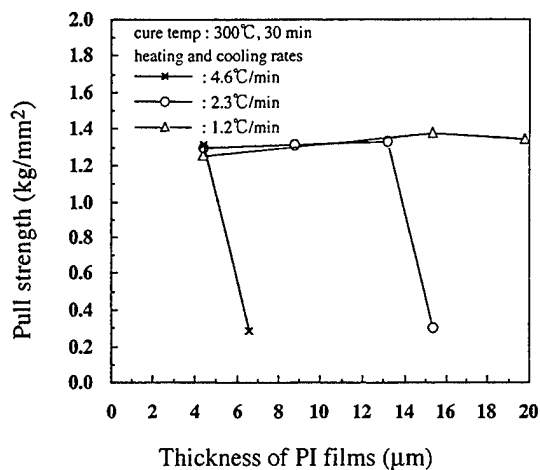
Fig. 2 Relation between polyimide films thickness and adhesive strength of samples cured at 300℃ for 30 min.
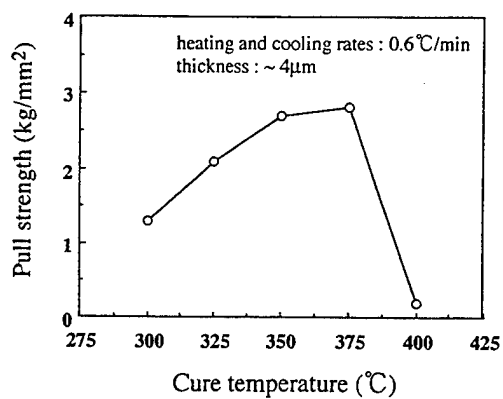
Fig. 3 Relation between cure temperature and adhesive strength with the thickness of about 4 μm.

The effect of cure temperature on the adhesion is shown in Fig. 3. The adhesion is increased with increasing the cure temperature except for the treatment at 400 ℃. The maximum strength of 2.8 kg/mm^2 was obtained with the sample cured at 375℃.

Chemical and physical interactions between the overlayer and a substrate govern the fracture of the resulting interface, and this, in turn, controls the adhesion of the overlayer/substrate system.[5] Therefore, it is important to learn the chemical states of surfaces of polyimide thin films. The measured concentration of chemical states in polyimide thin films after the cure treatment is shown in Table I.

Table I Measured concentration of various chemical states
in polyimide films after cure treatment.

C 1 s		
Chemical bond	Cure temperature of 300℃ (%)	Cure temperature of 375℃ (%)
C = O	1 3.6	5.6
C – OH	0	5.0
C – O C – N	3 0.4	2 6.0
C – H	5 6.0	6 3.4

The concentration of C=O bonds is lower for the sample with the higher treatment than that of the sample treated at the lower temperature. The treatment temperature may affect some chemical bonds in polyimide, resulting in easy breaks by the oxygen plasma ablation. In turn, the broken bonds may easily react with some elements on the alumina substrate such as oxygen or aluminum. Therefore, the higher concentration of C-OH bonds in the films was obtained for the sample treated at higher temperatures. However, the treatment at too high a temperature will give a definitive damage to the chemical bond in polyimide. IR absorption results are shown in Fig. 4. It is obvious that the decomposition of polyimide has occurred in the samples. Therefore the weakest adhesion is obtained.
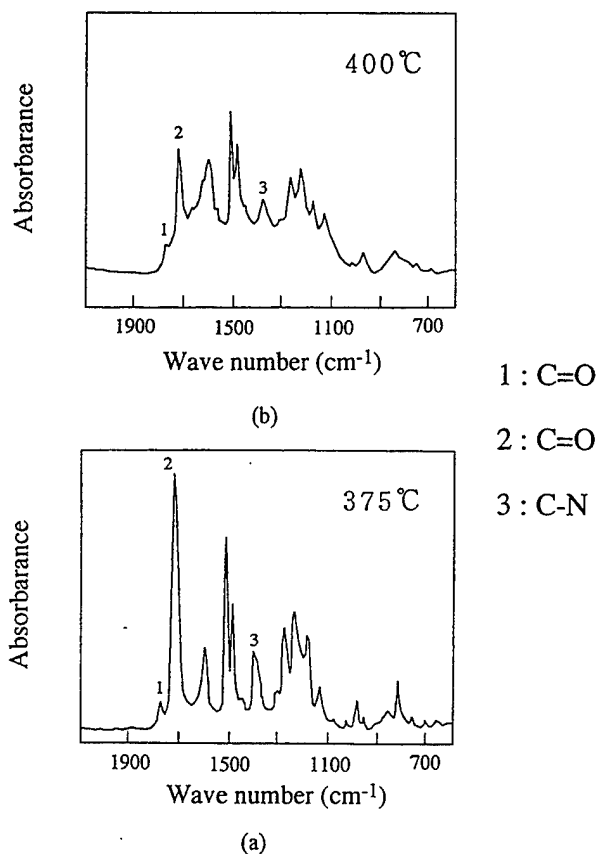
Fig. 4 IR absorption spectra of polyimide films cured at (a)375℃ and (b) 400℃.

CONCLUSIONS

Heating and cooling rates do not affect adhesion between polyimide thin films and an alumina substrate. The appropriate rates do not affect the adhesion to thicknesses of 20 μm in polyimide thin films. The adhesion increases with increasing the cure temperature of polyimide films to 375℃ because of the increase in C-OH bond that is created by the oxygen plasma ablation.

References

[1] Robert R. McBride, David F. Zarnow, and Raymond L. Brown, Advancing Microelectronics, **21**, 16(1994).

[2] Ming-Shyong You, A. Sanjoh, and T. Ikeda, Proc. of 8th Int'l. Microelectronics Conf., Ohmiya, (1994)pp.443-448.

[3] Masahito Ishi and Hiroshi Hata, Proc. of 8th Int'l. Microelectronics Conf., Ohmiya, (1994)pp. 225-230.

[4] Hyo-Soo Jeong, Y. Z. Chu, C. J. Durning, and R. C. White, Surface and Interface Analysis, **18**, 289(1992).

[5] G. D. Davis, B. J. Rees, and P. L. Whisnant, J. Vac. Sci. Technol. A, **12**, 2378(194).

STICKING PROBABILITY AND STEP COVERAGE STUDIES OF SiO₂ AND POLYMERIZED SILOXANE THIN FILMS DEPOSITED BY PLASMA ENHANCED CHEMICAL VAPOR DEPOSITION

JEREMY A. THEIL
Central Research Laboratory, Johnson Controls, Inc., Milwaukee, WI, 53209

ABSTRACT

This paper describes a method for estimating the effective sticking probability for plasma enhanced chemical vapor deposition (PECVD) of hexamethyldisiloxane (HMDSO) using SiO₂ and polymerized siloxanes deposited on specially prepared trench structures. Comparison of the data with direct Monte-Carlo simulation curves provides information about the incorporation probability relative to film growth. It is shown that besides variation in gas chemistry, the choice of trench and film dimensions influences the step coverage. The sticking probability is shown to increase with oxygen flow rate by about 30%, from 0:1 to 10:1 O_2:HMDSO flow ratio. This flow rate dependence is found to be consistent with work performed on tetraethoxysilane.

1. INTRODUCTION

The sticking probability is one of the most important parameters for describing film step coverage and developing deposition models. However, due to the lack of knowledge of the flux and surface kinetics of the deposition species for many chemical systems, the sticking probability is difficult to directly quantify. Instead much work has gone into developing models to relate the contour of a deposited film to the sticking probability [1-8]. In particular, several simulations have been created to estimate the sticking probability of CVD processes. For example, Kawahara et al. developed a Monte Carlo model with a single depositing species of constant sticking probability [1]. Watanabe et al., developed a one dimensional analytical model along with a test structure to perform actual measurements [2]. Ikegawa et al., used direct simulation Monte Carlo with finite element analysis techniques to determine film conformality based upon a full reaction model for thermal CVD processes for phosphosilicate glasses in molecular and transitional gas flow regimes [3]. More recently, work has been done to develop PECVD-based models, such as the string model developed by Yuuki, et al. for a-Si:H film growth by SiH_4 decomposition [4]. Predictive models have been used for PECVD processes to determine the relative concentration of multiple deposition components with different sticking probabilities for SiH_4 deposition [4,5]. However, these models have only been used to determine the overall sticking probability for PECVD processes whose chemistries is already well understood. One objective of this work is to apply the results of LPCVD models to PECVD processes, and demonstrate how they may be used as a tool for characterizing CVD systems of less well understood chemistries and processes. The other objective is to show how the sticking probability and conformality change as the ratio of the plasma feedstock gases varies for the $HMDSO/O_2$ deposition system.

2. EXPERIMENTAL

The films were deposited on (110) Si wafers with trenches of various aspect ratios. The deposition conditions were 250 mTorr, 30 sccm HMDSO, between 0 and 300 sccm of O_2, 300W, 250 kHz rf power, autotransformer-matched impedance at 2450Ω, and no substrate heating. The samples were placed on the grounded bottom electrode of a Plasmatherm PK-1241 parallel plate system with a 2.5 cm electrode gap. (The plasma was confined to the region between the two plates.) The deposition time was varied between 10 and 12 minutes to achieve approximately 3 μm films. Samples were then cleaved and imaged in full cross section in SEM backscatter mode operating at 20 keV. The samples were not coated with a conductive layer.

The test structure used for this experiment was made up of repeating sets of fully rectangular cross section trenches, produced by orientation dependent etching (ODE) of (110) Si [9-11]. The die measured 1.014 cm by 0.512 cm, and consisted of 74 sets of trenches, each set having 5 different widths (nominally 5, 10, 15, 20, and 30 μm) separated by nominally 10 μm wide walls,

for a total trench set width of 130 μm. The trench layout used repeating sets of trenches rather than grouping all trenches of a single width together, in order to minimize the dimension of detectable local chemical variations. The maximum trench width chosen was much smaller than the molecular mean free path length of 200 μm. The minimum Knudsen number (λ/D) for a trench was 7, well above the value of unity that defines the molecular flow limit. Two sets of wafers were fabricated to produce trenches that were 5 and 15 μm deep. These two sets of trenches gave aspect ratios of width:depth of 1:2.5 to 6:1. It should be noted that the 1:1 and 2:1 aspect ratios exist for both trench depths. During deposition, one die of each etched depth was coated, so that 10 different trenches were simultaneously exposed for each data point.

The trenches were formed in (110) Si using ODE with KOH [9-11]. The trench die pattern was transferred to an oxide mask using standard photolithographic and wet etch techniques, such that the trench walls were aligned with the (111). A two-step KOH etching procedure was used to produce a fully rectangular cross section trench with perpendicular sidewalls and flat bases, as shown in Figure 1 [12].

The estimation of the sticking probability for each data point was determined using curves generated by Kawahara et al., and Yuuki et al. [1,4]. The modeled sticking probability data were presented as a plot of isoprobability curves of film coverage as a function of trench aspect ratio. A limiting case equation of sticking probability equal to unity, and minimal topwall film thickness was also stated (for $\beta = 1$, and $d_{max}/D = 0$, $d_{min}/d_{max} = [1-((W/D)/[1+(W/D)^2]^{1/2})]/2$ (1) [4]. In order to systematically determine the sticking probability for the measured data, a sticking probability (β) parameterized equation was found by inductive reasoning and regression analysis:

$$d_{min}/d_{max} = \left(\frac{1}{1+\beta}\right)\left(1 - \left(\frac{1}{x}\right)\left(\frac{1}{\sqrt{\beta^{-3/2} + x^{-2}}}\right)\right) \qquad (2)$$

where, $x = W/D$, W is the trench width, D is the trench depth, d_{max} is the topwall film thickness, and d_{min} is the film thickness at the bottom of the sidewall (d_{min}/d_{max} is the fractional step coverage). Equation (2) reduces to equation (1) at unity sticking probability. This equation provided a fit within 5% to the curves for sticking probabilities equal to or greater than 0.1.

3. RESULTS

Figure 2 is a backscattered electron SEM image of a typical deposited film on a trenched surface. The deposition rate for the films is in the range of 3000Å/min. The aspect ratio of the trench is 1:2.5 (width:depth) with portions of a 1:1.5 trench on the right and a 2:1 trench on the left. As can be seen from examining the thickness of the sidewall layers in each trench, the highest aspect ratio trench has the thinnest sidewall material. The texture of the film is featureless in cross section, except for the sidewall material. It appears to have a columnar-like structure of low temperature sputtered films, oriented at 45° relative to the base. Energy dispersive x-ray mapping, and XPS did not detect any compositional differences of the sidewall and topwall material.

Figure 3 is a representative plot of experimental sticking probability data superimposed on a plot by Kawahara et al., and Yuuki et al. to show how the experimental data compare with modeled data [1,4]. The data come from two wafers processed simultaneously; one has 15 μm deep trenches and the other has 5 μm deep trenches. While the data follows the same trend as the modeled material, there are important differences. First, the experimental values for d_{min}/d_{max} increase more slowly with increasing aspect ratio compared to the model, instead of following a single sticking probability curve. In addition the data points from the 5 μm deep trenches tend to have a lower step coverage than the 15 μm deep trench of about the same aspect ratio. This difference in step coverage is within the standard error for the data collected from a single deposition, but is evident for every sample. The sticking probability estimation procedure uses Newton's iterative method to solve for β using equation 2, with the values of W/D and d_{min}/d_{max}.

Figure 4 is a plot of the sticking probability as a function of the O_2 gas flow rate. The data points are collected from trenches with a 2:1 aspect ratio. The sticking probability ranges from 0.39 to 0.78 for this aspect ratio. Overall, the sticking probability ranges from about 0.2 to almost unity. The error bars reflect the uncertainty in estimation of the sticking probability at each point.
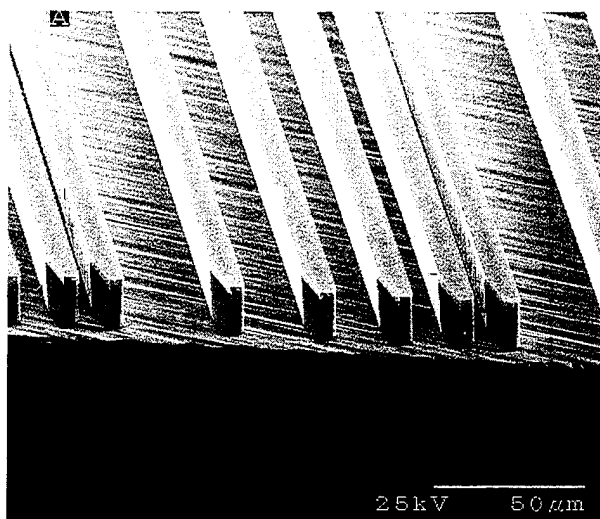
Figure 1: Secondary electron SEM image of edge of fully processed uncleaved (110) Si trench die used in experiments. Trench walls and bases consist of Si. Trench depth is 15 μm.
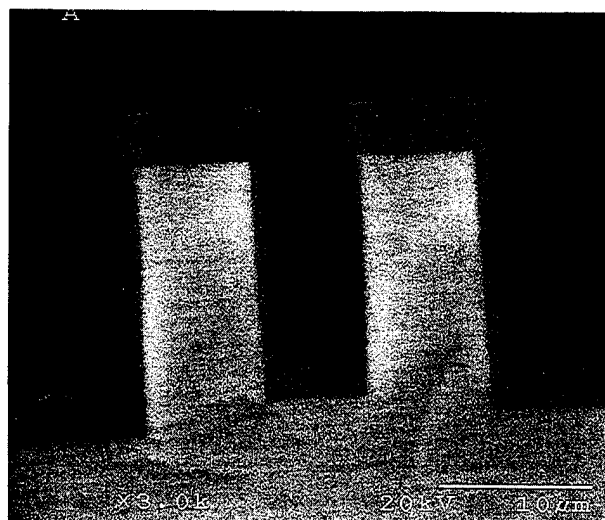
Figure 2: Backscattered electron SEM image of cleaved 6 μm wide x 15 μm deep trench with 3 μm oxide. Deposition conditions include 30 sccm HMDSO and 150 sccm O_2. Edges of the 30 μm trench to the left, and the 10 micron trench to the right can be seen. Note the differences in sidewall film thickness between all three trenches.
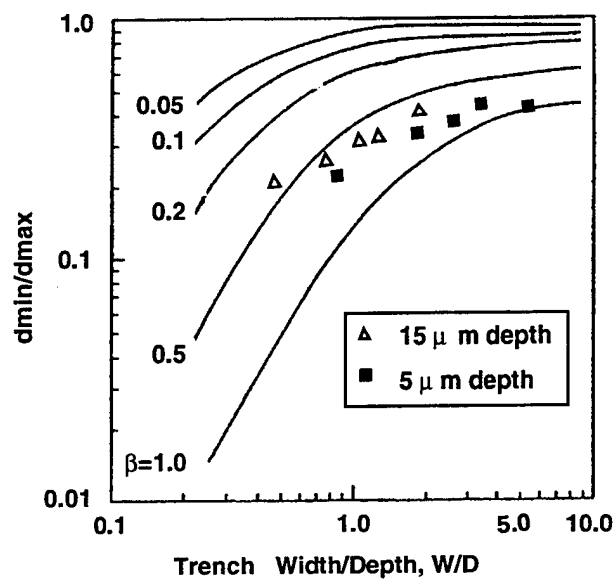
Figure 3: Ratio of film thicknesses as a function of trench aspect ratio. Data comes from the sample shown in Figure 2. The data are super-imposed on a plot of modeled curves by Kawahara et al. for comparison [1].
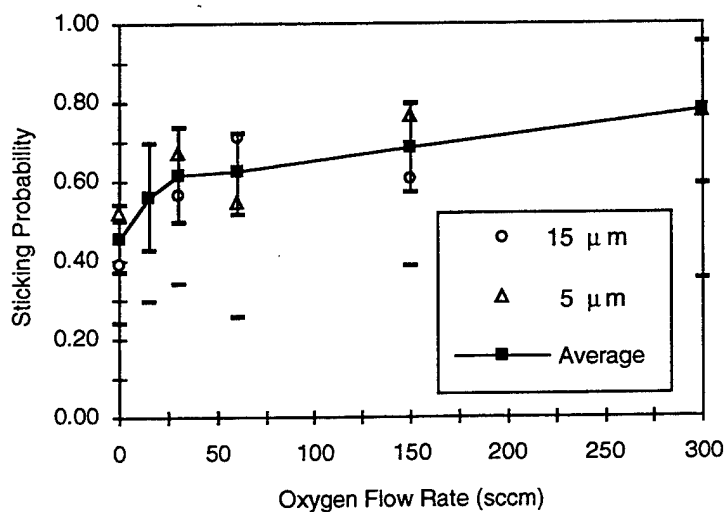
Figure 4: Sticking probability as a function of O_2 flow rate. Trench aspect ratio 2:1, 300W, 30 sccm HMDSO, 3 μm top layer film thickness. The lower set of bars represents the maximum deviation of measured data from plotted values.

The lower bars are data points showing the maximum difference between the 2:1 trench sticking probability and the estimated sticking probabilities for the other trenches. The figure shows that there is a drop in the sticking probability for very low O_2 flow rates, but that it is relatively constant above 30 sccm (1:1 HMDSO:O_2).

4. DISCUSSION

The flatter shape of the measured data relative to the modeled curves is caused by the presence of multiple deposition species. This can be shown by how the model used for deriving the curves is developed [4]. (The measured data in Figure 3 are superimposed upon curves generated by the model of Yuuki et al., and Kawahara et al. [4,1].) The model used is based upon several assumptions, including only one sticking probability that describes all depositing species, and a constant film thickness/trench depth ratio. The measured data in Figure 3, however, more closely match data from experiments by Tsai et al. [4, 13].They examined step coverage of PECVD a-Si:H films deposited from SiH_4, a chemical system known to have multiple depositing species. Because of the deviation of the single species model from experimental evidence, Yuuki et al. changed the model by allowing calculations using two sticking probabilities [4]. The calculations are performed on the assumption that the different species do not interact with each other on the surface. The best fit is then made by adjusting the sticking probability and the relative flux of each component. The shape of the multicomponent curve relative to the single component model shows significant deviation, but matches the experimental data [4]. The data from this experiment vary in a similar fashion, which provides experimental evidence for the assumption that the HMDSO/O_2 PECVD process has multiple deposition species for film growth.

The other important feature to note in Figure 3 is that the d_{min}/d_{max} values from the deeper aspect ratio trenches are slightly higher than the values from the wider aspect ratio trenches, (see, for example, the ~1:1 aspect ratio trenches, for both sets of points in Figure 3). The effect is evident for each sample measured. This effect is due to the occlusion of the trench opening during film growth as shown by Blech, and Ross and Vossen [6,7]. As the film becomes thicker, the trench opening narrows effectively increasing the trench aspect ratio. The cumulative effect of trench occlusion and aspect ratio change is characterized by the ratio of the topwall film thickness over the trench depth (d_{max}/D, occlusion ratio). As d_{max}/D increases, trench occlusion becomes more pronounced. For shallower trenches the effect is more pronounced than for a deeper trench, since a given thickness of deposited material alters the trench cross section more. The increased aspect ratio of the unfilled cross section increases selective filtering of the higher sticking probability precursor. The material on the bottom of the trench will receive a disproportionately higher flux of the lower sticking probability material. This explains the behavior of d_{min}/d_{max} when comparing two trenches with similar aspect ratios but different trench depths. According to the models, d_{max}/D shifts the curve by less than 2% for ratios wider than 2:1 [1,7]. For the presented data, in which the top wall film thickness is the same, for the 15 µm deep trenches d_{max}/D ranges from 0.17 to 0.28, and from 0.42 to 0.92 for the 5 µm deep trenches. It shows that the occlusion effects are relatively greater for shallower trenches. The greater trench occlusion lowers the relative flux reaching the trench walls, thus lowering step coverage within the trench.

When analyzing the measured data from a PECVD system, it is necessary to take into account the effect of multiple deposition species and the difference in trench dimensions. By choosing data from a single aspect ratio, the generalized behavior of the sticking probability will be self-consistent with respect to independent parameters, such as gas flow. In general, it is preferable to select trenches with dimensions close to the size of interest. Since the objective of this work is to understand deposition on a planar substrate, wider trenches are preferable because they receive fluxes that are more representative of the multiple species that a planar surface receives. Deeper aspect ratio trenches receive disproportionately more low sticking probability material on the trench sidewalls and base. Furthermore, wide trenches are relatively less susceptible to occlusion effects of the trench opening. However, the sensitivity of the measurement decreases by more than a factor of 2 for aspect ratios between 1:2 and 5:1, and a sticking probability of ~0.3. The 2:1 aspect ratio trench was selected for data analysis in this experiment because it is the best compromise between estimation sensitivity and minimization of deep trench effects.

Examining the details of the results provides several clues about the nature of the HMDSO/O_2 deposition process. The shape of the step coverage curve in Figure 3 implies that there is more than one depositing species influencing film growth, and that they have widely varying sticking probabilities. Earlier work shows that at low O_2 concentrations, deposited films are essentially polymerized methylated siloxanes, but above a dilution of about 1:5, HMDSO:O_2, films are predominantly oxide [14]. The change in slope for the sticking probability shown in Figure 4 occurred around 1:1 ratio. The direct relationship between sticking probability and oxygen flow rate is consistent with the work of Raupp et al., who examined SiO$_2$ film growth from TEOS and O_2 using microwave remote PECVD [15]. They attribute the increase in sticking probability to an increase in the surface reaction rate caused by higher atomic O production rates. For this capacitively-coupled system, a similar mechanism tied to the production rate of an excited oxygen species is likely to hold. Therefore, it is probable that surface oxidation reactions of the deposition precursor play a key role in film evolution for this process. Since a change in sticking probability is most often related to changes in surface composition or gas composition, the results imply that the incorporation processes may have relatively little influence on the final film composition.

5. SUMMARY

It has been shown that it is possible to estimate the sticking probability for PECVD processes in which the specific chemical species are not known, by quantifying step coverage of trenches. An equation has been found that fits the single component model curves in the range of 0.1 to 10 aspect ratio to within 5%. The fit of the experimental data with the published isoprobability plots has been attributed to the presence of multiple deposition species and the occlusion ratio, d_{max}/D. The primary criterion of selecting trench dimensions is to find trench features that approximate actual conditions of interest. In order to make measurements on nominally flat substrates, it is necessary to select a wide trench to minimize occlusion effects. Models that include multiple deposition species will improve the estimation process. For the HMDSO/O_2 PECVD system, it has been demonstrated that the sticking probability decreases as the ratio of O_2 to HMDSO decreases and that this does not coincide with the incorporation of methylated siloxane groups within the film. These findings help demonstrate that 1) there is more than one deposition species, and 2) surface oxidation may play a key role in oxide film growth for this chemistry.

REFERENCES

[1] T. Kawahara, A. Yuuki, and Y. Matsui, Jpn. J. Appl. Phys., **30**(3), 431 (1991).

[2] K. Watanabe, and H. Komiyama, J. Electrochem. Soc., **137**(4), 1222 (1990).

[3] M. Ikegawa, and J. Kobayashi, J. Electrochem. Soc., **136**(10), 2982 (1989).

[4] A. Yuuki, Y. Matsui, and K. Tachibana, Jpn. J. Appl. Phys., **28**(2), 212 (1989).

[5] C. Y. Chang, J. P. McVittie, and K. C. Saraswat, IEDM 93 Proceedings, 853 (1993).

[6] I. A. Blech, Thin Solid Films, **6**, 113 (1970).

[7] R. C. Ross, and J. L. Vossen, Appl. Phys. Lett., **45**(3), 239 (1984).

[8] L.-Y. Cheng, J. P. McVittie, and K. C. Saraswat, 2nd Int'l. Symp. on ULSI Science and Technology, 586 (1989).

[9] D. L. Kendall, Appl. Phys. Lett., **26**(4), 195 (1975).

[10] K. E. Bean, IEEE Trans. on Electron Devices, **ED-25**(10), 1185 (1978).

[11] J. B. Price, 2nd Int'l. Symp. on Silicon Mater. Sci. and Technol., **120**(3), 339 (1973).

[12] J. A. Theil, J. Vac. Sci. and Technol. A, submitted (1995).

[13] C.C. Tsai, J. C. Knights, G. Chang, and B. Wacker, J. Appl. Phys., **59**(8), 2998 (1986).

[14] J. A. Theil, J. G. Brace, and R. W. Knoll, J. Vac. Sci. and Technol. A, **12**(4), 1365 (1994).

[15] G. B. Raupp, D. A. Levedakis, and T. S. Cale, J. Vac. Sci. and Technol. A, **13**(4), to be published (1995).

Fourier Transform Infrared Spectroscopy of Polymer-Metal Interface Reactions

B.H. Cumpston, J.P. Lu, B.G. Willis, and K.F. Jensen
Department of Chemical Engineering
Massachusetts Institute of Technology
Cambridge, MA 02139

Abstract

Applications of Fourier transform infrared (FTIR) spectroscopy for probing polymer-metal interfaces are described with examples of polyimide (PI)-metal systems relevant to electronics packaging and poly(phenylene vinylene) (PPV) derivatives used in electroluminescent devices. Emphasis is placed on the detection and interpretation of interfacial reactions that influence performance characteristics (*e.g.*, adhesion, stability, and light emission) of polymer-metal structures. *In situ* infrared reflection absorption spectroscopy (IRRAS) is used to explore the formation of PI-on-metal interfaces, the hydrolytic stability of such interfaces, and the reactivity of PPV systems when exposed to ultraviolet light and oxygen. Differences between polymer-on-metal and metal-on-polymer interfaces are discussed. Models of the infrared optical processes in the thin film composites are used to distinguish between chemical and optical effects. The FTIR observations are supported by additional spectroscopic characterizations, specifically *ex situ* X-ray photoelectron spectroscopy (XPS).

Introduction

Metal polymer composites are found in a large number of technological applications including electronic devices, solar cells, floppy discs, mirrors, compact discs, and optical waveguides [1]. In the fabrication of microelectronic devices, polymers are gaining use as low dielectric layers in multilevel metallization schemes, in addition to established packaging applications. Conjugated polymers are also receiving increased attention for electroluminescent devices [2] including light-emitting diodes, large area flat panel displays, and backlights for active matrix liquid crystal displays. Precise control of properties at the polymer-metal interface is crucial to product performance and reliability in all of these applications. For example, chemical changes at the interface between the polymer and the metal electrode have been identified as a possible explanation for the relatively short operating lifetimes of electroluminescent devices, on the order of one hundred hours, far too short for commercial applications.

Building a microelectronic or optical device involves either the deposition of a metal onto a polymer or the formation of a polymer layer on top of the metal. In the metal-on-polymer (MOP) case, metal is deposited by sputtering or evaporation onto a fully cured polymer. The polymer interacts with a metallic surface formed by atoms or clusters of atoms impinging on the surface. In the polymer-on-metal (POM) case, a

solution of the polymer precursor is typically spin coated onto the metal and the precursor is then thermally converted to its final form. Alternatively, the polymer can be codeposited from separate vaporized monomer sources in a ultra high vacuum (UHV) chamber [3].

There are three major differences between the POM and MOP cases: (1) precursor versus polymer interaction with the metal, (2) presence or absence of solvent, and (3) thermal versus no thermal treatment after formation of the interface [4]. Additionally, in the POM case the polymer at the interface interacts with a native metal oxide, whereas in the MOP case the metal is truly metallic in nature. Kowalczyk *et al* found that the force of adhesion between the metal and polyimides is greater in the POM case [4] and attributed this effect to chemical reactions between the curing polymer and the underlying metal oxide.

X-ray photoelectron spectroscopy (XPS) has been a particularly effective tool for analyzing chemistry underlying the formation of MOP interfaces [5-14]. Being a UHV technique, XPS is readily compatible with investigations of the initial stages of interface formation by vacuum evaporation. By measuring atomic core levels of many metal/polymer systems using XPS, Burkstrand [15] was able to correlate force of adhesion, a macroscopic quantity, to the amount of oxygen present in the polymer, a microscopic property. He also found that metals with a high electronegativity are more likely to form oxygen complexes with the polymer, thus increasing adhesive strength. Chou and Tang [16] developed a simple model based on free energy calculations to predict whether or not a metal will have strong adhesion to a polymer; their model agrees with Burkstrand's experimental data.

Detailed *ab initio* calculations have also been performed to identify the reactions taking place at the polymer-metal interface and the effect they may have on interfacial adhesion [17]. These self-consistent field molecular orbital calculations show excellent agreement with XPS data for core atomic layers, and also for valence levels, as determined experimentally by ultraviolet photoelectron spectroscopy (UPS) [18]. Many interface studies have focused on polyimides because of their importance in microelectronics applications [19]. Studies of other polymeric systems, *e.g.*, polyethylene (PE), polystyrene (PS), polypropylene (PP), polydimethyl-siloxane (PDMS), silicone, poly(ethylene terephthalate) (PET), poly(ether ether ketone) (PEEK), and polyvinylalcohol (PVA), have led to analogous conclusions about interfacial interactions [22].

A small electron escape depth (< 100 Å) restricts interfacial analysis using XPS to very thin films, and the need for a UHV environment complicates studies of POM systems. FTIR, being an optical technique, has the advantage of not requiring a vacuum and, thus, it is capable of monitoring curing, oxidation, or degradation processes of polymers *in situ* in any environment [20]. The technique is particularly useful for probing the polymer-metal interface because it can detect changes in the polymer functional groups [21]. The utility of the technique has been demonstrated in a number of studies [6-8, 22-24], in particular, applications of polyimides to electronics packaging.

In this paper we focus on FTIR analysis of POM interfaces. Since no single spectroscopy technique suffices to explain the complex chemical interactions taking place at the polymer-metal interface, other techniques, specifically XPS and Auger electron spectroscopy (AES), are used to complement the interpretation of interfacial behavior. With the aid of examples from our research on polyimides and conjugated electroluminescent polymers, we illustrate the kind of information about the interface chemistry that can be derived from the application of FTIR and complementary techniques.

Experimental

All polymer films were prepared by spin coating onto metallized silicon wafers. Polymer film thicknesses were then determined by ellipsometry or profilometry. Polymer film thicknesses were maintained below 500Å to obtain a significant signal from the interface that is not washed out by bulk absorption. The metal films, nominally 3000Å thick, were prepared by e-beam evaporation (Al and Cr) or sputtering (Cu) onto (100) Si wafers.

FTIR was performed using a Nicolet Model 800 spectrometer capable of scanning from 400 cm^{-1} to 4000 cm^{-1}. For each FTIR scan, 8192 data points were collected, corresponding to a spectral resolution of 4 cm^{-1}. 250 scans were taken and averaged for each spectrum to increase the signal-to-noise ratio. *In situ* polyimide curing studies were performed using the infrared reflection absorption (IRRAS) technique [25]. For this characterization, the sample was clipped onto the front of an Al plate, which was heated from behind by a molybdenum wire resistive heater. A K-type thermocouple monitored the temperature on the sample side of the plate. The sample was placed in a stainless steel cell which could be purged with flowing gas or placed under vacuum. Calcium fluoride windows on the cell allowed the transmission of the IR beam. The IR beam from the interferometer passed through a wire-grid polarizer to obtain *p*-polarized light, parallel to the plane of incidence. The beam was incident on the sample at a grazing angle of approximately 20°, specularly reflected by the metal substrate, and detected by a room temperature deuterated triglycine sulfate (DTGS) detector.

Curing studies of polyimide thin films were performed by heating the films in vacuum to 400 °C in the following stages after softbaking in nitrogen for 30 minutes at 90 C: heat at 160 °C for one hour, 250 °C for 30 minutes, and 400 °C for 30 minutes. All curing was done at pressures less than 10^{-6} torr to prevent the thin film from burning off due to the presence of trace amounts of oxygen in inert gases. FTIR spectra were taken at each step in the curing process after cooling to room temperature in vacuum. This eliminates the need to correct the spectrum for vibrational transitions from excited energy levels. The polyimides studied are (i) biphenyltetracarboxylic dianhydride (BPDA) - p-phenylene diamine (PDA or PPD) and (ii) 4,4'-(hexafluroisopropylidene)-bis(phthalic anhydride) (HFDA) - 4,4'-bis(4-aminophenoxy) biphenyl (APBP). The structures of these two polymers are shown in Figure 1.
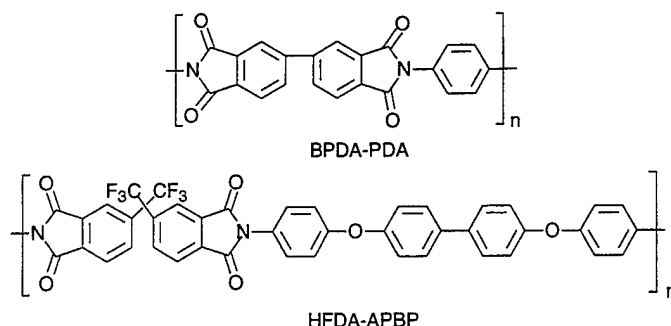
BPDA-PDA

HFDA-APBP

Figure 1. Structures of BPDA-PDA and HFDA-APBP.

Hydrolysis studies of the cured polyimide films were performed by placing the fully cured polymer-on-metal samples into an oven controlled at 85 °C and 85% relative humidity for 100 hours. *Ex situ* FTIR characterization of these films was performed using attenuated total reflection (ATR). In this method, the IR beam was multiply internally reflected in a KRS-5 crystal sandwiched between two pieces of the same sample. ATR is the method used for hydrolysis studies since the harsh treatment also effects the reflectivity of the metal substrate. These changes in reflectivity would produce artifacts in the IRRAS technique.

Computer simulations of infrared spectra were performed using the 2×2 matrix method couple with the Kramers-Kronig relationship. Details of these calculations can be found elsewhere [26-28]. In brief, optical constants are calculated based on the transmission spectrum of an isotropic polymer sample. The matrix method can then be used to determine IRRAS spectra for any film thickness based on the optical constants. This technique is used to differentiate between optical effects and true chemical or orientation changes in the polymer film.

Photo-oxidation studies of electroluminescent polymers are performed by exposing the polymer to dry air from an FTIR purge gas generator. Films are UV irradiated using an unfiltered low pressure ozone-free mercury lamp. The 254 nm line is the strongest and the incident intensity of this line is approximately 144 $\mu W/cm^2$. The irradiance of the second most intense line at 436 nm is about 15 $\mu W/cm^2$. The idealized general structure of the electroluminescent polymers studied is shown in Figure 2.
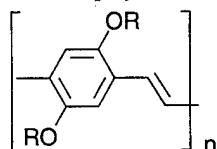
Figure 2. Structure of poly(phenylene vinylene) (PPV) derivatives used in this study.

Polymer films were examined *ex situ* by XPS using a Surface Science Instruments SSX100 spectrometer with monochromatic $Al_{K\alpha}$ (1486.6 eV) radiation. The resolution of the spectrometer was about 0.8 eV and a spot size of 600 μm was used. The thin polymer films were slightly conducting but 5 eV charge compensation was necessary. The samples were referenced to the gold $4f_{7/2}$ peak at 84.0 eV and to the carbon 1s peak at 285.0 eV. To change the signal probing depth, the take-off angle of the photoelectrons was varied by tilting the sample.

Discussion

Effect of Film Thickness - Interface vs. Bulk Signal

It is appropriate to first illustrate the ability of the IRRAS technique to observe chemistry at the polymer-metal interface. This is done by comparing the spectra of polymer films of decreasing thicknesses. As the film gets thinner, the ratio of interfacial signal to bulk signal increases, so that interfacial effects are more clearly observed. When BPDA-PDA is coated onto Au, the IR spectrum is independent of the thickness of the film. The chemical inertness of Au prevents interactions from occurring with the polyimide film. However, on more reactive metals, interactions at the interface are observed. This is illustrated in Figure 3 for the case of fully cured BPDA-PDA on Cr/Cr_xO.
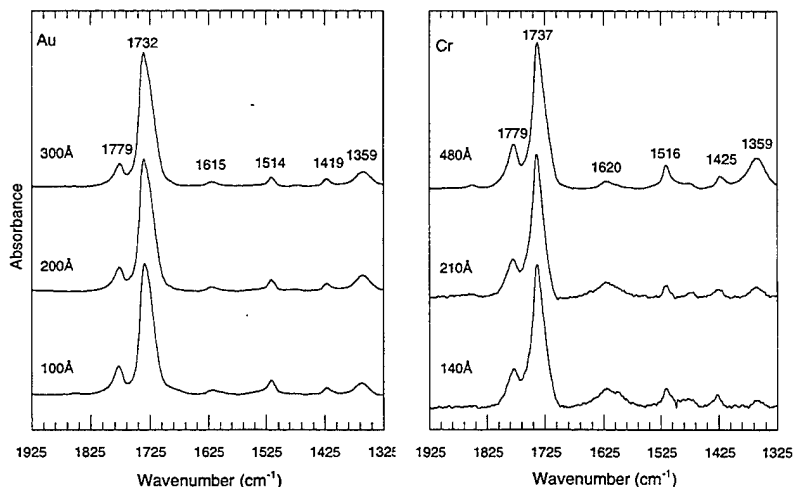
Figure 3. IRRAS spectra of BPDA-PDA on Au and Cr/Cr_xO
as a function of polymer film thickness.

The ratio of the imide C-N stretch (1359 cm^{-1}) to the semicircle stretch of the aromatic rings (1510 cm^{-1}) decreases for thinner films, while the absorption band around

1620 cm^{-1} (quadrant stretching of aromatic rings) becomes broader, indicating that there is some interaction between the polymer and the Cr/Cr_xO substrate. A modified polyimide layer is formed near the interface, which is significantly different from the bulk film. Angle-resolved XPS experiments show a nitrogen deficiency at the interface as the result of a carboxylate intermediate [29]. Fully cured BPDA-PDA films do not display the same behavior when coated onto Al/Al_2O_3, suggesting that there is less interaction between the polymer and this substrate.

Simulation of IR Spectra:

Different IR sampling techniques can give significantly different results. Reflection spectra often show changes in peak positions and shapes relative to transmission spectra, particularly when studying very thin films [27, 28]. It is important, therefore, to have a detailed understanding of optical effects in the film so that these effects are not misinterpreted as chemical changes. The curing of HFDA-APBP, an isotropic polyimide, will be used to illustrate this point. The left side of Figure 4 shows experimental IRRAS spectra for fully cured HFDA-APBP films on Cr/Cr_xO.
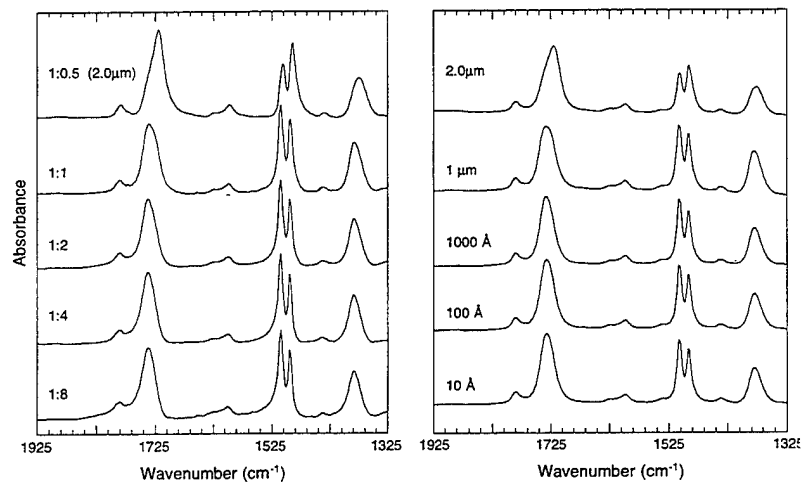
Figure 4. Experimental (left) and simulated (right) IRRAS spectra of fully cured HFDA-APBP films on Cr/Cr_xO as a function of film thickness. Numbers on the left-hand side refer to dilution ratios yielding approximately the thickness shown on the right-hand side.

Qualitatively, the presence of all peaks is seen in each of the spectra; however, there are differences in the thickest film. In particular, the relative intensities of the two aromatic ring semicircle stretching peaks at 1510 cm^{-1} and 1495 cm^{-1} have reversed in the 2 μm film. It is also apparent that the peaks in the thickest film are at slightly lower frequencies than in the thinner films. The right side of Figure 4 shows simulation results

for HFDA-APBP on Cr/Cr_xO as a function of film thickness. The simulation results show excellent agreement with experiments, indicating that the observed spectral changes are the result of optical effects only, and are not due to chemical or orientation changes in the polyimide film.

In Situ Investigations of Curing Chemistry

The curing of polyamic acid precursors to form polyimides may also be studied using the IRRAS technique. Figure 5 shows the temperature evolution of selected absorption bands during the curing of BPDA-PDA on an Al/Al_2O_3 substrate. On this substrate, BPDA-PDA follows a very characteristic cure. After soft-baking, the spectrum is dominated by bands from the polyamic acid precursor. After heating to 160 °C, imide C=O and C-N peaks increase at the expense of polyamic acid features, such as the amide C=O. An anhydride species is also observed, which is formed as an intermediate and then eventually converted to the polyimide. The anhydride intermediate forms due to the back-reaction of the precursor to its diamine and dianhydride components. The imide C-N stretching mode at 1350 cm^{-1} is typically used as the reference for quantifying the imidization reaction, since there is no interference from other species in this region of the spectrum. The film appears to be fully imidized after heating at 400 °C, when all peaks associated with the precursor polymer have disappeared.
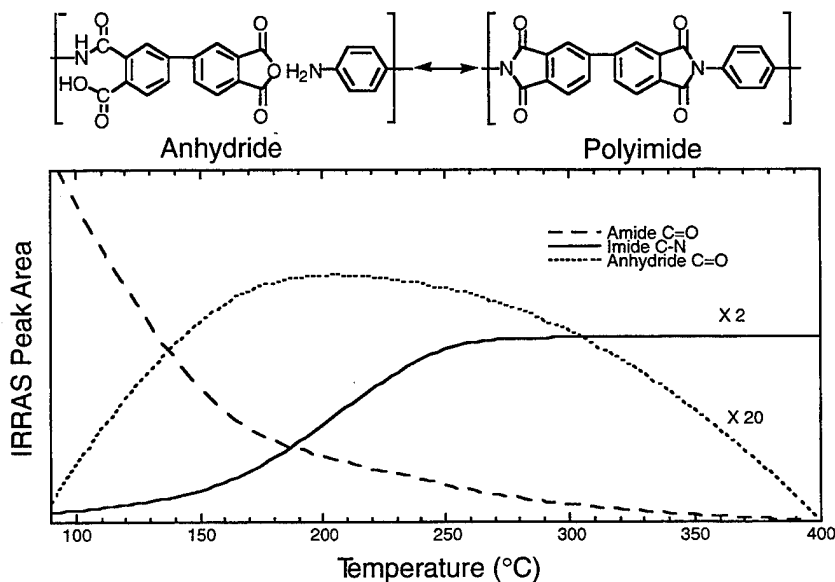
Figure 5. Curing process of BPDA-PDA on Al/Al_2O_3.

Thin BPDA-PDA films (~400Å) cured on Cr/Cr_xO behave very similarly to the film cured on Al. Again, imide features begin to form after heating to 160 °C and are

fully formed after heating at 400 °C. An anhydride intermediate is also detected during curing, but converts completely to the imide. However, it has been shown that when extremely thin BPDA-PDA films (~100Å) are cured on Cr/Cr_xO in nitrogen, a carboxylate intermediate is detected in addition to the anhydride [30]. This carboxylate intermediate is also completely converted to the imide by 250 °C. Since the carboxylate species were not detected in the thicker films, we may conclude that the carboxylate form in small amounts very near the interface. In the case of thicker films, the stronger bulk signal washes out information from the interface.

BPDA-PDA cured on Cu/Cu_xO exhibits markedly different behavior. Imide features begin forming at 160 °C, but above this temperature we see large amounts of a carboxylate species forming. As the cure progresses to higher temperatures, the carboxylate (as well as the anhydride) intermediates are converted to the imide. However, even after curing at 400 °C, a small amount of a polyamic acid-like carbonyl persists at 1723 cm^{-1}. Again, this suggests that there is a modified polyimide layer near the polymer-metal interface [29].

It is evident, since the carboxylate species is observed in these relatively thick films on Cu/Cu_xO, that more of this intermediate is formed than when the polymer is on Cr/Cr_xO. Based on these results, a ranking of the level of interaction can be written as follows: $Cu/Cu_xO > Cr/Cr_xO > Al/Al_2O_3$. Figure 6 shows spectra of BPDA-PDA cured on Cu, Al, and Cr substrates at the intermediate temperature of 160°C. The carboxylate intermediate is not detected when HFDA-APBP is cured on any of the substrates. This polyimide probably does not interact as strongly with the metal/metal oxide because of the fluorine groups.
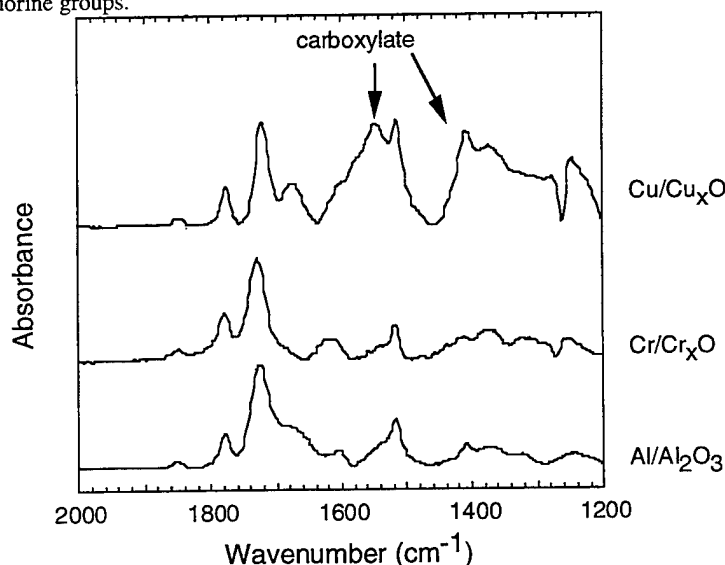
Figure 6. Intermediate curing step for BPDA-PDA on three different metal substrates.

110

Relevance to Adhesion and Environmental Stability.

Strong adhesion of the polymer to the metal/metal oxide interface is important in virtually every application of these systems. The level of chemical interaction between the polymer and the substrate is directly related to the force of adhesion at the interface. Island blister adhesion measurements [31] have been performed for BPDA-PDA on both Al/Al_2O_3, where the interaction is weak, and Cr/Cr_xO, where the interaction is stronger [30]. The force of adhesion data range from 28 to 51 J/m^2 on Al/Al_2O_3 and from 384 to 721 J/m^2 on Cr/Cr_xO. Although the results demonstrate a fair amount of scatter, which is typical for adhesion measurements, it is clear that there is greater strength at the Cr/Cr_xO interface, thus demonstrating a higher degree of chemical interaction.
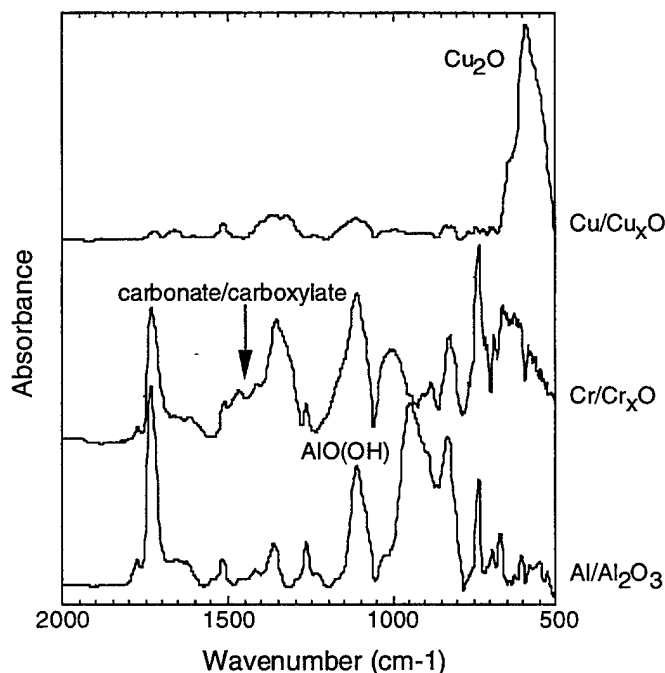
Figure 7. BPDA-PDA on three different metal substrates after 100 hours at 85 °C and 85% relative humidity.

Environmental stability is also of great concern to the stability of the interface since applications may involve high temperatures and/or high humidity, which accelerate existing degradation processes or initiate entirely new chemical pathways. To study these effects, the polyimide-on-metal structures were fully cured, then removed from vacuum and transferred to an oven held at 85 °C and 85% relative humidity. After treatment for

111

100 hours, the samples were removed and examined by ATR. ATR spectra of BPDA-PDA films on Al/Al_2O_3, Cr/Cr_xO, and Cu/Cu_xO after treatment, are shown in Figure 7.

On Al/Al_2O_3, the intensity of the peaks associated with the imide moieties has decreased slightly after treatment. In addition, bands due to aluminum oxide (960 cm^{-1}) and hydroxide (1100 cm^{-1}) grow. This indicates that air and/or moisture is diffusing through the polymer film and further oxidizing the substrate. On Cr/Cr_xO, the polymer shows a slightly greater attenuation of the imide features than on Al. There is either a carboxylate or carbonate forming during the hydrolysis treatment, evidenced by a broad feature centered around 1400 cm^{-1}. When BPDA-PDA is treated on Cu/Cu_xO, the film is virtually destroyed with virtually no imide-related bands remaining. There is a large formation of Cu_2O (600 cm^{-1}), which results from oxidation of the substrate. These results show that although a moderate amount of chemical interaction at the polymer-metal interface is useful in promoting adhesion, too much interaction can lead to catastrophic failure of the interface under environmentally rigorous situations. By comparison, the less reactive HFDA-APBP show much greater hydrolytic stability on all three substrates.

Bulk and Interfacial Reactions Relevant to Electroluminescent Polymers.

With the recent discovery that polymers can be used in electroluminescent (EL) devices [2] there has come a concentrated effort to understand how these materials behave and how to improve device performance. These light emitting devices provide a technologically exciting new field in which to study polymer/inorganic interfaces. The basic structure of a simple polymeric light-emitting device is shown in Figure 8. In such a device, there is a polymer-metal interface and a polymer/ITO interface, where ITO is indium tin oxide. The rigorous environmental condition that these devices are exposed to is a large electric field of about 1 MV/cm, which produces local heating. In addition, the polymers themselves are prone to photo-degradation in air.

□ glass
□ ITO
▨ polymer (~1000 Å)
■ metal
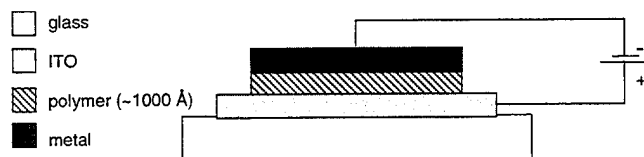
Figure 8. Typical polymeric light-emitting diode device structure.

The metallic electron injecting contact has proven to be particularly problematical in these devices. Calcium and silver/magnesium alloys have been shown to be the most efficient electrodes, but the reactivity of these metals dictates that special encapsulation steps must be taken in order to operate the device under ambient conditions. Aluminum electrodes have been used, but one must sacrifice light-emitting efficiency for improvements in lifetime. Short operating lifetimes continue to plague polymer-based EL devices. It is likely that some air permeates through encapsulation materials or is

present as an impurity in the polymer; it is unclear whether the polymer and/or the metal become oxidized during device operation.

We have studied both photo- and electric field-induced degradation of a family of polymers having a conjugated backbone and alkoxy side groups to improve the processability of the polymer (*cf.* Figure 2). IRRAS has been coupled with XPS and transmission IR spectroscopy to explain the bulk degradation of the polymer film under these conditions. When films were exposed to dry air in the absence of light, no change was observed by IRRAS. Also, when films were exposed to UV irradiation in a vacuum of less than 10^{-6} torr, no change was observed after up to 48 hours of exposure. However, when films were simultaneously exposed to UV and air, the polymer oxidized. The evolution of the spectrum for a film of poly(2-methoxy,5-(2'-ethylhexoxy)-1,4-phenylene vinylene) (MEH-PPV) cast onto Al is shown in Figure 9. The most obvious change is the growth of the carbonyl peak around 1723 cm^{-1}. At the end of 36 hours of exposure, the carbonyl peak has shifted from 1723 cm^{-1} to 1745 cm^{-1}. Also, there is a marked attenuation of the peaks associated with the phenyl rings at 1500, 1415, and 1035 cm^{-1}. *Ex situ* ATR spectra confirmed that the ring structure was destroyed and *not* simply reoriented in the film with reduced sensitivity of the IRRAS technique.
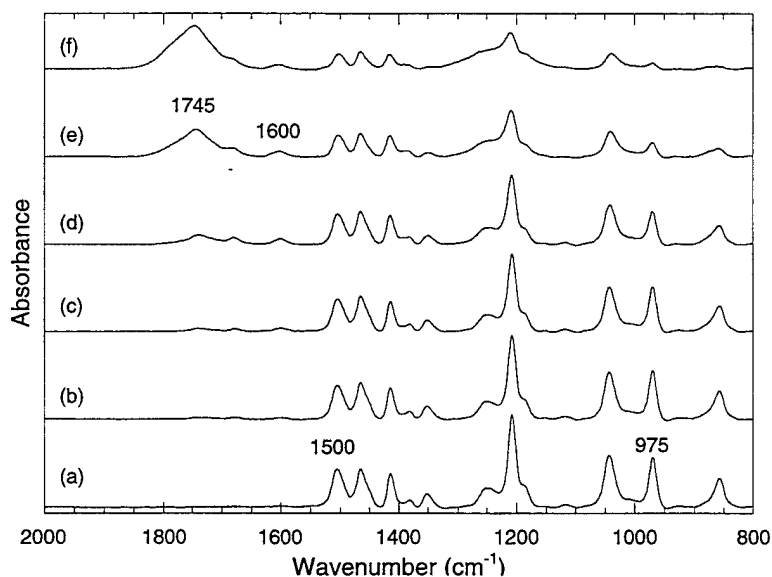
Figure 9. IRRAS spectra of 400 Å films of MEH-PPV on Al. Spectra are shown for the as-coated film (a), and after exposure to dry air and UV irradiation for (b) 2h, (c) 5h, (d) 12 h, (e) 24 h, and (f) 36 h.

The band at 975 cm^{-1}, associated with the vinyl double bond in the polymer backbone, is attenuated, but not fully destroyed during the oxidation. The decrease in conjugation length is also observed by the growth of the phenyl band at 1600 cm^{-1} which becomes IR active as the symmetry of the polymer is destroyed. The position of the carbonyl peak along with the persistence of the C-O peak at 1200 cm^{-1} is indicative of an ester or acid and this assignment is future supported by XPS data.

The observations of FTIR and XPS may be explained in terms of the mechanism illustrated Figure 10. This mechanism involves singlet oxygen formed by energy transfer from the polymer during photoluminescent operation, and since photoluminescence and electroluminescence pathways are identical for PPV derivatives [32], electroluminescent operation could likewise produce excited-state singlet oxygen. This singlet oxygen then undergoes a 1,2-cycloaddition across the vinyl double bond in the polymer backbone, shortening the conjugation length and blue-shifting the light emission. This oxidized segment subsequently initiates a free radical process ultimately leading to the formation of carbonyl containing groups such as esters [33]. The carbonyl group is known to quench luminescence in the polymer by preventing the recombination of electron-hole pairs [34, 35].
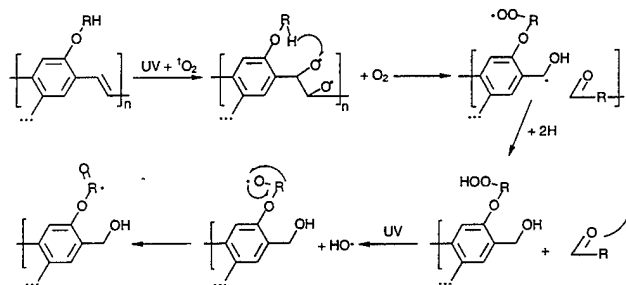
Figure 10. Proposed mechanism for the photo-oxidation of PPV derivatives.

Conclusion

The utility of Fourier transform infrared (FTIR) spectroscopy in probing and understanding polymer-metal interfaces has been illustrated with examples of polyimide (PI)-metal systems relevant to electronics packaging and poly(phenylene)vinylene (PPV) derivatives used in electroluminescent devices. *In situ* infrared reflection absorption spectroscopy (IRRAS) provides insight into the formation of PI-on-metal interfaces, the hydrolytic stability of such interfaces, and the reactivity of PPV systems when exposed to ultraviolet light and oxygen. Models of the infrared optical processes in the thin film composites further assist in distinguishing between chemical and optical effects. While the bulk degradation of the PPV derivatives is relevant to the stability of electroluminescent polymer-based devices, it is also important to note that interfacial reactions occur to a considerable extent in these systems. At the polymer-metal interface,

electrochemical reactions take place that lead to the oxidation of the metal and the formation of gas, which escapes by rupturing the surface of the device. There is also the possibility that metal ions may diffuse into the polymer film, driven by the electric field. There is still much to be understood about the degradation of these devices, but the IR techniques, complemented with those of other surface analyses, are useful tools, as we have demonstrated for polyimide films.

Acknowledgments

References

1. K.M. Anetsberger, in *Metallized Plastics 1: Fundamental and Applied Aspects*, edited by K.L. Mittal (Plenum Press, New York, 1989), p. 29.
2. J.H. Burroughes, D.D.C. Bradley, A.R. Brown, R.N. Marks, K. Mackay, R.H. Friend, P.L. Burns, and A.B. Holmes, Nature **347,** 539 (1990).
3. J.R. Salem, F.O. Sequida, J. Duran, W.Y. Lee, and R.M. Yang, J. Vac. Sci. Technol. **A4,** 369 (1986).
4. S.P. Kowalczyk, Y. Kim, G.F. Walker, and J. Kim, Appl. Phys. Lett. **52,** 375 (1988).
5. R. Haight, R.C. White, B.D. Silverman, and P.S. Ho, J. Vac. Sci. Technol. **A6,** 2188 (1988).
6. D.Y. Shih, J. Parasczak, N. Klymko, R. Flitsch, S. Nunes, J. Lewis, C. Yang, J. Cataldo, R. McGouey, W. Graham, R. Serino, and E. Galligan, J. Vac. Sci. Technol. **A7,** 1402 (1989).
7. D.Y. Shih, N. Klymko, R. Flitsch, J. Parasczak, and S. Nunes, J. Vac. Sci. Technol. **A9,** 2963 (1991).
8. M.C. Burrell, P.J. Codella, J.A. Fontana, J.J. Chera, and M.D. McConnell, J. Vac. Sci. Technol. **A7,** 55 (1989).
9. T. Strunkus, C. Hahn, and D. Frankel, J. Vac. Sci. Technol. **A9,** 1272 (1991).
10. M.J. Goldberg, J.G. Clabes, and C.A. Kovac, J. Vac. Sci. Technol. **A6,** 991 (1988).
11. S.C. Freilich and F.S. Ohuchi, Polymer **28,** 1908 (1987).
12. J.W. Bartha, P.O. Hahn, F. Legoues, and P.S. Ho, J. Vac. Sci. Technol. **A3,** 1390 (1985).
13. R.M. Tromp, F. Legoues, and P.S. Ho, J. Vac. Sci. Technol. **A3,** 782 (1985).
14. G.M. Adema, I. Turlik, L.T. Hwang, G.A. Rinne, and M.J. Berry, IEEE Trans. **13,** 766 (1990).
15. J.M. Burkstrand, J. Appl. Phys. **52,** 4795 (1981).
16. N.J. Chou and C.H. Tang, J. Vac. Sci. Technol. **A2,** 751 (1984).
17. A.R. Rossi, P.N. Sanda, B.D. Silverman, and P.S. Ho, Organometallics **6,** 580 (1987).

18. P.S. Ho, in *Principles of Electronic Packaging*, edited by D.P. Seraphin, R.C. Lasky, and C. Li (McGraw Hill, New York, 1989), p. 811.

19. H. Satou, H. Suzuki, and D. Makino, in *Polyimides*, edited by D. Wilson, H.D. Stenzenberger, and P.M. Hergenrother (Chapman and Hall, New York, 1990), p. 227.

20. J.P. Lu, D.Volfson, F. Trusell, and K.F. Jensen, in *Chemistry at Polyimide-Metal Interfaces: in situ FTIR Studies of Polymer Curing Processes and Thermal Stability*, 1993 (Materials Research Society), p. 518.

21. J.L. Koenig, *Spectroscopy of Polymers* (American Chemical Society, Washington, D.C., 1992).

22. W.C. Stewart, J. Leu, and K.F. Jensen, , 1989 (Materials Research Society), p. 285.

23. D.S. Dunn and J.L. Grant, J. Vac. Sci. Technol. **A7,** 253 (1989).

24. K. Kelley, Y. Ishino, and H. Ishida, Thin Solid Films **134,** 271 (1987).

25. R.G. Greenler, J. Chem. Phys. **44,** 310 (1966).

26. W.R. Salaneck and J.L. Brédas, Synthetic Metals **67,** 11 (1994).

27. D.L. Allara, A. Baca, and C.A. Pryde, Macromolecules **11,** 1215 (1978).

28. A.N. Parikh and D.L. Allara, J. Chem. Phys. **96,** 927 (1992).

29. J.P. Lu, P.V. Nagarkar, D. Volfson, F. Trusell, K.F. Jensen, and S.D. Senturia`, J. Vac. Sci. Technol. **in press** (1995).

30. M.M. Richter, F.R. Fan, F. Klavetter, A.J. Heeger, and A.J. Bard, Chemical Physics Letters **226,** 115 (1994).

31. H. Nishino, G. Yu, A.J. Heeger, T.A. Chen, and R.D. Rieke, Synthetic Metals **68,** 243 (1995).

32. C. Zhang, S. Höger, K. Pakbaz, F. Wudl, and A.J. Heeger, J. Electronic Materials **22,** 413 (1993).

33. H. Vestweber, J. Pommerehne, R. Sander, R.F. Mahrt, A. Greiner, W. Heitz, and H. Bässler, Synthetic Metals **68,** 263 (1995).

34. F. Papadimitrakopoulos, M. Yan, L.J. Rothberg, H.E. Katz, E.A. Chandross, and M.E. Galvin, Mol. Cryst. Liq. Cryst. **in press** (1995).

35. M. Yan, L.J. Rothberg, F. Papadimitrakopoulos, M.E. Galvin, and T.M. Miller, Physical Review Letters **73,** 744 (1994).

IN-SITU XPS STUDY OF THE ALUMINUM
POLY(p-PHENYLENEVINYLENE) INTERFACE

K. KONSTADINIDIS*, F. PAPADIMITRAKOPOULOS**, M. GALVIN* AND R. OPILA*
*AT&T Bell Laboratories, Murray Hill, NJ 07974
**Institute of Materials Science, University of Connecticut, Storrs, CT 06269

ABSTACT

The chemical and electronic properties of aluminum/poly(p-phenylenevinylene) (PPV) interfaces were studied *in situ* using x-ray photoelectron spectroscopy (XPS). It was observed that the aluminum atoms react with the oxygen-containing groups present as impurities on the surface of PPV to form Al-O-C linkages. The *Al* atoms also interact with the π-system of the polymer as indicated by changes in the valence band. Contrary to to recent suggestions (Ettedgui *et al.*[1]) the relation between surface oxygen content and band bending is not straightforward, as shown by deposition on PPV surfaces prepared by two different synthetic routes.

INTRODUCTION

One of the factors affecting the stability and reliability of electroluminescent devices using organic materials as light emitters is the metal/organic interface. In the case of PPV, aluminum has been suggested for use as the electron-injecting electrode. Recently, there have been several experimental and theoretical studies of the interface between aluminum and conjugated polymers as well as small molecules.[1-5]

Ettedgui *et al.*[1] studied Al/PPV interfaces using XPS. They concluded that the onset of polymer band bending (i.e. shift of the C1s peak to higher BE with *Al* coverage) depends on the oxygen surface concentration (a parameter dependent on sample preparation). They observed the onset of band bending with as little as 1 Å coverage for 5% surface oxygen, and as much as 30 Å for 10% surface oxygen.

In this paper we report results of *in-situ* XPS measurements during *Al* deposition on PPV surfaces. From the C 1s, O 1s and Al 2p core levels as well as the valence band we get information about the chemical and electronic properties of the Al/PPV interface as it forms.

EXPERIMENTAL

The PPV films were prepared by converting the precursor at 200°C in an inert atmosphere. The precursor was synthesized using two different routes. The first one has been

117

described elsewhere,[6] and the second one is proprietary. The surface concentration of oxygen of the films was around 4 atom % when measured at 10° take-off angle using XPS. The exposure of the samples to air was limited to a few minutes during sample loading. During sample preparation and transfer care was taken to avoid the simultaneous exposure of the samples to both oxygen and light in order to prevent photo-oxidation of the polymer found to occur when PPV is exposed to light in the presence of oxygen.[7]

The XPS experiments were performed using a Scienta 300 spectrometer at Lehigh University. Details about the instrument and the metal deposition can be found elsewhere.[8-9]
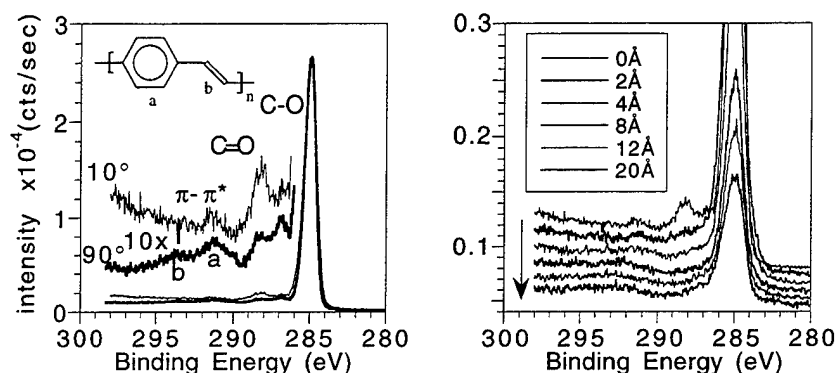
Figure 1. C $1s$ XPS spectra of (a) PPV films at 10° and 90°, and (b) PPV films at 10° as a function of Al coverage.

RESULTS

Fig. 1a shows the C $1s$ spectrum of a PPV film (1st synthetic route) acquired at two take-off angles. Besides the main peak at 284.8 eV originating from the aromatic and aliphatic parts of the molecule, there is more structure at high binding energy, which is better shown in the tenfold expanded spectra. The peak at 286.5 eV corresponds to carbon single-bonded to oxygen, which could come from either hydroxyl or methoxy groups, while the peak at 288.2 eV corresponds to carbonyl carbons. The higher relative intensity of the carbonyl peak at 10° photoelectron take-off angle indicates that the surface is richer in carbonyl groups. The two broad peaks observed at 291.5 eV and 294.5 eV are the $\pi - \pi^*$ shake-up peaks originating from the phenylene and vinylene groups, respectively. The loss of the latter at 10° indicates the lack of vinylene groups in the near surface region, which is consistent with the increased concentration of oxygen impurities (such as carbonyl, methoxy, and hydroxy substituents on the vinyl group) at the surface. This is also supported from the surface composition data calculated by integrating the C $1s$ and O $1s$ peaks. At 10°, with a sampling depth of approximately 15 Å , the fraction of oxygen is 4.1-atom %, while

118

at 90° with a 90 Å sampling depth, the fraction is only 1.6 atom % oxygen. It should be noted here that these values for the atomic composition represent a convolution of the actual concentration profile and a weighting function that decays exponentially with depth. More detailed angle resolved experiments[10] show that the actual oxygen concentration on the surface is approximately double the concentration measured at 10° take-off angle.

The C $1s$ spectra after Al metal deposition of 0, 2, 4, 8, 12, and 20 Å are shown in Fig.1b for a 10° take-off angle. There are no significant shifts in the main peak that would indicate band bending. It is observed that at the lowest coverage of 2 Å the carbonyl peak disappears.
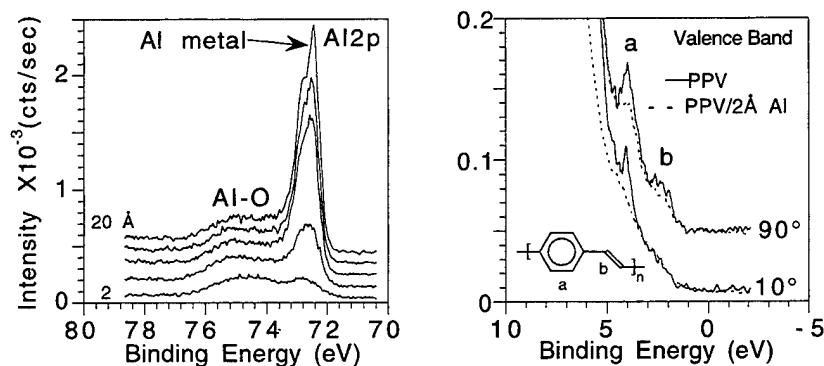
Figure 2. (a) 10° Al $2p$, and (b) valence band XPS spectra of a PPV film as a function of Al coverage.

Fig. 2a shows the Al $2p$ spectra as a function of coverage. At the lowest coverage of 2 Å there is a mixture of oxide and metallic aluminum on the surface. The oxide peak comes from Al atoms that have reacted with the carbonyl and other oxygen containing groups of the surface. As the coverage increases, the metal-to-metal oxide ratio increases indicating that the oxide is located at the Al/PPV interface and not at the metal vacuum interface (as would be the case if the metal was oxidized by residual oxygen in the vacuum chamber).

Recent theoretical calculations and UPS experiments[4] have shown that the valence band spectrum of PPV has two distinct bands, one around 2 eV and the other around 4 eV. These are associated with the vinylene and phenylene groups of the polymer chain, respectively. The valence band spectrum of our sample acquired using XPS at 10° and 90° take-off angles is shown in Fig.2b. Also shown is the same region after a 2 Å Al metal deposition. It is observed that, at 10° the sharp band at 4.1 eV (b) associated with the phenylene group disappears. At 90°, on the other hand, the phenylene peak is only slightly attenuated even after a 2 Å Al deposition. The broad vinylene peak around 2 eV (b) is only observed at 90°, in agreement with the previous conclusions that the top surface is depleted of vinylene groups due to substitution by oxygen containing groups.

DISCUSSION

The C 1s core level spectra of PPV, converted under the conditions described above, show that the surface of the film contains oxygen impurities in the form of carbonyl, methoxy, and hydroxy substituents on the vinylene group. The hydroxy and methoxy substituents are products of side reactions during the preparation of the soluble PPV precursor, while the carbonyl substituents are products of oxidation during the thermal conversion of the precursor to PPV.[7] The higher concentration of carbonyl groups on the surface than in the bulk, as evidenced by the angle resolved spectra, makes these groups the primary targets of reaction with the vapor-deposited Al atoms. At the lowest Al metal coverage examined (2 Å) the carbonyl peak disappears due to the reaction with the metal atoms, with $Al - O - C$ the most probable product. The O 1s and Al 2p spectra also support this conclusion. The O 1s peak shifts to lower binding energy where metal oxide binding energies are found, while the Al 2p peak shows a mixture of Al metal and $Al - O$. Reaction of the Al atoms with hydroxy or methoxy groups is more difficult to discern, since the shift in the binding energy would be small compared to the original value.

Further evidence of interaction of the metal with the polymer comes from the valence band spectra, where the signature peak of the phenylene peak disappears at a coverage of 2 Å. Theoretical modeling and experiments with model compounds[5] have shown that when Al metal atoms interact with a pristine PPV surface, the result is reaction with the vinylene group and disruption of the conjugation. In the present case, the oxygen impurities immediately react with the metal atoms. However, the results suggest that the surface phenylene groups also take part in the reaction with the deposited metal atoms at the early stages of deposition. This discrepancy with theoretical predictions and experimental data on oxygen free surfaces is due to the presence of oxygen impurities on the surface of the sample. These impurities deplete the near surface region of vinylene groups and leave the phenylene groups available for interaction with the Al atoms.

Following a 2 Å Al deposition, the phenylene peak in the PPV valence band spectrum disappears at a 10° take-off angle. However, it is clearly present in the 90° spectrum (Fig.5). This observation indicates that the reaction is limited to the near surface region, and no significant diffusion of the metal atoms has occurred. The lack of metal atom diffusion into the bulk of the polymer is indicative of the high reactivity of the metal atoms with the surface oxygen impurities. The high reactivity results in cluster growth of the Al film, which is reflected in small shifts in the Al 2p binding energy. These results have been explained in detail elsewhere.[9] Similar shifts have also been observed during titanium deposition on self-assembled monolayer surfaces terminated with groups of varying reactivity.[8]

No band-bending was observed in the PPV C 1s spectra even at the highest Al coverage (20 Å). This is in disagreement with previously published work by Ettedgui et al.[1] who observed a gradual shift of the C 1s peak of approximately 0.5 eV. They correlated the onset of band-bending with the oxygen content of the surface, claiming that higher surface oxygen content results in the formation of a thicker oxide layer that delays (or-even prevents)

the onset of band bending to higher metal coverage by preventing the metal from interacting directly with the polymer. We have presented direct evidence (i.e. valence band spectra) that Al *does* interact with the polymer, and even with oxygen-free groups such as the phenyl groups. Despite the fact that our films were not converted *in-situ* in the UHV system (as Ettedgui et al.[1] did with their samples), the oxygen content of our films is 4 atom %, which is lower than the 5 atom % reported by Ettedgui et al.[1] However, no significant or consistent shift was observed, although we noticed a slight broadening of the C 1s peak. In addition, the energy resolution was much better in our case judging from the FWHM of the C 1s peak of PPV (0.9 *eV* vs. 1.5 *eV*).
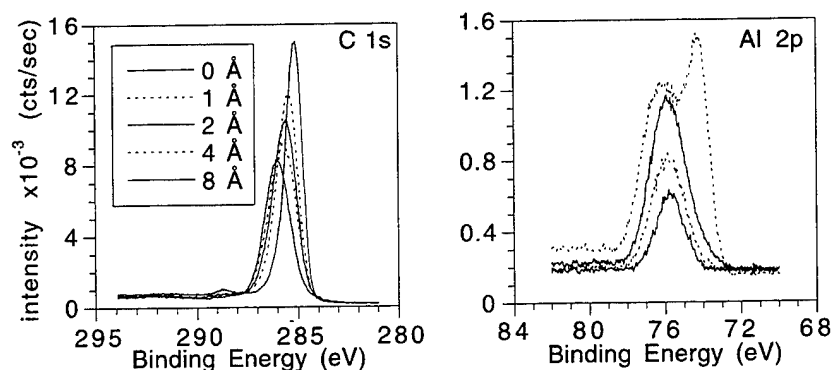
Figure 3. (a) C 1s, and (b) Al 2p XPS spectra of a PPV film (alternate synthetic route) at 10° as a function of Al coverage.

Preliminary results on PPV prepared using a proprietary alternate synthetic route have shown that band-bending and surface oxygen concentration are not related in a straightforward manner. In particular, deposition on the PPV surfaces has resulted in immediate C 1s band bending* (Fig. 3a) even though the surface oxygen concentration of the new sample was the same as the old. The new route however differs from the old one in that it provides PPV films free of carbonyl groups. This observation suggests that the kind of oxygen present in the film and not only its total concentration is what determines band-bending. This observation indicates the important role carbonyl groups play in the electronic properties of the interface, in addition to the dramatic effect they have on the luminescence of the film itself.[6]

---

* Note that the Al 2p spectrum (Fig.3b) does not shift at all, ruling out charging as the cause for the C 1s shift. It is also noteworthy that metallic Al appears only at the last deposition step, although band bending is directly correlated to interaction of the polymer with the metal. –

CONCLUSIONS

Our results show that, during the formation of the Al/PPV interface, oxygen-containing groups (primarily carbonyls near the surface) are the primary reactive sites for the deposited metal atoms, resulting in the formation of $Al - O - C$ linkages with the surface. Contrary to theoretical predictions, Al atoms *do* interact with the phenylene groups of the polymer molecule as changes in the valence band suggest. The high reactivity of the oxygen-modified PPV surface results in the immobilization of the deposited metal atoms, preventing surface and bulk diffusion and promoting cluster growth of the metal overlayer. Our results also suggest that the relationship between the onset of band bending and surface oxygen content is more complex than previous reports[1] suggested.

ACKNOWLEDGEMENTS

REFERENCES

[1] E. Ettedgui, H. Razafitrimo, K. T. Park, Y. Gao, and B. R. Hsieh, J. Appl. Phys. **75**, 7526 (1994).

[2] Y. Gao, K. T. Park, and B. R. Hsieh, J. Appl. Phys. **73**, 7894 (1993).

[3] P. Dannetun, M. Boman, S. Stafström, W. R. Salaneck, R. Lazzaroni, C. Fredrickson, J. L. Bredas, R. Zamboni, and C. Taliani, J. Chem. Phys. **99**, 664 (1993).

[4] P. Dannetun, M. Lögdlund, M. Fahlman, M. Boman, S. Stafström, W. R. Salaneck, R. Lazzaroni, C. Fredrickson, J. L. Bredas, S. Graham, R. H. Friend, A. B. Holmes, R. Zamboni, and C. Taliani, Synth. Metals **55-57**, 212 (1993).

[5] C. Fredrickson, R. Lazzaroni, J. L. Bredas, P. Dannetun, M. Lögdlund, and W. R. Salaneck, Synth. Metals **55-57**, 4632 (1993).

[6] F. Papadimitrakopoulos, K. Konstadinidis, T. M. Miller, R. Opila, E. A. Chandross, and M. E. Galvin, Chem. Mater. **6**, 1563 (1994).

[7] F. Papadimitrakopoulos, M. Yan, L.J. Rothberg, H.E. Katz, E.A. Chandross and M.E. Galvin, Mol. Cryst. Liq. Cryst. **69**, 663 (1994).

[8] K. Konstadinidis, P. Zhang, R. L. Opila, and D. L. Allara, Surf. Sci. accepted (1995).

[9] K. Konstadinidis, F. Papadimitrakopoulos, M. Galvin, and R. L. Opila, J. Appl. Phys, in press (1995).

[10] F. Papadimitrakopoulos, K. Konstadinidis, and M. E. Galvin, Macromol. submitted (1995).

Part V

Primers for Interface Preparation

PLASMA POLYMERIZED PRIMERS FOR RUBBER TO METAL BONDING: CHARACTERIZATION OF THE INTERPHASE

Y. M. Tsai*, F. J. Boerio*, and Dong K. Kim**
*Department of Materials Science and Engineering, University of Cincinnati, Cincinnati, Ohio
45221-0012
**The Goodyear Tire & Rubber Co., Akron, Ohio 44309-3531

ABSTRACT

Plasma polymerized acetylene films contained mono- and di-substituted acetylene groups, aromatic groups, and carbonyl groups which resulted from reaction of residual free radicals with oxygen when the films were exposed to the atmosphere. There was some evidence for formation of acetylides in the interphase between the films and the substrates. Reactions occurring in the interphase between the plasma polymerized films and natural rubber were simulated using a model rubber compound consisting of a mixture of squalene, zinc oxide, carbon black, sulfur, stearic acid, diaryl-p-diphenyleneamine, and N,N-dicyclohexyl-benzothiazole sulfenamide (DCBS). Zinc oxide and cobalt naphthenate reacted with stearic acid to form zinc and cobalt stearates. The stearates reacted with the benzothiazole sulfenamide moiety of DCBS and with sulfur to form zinc and cobalt accelerator complexes and perthiomercaptides. The complexes and perthiomercaptides reacted with squalene and the plasma polymer to form pendant groups which eventually disproportionated to form crosslinks between squalene and the primer. Migration of double bonds during reaction of the model rubber compound with the films resulted in formation of conjugated double bonds in squalene.

INTRODUCTION

Recently we have been interested in the use of plasma polymerized acetylene films as primers for rubber-to-metal bonding. The breaking strength of miniature lap joints prepared using natural rubber as an "adhesive" to bond together steel substrates coated with thin films of plasma polymerized acetylene was equal to that of similar joints prepared from brass substrates [1]. FTIR spectra of the as-deposited films were characterized by bands related to mono- and di-substituted acetylene, methyl, and methylene groups. Peaks related to aromatic structures were observed in positive SIMS spectra. Results from AES showed that the oxide on the substrate surface was partly reduced during deposition [1,2].

An important question regarding the use of plasma polymerized films as primers for rubber-to-metal bonding concerns reactions in the interphase between natural rubber (NR) and the primer. These interphases are difficult to characterize because they are buried and because the reactions which occur are complex. Several investigators have simulated reactions occurring in the interphase between NR and brass utilizing model compounds in which NR is replaced by a low molecular weight organic compound having a similar structure [3-6]. We have reported preliminary results in which a model compound containing squalene instead of NR was used to simulate reactions in interphases between NR and plasma polymerized acetylene films [1]. The

125

purpose of this paper is to report new results obtained using infrared spectroscopy to characterize reactions between plasma polymerized acetylene films and the model rubber compound.

EXPERIMENTAL

1010 cold-rolled steel (CRS) sheets 0.5 mm thick were obtained from The Goodyear Tire and Rubber Company (Akron, Ohio). The as-received steel substrates were mechanically polished, rinsed in distilled water and acetone, and blown dry with nitrogen.

Plasma polymerization and etching were carried out in a tubular reactor which was inductively coupled to an RF (13.56 MHz) power supply. A detailed description of the reactor has been presented elsewhere [7]. Prior to plasma polymerization, the polished substrates were etched in an argon plasma for 10 minutes. Plasma polymerized films of acetylene were then deposited on the substrates using argon as the carrier gas. The thickness of the films was determined by using a Rudolph Research Model 436 ellipsometer to examine polished steel substrates before and after deposition of the films.

Reflection-absorption infrared (RAIR) spectra of plasma polymerized films were obtained using a Perkin-Elmer 1800 Fourier-transform infrared spectrophotometer and a reflection accessory from Harrick Scientific Co. An angle of incidence of 80° was used to obtain the spectra. RAIR was also used to examine primed steel substrates after reaction with a model rubber compound consisting of squalene (100 parts per hundred or phr), zinc oxide (10 phr), carbon black (10 phr), sulfur (5 phr), stearic acid (2 phr), and N,N-dicyclohexyl-benzothiazole-sulfenamide (DCBS), cobalt naphthenate, and diaryl-p-diphenylene-amine (each 1 phr). Polished steel substrates primed with plasma polymerized acetylene films were immersed into a stirred mixture of these materials at a temperature of $150^{\circ}C$. During the reaction, the mixture was purged with nitrogen to reduce oxidation. At times between 1 and 100 minutes, substrates were removed from the mixture, rinsed with hexane, dried, and examined using RAIR.

During the reaction, aliquots were removed from the mixture using a pipette, placed in a glass bottle, and allowed to stand overnight so that the insoluble components would settle to the bottom of the bottle. A few drops of the liquid were placed onto a KBr pellet and examined by transmission infrared spectroscopy to determine the effect of the reaction on the structure of squalene. Raman spectra were obtained from several aliquots using a Bio-Rad FTS-60A FTIR system equipped with FT/Raman accessory.

RESULTS AND DISCUSSION

The RAIR spectrum of an as-deposited plasma polymerized acetylene film (thickness ~63.5 nm) on a polished steel substrate is shown in Figure 1A. Peaks characteristic of hydrocarbons were observed near 2960, 2928, 2870, 1450 and 1375 cm^{-1}. The strong band near 3295 cm^{-1} was assigned to CH stretching in monosubstituted acetylene groups (R-C≡C-H) [8]. Weak bands related to -C≡C- stretching in mono- and di-substituted acetylene were observed near 2103 and 2210 cm^{-1}, respectively [8]. A band assigned to C=C stretching was observed near 1600 cm^{-1}. The band near 916 cm^{-1} was related to the CH$_2$ wagging mode of vinylidene groups. A weak band near 1950 cm^{-1} was assigned to C=C=C stretching. A weak band possibly related to acetylide species [9] was observed near 3250 cm^{-1} in spectra of films that were only a

few nanometers in thickness. Bands near 3055, 3027, 1595, 1510, 1495, 758 and 700 cm^{-1} were assigned to aromatic rings. The band near 3455 cm^{-1} was
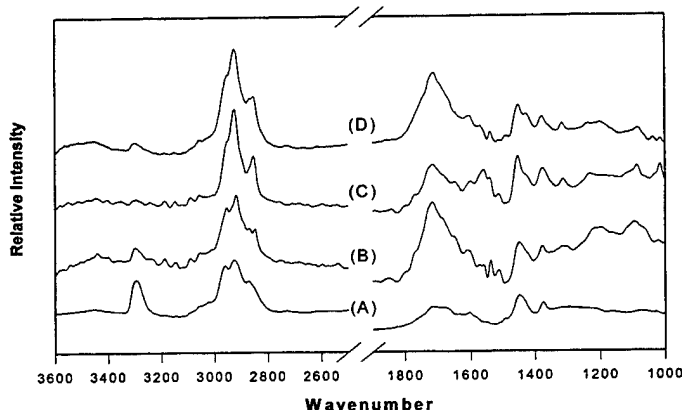
Figure 1. (A) - Reflection-absorption infrared spectrum of an as-deposited plasma polymerized acetylene film with a thickness of 63.5 nm on a polished steel substrate. Spectra shown in (B), (C), and (D) were obtained after reaction of similar films with the model rubber compound for 15, 30, and 45 minutes, respectively.

assigned to O-H groups while bands near 1715 and 1680 cm^{-1} were assigned to C=O groups resulting from the reaction of trapped radicals with atmospheric oxygen and moisture.

Infrared spectra of plasma polymerized acetylene films on steel substrates after reaction with the model rubber compound for various times are shown in Figures 1B-1D. After 15 minutes, the intensity of the band near 3295 cm^{-1} decreased greatly and new bands appeared near 1765, 1649, 1539, and 1512 cm^{-1}. After 30 minutes reaction time, additional bands appeared near 1011, 1030, 1085, 1232, 1320, 1430, and 1551 cm^{-1}. The band which appeared near 1539 cm^{-1} was related to zinc or cobalt stearate which were formed by reaction of ZnO and cobalt naphthenate with stearic acid. Bands which appeared near 1011, 1030, 1085, 1232, 1320, 1430, and 1551 cm^{-1} after 30 minutes were all related to the benzothiazole sulfenamide moiety of DCBS.

The band which appeared near 1649 cm^{-1} after 15 minutes of reaction was related to C=C double bonds in squalene. Linning and co-workers observed a band near this frequency in infrared spectra of NR cured with sulfur either with or without accelerators and observed a similar band in infrared spectra of squalene reacted with sulfur [10]. We observed a strong band near 1667 cm^{-1} in the infrared spectrum of squalene, indicating that squalene is mostly the trans isomer. We did not observe a band near 1649 cm^{-1} in transmission infrared spectra of squalene or the model rubber compound after reaction for a few minutes. However, a band did appear near 1649 cm^{-1} in transmission spectra of the model compound after reaction for 15 minutes. This band, which became stronger as reaction time increased, was most likely related to a C=C double bond with an attached sulfur or to conjugated double bonds [10].

We have also obtained Raman spectra of the model compound as a function of reaction time. For short reaction times, only one band near 1670 cm^{-1} was observed. New bands, which were attributed to conjugated double bonds [11], were observed near 1646, 1640, 1628, 1600, and 1580 cm^{-1} in Raman spectra of the model compound after 90 minutes. These observations support the assignment of the band near 1649 cm^{-1} in RAIR spectra of plasma polymerized acetylene films after reaction with the model rubber compound (see Figure 1) to conjugated double bonds and also support the conclusion that crosslinking occurred between squalene and the plasma polymerized film.

RAIR spectra shown in Figure 1 provide some information regarding the crosslinking mechanism. As indicated above, the bands near 1011, 1030, 1085, 1232, 1320, and 1430 cm^{-1} which appeared after 30 minutes (see Figure 1C) were all related to the benzothiazole sulfenamide moiety of DCBS. According to Chapman and Porter [12], the early stages of curing natural rubber with sulfur, an accelerator, and an activator involve formation of zinc stearate and then a zinc accelerator complex or a zinc accelerator perthiomercaptide complex. The zinc accelerator complex has the structure (I) while the zinc accelerator perthiomercaptide has structure (II) where X is an accelerator fragment and L is a ligand:

<div style="text-align:center">

L   L
↓   ↓
XSZnSX   (I)   XSS$_a$ZnSS$_b$X   (II)
↑   ↑
L   L

</div>
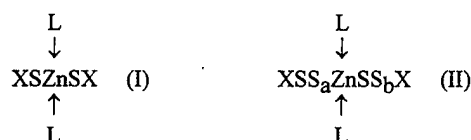
Since the accelerator used here was N,N-dicyclohexyl-benzothiazole-sulfenamide (DCBS), X has the structure III:

(III)
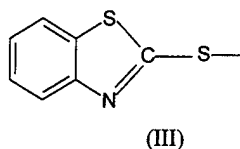
and the ligand L has the structure (IV):

(IV)
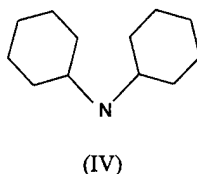
The zinc accelerator perthiomercaptide reacts with rubber to form accelerator perthiomercaptide pendant groups such as (V) which eventually disproportionate to form crosslinks such as (VI). In the current case, the DCBS moieties were most likely present as the zinc or cobalt accelerator perthiomercaptide (V) or an accelerator perthiomercaptide pendant group (VI).
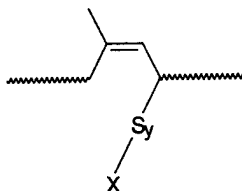
(V)
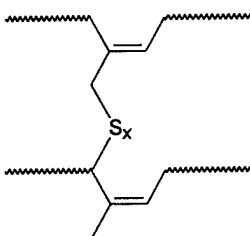
(VI)

The appearance of bands related to the benzothiazole sulfenamide moiety of the DCBS accelerator after 15 minutes reaction between the plasma polymerized film and the model rubber and their gradual disappearance after about 30 minutes was consistent with the formation of pendant groups such as (V) and their disproportionation to form crosslinks such as (VI).

The assignments of the bands near 1512 and 1765 cm^{-1} are not known at this time. No bands were observed near these frequencies in the infrared spectra of any of the neat compounds in the model rubber. However, a band was observed near 1512 cm^{-1} in transmission infrared spectra of the model rubber compound after reaction for five minutes but the intensity of this band did not seem to change as a function of reaction time. This band is probably related to an as yet unknown product which forms quickly in the reaction mixture. Linning and co-workers observed a band near 1765 cm^{-1} in infrared spectra of squalene after reaction with sulfur but did not discuss it [10]. This band is probably related to carbonyl stretching in ester groups in strained cyclic compounds or with electron withdrawing groups attached [13].

As the reaction between the plasma polymerized film and the model rubber compound progressed, there were significant changes in the spectra in the region between 3000 and 2800 cm^{-1} (see Figure 1). After 15 minutes, the band near 2870 cm^{-1}, which was characteristic of the plasma polymerized film, began to disappear and a shoulder began to appear near 2852 cm^{-1}. After 30 minutes, the band near 2852 cm^{-1} was well resolved but the band near 2870 cm^{-1} was not observable. The new band which appeared near 2852 cm^{-1} was related to CH$_2$ stretching in squalene and its appearance provided additional support for "crosslinking" between squalene and the plasma polymerized primer.

CONCLUSIONS

Plasma polymerized films of acetylene on polished steel substrates contained various functional groups, including mono- and di-substituted acetylene, aromatics, methyl, and methylene groups. The films also contained carbonyl groups which apparently resulted from reaction of residual free radicals with oxygen when the films were exposed to the atmosphere. Some acetylides may have formed in the interphase between the films and the steel substrates. When the plasma polymerized films were reacted with a model rubber consisting of a mixture of squalene (instead of natural rubber), zinc oxide, carbon black, sulfur, stearic acid, cobalt naphthenate, diaryl-p-diphenyleneamine, and N,N- dicyclohexylbenzothiazole sulfenamide, another interphase was created. Zinc oxide and cobalt naphthenate reacted with stearic acid to form stearates. The stearates reacted with the benzothiazole sulfenamide moiety of N,N-dicyclohexylbenzothiazole sulfenamide and sulfur to form rubber-bound pendant perthiomercaptide groups. Eventually the perthiomercaptides underwent disproportionation to form sulfidic crosslinks between the plasma polymerized acetylene films and squalene. Migration of double bonds in squalene during the reaction resulted in the formation of conjugated dienes and trienes.

ACKNOWLEDGMENTS

REFERENCES

1. Y. M. Tsai and F. J. Boerio, Surf. Interface Anal., accepted for publication, 1995.
2. Y. M. Tsai, U. R. Aggarwal, F. J. Boerio, D. B. Zeik, S. J. Clarson, W. J. van Ooij and A. Sabata, J. Appl. Polym. Sci.: Applied Polymer Symposium **54**, 3 (1994).
3. W. J. van Ooij and A. Kleinhesselink, Appl. Surface. Sci. **4**, 324 (1980).
4. W. J. van Ooij, Rubber Chem. Technol. **51**, 52 (1978).
5. W. J. van Ooij, W. E. Weening, and P. F. Murray, Rubber Chem. Technol. **54**, 227 (1981).
6. J. J. Ball, H. W. Gibbs, and P. E. R. Tate, J. Adhesion **32**, 29 (1990).
7. D. B. Zeik, S. J. Clarson, C. E. Taylor, F. J. Boerio, W. J. van Ooij, and A. Sabata, presented at 205th National Meeting of the American Chemical Society, Denver, CO, 1993.
8. N. B. Colthup, L. H. Daly, and S. E. Wiberley, Introduction to Infrared and Raman Spectroscopy, 3rd Edition, Academic Press, San Diego, CA, 1990, Ch. 6.
9. C. C. Chang and R. J. Kokes, J. Catal. **28**, 92 (1973).
10. F. J. Linning, E. J. Parks, and J. E. Stewart, J. Res. NBS **68A**, 499 (1964).
11. J. R. Shelton, J. L. Koenig, and M. M. Coleman, Rubber Chem. Tech. **44**, 904 (1971).
12. A. V. Chapman and M. Porter, in Natural Rubber Science and Technology, A. D. Roberts, Ed., Oxford Science Publications, Oxford, UK, 1988, Ch. 12.
13. N. B. Colthup, L. H. Daly, and S. E. Wiberley, Introduction to Infrared and Raman Spectroscopy, 3rd Edition, Academic Press, San Diego, CA, 1990, Ch. 9.

THE ROLE OF COUPLING AGENTS IN COMPOSITE DURABILITY

K.S. Macturk[*], C.L. Schutte, C.R. Schultheisz, D.L. Hunston and M.J. Tarlov[**]
Polymers Division, National Institute of Standards and Technology, Gaithersburg, MD 20899
[*] National Research Council Research Associate; [**] Process Measurements Division

ABSTRACT

We investigated the role of coupling agents with respect to the relative durability of glass fiber/epoxy matrix composites exposed to water, which degrades both glass fibers and the fiber-matrix interface. Interface chemistry was tailored by coating fibers with mixtures of different coupling agents. Single-fiber fragmentation test results showed little decrease in the strengths of the interface and a slight decrease in fiber strengths upon exposure to water. XPS results showed expected variations in surface composition. Contact angle measurements demonstrated variations in surface hydrophobicity as coupling agent mixtures were changed.

INTRODUCTION

Many studies highlight the relationship between the fiber-matrix interface and composite properties.[1,2,3] The behavior of the interface upon exposure to hostile environments is of special concern. In this work we attempt to "engineer" the interface to achieve strength and durability. To this end, coupling agent hydrophobicity and reactivity with the matrix is varied in an effort to increase resistance to moisture attack on the strength of both the fiber and interface, as measured by a single-fiber fragmentation test. X-ray photoelectron spectroscopy (XPS) and contact angle measurements provide insight into the interface chemistry, which is related to the mechanical properties. The goal is to better understand the decrease of strength in glass fibers and the interface caused by water. Improved composite durability will allow wider use of these materials in several new markets including automotive applications, deep water oil production and transportation infrastructure.

The single-fiber fragmentation test consists of applying tension to a dogbone sample of epoxy resin containing a single glass fiber. When the applied stress exceeds the failure stress of the fiber, the fiber begins to fragment. As the applied stress increases, fragmentation continues until the stress transferred across the interface via shear is no longer sufficient to fracture the fiber fragments. Completion of the fragmentation process is referred to as saturation. The average fiber fragment length at saturation (L_s) is related to the critical length ($L_c=4L_s/3$). The raw data consist of the number of breaks as a function of strain.

The effective interfacial shear strength (τ) is related to the apparent strength of the fiber at the critical length (σ_f), the critical length and the diameter (d) of the fiber fragment[4]

$$\tau = \frac{\sigma_f\, d}{2\, L_c} \qquad (1)$$

The fragmentation test has been used to study the effect of various environmental conditions.[5,6,7,8,9]

Equation (1) requires the strength of the fiber at the critical length in the resin be known. Traditionally, the fiber strength at the critical length is evaluated by tedious measurements of single fiber strengths at longer lengths extrapolated to the value of strength at the critical length. An additional complication results from loss of glass fiber strength due to moisture.[10] Also, it is difficult to simulate the conditions the fibers experience in the resin. The following approach is intended to circumvent these difficulties.

The strength of glass fibers is limited by the presence of surface defects which act as stress concentrators.[11] The strength of the fibers is expressed using a two parameter Weibull probability model. The probability of survival (P_s) at stress (σ) for a fiber of length L is

$$P_s = \exp\left[-\frac{L}{L_0}\left(\frac{\sigma}{\alpha_0}\right)^{\beta}\right] \qquad (2)$$

where α_0 is a scale parameter for a length L_0 and β is the shape parameter that is independent of length. Strengths of fibers are assumed to depend on critical flaws whose spatial locations follow a Poisson distribution.[12] The probability of survival at a given stress level is

$$P_s = \exp[-\lambda(\sigma)L] \qquad (3)$$

where $\lambda(\sigma)$ is a cumulative flaw density, or the number of critical flaws per unit length up to stress σ. Equating the probabilities of survival, substituting the number of breaks $n(\sigma)$ in length L_0 for $\lambda(\sigma)$, and taking the logarithm twice gives the relation between the experimentally accessible variables (n and σ) and the Weibull parameters (α_0 and β)

$$\ln[n(\sigma)] = \beta\ln\sigma - \beta\ln\alpha_0 \qquad (4)$$

The value of the stress is found by measuring strain in the dogbone during the test and the tensile modulus of the fiber. The Weibull parameters are found from a plot of $\ln[n(\sigma)]$ vs. $\ln(\sigma)$ (slope=β, intercept= -$\beta\ln\alpha_0$, Figure 1). The critical length fragment strength ($<\sigma_f>$) is

$$< \sigma_f >= \alpha_0 (L_0/L_c)^{1/\beta} \qquad (5)$$

Thus, interface and fiber strengths are evaluated as a function of moisture exposure.

EXPERIMENTAL METHOD*

Single-Fiber Fragmentation Test

Single filaments of unsized E-glass (donated by Owens-Corning) with a diameter range of 12-20 μm were coated with solutions containing mixtures of two different silane coupling

---

* Certain commercial materials and equipment are identified in this paper in order to specify adequately the experimental procedure. In no case does such information imply endorsement by the National Institute of Standards and Technology, nor does it imply necessarily that the items are the best available for the purpose.

agents. The first was n-octadecyltrichlorosilane $(Cl_3Si(CH_2)_{17}CH_3)$ which is denoted OTS. It was chosen because it is hydrophobic. However, it has the disadvantage of being unreactive with the epoxy. The second, 3-aminopropyltriethoxysilane, denoted APS, $(EtOSi(CH_2)_3NH_2)$ was chosen because the amine group reacts with the epoxy resin and it is relatively hydrophilic.

Solutions of silane mixtures were deposited on the fibers from a 0.1% by weight silane solution of a 50/50 mixture by volume of tetrahydrofuran (THF) and ethanol (0.72 moles THF/mole ethanol). Three silane ratios were used, 100% APS, 100% OTS, and a 50%/50% mixture of each by volume (2.6 moles APS/mole OTS). Silanes were added to the solvent solution and mixed for one hour at room temperature. Fibers were

Figure 1 Natural logarithm of the number of breaks vs. the natural logarithm of stress. The slope is β and the intercept is $-\beta \ln \alpha_0$.

dipped in 100 ml of the silane solutions for 2 minutes. The fibers were then removed from the solution and hung in a graduated cylinder to dry overnight.

Single-fiber fragmentation test samples were prepared using the procedure of Drzal.[13,14] Dogbone samples were made by aligning a single fiber in a mold, casting DGEBA epoxy resin (Epon 828, Shell) containing 14.5 phr metaphenylenediamine as a curing agent, and then curing the mold in an oven at 75 °C for 2 hrs followed by 2 hrs at 125 °C. Prior to conditioning the dogbones in water the sample ends were coated with a 5 minute epoxy to reduce transport of water along the fiber. The samples were conditioned in 75 °C distilled water for 2 to 10 weeks. Samples were removed from the 75 °C water and placed in room temperature distilled water for one day prior to testing.

The fragmentation test procedure was similar to that described in an earlier paper.[14] The fiber was examined with an optical microscope to ensure suitable fiber alignment. The initial number of breaks, if any, were counted, and the diameter of the fiber was measured. Two marks were placed on the sample surface approximately 1 cm apart to measure strain in the sample during the test. Next, the sample displacement was increased. After 10 minutes the number of breaks, if any, was recorded and the sample strain measured. The process was repeated until the number of breaks in the sample reached saturation. Three to five samples were tested for each condition.

Silicon Wafer Sample Preparation

In order to characterize the silane coatings with XPS and contact angle measurements more easily, flat plate samples were prepared. Single crystal silicon wafers of (111) orientation with a thickness of 575 ± 50 μm (Silicon Sense) were used to simulate the glass surface. Wafers were cut to 1.6 cm by 1.1 cm, rinsed with THF followed by distilled water and
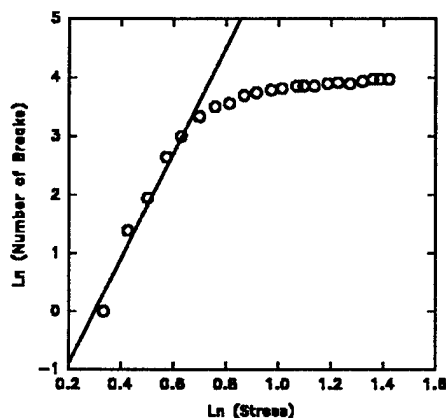
allowed to dry overnight. Next, the wafers were dipped in the silane solution as described in the previous section for the fibers.

XPS Analysis

XPS data were acquired using a VG ESCA Lab system. Excitation was provided by an Al anode operating at 240 Watts. The analyzer was operated in the retarding mode at a pass energy of 100 eV.

Contact Angle Measurements

We measured advancing and receding contact angles of deionized water on the treated silicon wafer surfaces using a contact angle goniometer (Rame-Hart, Model 100). The values of the contact angles were measured three times in three different areas of the surface resulting in a reproducibility of ± 3 °.

A dynamic contact angle analyzer (Cahn, Model DCA-312) was used to measure the contact angle of deionized water on the silane coated glass fibers. A platform speed of 100 μm/sec was used. Seven to eight fibers of each sample type were placed on a piece of tape and submerged simultaneously to produce sufficient signal. Three runs were done for each sample type for a reproducibilty of ± 2 °.

Figure 2 Number of breaks vs. applied strain for a dry and water conditioned sample.

RESULTS AND DISCUSSION

Raw data for two 50 % APS samples are shown in Figure 2. The horizontal shift between dry and wet (75 °C, 2 weeks) samples indicates more fiber breaks at lower applied strain due to degradation of the fiber. The vertical change in the total number of breaks relates to changes in the strength of both fiber and interface.

Results for the interfacial shear strength as a function of time in 75 °C distilled water are given in Figure 3. As expected, the dry 100 % APS coupling agent, which reacts with the epoxy, produces the strongest interface. The 100 % OTS (0% APS) gives the weakest interface. The 50% APS results are

Figure 3 Interfacial shear stress vs. time in 75 °C distilled water.

between the 0% and 100% values. Figure 3 also shows a slight decrease in interfacial strength for the 0 % APS samples aged in water. The interface strengths of the 100 % APS samples remain constant over times of 1800 hours.

Fiber strengths for different coatings are compared in Figure 4 which shows the fiber strength for a length of 15 mm versus time in 75 °C water. For the 100 % OTS samples, the fiber strength is fairly constant as a function of time in water. In contrast, for both the 50% and 100 % APS samples, the fiber strength appears to decrease as time in water increases. There are two possible explanations which, taken independently or collectively, may explain this behavior. First, the more hydrophobic OTS may produce a "barrier" coating which protects the fiber from water damage. Second, poor stress transfer during swelling of the OTS samples may result in less stress corrosion of the fiber.

Figure 4 Fiber strength at a length of 15 mm vs. time in 75 °C distilled water.

The values of advancing and receding contact angles of deionized water for the three mixtures of coupling agent on both fibers and wafers are shown in Figure 5. These results support the idea that the 100 % APS coating is more hydrophilic while the 100 % OTS coating is more hydrophobic. The contact angles for the treated fibers and silicon wafers are similar and show the same trends. These preliminary data suggest that under similar reaction conditions the resulting coatings on the fiber and wafer are chemically similar. Preliminary ellipsometric analyses of coated Si wafers yield thickness values in the range of 2.5 nm. These results suggest similarly thin coatings on the fiber. Work is ongoing to investigate this relationship more fully.

Preliminary XPS results indicate the surface chemical composition changes with the mixture of coupling agent deposited on the surface. As expected, the intensity of the nitrogen peak grows with increasing percentage of APS. The nitrogen increase correlates well with the increase in the interface strength of dry

Figure 5 Advancing and receding contact angles for glass fibers and silicon wafers vs. % amino coupling agent.

samples and is consistent with the lower contact angle of the 100 % APS samples, since the hydrophilicity should increase with the amount of nitrogen present.

CONCLUSIONS

Preliminary results showed that interfacial shear strength was controlled by chemical composition of coupling agent mixtures deposited on the fiber surface. The 100 % APS gave the strongest interface and best retained its strength over time in 75 °C distilled water. The hydrophobic 100 % OTS coating seemed to reduce the loss of fiber strength over time in water. Contact angle results demonstrated that the surface hydrophobicity changed with different silane mixtures. XPS results indicated the surface composition varied with the mixture of coupling agent. Work is continuing to better understand the relationship between surface composition and mechanical property changes upon aging. This type of information will lay the groundwork for increased use of structural composites in applications where they are exposed to moisture.

REFERENCES

1. J.J. Lesko, R.E. Swain, J.M. Cartwright, J.W. Chin, K.L. Reifsnider, D.A. Dillard, J.P. Wightman, J. Adhesion 45, 43 (1994).
2. E. Mader, K. Grundke, H.-J. Jacobasch, G. Wachinger, Composites 25, 739 (1994).
3. A.M. Serrano, I. Jangchud, R.K. Eby, K.J. Bowles, D.T. Jayne, Mat. Res. Soc. Proc. 305, 105 (1993).
4. A. Kelly, W.R. Tyson, J. Mech. Phys. Solids 13, 329 (1965).
5. V. Rao, L.T. Drzal, Polymer Composites 12, 48 (1991).
6. M.J. Fowlkes, W.K. Wong, Polymer 28, 1309 (1987).
7. L.T. Drzal, M.J. Rich, M.F. Koenig, J. Adhesion 18, 49 (1985).
8. A.T. DiBenedetto, P.J. Lex, Polym. Eng. and Sci. 29, 543 (1989).
9. X.S. Bian, L. Ambrosio, J.M. Kenny, L. Nicholais, A.T. DiBenedetto, Polymer Composites 12, 333 (1991).
10. R.J. Charles, J. Appl. Phys. 29, 1549 (1958); J. Appl. Phys. 29, 1554 (1958).
11. A.A. Konkin, in Handbook of Composites, Vol. 1:Strong Fibers, edited by W. Watt and B.V. Perov (Elsevier Science, New York, 1985), p. 255.
12. H.D. Wagner, A. Eitan, Appl. Phys. Letters 56, 1965 (1990); see also B. Yavin, H.E. Gallis, J. Scherf, A. Eitan, H.D. Wagner, Polymer Composites 12, 436 (1991).
13. L.T. Drzal, M.J. Rich, J.D. Camping, W.D. Park, in Proc. of 35th Ann. Tech. Conf., Reinforced Plastics, (Composites Institute, 1980), p.1.
14. C.L. Schutte, W. McDonough, M. Shioya, M. McAuliffe, M. Greenwood, Composites 25, 617 (1994).

ADHESIVE SYSTEMS BASED ON
FUNCTIONALIZED BLOCK COPOLYMERS

RANDALL S. SAUNDERS[*] AND MICHAEL S. KENT[*]
[*]Sandia National Labs, Dept. 1815, P.O. Box 5800, Albuquerque, NM. 87185-0367

ABSTRACT

Functionalized block copolymers were synthesized as adhesion promoters using Ring-Opening Metathesis Polymerization (ROMP). They were designed for glass/epoxy and copper/epoxy interfaces. The former contained triethoxysilane groups in the first block and secondary amine groups in the second. The latter contained imidazole groups in the first and amine groups in the second block. These block copolymers were shown to form ordered monolayers on the respective glass and copper surfaces using neutron reflectivity. Adhesion measurements showed an enhancement of adhesion after application of these block copolymers.

INTRODUCTION

In the manufacturing of printed wiring boards, often adhesion is a concern between a glass weave and an epoxy matrix, and between an epoxy matrix and a copper substrate. The goal of this work is to develop novel functionalized block copolymers to promote adhesion at inorganic substrate/polymer interfaces. The idea is that one block will be functionalized in order to react with the inorganic substrate, and the other block will be able to react with the polymer matrix. We envision several potential advantages of functionalized block copolymers over small molecule coupling agents, including greater control over the structure of the interphase region and enhanced adhesion through both entanglement and covalent bonding between the block copolymer and the polymer matrix.

Our program involves four key elements: the synthesis of suitable functionalized block copolymers, characterization of the conformation of the copolymers at the interface by neutron reflectivity, characterization of the degree of bonding by spectroscopy, and measurement of the mechanical properties of the interface. In this paper we discuss block copolymers designed as adhesion promoters for the glass/epoxy and copper/epoxy interfaces. For the glass/epoxy interface we have synthesized diblocks with one block containing triethoxysilane groups to bond to the glass, and the other block having secondary amine groups to bond to the epoxy. We have also made a triblock copolymer where the middle block is hydrophobic in order to promote moisture resistance. For the copper/epoxy interface we have made a diblock with one block containing imidazole groups to bond to copper and a second block containing the secondary amines, again to bond with the epoxy matrix. Below we describe the synthesis of the block copolymers by living, ring-opening metathesis polymerization (ROMP)[1,2] and the first characterization data obtained by NMR spectroscopy, small-angle x-ray scattering (SAXS), and neutron reflectivity. We also report here some preliminary adhesion measurements of these systems.

EXPERIMENTALS

Neutron reflectivity experiments were performed using the POSY II reflectometer at the Intense Pulsed Neutron Source at Argonne National Labs. Small-Angle x-ray scattering was performed using a Rigaku instrument with a 1.54-Å Cu Ka rotating-anode point source, Charles Supper double mirror focusing optics, and a Nicolet two-dimensional detector.

Synthesis

General

All reactants were purchased from Aldrich Chemical Company. Tetrahydrofuran was used as the polymerization solvent, and was vacuum distilled from a sodium/benzophenone ketal solution immediately prior to use. The molybdenum based initiator ((2,6-diisopropyl-phenyl-imido)neophylidine-molybdenum-bis-t-butoxide)[3] was purchased from Strem and used without further purification. All polymerizations were performed under an inert atmosphere in a Vacuum Atmospheres dry box.

Monomers

$$\underset{\textbf{1}}{\text{—Si(OEt)}_3} \qquad \underset{\textbf{2}}{} \qquad \underset{\textbf{3}}{\text{—N—}} \qquad \underset{\textbf{4}}{\text{—O(CH}_2)_7\text{CH}_3}$$
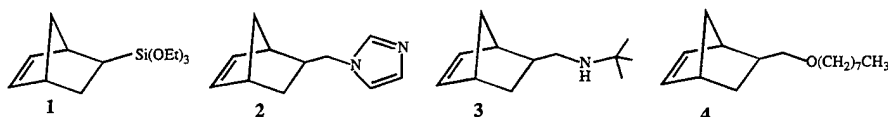
Triethoxysilyl norbornene (1) was purchased from HULS and was dried by distilling from and storing over sodium hydride. The monomer was filtered through activated neutral alumina immediately prior to use.

5-(n-methylimidazole)-2-norbornene (2): dicyclopentadiene (63.0g, 0.477 mol) and freshly distilled allylimidazole (75.0g, .694g) were heated to reflux neat for 16 hrs. After cooling down, the solution was vacuum distilled at 0.1 torr. After taking a cut from 50-100^{0}C, 65.3g (54%) of the pure product came over at 105-110^{0}C. This monomer was then dried by distilling from and storing over calcium hydride, and filtering through a bed of activated neutral alumina immediately prior to use.

5-(t-butylaminomethyl)-2-norbornene (3): step 1: allyl-t-butylamine. Allylbromide (140g, 1.16mol) was slowly dripped into a flask containing 500 mls. of mechanically stirred t-butylamine. This exothermic reaction was contained using a condenser fitted onto the flask. At the end of the addition, the solution was stirred overnight, and the precipitates were filtered off and washed with ether. The filtrate was distilled at atmospheric pressure with the final product coming over at 105^{0}C. step 2: dicyclopentadiene (14.0g, .11mol) and allyl-t-butylamine (above, 60.0g, .53mol) were heated neat in a high pressure reactor at 185^{0}C for 15 hrs., and then cooled to room temperature and the solution distilled under vacuum at 0.1 torr. The pure product was collected at 36^{0}C. This monomer was dried by distilling from and storing over calcium hydride and filtering through alumina immediately prior to use.

5-(octaoxymethyl)-2-norbornene (4): sodium hydride (4.50g, .187mol) and 120mls dry thf were placed in a three-neck flask fitted with a condenser and addition funnel. Iodooctane (40.0g, .167mol) was then added to the flask with a nitrogen purge. The solution was slurried, and a solution of norbornene-2-methanol (21.7g, .175mol) in 40mls dry thf were placed in the addition funnel. The slurry was heated to 50^{0}C and then the norbornene-2-methanol solution

slowly dripped into the slurry with stirring. After complete addition, the solution was stirred for 30 minutes and then allowed to cool to room temperature. The solvent was removed under reduced pressure, and the resulting cloudy oil was distilled at 0.1 torr, with the product coming over at 120°C (a yield was not recorded for this monomer). The monomer was further purified by distilling from and storing over sodium hydride, and filtering through alumina immediately prior to use.

Partially deuterated forms of the above monomers were made identically to the reaction schemes above by starting with a partially deuterated dicyclopentadiene.

Block copolymers

Four block copolymers were made and are shown below. They are designated by the monomer repeat unit number.

Block Copolymers for the glass/epoxy interface   *Block Copolymers for the copper/epoxy interface*
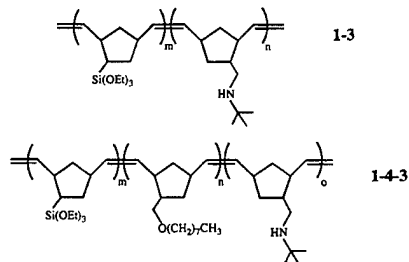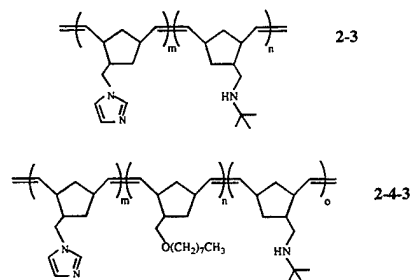
Typically 1g of polymer was formed in 15 mls. dry thf by stirring the appropriate amount of the molybdenum initiator with the appropriate amount of the first monomer, then upon complete consumption, the appropriate amount of the second monomer, etc. After the polymerization of the final block, the living chain ends were terminated by the addition of benzaldehyde. These block copolymers were characterized by proton NMR, which showed complete consumption of all monomer in most cases. The 1-3 and 1-4-3 block copolymers were used straight from the thf solution, whereas the 2-3 and 2-4-3 block copolymers were precipitated from acetonitrile, dried, and redissolved in chloroform for future use.

Each block in all of the polymers had a targeted molecular weight of 15,000 g/mol. By NMR, the only difference was that the immidazole blocks were less than 15,000 g/mol: typically they ended up being 10,000 g/mol. All the other blocks were assumed to be the targeted molecular weight. One additional diblock of the 2-3 system was made that had a molecular weight of 10,000 / 40,000 g/mol (to see the effect of lengthening block 3).

In all cases, a designation of d that immediately follows the number of the block indicates that the block is selectively deuterated over the other blocks in the polymer. These partially deuterated blocks contained 4 to 5 deuteriums per repeat unit.

Block copolymer treatment of surfaces

For the glass/epoxy interface the diblock (1-3) or triblock (1-4-3) was dissolved in isopropanol at a concentration of 0.02 g/ml, and clean silicon wafers were submersed in the solution for several hours. A small amount of tin octoate was added to promote hydrolysis of the ethoxysilane groups. The wafers were removed and rinsed with excess isopropanol, and dried.

139

For the copper/epoxy interface, the diblock (**2-3**) was dissolved in either thf or methanol at the same concentration as above, and a silicon wafer coated with a copper layer was submersed in the solution for several hours. It was then removed and rinsed with excess solvent, and dried.

Adhesion sample preparation and testing

Lap sheer samples were made by coating glass slides or copper coupons with the appropriate block copolymers, then applying a 1 in^2 epoxy resin on top, then curing for 2 hrs. at 170°C. Yield strengths were measured by pulling these samples on an Instron. Floating roller peel samples were prepared for copper epoxy interface by treating a copper foil with the block copolymer (**2-3**), then curing a layer of epoxy on top, then measuring the strength required to peel the copper from the epoxy.

RESULTS AND DISCUSSION

Synthesis

The monomers used in this study are readily available through Diels-Alder reactions of the appropriate vinyl or allyl compounds with cyclopentadiene. The monomers are thus relatively inexpensive. The polymerization of these monomers appears to be efficient and quantitative as observed by ^{1}H NMR (figure 1). In figure 1a, a representative monomer spectrum is shown. With all monomers, proton signals are seen between 5.8-6.4 ppm. which are associated with the protons on the carbons of the highly strained double bonds. Figure 1b shows the NMR spectrum of the **1-4-3** triblock copolymer taken straight from the polymerization solution. This spectrum indicates a complete disappearance of all signals between 5.8-6.4 ppm., and the appearance of a broad polymer peak, typical of polynorbornenes, between 5.2-5.6 ppm.

Gel Permeation Chromatography (GPC) has proved quite difficult for these block copolymers due to the presence of the amine functionalities. These amine groups cause the polymers to stick onto GPC columns. This phenomena has been observed by other researchers. There are other arguments for the existence of a living polymerization, and thus formation of block copolymers. First of all, it is well documented that the initiator used here is able to polymerize most norbornene-type monomers in a living fashion[4-7]. Second, it is known that bulk block copolymer materials phase separate in a well-ordered fashion on a meso-scale[7], and this results in well defined scattering peaks observed in small-angle x-ray scattering (SAXS). Figure 2, showing the SAXS pattern for the **1-4-3** triblock, demonstrates several scattering peaks, indicating the presence of meso-phase separation brought on by a block copolymer. All four block copolymer samples discussed here show typical phase separation scattering peaks, which can only be brought about by the presence of block copolymers. Therefore all of these materials have the desired block copolymer structure.

Characterization of adsorbed films by neutron reflectivity

It is important in these systems to determine what is the conformation of the block copolymers on the substrate to which they are adsorbed: whether one block is preferentially adsorbed or the blocks are mixed, and whether they form monolayers or multiple layers. To

monomer 3

characteristic
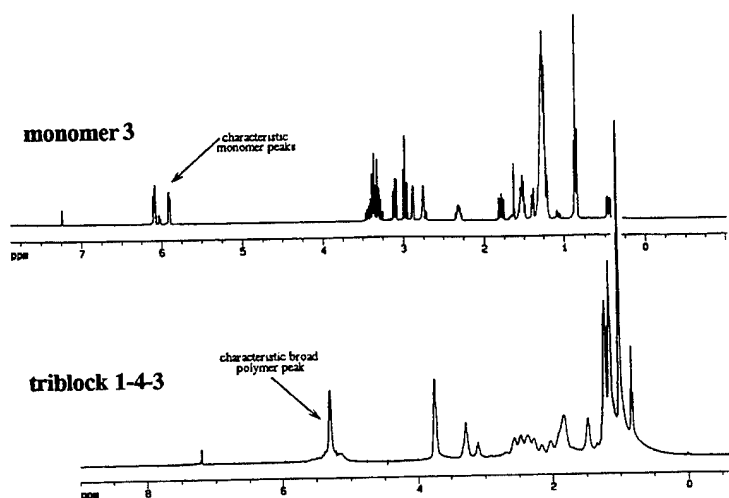monomer peaks

Figure 1. Typical ^{1}H NMR of a norbornene monomer (top) and of the **1-4-3**
triblock copolymer (bottom).
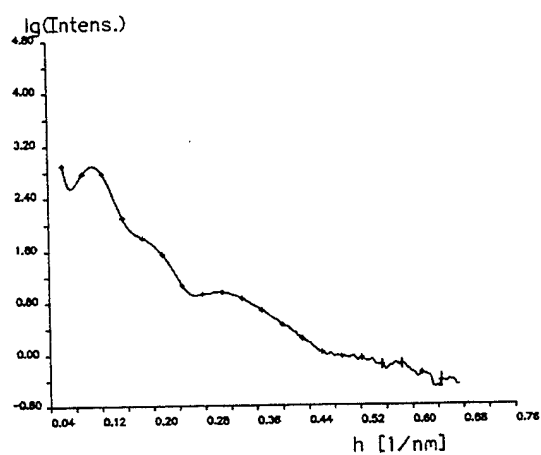
triblock 1-4-3

characteristic broad
polymer peak

Figure 2. Small-angle x-ray scattering pattern of triblock **1-4-3**.

address this question we prepared block copolymer samples with partially deuterated amine blocks (block **3**) for the silicon surfaces, and partially deuterated imidazole blocks (block **2**) for the copper surfaces, and examined adsorbed films of these polymers by neutron reflectivity. With this technique the neutron refractive index profile normal to the surface is obtained with ~5Å resolution. The selective deuteration allows one to distinguish between the blocks.

For the silicon surfaces, figure 3 shows the neutron reflectivity pattern for an untreated silicon surface (a), the **1-3** diblock copolymer treated silicon surface (b), and the **1-4-3** triblock copolymer treated surface (c). The reflectivity patterns suggest several things: first of all, the only way to interpret the data is to say that there are well-ordered monolayers adsorbed onto the silicon surface in both the diblock and triblock case. In the diblock case (b) the trace is shifted down and to the right compared with the untreated surface. This implies that the amine block is the block sticking up away from the surface. In the triblock case (c) the trace is shifted up and to the left, indicating the amine block is sticking down onto the silicon substrate, and the triethoxysilyl block is sticking up away from the surface. The latter case is counter intuitive, but can be explained by taking into account the solvent that was used for the adsorption. The hydrophobic middle block **4** of triblock **1-4-3** does not like the isopropanol environment, and most likely creates micelles in solution. This micellization may hide block **1** in the center, and thus only block **3** would be on the outer shell of the micelle, thus it would be the only block available to adsorb onto the surface.

Results for the diblock copolymer onto copper (with targeted block lengths of 15K-15K) adsorbed from a solution in methanol are shown in figure 4a. The main effect of the adsorbed copolymer on the reflectivity is to shift the fringes to lower q. This is consistent with the imidazole block (block **2**) selectively adsorbing to the surface, as shown in figure 4b. The curves in figures 4b-d were calculated using the known atomic compositions of the blocks and assuming a 30Å thickness for the layers formed by each block, which is consistent with the size of the shift observed in figure 4a. Thus, these data suggest that the copolymer adsorbs in a monolayer film onto the copper, and that the blocks form separate layers with the imidazole block (block **2**) adsorbed selectively to the surface (by comparison to the theoretically calculated curve shown in figure 4b).

Adhesion testing

Lap sheer samples were made for glass surface by adsorbing the block copolymer **1-3** onto two microscope slides, and curing a layer of epoxy between the two slides. When pulled on the instron, all of the samples failed in the glass slide rather than in the epoxy layer or the interface, thus only qualitative results can be reported at this time. It was observed that untreated glass slides had poor epoxy wetting characteristics; the epoxy would bead up when applied to the surface. However, when treated with the block copolymer, the epoxy formed uniform layers without beading up. Another test was to place the post-cured lap sheer sample in boiling water for several days to weaken the epoxy layer. It was observed that untreated lap sheer samples fell apart in boiling water whereas block copolymer treated samples did not. Therefore there is some enhancement of adhesion due to the application of the block copolymer.

Lap sheer samples for copper coupons treated with the **2-3** diblock were more straightforward. Failure always occurred near the interface, and thus quantitative results could be obtained. We discovered that untreated (microetch only) copper samples had an ultimate yield strength of 1250 lb/in^2, brown oxide samples (industry standard chemical roughening) had a
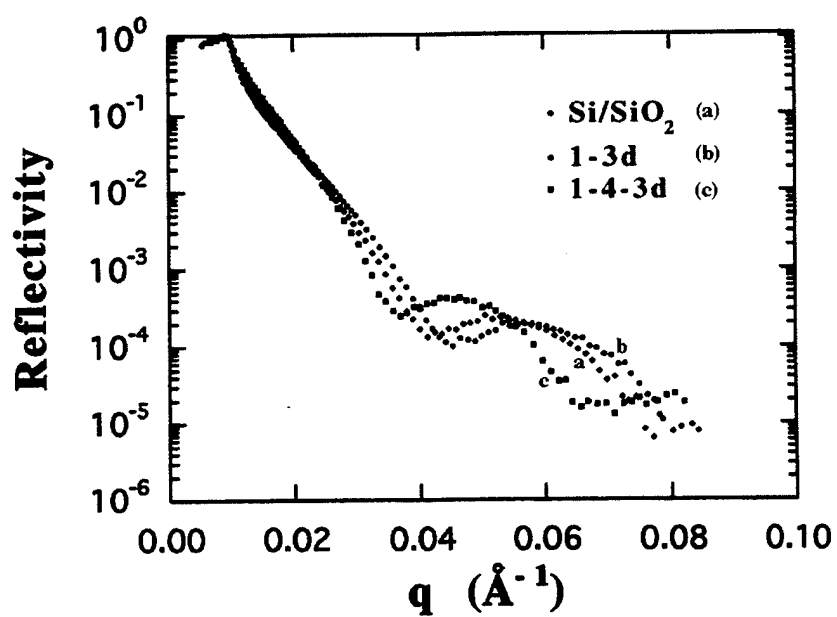
Figure 3. Neutron reflectivity data for: a) untreated silicon surface, b) diblock
copolymer **1-3d** treatment (d stands for partial deuteration of block 3),
and c) triblock copoymer **1-4-3d** treatment.
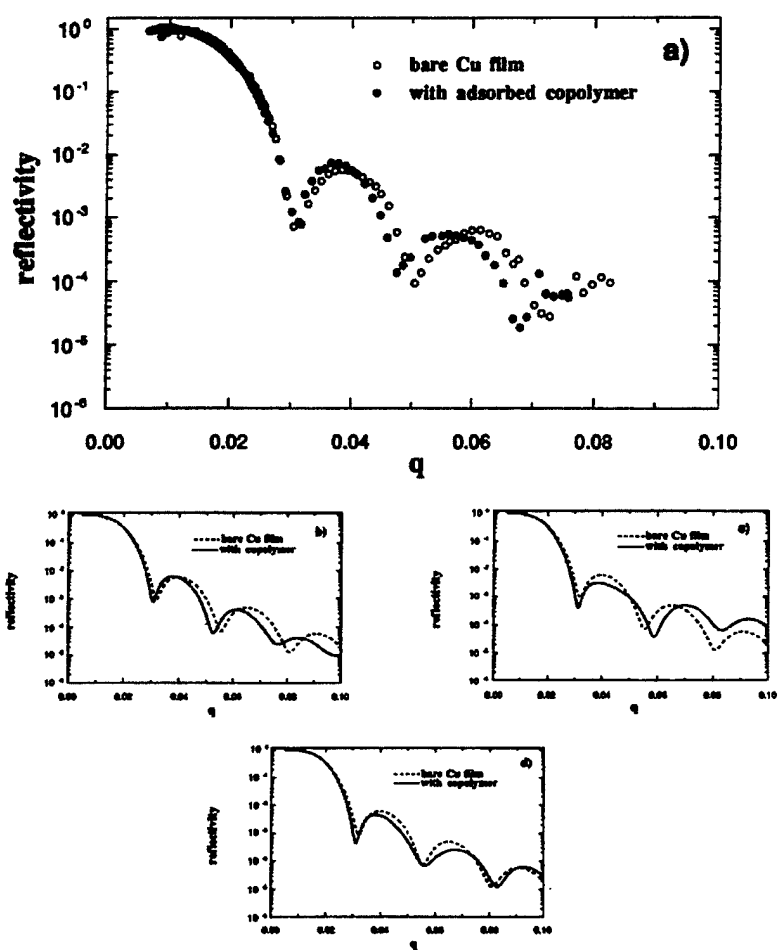
Figure 4. Neutron reflectivity for: a) actual data of adsorbed block copolymer **2-3**, b) theoretical calculation for block **2** selective adsorption onto copper, c) theoretical calculation for block **3** selective adsorbtion onto copper, and d) for blocks **2** and **3** randomly mixed as a single layer adsorbed onto copper.

strength of 1670 lb/in^2, and block copolymer treated samples had a strength of 1720 lb/in^2. This represents a 40% increase in adhesion over no treatment at all, and a comparable adhesion to that of the brown oxide treatment.

Floating roller peel tests were also conducted on copper surfaces with a cured epoxy layer. We observed that peel strengths for untreated copper were 1.55 lb/in., those for the brown oxide treatment were 8.2 lb/in., and for the diblock **2-3** treatment we obtained peel strengths of 3.09 lb/in. Thus in the case of the peel tests we were able to double the strength over untreated samples, but were not able to obtain the strength observed by the brown oxide treated samples. It is known that the brown oxdex treatment promotes a roughening of the surface, which increases the surface area significantly. If this factor is taken into account, perhaps our materials are comparable, on a per unit surface area basis, to strengths obtained from brown oxide treatments.

CONCLUSION

In this paper, we have demonstrated the ability to make diblock and triblock copolymers using a living ROMP technique, which are capable of bonding to silicon and copper surfaces depending on the functionalities. The existence of a block rather than random copolymers was substantiated by the SAXS patterns of these materials. Upon selectively deuterating one block, we were able to show by neutron reflectivity that in all cases, both on silicon surfaces and on copper surfaces, they form ordered monolayer structures. We demonstrated qualitatively that adhesion is enhanced on glass surfaces by treating them with the appropriate block copolymer. We also observed that treating copper surfaces with their appropriate block copolyemers increased both the lap-sheer yield strength, and the peel strength of these samples. Future work will include varying the number and type of reactive sites on the polymer chain to determine the effect on adhesion.

ACKNOWLEDGEMENTS

REFERENCES

1. R. H. Grubbs and W. Tumas, Science, **243**, 902 (1989).
2. R. R. Schrock, Acc. Chem. Res., **23**, 158 (1990).
3. R. R. Schrock et al, J. Am. Chem. Soc., **112**, 3875 (1990).
4. R. R. Schrock et al, Macromolecules, **24**, 4495 (1991).
5. R. R. Schrock et al, J. Am. Chem. Soc., **113**, 6899 (1991).
6. R. S. Saunders et al, Macromolecules, **25**, 2055 (1992).
7. R. S. Saunders et al, Macromolecules, **24**, 5599 (1991)(and references contained therein).

COMPOSITION-STRUCTURE-PROPERTIES RELATIONSHIP AND DURABILITY OF MODIFIED ORGANOSILICATE POLYMERIC COMPOSITE

SVETLANA V. TCHOUPPINA AND LARISA N. KRASIL`NIKOVA
Russian Academy of Sciences, Silicate Chemistry Department, Odoevsky Str., 24/2,
St.-Petersburg, 199155, Russia

ABSTRACT

The present work was aimed at the development of new organosilicate polymeric composite, based on polydimethylphenylsiloxane/polyurethane (PDMPS/PU) miscible blend, filled with silicates and metal oxides. Considerable improvement of mechanical and corrosion-protective properties due to introduction of polyurethane has been observed. Coatings with sufficient thermostability (up to 300° C) have been obtained in the case of 20% polyurethane content, related to amount of binders. The effects coating heat treatment temperature and curing conditions on adhesion of metal/composite interface have been studied. Surface energy characteristics of this coating have been obtained and were correlated with its microstructure, determined from Scanning Electron X-ray Microprobe Analyses. Recently developed composite appeared to show increased durability in atmosphere operation conditions.

INTRODUCTION

Composite based on polyorganosiloxane - silicate - oxide systems find wide-spread use in modern engineering [1-4]. As their principal and the most substantial components are polymers, having organic groups, and silicates, they are referred to as organosilicate materials or polymeric composites. Strong bonds, including chemical bonding, proved to occur between these main components during states of making [5] and heat-setting [6]. Its composition and structure afford complex of valuable technical properties for coatings, hermetics, adhesives and high-temperature resistant glassplastic binders over a wide temperature range.

Although polyorganosiloxane is one of the most widely used polymers due to its high resistance to heating, oxidation, radiation, humidity as well as for fine electric insulating characteristics and inertness to many common reagents, combining it with other polymers broadens the potential areas of polyorganosiloxane utilization even further. As is known, such a combination might be a co-condensation product, obtained by heating partially condensed polyorganosiloxane with an organic polymer that contains a considerable proportion of reactive groups, or a simple mixture. It will be noted that properties of coating based on polymeric blend are defined generally by the degree of compatibility of its components [7].

Examination of these systems is of great theoretical and practical interest because it may lead to formulation of new material receiving in accordance with rule of additiveness a new property or improved complex of known ones [8].

The present paper describes the development of new organosilicate polymeric composite with excellent adhesion to metals, bending and impact resistance as well as improved weathering resistance, based on PDMPS/PU miscible blend.

MATERIALS AND METHODS

The materials used were as follows: commercial polydimethylphenylsiloxane with 1% OH-end groups content of following formulation $\{[C_6 H_5 SiO_{1.5}]_{1.37} [(CH_3)_2 SiO]\}_n$ (KO-921) and commercial linear prepolymer based on polyether, polytetrahydrofuran, and 2,4-toluylendiisocyanate with 5.2- 6.3% isocyanate groups content (SKU-PFL). Commercial Diamet, aromatic diamine, 4,4'-methylen-bis(o-chloro-aniline), for PU component and tetrabutoxytitan for PDMPS were in use as curing agents.

Adhesion was scored on a four-point scale in accordance with GOST 15140-78 by means of grid nicks.

Bending tests were performed following the procedure described in GOST6806-73.

In order to determine impact resistance of films and coatings we used custom scientific instrument falling weight impact tester U-1 (GOST 4765-79) and samples on aluminium substrates.

Data in coating hardness were obtained by conventional method (GOST 5233-67) on pendulum device M-3.

To define polymer distribution Scanning Electron X-ray Microprobe Analyses of PDMPS/PU films were carried out with microanalyzer "Camebax" of French firm Setaram. Blend with component ratio 80:20, doped with TBT, was spread on Teflon substrate and cured at normal temperature. At least three independent measures were performed on internal and external surfaces of each sample.

Critical surface tensions were defined by Zisman's method [9]. Contact angle measurements were made on horizontal microscope. Compounds of ethyleneglicol homologous series and its solutions with surface tension less than $50 \cdot 10^3$ J/m^2 were employed as test fluids.

Corrosion resistance of coatings was defined in accordance with GOST 9.074-77 in apparatus of artificial weather (IP-1-3).

RESULTS AND DISCUSSION

Over a wide range of PDMPS/PU concentration ratios at normal temperature these blends appeared to form transparent solutions in common solvent and transparent films, deposited from these solutions; in other words, this polymeric system demonstrated kinetical stability. Rheological study proved this system to be pseudocompatible; the blend rheological properties were quite similar to those of the original polymers.

Because of original polymer properties and organosilicate composite purpose blends with dominant PDMPS content were chosen as a subject of further investigation.

Table I represents properties of polymeric films (cured under addition of tetrabutoxytitan (TBT) and heating at 120° C during 3 hours) in comparison with those for original polymers. Only 120° C was found to be enough for network structure formation of a binder controlled by means of oil-and-gasoline resistance testing.

The effect of heating at 150° C on PDMPS/PU films colour changes was observed. However, after 20-hours exposition under 200° C the adhesion of PDMPS/PU films to steel and aluminium bases was equal to original, while PU film adhesion decreased to 3-4 points. Blends with 20% content of PU showed high water-repellency and sufficient thermostability, and

Table I. Physical-mechanical Properties of Polymeric Films.

Properties	Blend composition, PU:PDMPS			
	10:90	20:80	PDMPS	PU
Adhesion, point	1	1	4	1
Bending strength, mm	20	1	20	1
Impact strength, N·cm	10	50	10	50
Contact angle , degree	90	90	90	78
Impact strength after heating at 250° C, N·cm	20	50	20	destruction at 200° C
Critical surface tension, J/m^2, $\times 10^{-3}$			21.0	22.5

improved mechanical properties, therefore, 20% PU content can be considered as the most favourable. These films were studied on Scanning Electron X-ray Microprobe Analyzer.

Silicon element content in top and bottom layers of coating appeared to be 12.7 and 9.0%, respectively, indicating nonuniformity of coating over its thickness and giving the evidence of preferable location of PU at the boundary with substrate and concurrent saturation of external layer with PDMPS. It is such structure of coating to explain increased adhesion and high water-repellency of films, based on combined binder.

Due to high sensitivity of PU even to small amounts of moisture, fillers with low moisture-keeping-ability were used for reinforcement of this polymeric matrix. New organosilicate composite, marked OS-51-PU, was compared with its analogue OS-51-03-1 (without PU) and commercial OS-51-03 (differing from OS-51-03-1 in its silicate part).

The setting of coatings was carried out at 120 °C in addition of curing agents TBT, typical for polyorganosiloxanes, and Diamet, general used for PU curing.

Differences in composition and curing conditions were reflected by coating properties and energetical level of their surface, assessed by means of Zisman's critical surface tension (γ_c). For OS-51-03-1, OS-51-PU (in presence of Diamet) OS-51-PU (in absence of Diamet) coating $\gamma_c \cdot 10^{-3}$ was equal to 37.0, 45.6, 37.1 J/m^2, respectively. Almost the same values of γ_c for OS-51-03-1 and OS-51-PU (in absence of Diamet) confirmed obtained earlier data on polymer distribution in coating matrix. Diamet dopping caused quick setting of PU interfering will the natural orientation in coating volume.

Table II represents data on polymeric composites properties.

Data have been published indicating that introduction of PU results in considerable improvement of mechanical properties, especially bending strength, without essential change in heatresistance, however,some decreasing of hardness for OS-51-PU coatings is defined primarily by the presence of PU component too .

Table II. Mechanical Properties and Heat-resistance of Polymeric Composites.

composite	curing conditions	Adhesion, point	Bending strength, mm thickness, μm 50	200	Hardness, in per unit	Heatresist-ance, °C
OS-51-03	TBT,	2	1	20	0.5	400
OS-51-03-1	120° C,	2	1	20	0.6	350
OS-51-PU	3 h	1	1	3	0.4	300
OS-51-PU	TBT, Diamet	1	-	1	0.3	300
OS-51-PU	TBT, Diamet, 120 °C, 3 h	1	-	3	0.4	300

Data presented in Table II were utilized for evaluation of quality reserve **R** in accordance with the following equation [10]:

$$R = \sum_{i=1}^{n} k_i \frac{x_{io}}{x_{imax}} \quad , (1)$$

where k_i - contribution of property "i" in comprehensive rating of coating quality (the summary of k_i equal to 1), x_{io} and x_{imax} - the actual and maximum value of property "i", respectively, and "n" is number of properties.

It is a matter of fact that property contribution is dependent on coating purpose. In atmospheric conditions operating coating is affected by several varying factors (oxidizing air, moisture, lighting, temperature, ets.) and changes in properties. According to method of expert qualimetry for atmosphere-resistant coating the contribution of each property (adhesion, hardness, flexibility) in complex quality rating is equal to 0.127, 0.042, 0.037, respectively [11]. Quality reserve evaluated in accordance with equation (1) is equal to 0.53, 0.55 and 0.86 for OS-51-03, OS-51-03-1 and OS-51-PU coating, respectively.

OS-51-PU coating also compared favourably with OS-51-03 and OS-51-03-1 coatings in corrosion- protective properties. Corrosion resistance was estimated after accelerated testings simulated atmospheric conditions of temperate climate regions by means of quantitative method of appearance rating (Fig.1). According to this method [12] all types of coating failure, causing the changes of decorative (Ad) and protective (Ap) properties during testing, relative estimation of property change degree and contribution of each type of failure to the general characteristic of coating state are considered.

150
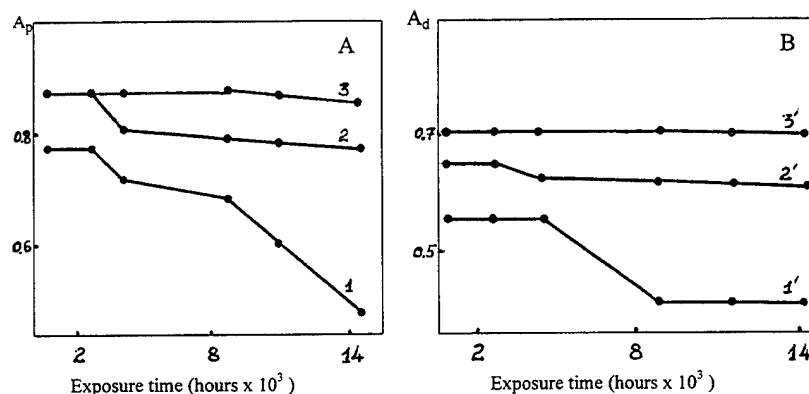
Fig.1. Changes of corrosion-protective (A) and decorative (B) properties with testing time for coatings
OS-51-03 (1 and 1'); OS-51-03-1 (2 and 2'); OS-51-PU (3 and 3')

It is seen that in the case of OS-51-PU the induction period of operation is longer than in other cases (1 year), at the time when its state changes slightly those of OS-51-03 and OS-51-03-1 change markedly, during the period of 20 months OS-51-03 coatings reach its limit while OS-51-03-1 and OS-51-PU coatings conserve their resource of operational properties.

The results show that both induction time and quality reserve increase from base OS-51-03 coating to OS-51-PU one. Long service life (no less than 5 years in tropical regions) for OS-51-03 was proved by numerous accelerated tests and long-term operation time in conditions of any climate zone [1]. The longer induction period and the higher coefficient R for OS-51-PU coating, in comparison with OS-51-03, permit to expect more prolonged durability.
Computation according to the procedure for forecasting of coating durability [13] based on data of expert qualimetry estimated this merit to be equal to 1.6.

REFERENCES

1. N.P.Kharitonov, V.A.Krotikov, V.V.Ostrovsky. Organosilikatnye compozitsii, (Nauka, Leningrad ,1980), p.91.
2. Organosilikatnye i kremniyorganicheskiey materialy v praktike stroitelnych, protivokorrosionnykh, zashitno-dekorativnykh, remontnykh i restovratsionnykh rabot, edited by V.A.Krotikov, (Znanie, Leningrad, 1991).
3. G.S.Buslaev, V.V.Sergeeva, Lakokrasochnye matherialy i ikh primeneniye, **2**, 3 (1994).
4. G.V.Belinskaya, I.B.Peshkov, N.P.Kharitonov, Zharostoikaya izolyatsiya obmotochnych provodov, (Nauka, Leningrad 1978), p.159.
5. V.A.Krotikov, N.P.Kharitonov, in Neorganicheskiye i organosilikatnye pokrytiya, edited by M.M.Shultz (Nauka, Leningrad, 1975), p.374-383.
6. V.A.Krotikov, N.P.Kharitonov, L.V.Filina, et al., Neorganicheskiye materialy, **6**, (2), 362 (1970).

7. V.E.Gul', V.N.Kuleznev. Struktura i mechanicheskiye svoistva polimerov, (Vysshaya shkola, Moskva1972).

8. W.Berger. Sitzungsber. der Acad. der Wiss. der DDR, Math.-Natur.-Techn., **15**, 5 (1982).

9. W.A.Zisman, Ind. Chem., **55**, N10, 19 (1963).

10. V.V.Verholantsev et al., Lakokrasochnye materialy i ikh primeneniye, **6**, 20 (1979).

11. K.A.Krishtoff, et al., Lakokrasochnye materialy i ikh primeneniye, **5**, 35 (1979).

12. GOST 9.407-84. Unified system of corrosion and aging protection. Paint coatings. Method of appearance rating.

13. M.I.Karyakina, N.V.Maiorova, Lakokrasochnye materialy i ikh primeneniye, **5**, 41 (1985).

Part VI

Interfaces and Composites

ENVIRONMENTAL EFFECTS ON INTERFACE BEHAVIOR IN GRAPHITE / EPOXY SINGLE FIBER COMPOSITES

LINDA S. SCHADLER, MICHAEL J. KOCZAK, AND MAHER S. AMER
Department of Materials Engineering, Drexel University, 32nd and Chestnut Sts., Philadelphia, PA 19104.

ABSTRACT

Toray M40 graphite fiber / Epon 828 epoxy resin single fiber composites with both sized and unsized fibers were exposed to distilled water at 50°C and 100°C, 10% NaOH and HCl aqueous solutions at 50°C, and air at 100°C. Micro Raman spectroscopy was used to measure the strain and interfacial shear stress profiles as a function of environmental exposure. It was found that the degradation mechanism is primarily a mechanical failure of the fiber/matrix interface.

INTRODUCTION

It is well understood that the exposure of most fiber reinforced polymer composites to aqueous environments results in a degradation in their mechanical properties[1,2]. Degradation can occur in the matrix[2], the fiber[3], or the interface / interphase region[2,4-7] (in this paper 'interface' is used to describe the fiber/matrix interface and the interphase region). The mechanisms of degradation, however, are still not clear, and before fundamental modeling of failure and prevention of degradation can occur, these mechanisms must be understood and quantified. This paper focuses on interface / interphase degradation because it is a notoriously weak link in a composite, and a deterioration of interface adhesive properties affects the off axis mechanical properties and the toughness of the composite[1,8].

Interface degradation can be the result of a several mechanisms[2-7] including a reduction in matrix elastic modulus (matrix plasticization), relaxation of compressive radial stresses, or bond failure at the interface. Bond failure can be the result of hydrolysis reactions[5] or mechanical tensile stresses at the fiber matrix interface[9]. To date there is no clear understanding of which mechanism dominates, primarily because this is matrix and fiber system dependent. In this study we demonstrate how micro Raman spectroscopy can be used to determine which degradation mechanisms prevail and prove that in the graphite / epoxy system studied, degradation is due to mechanical failure in the interface region.

EXPERIMENTAL APPROACH

Using micro Raman spectroscopy, interface degradation was observed by monitoring the interfacial shear stress distribution along the fiber as a function of environmental exposure in both single fiber composites. In the following sections, the details of composite fabrication, environmental exposure, matrix modulus determination, and the use of micro Raman spectroscopy (MRS) to measure the interfacial shear stress are outlined.

Composite Fabrication

All composites had a matrix of Shell Epon 828 cured with metaphenylene diamine m-PDA (stoichiometric ratio 14.5phr). The matrix had the following properties: a glass transition temperature of 160°C, a coefficient of thermal expansion of $50*10^{-6}$ K^{-1}, and a modulus of 3.6 GPa. The graphite fibers were Toray M40 sized and unsized with a modulus of 392 GPa, an average diameter of 6.5 μm, an average strain to failure of 0.7%, (sized) and a coefficient of thermal expansion in the axial direction of $-1.2*10^{-6}$ K^{-1}. The sizing is an epoxy compatible sizing

155

and is a pure epoxy resin.

Single fibers were placed into a dog bone shaped mold (ASTM D 1708-84) and the mold was filled with resin and curing agent. The composites were cured for 2 hours at 75°C followed by 2 hours at 125°C. The samples had a gauge length 50 mm long, 5 mm wide, and 2.5 mm thick. Single fiber composites were used to isolate the effect of the interface from fiber / fiber interaction and to control the alignment of the fibers. The effect of fiber / fiber interaction is currently under study and will be reported in a future publication.

Environmental Exposure

Composites were immersed in distilled water at 100°C and 50°C, and 10% aqueous solutions of HCl and NaOH at 50°C. The weight gain was determined as a function of time. The level of saturation was calculated by dividing the weight gain at a given time over the maximum weight gain. Samples were removed after achieving different levels of saturation, namely 25%, 50%, 75%, and 94-98%. Another set of samples was exposed to 100°C in air for 93.5 hours, the same time required to reach 94% saturation in boiling water.

In addition to composite samples, cubes of matrix were placed in the 4 environments and the matrix volumetric strain and weight gain were recorded. The following summarizes those results: 1) in 100°C boiling water, the weight gain was linear with the square root of time and eventually reached a plateau at 3.28%, 2) in 50°C distilled water, two stage absorption behavior was observed and the maximum weight gain was 3.05%, 3) the aqueous solutions of HCl and NaOH caused a weight gain of 3.1% and 2.44% respectively.

Matrix Modulus Determination

The modulus of the matrix was tested both before and after environmental exposure using dynamic mechanical analysis (DMA) and tensile testing. The DMA parameters were a heating rate of 5°C per minute and a frequency of 1 Hz under nitrogen atmosphere. The tensile tests were run at a strain rate of .25%/min. -

Strain Profiles and Interfacial Shear Stress Measurements

The Raman effect is inelastic scattering of visible light. Monochromatic light is used to excite the sample to a virtual excited state (Figure 1). If the sample drops from the excited state into a normal vibrational mode, the resulting scattered light has lower energy than the incident light. In addition, the sample may start from an excited vibration mode and drop into the ground state and the resulting scattered light has higher energy than the incident light. These are called Stokes and anti-Stokes scattering respectively. When strain is applied to a crystalline sample, the interatomic distance changes, and thus the vibrational frequency of some of the normal modes change. This results in a shift in the Raman peak position (Raman frequency) with applied strain (Figure 1). In tension and slight compression, there is a linear relationship between the Raman peak shift and the applied strain. The slope of this line is the Raman Frequency Gage Factor - RFGF. Once the RFGF is known, an unknown strain in an embedded fiber can be calculated using equation 1 where ε_i is the strain, v_0 is the Raman peak position at zero strain, and v_i is the Raman peak position observed.

$$\varepsilon_i = (v_i - v_0) / RFGF \qquad [1]$$

The measurements were taken with an ISA Raman microprobe with a notch filter and a Jobin Yvon HR 640 spectrometer attached to a modified Olympus microscope. An argon ion laser (the 514.5 nm line) was used and the power at the sample was 2mW. A low power was used to prevent local heating effects. The spectra were recorded with a charge coupled device interfaced with a PC for data storage and manipulation.

Monochromatic light Elastic + inelastic Scattering

ν_e

ν_0

Energy

$\nu_e = \nu_0$ Rayleigh Scattering

$\nu_e = \nu_0 \pm \omega$ Stokes scattering

anti-Stokes scattering

} vibrational levels

E_0

(a)

Raman Peak Position
Wave numbers (cm^{-1})

Slope = 10.4

1584
1582
1580
1578
1576
1574

0 0.1 0.2 0.3 0.4 0.5 0.6 0.7 0.8
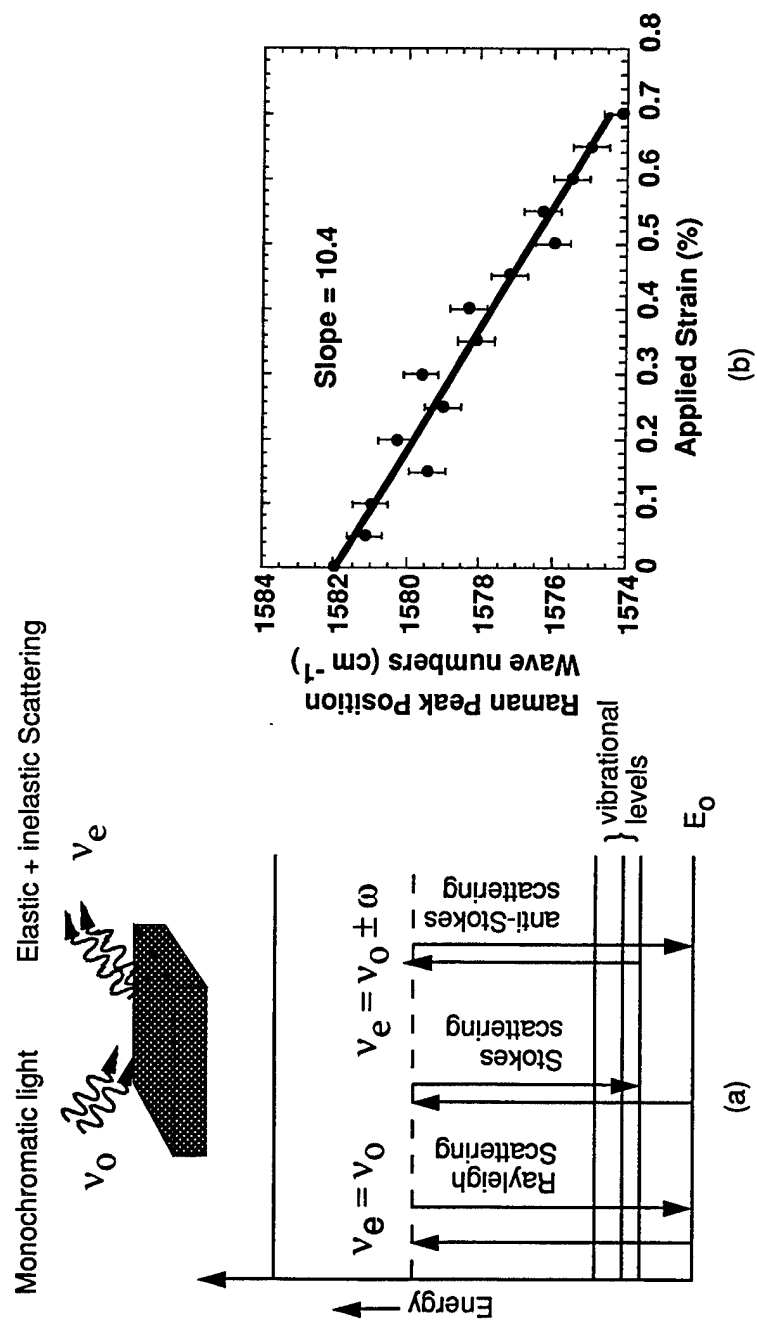
Applied Strain (%)

(b)

Figure 1. A schematic showing (a) the Raman effect and (b) the shift in the Raman peak position with applied strain.

Fibers were calibrated in air and the Raman peak shift as a function of known applied strain determined. A single fiber 10 cm long was placed in a small loading device capable of $1 \mu m$ resolution in the linear deformation (a resolution of .01% in the applied strain). For Toray M40 fibers, the peak assigned to the E_{2g} mode shifts -10.4 cm^{-1}/% strain, and the second order A_{1g} peak shifts 25.14 cm^{-1}/% strain. The maximum error in determining the peak position was found to be $\pm$ 0.5cm-1 which is a error in the strain of ± 0.04%.

Tensile tests were conducted on unexposed and exposed composite dog bone samples. The composites were loaded incrementally, and the strain in the fiber scanned at several applied strain levels. In addition, the residual strain due to fabrication and subsequent exposure was recorded. From the strain profiles, the shear stress, τ, can be calculated using a force equilibrium in the fiber axial direction[11].

$$\tau_i = E * (D/4) * (d\varepsilon_i / dx) \qquad [2]$$

where $d\varepsilon/dx$ is the change in strain with distance along the fiber, D is the fiber diameter, and E is the fiber modulus. The change in strain with distance, $d\varepsilon/dx$, was determined by fitting a curve through the strain points using a locally weighted least square error fitting routine and taking the derivative of the resulting curve. The maximum error in the shear stress determined from the accumulated errors is ± 5 MPa.

From the interfacial shear stress (ISS) profiles, the stress transfer mechanism can be determined. For example, if the interfacial shear stress is highest at the fiber end and constantly decreasing to zero in the fiber middle, this is classic Cox model loading and indicative of an ideal interface[10]. If the interfacial shear stress is close to the matrix yield stress near the fiber end and is constant for some distance along the fiber length, this is indicative of matrix yielding limiting the stress transfer behavior[12]. If the interfacial shear stress is constant near the fiber end but a low value, this is indicative of a frictional stress transfer mechanism[12]. These three types of loading are illustrated in Figure 2.

The strain profiles and interfacial shear stress were determined for as-prepared, hydrothermal, and thermally exposed samples at various levels of saturation. The term maximum ISS is defined as the maximum ISS observed at any applied strain level averaged over all the fiber fragments tested.

RESULTS AND DISCUSSION

Residual Strain

The residual strain due to fabrication and environmental exposure was measured by observing the Raman frequency of the embedded fiber before applying external loading to the composite. This was compared to a fiber in air with zero applied strain. The residual strains are a summation of the compression strains during curing, compressive strains during cooling due to the differences in coefficient of thermal expansion, tensile strains due to matrix swelling[13], and any strain relaxation that occurs at elevated temperature. It should be noted that axial strains measured which are the result of a volumetric strain such as differences in CTE and/or matrix swelling are indicative of radial strains of the same sign[9]. Therefore a tensile residual axial strain implies a tensile radial strain.

The residual strain due to fabrication in the as-prepared sized fiber composite was -0.15% strain and -0.2% in the unsized composites. These strains are the result of cooling from 125°C to room temperature. Adsorption of the various environmental media and the resulting matrix swelling caused the axial residual strains in the fiber to increase during exposure. The residual strains as a function of matrix weight gain (degree of saturation) are shown in Figure 3. All

$$\sigma \pi r^2 + 2\pi r \ \tau \delta x = (\sigma + \delta\sigma)\pi r^2$$

$$\tau = E \frac{r}{2} (\delta e / \delta x)$$
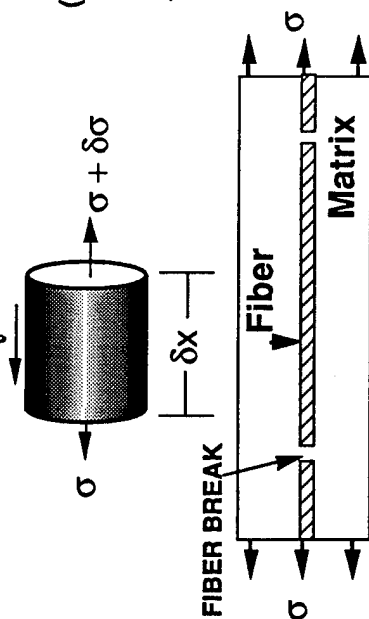
(a)

(b) Perfect Bonding -Shear Lag Model
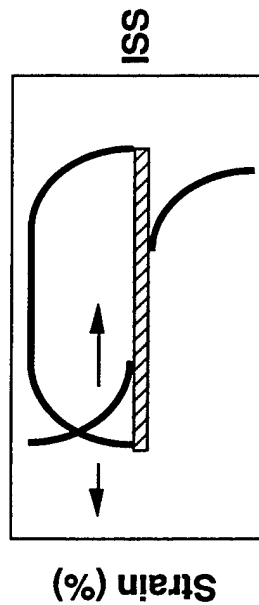
(c) Stress Transfer Limited by Matrix Yield Strength
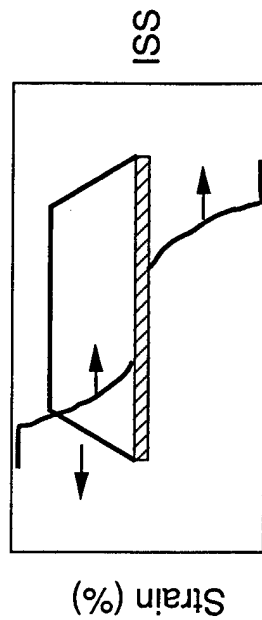
(d) Frictional Stress Transfer Mechanism

Figure 2. A schematic showing (a) the force equilibrium between fiber strain and ISS and (b - d) three types of stress transfer mechanisms.

159

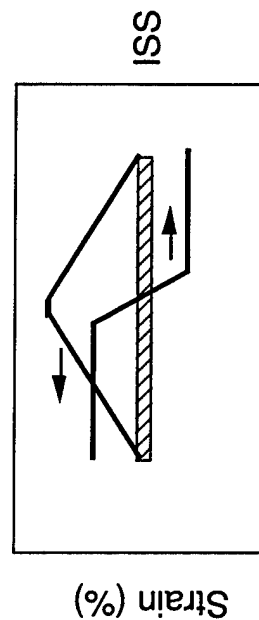measurements were taken at room temperature. The fiber residual strain in samples exposed to 50°C distilled water increased up to 0.5%. Samples exposed to boiling water showed only a +0.1% strain at 94% saturation. This low value is probably the result of strain relaxation that took place during exposure. As the matrix swelled and placed the fiber in tension, the temperature was close enough to the glass transition temperature to allow the strains to relax. Hence, the composites exposed to boiling water had relaxed to a lower strain during exposure than the composites exposed to 50°C. This resulted in a lower strain upon cooling. Thus, the exact strain induced during exposure is unknown.

Clear evidence that the fiber experienced strains higher than 0.7% (the failure strain of the fiber) during exposure to boiling water is that the fiber failed during exposure to saturation levels of 50% or greater. This was observed for all environments at saturation levels of 50% or greater.

In 10% aqueous solutions of HCl and NaOH, the maximum residual strain was about 0.25% (Figure 3) but shows a trend similar to the samples exposed to 50°C distilled water. The lower residual strains are the result of lower matrix swelling during exposure.
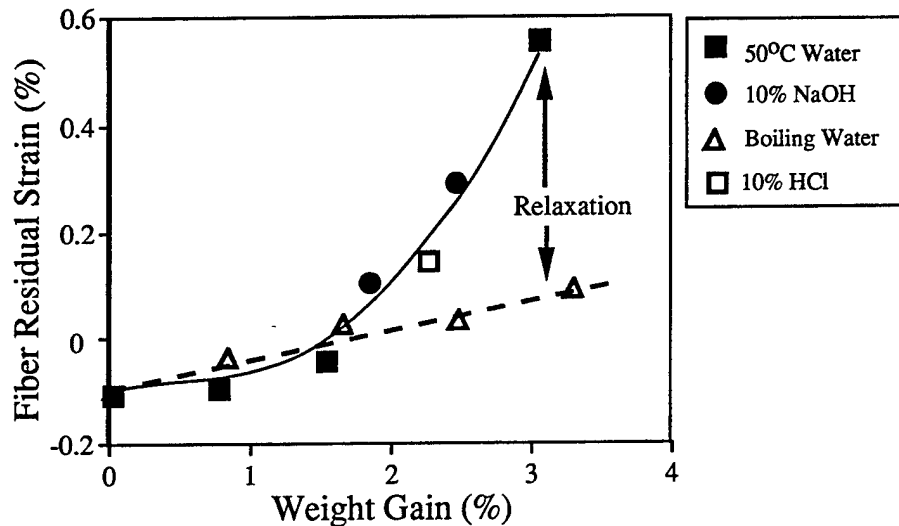
Figure 3.   Axial residual strain in the fibers as the result of weight gain during exposure to various aqueous environments. The arrow indicates, the relaxation that probably occurred during exposure for the samples exposed to boiling water.

Strain Profiles and Interfacial Shear Stress in Unexposed Composites

During the tensile test on the unexposed composite with sized fibers, the first fiber fragmentation was observed at 0.8% applied strain. This is consistent with a nominal strain to failure of 0.7% plus the -0.15% residual strain in the fiber. The fiber strain profile at this applied strain level is shown in Figure 4a. Note that because this is a long fragment, only half of the fragment is shown. The fiber strain builds from zero at the fiber end to a strain equal to the matrix strain and eventually stabilizes. At this strain level, the ISS profiles for most of the fragments show a plateau between 35 and 40 MPa which was the maximum ISS observed for all strain levels. This high and constant ISS value is indicative of stress transfer limited by the matrix yield stress[12]. At 1.0% applied strain interfacial failure occurred near the fiber end as indicated by the

lower (20 MPa) but constant ISS value.

In the unsized fiber composites, the fibers failed at 1.2% strain. Given the residual strain of -0.2%, this is a nominal failure strain of 1.0% which is significantly higher than the sized fibers. The strain profile and ISS at 1.2% applied strain are shown in Figure 4b. Notice that the maximum ISS is almost 40 MPa and is constant near the fiber end for about 100μm. This is very similar to the composite with sized fibers indicating that the sizing had little effect on the ISS profile. Behavior similar to the sized fiber composites is also observed at higher applied strain levels.

The similarity in behavior of the sized and unsized fibers is somewhat surprising. Although the main purpose of sizing is to protect the fiber, it has also been known to increase the interfacial shear stress because of the improved wetting between matrix and fiber and thus improved bonding during curing. In this system, the maximum ISS is not affected by the sizing. It has been suggested that this is because in both cases, the maximum ISS is limited by the shear strength of the fibers' outer layers. This matter is under investigation, but preliminary results show that interface failure occurred in the matrix region.

Strain and Interfacial Shear Stress Profiles for the Exposed Composites

Figure 5 shows a comparison of the ISS at 0.8% for the composites exposed to boiling water up to 95% of saturation for both the sized and unsized fibers. The results for the two fiber systems are similar: fiber failure occurred during exposure, the maximum ISS dropped to 20 MPa, and the ISS is still constant near the fiber end. This low but constant ISS is indicative of a frictional stress transfer mechanism, implying that the interface bond failed[12]. The mechanism of failure/degradation is discussed in the next section.

Only sized fiber composites were placed in 50°C 10% aqueous solutions of NaOH and HCl and distilled water. Table I shows the maximum ISS as a function of saturation for all the samples tested including exposure to 100°C air for the same amount of time it took to reach 95% of saturation in water. The maximum ISS only dropped to 30 MPa for these two environments. Note also that the matrix strain and fiber residual strain at saturation are lower in both these systems compared to composites exposed to 50°C water. .

Mechanism of Degradation

The mechanism of degradation observed in this composite system could be due to matrix plasticization, chemical bond failure, or mechanical bond failure. Matrix plasticization reduces the matrix modulus which would reduce the interfacial shear stress according to the shear lag model[10]. In order to measure any change in matrix modulus due to exposure both tensile tests and dynamic mechanical analysis was performed on the pure matrix. The DMA results (Figure 6) show that there is no significant decrease in the modulus (although a decrease in glass transition temperature was observed). The modulus obtained from tensile tests also did not change. It could be argued, however, that the matrix in the region near the interface has somewhat different starting properties and a different response to environmental exposure than the bulk matrix. Thus macroscopic testing does not suffice to rule out plasticization. The observation that both the sized and unsized fiber composites behaved the same, however, is strong supporting evidence that matrix plasticization is not the cause of the reduction in interfacial shear stress. If matrix plasticization were the cause of the reduction in ISS, then the sized and unsized fibers which have different curing agent to resin ratios should have responded differently to hydrothermal exposure as documented by Drzal et al.[2].

Therefore the degradation mechanism is either chemical or mechanical interface failure. Chemical bond failure would be the result of hydrolysis and should depend on the temperature of exposure as well as the pH of the solution. The temperature did not affect the degradation in ISS and both an acidic and alkaline aqueous solution reduced the amount of degradation. This implies that chemical degradation is not a primary degradation mechanism. The most compelling evidence is for mechanical degradation of the interface. Figure 7 shows the maximum ISS vs. the matrix swelling strain. All the samples, sized and unsized and for each exposure condition, fit on the
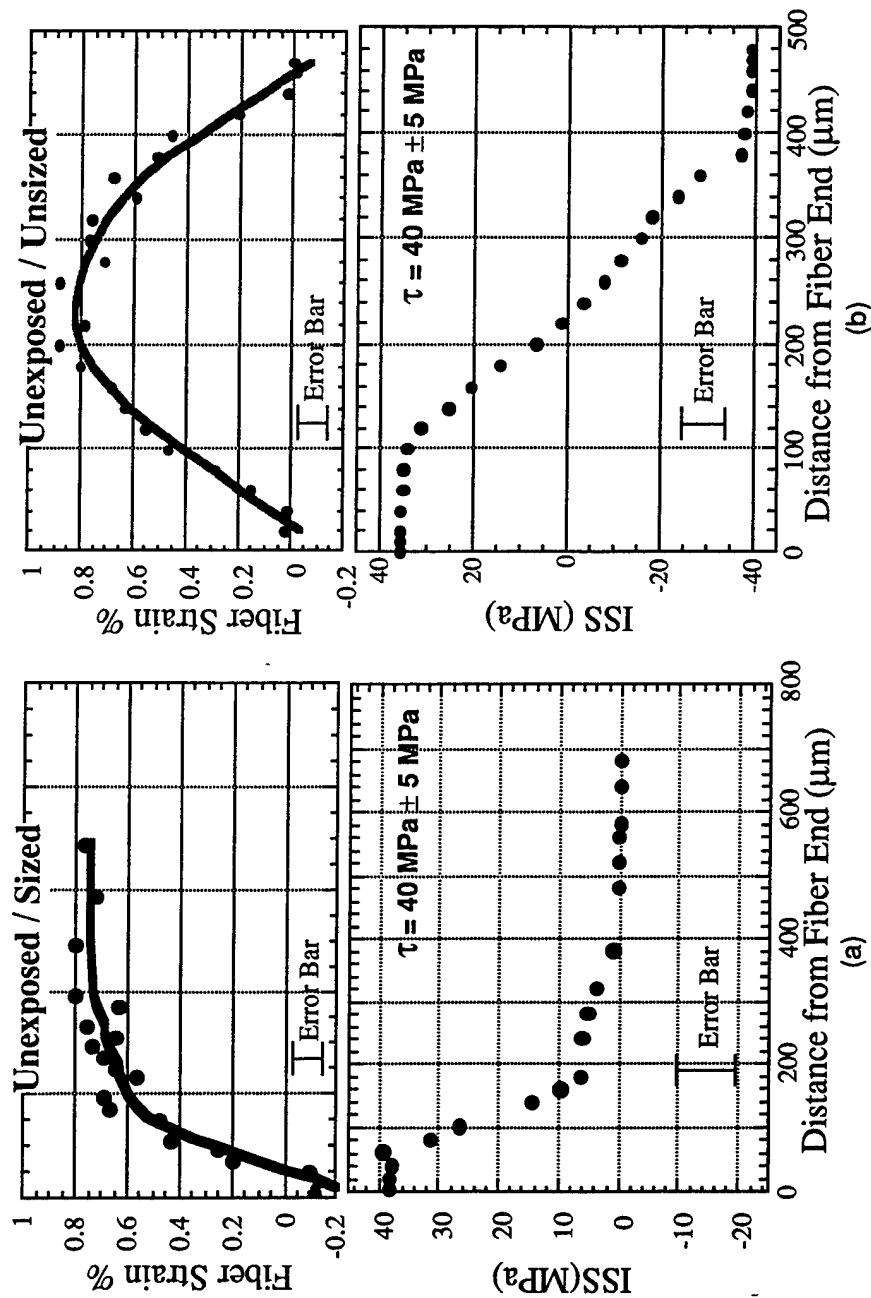
Figure 4. Strain and interfacial shear stress profiles for unexposed single fiber composites, (a) sized fibers, and (b) unsized fibers.
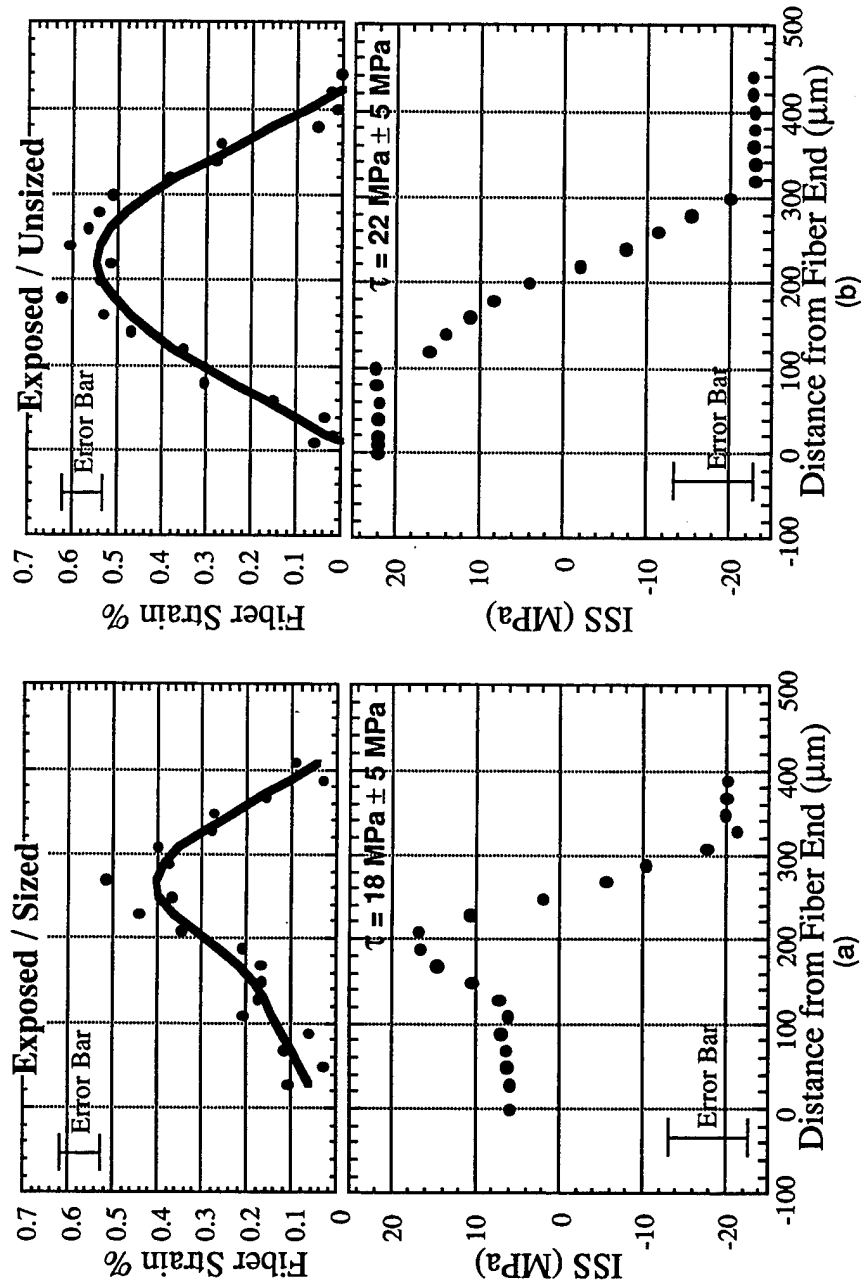
162

Figure 5. Strain and interfacial shear stress profiles for single fiber composites exposed to boiling water up to 94% of saturation, (a) sized fibers, and (b) unsized fibers.

same curve. This strongly implies that interface degradation occurs when the radial strain in the interface due to matrix swelling is large enough during exposure to cause failure of the interfacial bonds. This results in the frictional stress transfer mechanism (a low but constant ISS) observed after exposure.

A second possibility is that the radial tensile strain causes an apparent reduction in the maximum ISS because the residual strain reduces the shear stress necessary to cause yielding. This would explain the slow reduction in the maximum ISS from 40 MPa to 30 MPa as a function of matrix strain. The pressure dependence (or normal stress dependence) of the yield stress is well established[14], and in addition, using a von Mises type criterion, a radial tensile strain would reduce the shear stress required to cause yielding[14]. This hypothesis is under investigation.

The discrepancy in the literature about which degradation mechanism predominates[2-7] may depend on the kinetics of chemical vs. mechanical degradation. In addition, the mechanism of matrix plasticization versus a mechanical failure of the bonds is also system dependent. Clearly some matrices are more susceptible to matrix plasticization than others[2,6].

Table I. Summary of weight gain, matrix strain, fiber residual strain, and interfacial shear stress (ISS) for samples tested under a variety of environmental conditions.

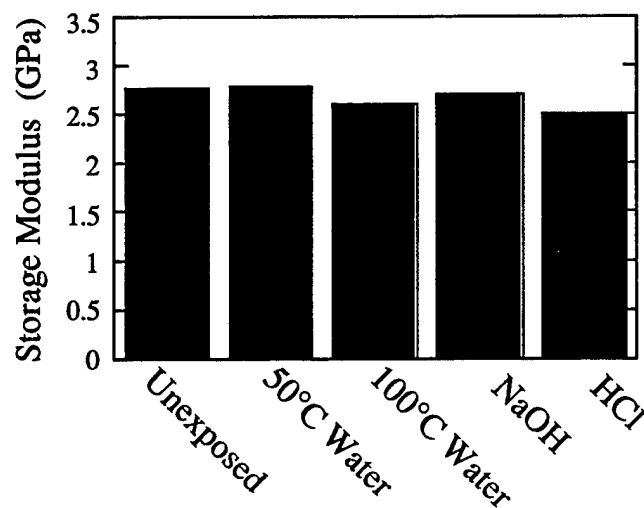| Exposure Condition	Weight Gain (%)	Degree of Saturation	Matrix Strain (%) ± 0.1%	Fiber Residual Strain (%) ± 0.05%	Maximum ISS (MPa) ±5MPa
Unexposed	0	0	0	-0.1	40.0
Boiling Water Sized Fibers	0.87	.25	0.2	-0.03	40.3
"	1.74	.5	0.43	0.03	30.3
"	2.61	.75	0.65	0.04	28.2
"	3.28	.94	0.86	0.1	20.8
Boiling Water Unsized Fiber	3.3	.95	0.87	.1	21.1
50°C Water Sized Fibers	.75	.24	0.15	-0.09	38.5
"	1.52	.49	0.32	-0.04	37.3
"	2.28	.74	0.5		33.2
"	3.04	.98	0.94	0.56	21.4
10% NaOH Sized Fibers	1.83		0.45	0.11	37
"	2.44		0.64	0.3	30
10% HCl Sized Fibers	3.1		.73	0.2	30
100°C Air				-0.35	38

Figure 6.   The storage modulus obtained using dynamic mechanical analysis for Epon 828 m-PDA cured epoxy resin as a function of exposure to aqueous environments. All samples were tested after achieving 95% or greater degree of saturation.
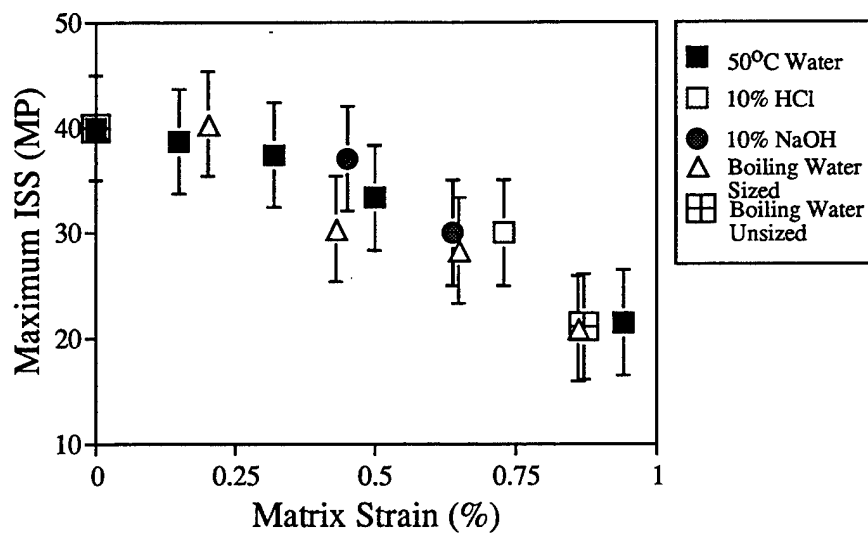

Figure 7.   The maximum interfacial shear stress vs. matrix swelling strain due to exposure to several aqueous environments.

Application to Bulk Composites

The axial and radial tension in the fiber interface region due to matrix swelling is strongly affected by the volume fraction of fibers. At some point the matrix swelling will cause radial compressive strains instead of tensile strains at the interface because of the constraint of neighboring fibers[9]. This will suppress the mechanical degradation mechanism. It is well documented, however, that there is an inhomogeneous distribution of fibers in a composite and that in joints and corners where there is a low volume fraction of fibers, the current degradation mechanism will apply. Therefore, this single fiber work is relevant to bulk composite failure in regions with a high volume fraction of resin. The volume fraction at which the radial strains will become compressive instead of tensile is under investigation.

CONCLUSIONS

1. The sizing on Toray M40 fibers does not significantly affect the maximum interfacial shear stress or the mechanism of degradation in boiling water.
2. The mechanism of degradation in Toray M40 / Epon 828 - mPDA cured matrix composites is primarily mechanical failure of the interface due to matrix swelling. This was proved by showing that matrix plasticization did not occur and that the degradation was independent of the pH of solution and the temperature of the environment. Degradation depended strongly on the matrix swelling strain.
3. The presence of HCl and NaOH decreases the matrix swelling of the matrix by about 25%. This reduces the amount of interfacial degradation.

ACKNOWLEDGMENTS

REFERENCES

1. G.S. Springer, Environmental Effects on Composite Materials Vol. II., edited by G.S. Springer (Technomic Publishing, Lancaster, PA, 1984), chapter 1.
2. L.T. Drzal, M. J. Rich, M. F. Koenig, J. Adhesion, 18, 49 (1985).
3. C. Lhyman and J.M. Schultz, J. Mater. Sci., 18, 29 (1979).
4. D.A. Biro, G. Pleizier, Y. Deslandes, Comp. Sci. Tech., 46, 293 (1993).
5. U. Guar, B. Miller, Polymer Composites, 11, 217 (1990).
6. M.S. Amer, M.J. Koczak, C. Galiotis, L. S. Schadler, Adv. Comp. Lett. 3, 17 (1994)
7. D.H. Kaelble, P.J. Dynes, L. Maus, J. Adhesion, 8, 121 (1976).
8. I.M. Daniel, G. Yaniv, G. Peimanidis, J. Engineering Materials and Technology, 110 169 (1988).
9. F.W. Crossman, R.E. Mauri, W.J. Warren in Advanced Composite Materials Environmental Effects, ASTM STP 658, edited by J. Vinson (American Society for Testing and Materials, Philadelphia, PA, 1978) pp.205-220.
10. H.L. Cox, Brit. J. Appl. Phys., 3, 72 (1952).
11. N. Melanitis, C. Galiotis, P.L. Tetlow, C.K.L. Davies, J. Comp. Mat. 26, 574 (1992).
12. L. Dilandro, A.T. Dibenedetto, J. Groeger, Poly. Comp., 9, 209 (1988).
13. H.T. Hahn, J. Comp. Mat. 10, 266 (1976).
14. I.M. Ward and D.W. Hadley, An Introduction to the Mechanical Properties of Solid Polymers, (John Wiley and Sons, New York, 1993), pp.214-244.

INTERACTIONS OF PHENOL RESIN PRECURSOR
AND CALCIUM ALUMINATES

MASAKI HASEGAWA*, G. K. DINILPREM PUSHPALAL*, TOMONORI TAKATA*,
NAOMI MAEDA** AND TADASHI KOBAYASHI**
  *Toin University of Yokohama, Department of Materials Science and Technology, Yokohama,
  Japan
**Maeta Concrete Industry Ltd., Central Research Laboratory, Yamagata, Sakata, Japan

ABSTRACT

Here we investigated the interactions of phenol resin precursor and calcium aluminates, in relation to a recently innovated cement based material having a high flexural strength of more than 120MPa. An anhydrous phenol resin precursor was used as the binder and water was not contained in the initial composition.

The method of processing consists of mixing of the cement, the phenol resin precursor, and small amounts of N-methoxymethyl 6-nylon and glycerol under high shear. Addition of the 6-nylon and glycerol was necessary to produce viscoelastic cement paste through a twin roll mill. Setting of calendered sheets takes place during the heat curing at 200°C.

The best combination for high flexural strength among all the cements tested is the mixture of calcium aluminate cement and the resole type of phenol resin. Resulting outstanding affinity suggested specific interactions between the phenol resin and calcium aluminate.

We here propose the interaction evidence of phenol moiety-calcium aluminate, based on the experimental data of differential scanning calorimetry and conduction calorimetry.

INTRODUCTION

It has been well-established that cement hardened in the presence of sufficient amount of water can be used to form architectural cement materials. Ordinary hardened cement material, however, shows flexural strength of less than 20MPa, and therefore, enhancement of the flexural strength of the cement has been a long standing problem in the field of cement technology.

Recently we innovated a new type of composite material which consists of phenol resin and calcium aluminate cement and which shows excellent flexural strength (>120MPa).

The flexural strength of the innovated material is unusually high, compared to ordinary cement based materials and even to various types of polymer cement composites. The combination of resole type phenol resin and calcium aluminate cement display unique properties relative to several phenol/powder combinations attempted. Based on these observations, we have assumed certain specific interactions between the phenol resin and calcium aluminate cement to occur during hardening. Of further interest is that the present composite material is fabricated by an essentially anhydrous compositions. The necessary water for hardening is furnished by the precursor during thermal curing between 130°C-170°C, which we considered as the fundamental principle on which the innovation rests [1] [2] [3]. The main purpose of the present report is to discuss the specific affinity between calcium aluminate and phenol moiety.

EXPERIMENTAL DETAILS

Materials

Calcium aluminate cement (r.d. 3.01) used is mainly composed of 54.3wt% Al_2O_3, 37.0wt% CaO, 4.5wt% SiO_2 and 1.5wt% Fe_2O_3 (here after this cement is abbreviated as CAC). The main mineral constituent of CAC is monocalcium aluminate (CA), but CA_2, $C_{12}A_7$, C_2AS and αAl_2O_3 have also been identified by X-ray diffraction.

For differential scanning calorimetry analyses, pure monocalcium aluminate (CA) was also used to identify the most favorable mineralogical component of CAC. The pure CA was prepared by reacting equimolar amounts of $CaCO_3$ and Al_2O_3 powder at 1450°C.

To confirm the affinity between CAC and phenol resin, ordinary portland cement, alumina and silica powder were also used. Ordinary portland cement (r.d. 3.16) is mainly composed of 5.3wt% Al_2O_3, 64.4wt% CaO, 22.0wt% SiO_2 and 3.0wt% Fe_2O_3 (here after this cement is abbreviated as OPC). Alumina powder (r.d. 3.95) contains 99.6wt% Al_2O_3. Silica powder (r.d. 2.63) contains 92.0wt% SiO_2 and 6.0wt% Al_2O_3.

Commercially available resole type phenol resin precursor was used as the main binder. The precursor is essentially anhydrous and soluble in methanol, and contains 58.0wt% of nonvolatile matter. Specific gravity is 1.06 and viscosity is 250cps.

N-methoxymethyl 6-nylon was incorporated to modify the phenol resin and to develop the plasticity of the paste. Glycerol was used as a plasticizer.

Methods

General method of preparing specimens is nearly equal to the technology of macro-defect free cement developed by Birchall and coworkers [4] at Imperial Chemical Industries in the early 1980's. Powder-resin paste was mixed under high shear and calendered through a twin roll mill to obtain the flexible sheets. The calendered sheets were allowed to cure at 200°C for 18 hours. The mix proportions are given in Table I.

Table I. Mix proportions.

Mix No.	Cement, compound	Phenol resin precursor+ modifier content (vol %)	Mix proportions by weight						
			Solid substances				Methanol solution of phenol resin precursor	Modifier (N-methoxymethyl 6-nylon)	Plasticizer (glycerol)
			CAC	OPC	Al_2O_3	SiO_2			
1	CAC	42.4	100				24.07	1.93	2.60
2	OPC	42.4		105			24.07	1.93	2.60
3	Al_2O_3	42.4			131		24.07	1.93	2.60
4	SiO_2	42.4				87	24.07	1.93	2.60

The cured sheets were tested for flexural strength. The specimen size was 25 mm wide, 200 mm long and 2mm thick. Half of each specimen was subjected to a three point bend test in which the span-depth ratio was 40. The remaining part of each specimen was placed in water at 20°C. After 7 days immersion in water, the flexural strength was again measured in the same manner.

Differential Scanning Calorimetry (DSC) analyses were made on several powders (CAC, CA, Al_2O_3, SiO_2) +phenol resin combinations to understand their interactions during hardening. Each powder was mixed with phenol resin in resin-powder ratio of 0.5, then the paste was vacuum dried at 30°C for 24 h. The resulting lumps were ground and pressed into an aluminum crucible. The DSC analyses were carried out on about 10 mg of the sample at a heating rate of 10°C per minute.

The influence of phenol resin on the normal hydration of cement was studied by conduction calorimetry as described by Rodger *et al.* [5]. CAC, CAC-resin composite (Mix No.1) and SiO_2-resin composite (Mix No.4) were analyzed. Both CAC-resin and SiO_2-resin composites were ground and sieved to a size of less than 53 μm, and then used in calorimetry. After mixing the powder and water, the heat evolution curves were recorded at 20°C using a conduction calorimeter. The water-powder ratio was 0.5.

RESULTS AND DISCUSSION

Influence of Basic Components on Strength and Water Resistivity

Fig. 1 shows the original flexural strength and residual strength after 7-day water immersion. The original flexural strengths of non-cement based specimens are half of the CAC based specimen, although the total porosity and maximum pore size of the microstructure are found to decrease [6]. The flexural strength of the CAC based specimen is higher than that of the OPC based specimen. After 7 days in water, the flexural strength of both non-cement based specimens decreases by about 60%, while CAC based specimen increases by 9%.

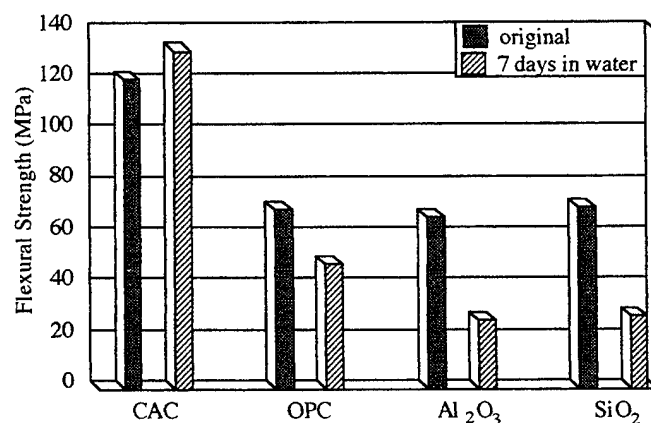Fig. 1. Original flexural strength and residual strength after 7-day water immersion.

In the OPC based specimen, the reduction of flexural strength appears after water immersion, but the loss in strength is only 30%.

The most striking feature of above result is its water resistivity depending on the base material. Thus, it is easily inferred that the water resistivity is not an individual property of

hardened resin itself. It is supposed that the phenol resin and cement have mutual influence and affinity related to their bond properties. There are two hypotheses to account for strength loss of the non-cement based specimens. These may be summarized as follows:

1. The interparticle bond strength of the non-cement based material is less than that of the cement based composite due to the absence of a strong interphase region [6]. Thus, the mechanical breaking of weak van der Waals bonds occurs, in the same manner of low fired clay bricks when water ingresses into the structure.

2. The system of the non-cement based material exists in an unstable state because the organic-inorganic interaction does not occur.

Differential Scanning Calorimetry Analyses

Generally, the hardening of the phenol resin precursor used here takes place at 130 - 170°C by the reaction of methylene bridge formation. Thus, thermal analyses would give more insight as to the mutual influence of phenol resin and cement: that is, the system is measured as a function of temperature.
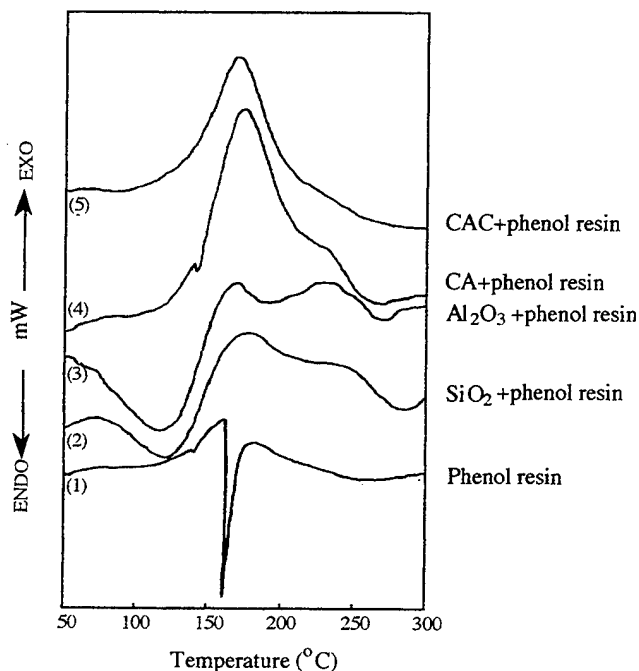

Fig. 2. DSC thermograms.

Curve 1 in Fig. 2 shows a DSC thermogram of the phenol resin precursor. The sharp endothermic peak around 162°C is seen, corresponding to a hardening reaction of the resin. In

170

the case of CAC+phenol resin (curve 5), an endothermic peak is not seen and may be overlapped by a large broad exothermic peak around 171°C. Curve 4 of CA+phenol resin is essentially the same as curve 5. This indicates that CA is the component of the cement which seems to be responsible for any possible interactions. On the other hand, in the cases of SiO_2 and Al_2O_3 (curves 2 and 3) which are inert fillers, neither a sharp endothermic peak nor broad exothermic peak is seen. The difference between these peaks seems to depend on the stabilization in each system. From the above results, it is suggested that there is an interaction between calcium aluminate and phenol resin.

Conduction Calorimetry

Fig. 3 shows the integral heat evolution curves obtained from a hydrating mix of CAC, CAC-resin composite (Mix No.1) and SiO_2-resin composite (Mix No.4). The curve of CAC shows a sharp increase in the amount of heat evolution at about 15 hours, thus indicating the heat of hydration. The presence of phenol resin in CAC results in lack of such a sharp increase, however the amount of heat evolved increases gradually as the time proceeds. In case of SiO_2-resin composite, the amount of heat evolved remains nearly constant up to the test termination at 168 hours.
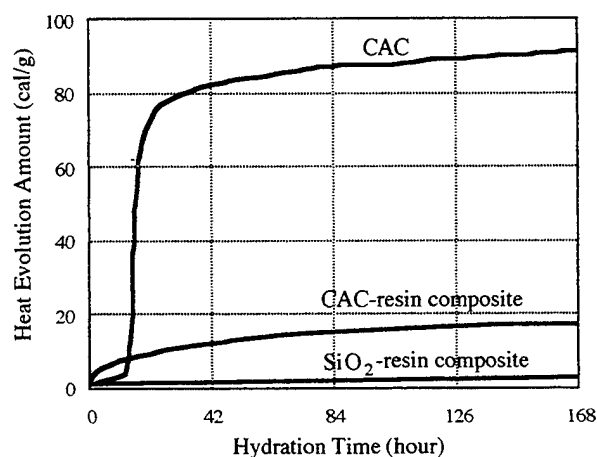
Fig. 3. Integral heat evolution curves for CAC, CAC-resin composite
and SiO_2-resin composite.

These results suggest that CAC becomes less sensitive to water in the presence of phenol resin. This may be due to the following reasons.
1. The presence of phenol resin retards cement hydration as described by Vipulanandan and Krishnan for water soluble phenol [7] or the hydration ability of cement is overtaken by the phenol resin.
2. A hard phenol resin layer which may exist around the cement particles obstructs the water ingress into the cement particles, thereby preventing the cement hydration.

CONCLUSIONS

The knowledge gained from this work suggests that the resole type phenol and calcium aluminate interact to make a strong composite with high water resistivity. Differential scanning calorimetry shows difference in hardening between calcium aluminate and inert fillers. The large exothermic peaks in both calcium aluminate and calcium aluminate cement confirmed the stabilization of the calcium aluminate-phenol system. In contrast, high water resistivity is only given by calcium aluminate cement-phenol composite. Thus, it appears that the development of a strong bond by interactions is essential for durability. However, this study indicates that further investigation should be carried out to understand the reactions during setting of the composite.

ACKNOWLEDGMENTS

REFERENCES

1) T. Kobayashi, G.K.D. Pushpalal, M. Hasegawa, Japanese Patent Application No. JP 301514 / 92 to Maeta Concrete Industry Ltd., Japan (1992).
2) T. Kobayashi, G.K.D. Pushpalal, M. Hasegawa, European Patent Application No. 93307706 to Maeta Concrete Industry Ltd., Japan (1993).
3) T. Kobayashi, G.K.D. Pushpalal, M. Hasegawa, U. S. Patent Application No. 93307706 to Maeta Concrete Industry Ltd., Japan (1993).
4) J.D. Birchall, A.J. Howard, K. Kendall, "Cement Composition and Product," U. S. Patent No. 4410366 (1983).
5) S. A. Rodger, S. A. Brooks, W. Sinclair, G. W. Groves, D. D. Double, Journal of Material Science 20, 2853 (1985).
6) G.K.D. Pushpalal, N. Maeda, T. Kawano, T. Kobayashi, M. Hasegawa, T. Takata, Properties and Flexural Failure Mechanism of a High Strength Phenol Resin-Cement Composite, Submitted to 8th International Congress on Polymers in Concrete, Belgium (July 1995).
7) C. Vipulanandan and S. Krishnan, Cement and Concrete Research 23, 792 (1993).

RHEOLOGICAL PROPERTIES OF SILICA FILLED
POLY (METHYL METHACRYLATE)

DEREK P. RUCKER AND STACY G. BIKE
University of Michigan, Macromolecular Science and Engineering Program, Ann Arbor, MI 48109

ABSTRACT

Ceramic fiber spinning is critical to the manufacture of fibrous monolith ceramics, and understanding the interactions between the polymer matrix and ceramic particle filler is necessary to predict the flow properties of these systems. In this study, poly (methyl methacrylate) (PMMA) was filled with octadecanol-coated Stöber silica, and the rheological behavior of the filled polymers investigated at various filler volume fractions. The rheological behavior of these materials was studied in both dynamic and steady-state experiments. The time required for filled PMMA to reach steady-state behavior under constant shear stress was found to be long, on the order of an hour. The steady-state viscosities increased as expected with filler volume fraction, but did not correlate well with existing models. This is hypothesized to be a result of matrix-filler surface interactions, and will be investigated further in future work.

INTRODUCTION

Dispersion flow behavior is by no means a new field. From Einstein's work in 1905[1] through Tanaka and White's theory[2], much work has been done to correlate flow behavior to component material properties. Significant successes have been achieved in predicting steady-state viscosity for Newtonian fluids filled at low volume fractions with non-interacting particles[3,4,5]. Other research has extended these findings, both empirically and theoretically, to non-Newtonian fluids, interacting particles, and higher volume fractions[6,7]. What is missing, however, is an investigation of the time-dependent properties of these filled systems. Transient, time-dependent behavior is usually neglected in fluid dynamics treatments since in most fluids this behavior is limited to a very short times after flow is induced. This is not the case for filled polymers, however. Batch processing times for filled polymers vary greatly, but are typically no longer than 60 minutes[8]. Our research, however, has shown that poly (methyl methacrylate) filled with silica can take more than 60 minutes to achieve steady-state flow behavior. This would indicate that one cannot assume steady-state behavior for most processing times.

This paper describes the results from a non-polar ceramic filler in poly(methyl methacrylate), a strongly polar polymer. The overall study will include three different surface polarity fillers and three different polymers in various relative volume fractions. The ceramic filler used was colloidal silica with octadecyl groups chemically grafted to the surface. The volume fraction of filler was varied between 20 and 50 percent, typical for high solids applications such as ceramic fiber spinning[9].

EXPERIMENTAL

Materials

The materials used in this study were colloidal silica and poly(methyl methacrylate) (PMMA). The silica was made by condensation reaction of tetraethyl ortho silicate (TEOS) catalyzed by ammonium hydroxide in ethanol, in a technique developed by Stöber[10]. The reactant and catalyst ratios were determined from previous work by Davis[11] and Bogush[12]. The spherical particles were characterized using scanning electron microscopy, and their size was determined to be 0.45 µm in diameter, with a standard deviation of 0.07 µm. Octadecanol was then grafted to silanol surface sites through an esterification reaction at 180°C to give a uniform non-polar surface[13]. Besides providing a non-polar surface on the ceramic, the octadecanol provided steric stabilization,

preventing the silica particles from irreversibly aggregating when removed from ethanol. The grafted chains were too short, however, to result in entanglements or physical cross-links[14]. Thus, the particles still behaved as independent components within the polymer matrix.

The PMMA had a number average molecular weight of 25,000. It was purchased from Polysciences as 200 μm beads, and was used as received.

Filled Polymer Preparation

The coated silica and polymer beads were allowed to dry for 72 hours in an 85°C ventilated oven, and then were stored until use in a desiccator. The silica was mixed into the PMMA in a Brabender Plasticorder operating at 200°C and 60 rpm. To further eliminate adsorbed water on the polymer, the PMMA was melted and mixed in the Plasticorder for 20 minutes at 200°C prior to the addition of the filler. No degradation of the polymer matrix was observed during mixing.

Rheological Characterization

All experiments were performed using a Bohlin CS 50 controlled stress rheometer. A cone and plate geometry (40 mm diameter, 4° angle) was used to provide a constant stress field within the sample during testing. Tests were run at 200°C to ensure that the sample was fluid enough for measurable results, given instrument stress limitations. Samples were allowed to equilibrate at 200°C for 60 minutes prior to testing, to eliminate any residual stresses incurred during processing. It was determined that the instantaneous viscosity and dynamic moduli of samples changed linearly with time after an equilibration period of 1 hour. This indicates that there could be up to a 60% variation in sample properties over experiment run time (Figure 1.). Since the increase is linear for all parameters, the effects of thermal history on viscoelastic properties may be eliminated by normalizing the plots to a constant thermal exposure. For the purposes of this paper, however, only data that has similar residence times at elevated temperatures will be compared.
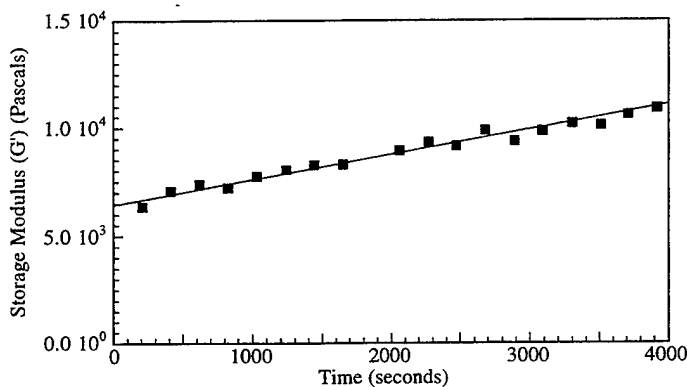
Figure 1. Variation in storage modulus with time at processing temperature. The sample used is 35% (vol) silica at a shear stress of 50 Pa and a frequency of 0.005 s^{-1}. The temperature is 200°C.

Four types of tests were performed: stress sweep at constant frequency, frequency sweep at constant stress, stress ramp, and creep compliance. The first type, stress sweep, gave a general idea of the linear viscoelastic region for these materials. Frequency sweeps were used to probe the sample structure without perturbation. Yield stresses for these materials were determined using a

60 second stress ramp. Creep compliance tests were used both to determine the time-dependent behavior of the system and to determine the steady-state viscosity for the material.

RESULTS AND DISCUSSION

Despite the fact that few filled ceramic processing applications operate within these materials' linear viscoelastic regime, these experiments were designed to remain within this region for comparison with existing work and future modeling purposes. The extent of the linear viscoelastic region was determined by oscillatory experiments in which the frequency was held constant, and the shear stress varied. The storage and loss moduli were measured by these experiments. A low shear stress plateau was expected in both moduli, followed by a gradual decrease. The onset of the decrease in moduli is generally considered to correlate to the end of the linear viscoelastic region. The data acquired from our materials, however, showed relative maxima in these moduli, with the shear stress corresponding to the maxima increasing with filler volume fraction. Increasing storage modulus is indicative of structure formation, and this sort of behavior has not been previously reported, nor does it fit linear viscoelastic theory. Further experiments suggested that the behavior is an artifact of the long stress relaxation times of these materials. The samples were still re-forming their equilibrium structure when the tests began, following a 2400 second equilibration time after loading. Longer equilibration times are thus desirable, but the properties of the materials changed with time at the operating temperature of 200°C. Ultimately we selected an equilibrium time of 3600 seconds, long enough for most equilibrium structure to be re-formed, but not long enough to significantly distort the viscoelastic properties by thermal degradation.

The frequency sweep experiments produced the expected results. As also noted by Sideridis[15], the moduli increased monotonically with frequency and filler volume fraction, and the behavior agreed with the literature.

Although there is controversy regarding the existence of a yield stress[16], stress ramp measurements were used to determine an "apparent yield stress" for the materials studied. As expected, and predicted by Tanaka and White, the yield stress increased with increasing filler concentration (Table 1.). The pure polymer exhibited no yield stress.

Table 1. Yield stress measurements for filled PMMA

Volume Fraction Filler	Apparent Yield Stress
0.20	233 Pa
0.35	333 Pa
0.50	1580 Pa

The creep compliance experiments represent our first attempt to quantify the highly time-dependent behavior of these materials that affected the stress sweep experiments. Repeated creep tests indicated that a shear stress of 20 Pa was within the linear viscoelastic region for both 0.20 and 0.35 silica volume fraction samples. Difficulty was encountered in determining the linear viscoelastic region for the 0.50 volume fraction sample because an applied stress of 20 Pa resulted in strains at the lower limit of instrument resolution. In such situations it is common to consider the limit of instrument resolution as the edge of the linear viscoelastic region. All creep compliance experiments were therefore performed at a shear stress of 20 Pa.

The compliance curves are shown in Figure 2. Steady-state for viscoelastic liquids is evidenced by a linear compliance curve (constant slope). As can be seen, none of the materials tested is approaching this condition rapidly, even after 2400 seconds. The shape of the curves, however, is nearly identical, indicating that all three samples have similar flow mechanisms. The scatter evident in the 0.5 volume fraction sample is a result of instrument noise; the shape of the curve is unaffected.
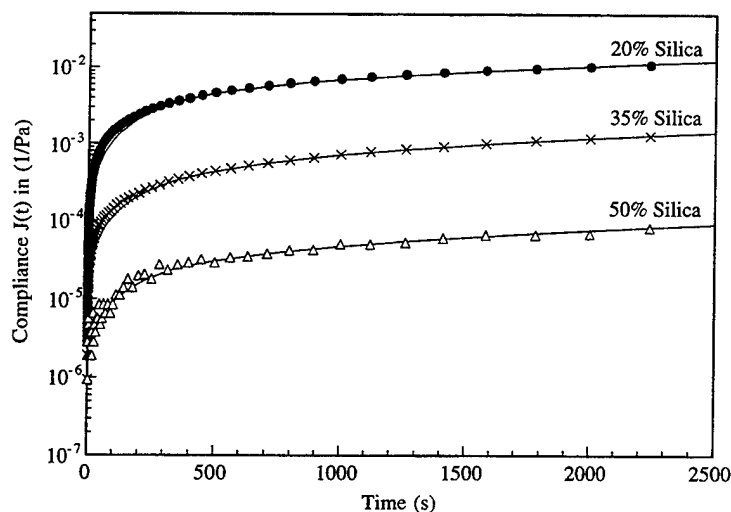
Figure 2. Creep compliance behavior for silica-filled PMMA. Samples were run at a shear stress of 20 Pa and a temperature of 200°C.

Besides time-dependent behavior, compliance curves also can give steady shear viscosity data. This is the most commonly reported parameter of filled systems, and the most often modeled. The steady shear viscosity is the inverse slope of the compliance asymptote. The compliance curves are not yet at equilibrium, but the steady-state viscosities can be estimated from the last few points on the graph. Since the slope is continually decreasing toward the asymptote, the estimated viscosities will be slightly low, but they will be sufficient to compare several of the theories found in the literature. The estimated viscosities and curve fits are found in Figure 3. The viscosity theories investigated were proposed by Mooney[3],

$$\eta_r = \exp\left[\frac{K\phi}{1 - \phi/\phi_m}\right] \tag{1}$$

Krieger and Dougherty[4],

$$\eta_r = \left[1 - \frac{\phi}{\phi_m}\right]^{-K\phi_m} \tag{2}$$

and Frankel and Acrivos[6].

$$\eta_r = 1 + \frac{9}{8}\left[\frac{(\phi/\phi_m)^{1/3}}{1-(\phi/\phi_m)^{1/3}}\right]$$
(3)

In all cases, ϕ is filler volume fraction, ϕ_m is maximum packing fraction, and K is an empirical constant. In Figure 3., K is set at 2.5 (after Einstein[1]), and ϕ_m at 0.63 (random packing of monodisperse spheres).
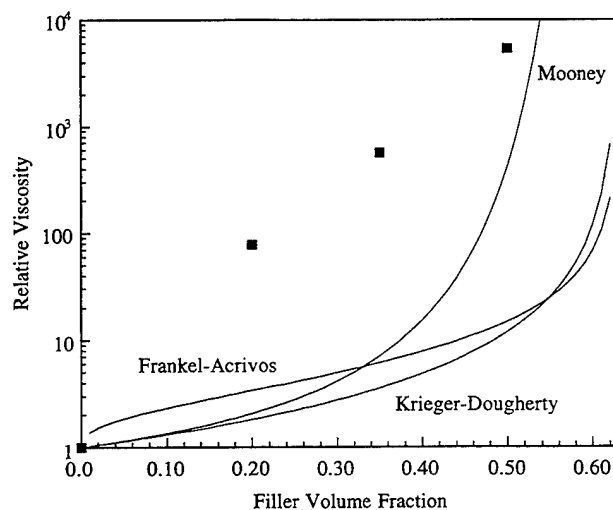

Figure 3. Approximate steady-state viscosities for silica filled PMMA. Data extrapolated from compliance curves and fit with existing viscosity models.

Even though the estimates for steady-shear viscosity are inherently low, all of the models examined predicted viscosities that are even lower. There are several explanations for this. The equations of Mooney and Krieger-Dougherty were developed based on the original model of Einstein. While the pairwise interactions postulated in these models certainly exist in all systems, at high filler volume fractions, many particles interact simultaneously in a cage or cell interaction model. This was the approach taken by Frankel and Acrivos, however, and their equation also could not describe our data. Some characteristic of our system must be not be taken into account by these models.

It is our belief that the discrepancy between our observed viscosities and those predicted by these models is a result of surface interactions between matrix and filler. These interactions, if present, would result in the formation of a stable structure that would resist deformation and flow, and would be evidenced by elevated steady-state viscosity. If this is correct, it would follow that increasing the surface polarity of the fillers would result in even stronger structure formation, and correspondingly higher viscosities. This will be investigated in future work.

While these models were all developed for Newtonian matrices, this is not likely to be the most significant factor contributing to the discrepancy between their predictions and our data. Polymers are inherently non-Newtonian, but the PMMA molecules used in this work are only 250 repeat units long, and the deviation from Newtonian behavior is negligible for the stress levels used in these experiments.

There are many other predictive theories, all applicable in certain situations, which were not fit to this data. The models of Einstein[1] and Batchelor[5] are applicable at far smaller filler volume fractions than are investigated here. More detailed models exist, namely those by Kerner[17] and Tanaka and White[2], but in the absence of extremely detailed information on both components (e.g. reciprocal Debye length and Hamaker constant) these were not applicable. The typical use of the Tanaka and White expression is empirical, with the unknown quantities acting as empirical parameters, but with only four data points, the number of adjustable parameters would nearly ensure a fit.

SUMMARY

The results of this work indicate that there is a need for further study in two areas of dispersion flow behavior, namely time-dependent properties and matrix-filler interaction effects. The application of any steady state theory to practice will be limited by transient time-dependent behavior, which has been shown in this work to persist for process-length times, at least for one system. Steady state viscosity approximations were compared to three existing theories and the data were not adequately described by any one theory. Since approximation errors would only have increased the discrepancy, it is evident that some phenomena exists in our system that did not affect those on which the models were developed. This phenomena has been hypothesized to be matrix-filler polar surface interactions, and will be studied in future work.

ACKNOWLEDGMENT

REFERENCES

[1] A. Einstein, Ann. Physik **17**, 459 (1905).
[2] H. Tanaka and J.L. White, J. Non-Newtonian Fluid Mech. **7**, 333 (1980).
[3] M. Mooney, J. Colloid Sci. **6**, 162 (1951).
[4] I.M. Krieger and T.J. Dougherty, Trans. Soc. Rheology **3**, 137 (1959).
[5] G.K. Batchelor, J. Fluid Mech. **83**, 97 (1977).
[6] N.A. Frankel and A. Acrivos, Chem. Eng. Sci. **22**, 847 (1967).
[7] D.G. Thomas, J. Colloid Sci. **20**, 267 (1965).
[8] D. Kovar and G.A. Brady (personal communication).
[9] Ibid.
[10] W. Stöber, A. Fink, and E. Bohn, J. Colloid Interface Sci. **26**, 62 (1968).
[11] K.E. Davis, Sedimentation and Crystallization of Hard-Sphere Colloidal Suspensions: Theory and Experiment, Ph.D. thesis, Princeton University, 1989.
[12] G.H. Bogush, M.A. Tracy, and C.F. Zukoski, J. Non-Crystalline Solids 104, **95** (1988).
[13] R.D. Badley, W.T. Ford, F.J. McEnroe, and R.A. Assink, Langmuir **6**, 792 (1990).
[14] L.J. Fetters, D.J. Lohse, D. Richter, T.A. Witten, and A. Zirkel, Macromolecules **27** (17), 4639 (1994)
[15] E. Sideridis, Comp. Sci. Tech. **27**, 305 (1986).
[16] D. De Kee and C.F. Chan Man Fong, J. Rheol. **37** (4), 775 (1993)
[17] E.H. Kerner, Proc. Phys. Soc. London **B69**, 808 (1956).

SYNTHESIS AND CHARACTERIZATION OF ORGANIC/INORGANIC INTERPENETRATING POLYMER NETWORKS

Barry J. Bauer, Catheryn L. Jackson, and Da-Wei Liu

National Institute of Standards and Technology, Gaithersburg MD 20899

ABSTRACT

Interpenetrating polymer networks have been synthesized by performing sol-gel chemistry and conventional organic polymerizations in mixtures of the monomers. The organic polymers were acrylates, and the inorganic phase was SiO_2 formed by hydrolysis of orthosilicates. Polymerizations were conducted at a variety of relative rates, and the chemistry was designed to allow different amounts of grafting between the components. The morphology was characterized by transmission electron microscopy and small angle neutron and x-ray scattering. Wide variations in morphology were observed depending on the polymerization conditions, ranging from grossly phase separated to dendritic to finely divided structures (at a 100Å size scale). The phases ranged from mixtures of the two components to relatively pure phases. The interface between the phases ranged from very narrow to relatively broad.

INTRODUCTION

Recently, organic-inorganic composites have been synthesized by forming the SiO_2 phase through sol-gel chemistry using interpenetrating polymer network techniques [1-7]. The polymerization scheme for the most general case is as shown below:

$$Si(OR)_4 + 2H_2O + Monomer + Solvent \rightarrow$$
$$SiO_2 + 4ROH + Polymer + Solvent$$
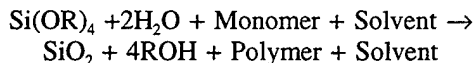
Two independent reactions can take place; the sol-gel reaction will form an inorganic component and the organic reaction will form an organic polymer. The resulting material is an interpenetrating polymer network (IPN) made up of organic/inorganic phases. If the solvent is a monomer, shrinkage is reduced since it becomes incorporated in the sample as a nonvolatile polymer. "Non-shrinking" composites can be prepared if the "R" group can polymerize with the organic monomer, since no weight loss occurs due to elimination of volatile components from the reaction mixture [6].

IPNs of two organic polymers are traditionally formed by independent polymerizations that give a sample that is microscopically phase separated, but macroscopically uniform [8]. The two polymerizations may be either sequential or simultaneous. At the beginning of the reaction, the two monomers or the monomer-polymer combination form a single phase, but phase separation occurs during polymerization and a finely divided morphology results. Grafting between the components of IPNs can also greatly affect the point of the phase separation and the nature of the resulting morphology. Studies of IPNs made from polymers that form miscible blends have shown that while the crosslinking reaction, without grafting between the components, can strongly promote phase separation [9], the opposite is true when grafting takes

place [10]. The two-phase morphology formed with IPN chemistry is often significantly different from that of a simple physical mixture of the two components. In particular, co-continuous morphologies can yield materials with bulk mechanical properties that are dominated by the minor component. In contrast, conventional silica filled polymers are made by physically mixing preformed silica into polymers, which tends to produce properties that are either dominated by the matrix polymer, or are an average of the properties of two components. For silica filled polymers formed by swelling an organic polymer or network in orthosilicate monomers and subsequently polymerizing by the sol-gel method [1-4], the silica is usually more finely dispersed than a physical mixture but the morphology often contains discrete particles.

In this paper we explore the morphologies of organic-inorganic IPNs synthesized with the SiO_2 phase made by sol-gel chemistry and the organic phase made from poly(2-hydroxyethyl acrylate) (HEA). The synthetic variables include the relative reaction rates (sequential vs. simultaneous polymerizations) and grafting. Small angle x-ray scattering (SAXS), small angle neutron scattering (SANS), and transmission electron microscopy (TEM) are used to learn how synthetic variables affect the resulting structures.

EXPERIMENTAL

The ungrafted HEA-series was prepared by adding a water/HF mixture to tetraethylorthosilicate (TEOS) in the presence of an organic monomer, 2-hydroxyethyl acrylate (HEA), and benzoyl peroxide. The concentration of benzoyl peroxide was kept constant but the amount of HF was varied by a factor of 70 so that the relative rates of the two polymerizations covered the range of vinyl > sol-gel to sol-gel > vinyl. All samples were thermally polymerized at 70°C until fully reacted, and then dried in vacuum at 100°C to remove the ethanol produced in the reaction. The grafted B-series was prepared by using equal weights of HEA and Tetrakis(2-acryloxyethoxy)-silane (TAEOS) and polymerizing as in the case of the TEOS system, also with a varied HF concentration. More synthetic details are presented elsewhere [11-12].

Small angle x-ray scattering was performed at the NIST Polymers Division SAXS facility [13-14]. Small angle neutron scattering (SANS) was performed at the 30 meter NSF instrument at NIST [13,15]. Thermogravimetric analysis (TGA) was used to determine the SiO_2 content of the specimens and the decomposition temperature profile. Approximately 5 mg of the sample was heated at 10 °C per minute from 30 to 800 °C in an air atmosphere. For the transmission electron microscopy (TEM) studies, ultra-thin sections were cryomicrotomed using a diamond knife at temperatures from -20 °C to -80 °C. The sections were imaged on a Philips 400T at 120 kV [13]. The contrast between the silica containing phase and the polymer was sufficient for imaging and no staining was required.

RESULTS AND DISCUSSION

We will first present a discussion and analysis of the scattering data. A double logarithmic plot of SAXS or SANS intensity, I, versus the scattering vector, q, for the HEA-series and the B-series, is shown in figure 1. The scattering vector is defined as q = $4\pi/\lambda(\sin(\theta/2))$, where θ is the scattering angle and λ is the wavelength. The variation in these series are the catalyst ratio and grafting. Both SANS and SAXS data are shown in arbitrary intensity units and are shifted vertically for clarity. Samples HEA-1 and HEA-2 have a constant

power law over a considerable q range, with a slope of approximately -3.1. At higher scattering angle, the slopes in the Porod region are all near $\partial\log(I)/\partial\log(q) = -4$, indicating strong phase separation into domains with little mixing of the phases. Samples HEA-4 and HEA-5 have power law scattering < -4, suggesting that broader interfacial areas exist. The B series have power laws of $\partial\log(I)/\partial\log(q) = -2.4$ for sample B-2 and -2.0 for sample B-7, indicating extensive mixing of the two components and weak phase separation. For example, a limiting power law of -2 is seen in the case of miscible polymer blends where intimate mixing of the two components occurs [19]. In addition, sample B-2 has an extended power law range down to $q = .004$ Å^{-1} and sample B-7 has very weak scattering at low-q with a weak peak at .035 Å^{-1}.

Small angle scattering from two phase materials is generally characterized as having contributions from the domain structures of the two phases, the interfacial regions between the domains, and mixtures of the two components within the phases. In cases where contributions from mixtures of components within the phases is negligible, data analysis in the Porod region can give characteristic phase size and interfacial thickness [16-18]. The scattering from a two phase mixture with volume, V, interfacial area, A, volume fraction of one component, ϕ, and interfacial thickness, T has

Figure 1. SANS and SAXS from PolyHEA/SiO$_2$ IPNs.

an asymptotic form as shown in equation 1. In this form the scattered intensity, I, is in both numerator and denominator, so that absolute intensity calibration is not necessary. The surface to volume ratio is related to characteristic phase sizes, with l_1 and l_2 being the average chord size of phases 1 and 2, with l_i equal to $4\phi_i$ V/S. [18]. T is a characteristic interfacial thickness characteristic of the zone of mixing between the two phases.
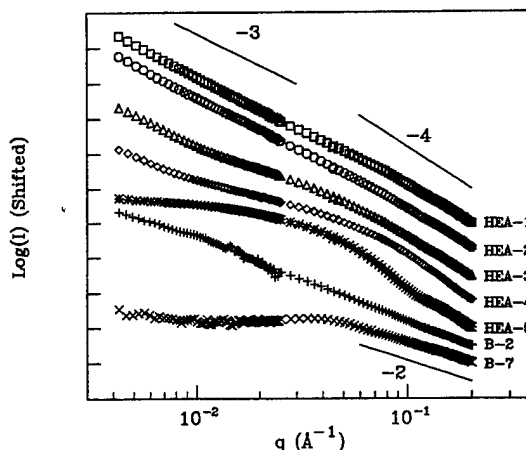
$$\frac{q^4 I(q)}{\int_0^\infty q^2 I(q)\,dq} = \frac{S/V \exp(-T^2 q^2)}{\pi\phi(1-\phi)} \qquad (1)$$

Table I list the catalyst concentration and SiO$_2$ content for the various samples as well as the values of the V/S and T calculated from the SAXS and SANS characterization. The B series samples never approach a region with a -4 power law, so a Porod analysis is impossible and values of V/S and T cannot be determined. For the HEA series, the samples with the lowest HF catalyst levels showed power law scattering over a wide q range. For samples where the vinyl polymerization is relatively fast compared to the sol-gel reaction, the domain sizes are largest and negligible interfacial thicknesses are measured. As the HF concentration increases, the domains become smaller and the interfaces become broader.

Sample	HF conc (g/g)	SiO$_2$ (g/g)	V/S (Å)	T (Å)	TEM (Å)	Comments
HEA-1	0.0004	0.10 - 0.23	>400	<4	300-3000	gross phase separation
HEA-2	0.0025	0.12	>400	<4	200-2000	dendritic
HEA-3	0.0026	0.15	>200	<4	600-2000	dendritic
HEA-4	0.0107	0.16	120	4	<100	fine texture
HEA-5	0.0270	0.15	140	9	<100	fine texture
B-2	0.0001	0.05	no Porod Region	---	100-200	mottled, fine texture
B-7	0.0004	0.05	no Porod Region	---	single phase	single phase

Table I. Sol-Gel IPNs

Sample HEA-1 has gross phase separation early in the polymerization forming large white clumps of polyHEA. It has been noted that polyHEA is not soluble in TEOS/H$_2$O without a cosolvent [1], so when the polyHEA is formed before the gelation of the TEOS, gross phase separation occurs. TGA of different parts of the sample gave SiO$_2$ contents between 0.10 and 0.23 g/g demonstrating the large size scale of the phase separation. SANS and SAXS techniques cannot see phases this large and can only see an average of structures within the phases. Scattering techniques that probe a larger size scale such as light scattering were not attempted, but the opaque, white appearance of the samples strongly suggest large domain sizes.

For the lower sol-gel rates in the HEA series, a dendritic morphology is observed by TEM as discussed below, and the power law scattering of fractals is present. For the higher sol-gel rates in the HEA series, there is a much smaller size scale present (larger V/S ratio) and broader interfacial areas are present. The gelation occurs first as in any sol-gel reaction in a good solvent with the organic phase then forming from the polymerization of the "solvent". In samples with covalent bonds between the organic and inorganic components, the low limiting power law suggests less complete phase separation, and in the case of B-7, a "copolymerization" giving a single phase seems evident.

The morphology of the organic/inorganic IPNs was also studied by TEM. For HEA-1, gross phase separation has occurred at an early stage of the polymerization and the sample is very non-uniform as is seen in figure 2. For HEA-2, a dendritic structure with fairly diffuse edges is seen with a size range of SiO$_2$ rich areas from 200-2000 Å as is seen in figure 3. The TEM of HEA-3 has a similar structure to HEA-2, but the edges of the domains of SiO$_2$ which have formed appear rounder. A much different morphology of very finely dispersed SiO$_2$ was observed for both HEA-4 and HEA-5. A TEM micrograph for a typical region of HEA-4 is shown in figure 4. The grafted B-series was less distinctive in character by TEM. B-2 has a mottled appearance of ~ 0.1μm scale superimposed on a finer texture. The texture of B-7 is very uniform over a large area, and is only slightly greater than that observed for a pure organic polymer containing no SiO$_2$ as is seen in figure 5.
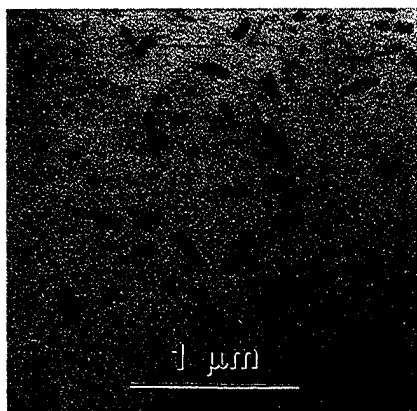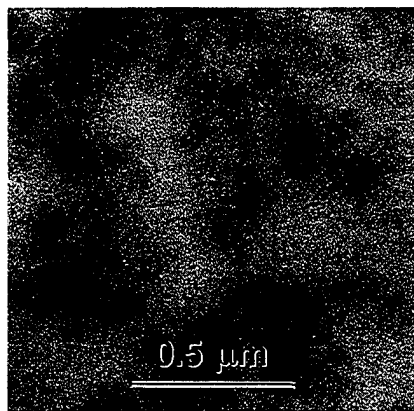
Figure 2. TEM of HEA-1.
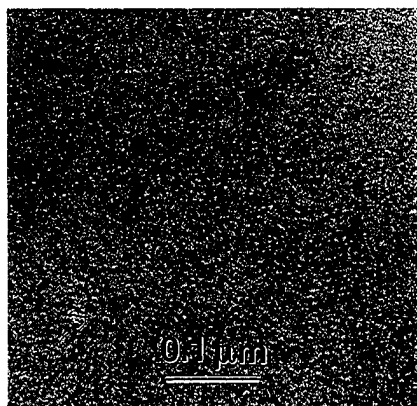
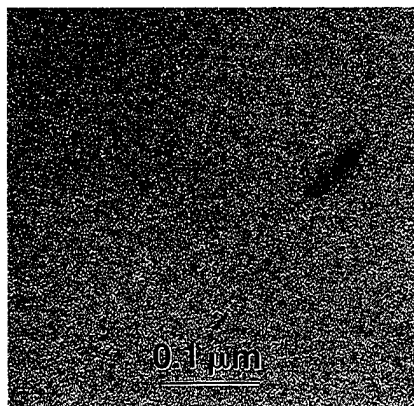

Figure 3. TEM of HEA-2.

Figure 4. TEM of HEA-4.

Figure 5. TEM of B-7.

CONCLUSIONS

A wide variety of morphologies have been prepared from the same starting materials by controlling the relative rates of polymerization and the amount of grafting between the components for the acrylate/SiO_2 IPNs described. These results are consistent with a similar series of organic-inorganic IPNs synthesized from an epoxy organic phase [20].

SANS and SAXS results for the two-HEA samples with the lowest sol-gel catalyst show a power law scattering over a wide angular range which is consistent with the dendritic structures seen in TEM. Porod analysis of the samples with the lower HF catalyst content

183

suggest sharp boundaries between the phases. The two samples with the highest sol-gel catalyst concentration have broader interfacial areas. The volume to surface ratio shows large sizes for the three samples with the low catalyst concentration and small sizes for samples with high catalyst concentration. These indicate two morphological types, one in which there are large dendritic structures with sharp interfaces, and another in which there are small structures with large interfacial areas. This is qualitatively in agreement with the TEM results. The B-series of samples contain monomers that have covalent bonds between the sol-gel and vinyl components. The phase separation in these samples is considerably weaker, as seen by both scattering and TEM.

REFERENCES

1. B. M. Novak, Adv. Mat., **5**, 422 (1993), and references within.
2. J. E. Mark, Y.-P. Ning, C.-Y. Jiang, W. C. Roth, Polymer, **26**, 2069 (1985).
3. C. J. T. Landry, B. K. Coltrain, M. R. Landry, J. J. Fitzgerald, V. K. Long, J. Polym. Sci., **26B**, 3702 (1993).
4. H. H. Huang, B. Orler, G. L. Wilkes, Macromolecules, **20**, 1322 (1987).
5. B. M. Novak, C. Davies, Macromolecules, **24**, 5481 (1991).
6. M. W. Ellsworth, B. M. Novak, Chem. Mat., **5**, 839 (1993).
7. M. W. Ellsworth, B. M. Novak, JACS, **113**, 2756 (1991).
8. L. H. Sperling, Intrepenetrating Polymer Networks, edited by D. Klempner, L. H. Sperling, and L. A. Utracki, (Advances in Chemistry Series 239, (1994), p. 3.
9. B. J. Bauer, R. M. Briber, C. C.Han, Macromolecules, **22**, 940 (1989).
10. B. J. Bauer, R. M. Briber and B. Dickens, Interpenetrating Polymer Networks, edited by D. Klempner, L. H. Sperling, and L. A. Utracki, (Advances in Chemistry Series 239, 1994), p. 179.
11. B. J. Bauer, C. L. Jackson, A. I. Nakatani, and J. D. Barnes, submitted for publication in Chemistry of Materials.
12. C. L. Jackson, B. J. Bauer, J. D. Barnes, PMSE Preprints, **71**, 85 (1994).
13. Certain commercial materials and equipment are identified in this paper in order to specify adequately the experimental procedure. In no case does such identification imply recommendation by the National Institute of Standards and Technology nor does it imply that the material or equipment identified is necessarily the best available for this purpose.
14. J. D. Barnes and F. Mopsik, 46th Annual Technical Conference Proceeding, Society of Plastics Engineers, **12**, 1179 (1988).
15. H. J. Prask, M. Rowe, J. J. Rush, I. G. Schroeder, J. Res. Natl. Inst. Stand. Tech., **98**, 1 (1993).
16. G. Porod, Kolloid Z., **124**, 83 (1951).
17. G. Porod, Kolloid Z., **125**, 51 (1952).
18. Roe, R.-J., Encyclopedia of Polymer Science and Engineering, (Wiley Interscience, New York, 1988) v. 17, p. 981-9.
19. C.C. Han, B. J. Bauer, J. C. Clark, Y. Muroga, Y. Matsushita, M. Okada, Q. Tran-Cong, T. Chang, I. C. Sanchez, Polymer, **29**, 2002 (1988).
20. B. J. Bauer, D.-W. Liu, C. L. Jackson, and J. D. Barnes, submitted for publication in Polymers for Advanced Technologies.

EFFECTS OF SURFACE MODIFICATION ON THE STRUCTURE OF ADSORBED BLOCK COPOLYMER MONOLAYERS

RAHOOL S. PAI-PANANDIKER AND JOHN R. DORGAN*
Colorado School of Mines, Golden, CO 80401, USA

ABSTRACT

Improving the processing and formability of ceramic components prior to firing (as green bodies) requires an enhanced understanding of how the polymeric binder components function. We report on the role of surface energetics on the structure of the copolymeric monolayers formed via adsorption from solution. Also, results on the effects of surface energetics on the kinetics of the adsorption are reported. A silicon wafer with an oxide layer is used as the surface and adsorption takes place from toluene. Surface energetics are varied by treatment of the oxide surface with a series of silane coupling agents which contain either amine, epoxide, or vinyl functional groups. The block copolymers used consist of relatively short poly(ethylene oxide) (PEO) blocks and much longer polystyrene (PS) blocks. Ellipsometry is used to determine the grafting density, σ (chains/nm^2), and Fourier Transform Infrared spectroscopy is used to investigate the copolymer on the surface. It is seen that the time required to reach equilibrium increases as the strength of the interaction between the copolymer and the surface increases. Also, the diblock copolymers appear to obey the scaling laws proposed by Marques and Joanny on all the surfaces studied. (i.e., $\sigma \propto 1/N_A$, when the copolymer is symmetric or moderately symmetric and $\sigma \propto 1/\beta^2$, when the copolymers are asymmetric, where N_A is the number of segments of the adsorbing block and β is the ratio of the size of the nonadsorbing block to that of the adsorbing block.)

INTRODUCTION

Polymer coils terminally attached to a solid surface constitute an interface of particular interest. For example, they are used to enhance the biocompatibility of artificial implants, in affinity chromatography and in electrode modification applications. They are also used in the stabilization and flocculation of colloidal particles such as those used as precursors ("green bodies") to the sintering of ceramics.[1] It is important to understand the polymer-inorganic interface problem to improve the processibility and formability of the "green body."

Many studies have addressed diblock copolymer behavior at the solid-liquid interface.[2,3] Scaling laws have been proposed for three different regimes of symmetry by Marques and Joanny.[4] However, as pointed out by Guzonas et al, the predicted scaling behavior in two of the three regimes is similar and hence they suggested a slightly different classification based on the value of β; Copolymers with $\beta > N_A^{0.5}$ are identified as highly asymmetric (Tail regime), those with $1 < \beta < N_A^{0.5}$ as moderately asymmetric and those with $\beta < 1$ as symmetric (Head regime).[5] The crossover at $N_A^{0.5}$ is indicative of crossover from the head regime (in which the size of the adsorbing block dictates the surface coverage) to the tail regime (in which the

---

* Author to whom correspondence should be addressed

excluded volume interactions of the nonadsorbing blocks dictates the surface coverage). Our previous studies have focused on the adsorption behavior of block copolymers on to a native oxide layer of the silicon wafer.[6,7,8] Silane coupling agents are extensively used to enhance the adhesion of organic polymers to inorganic surfaces. Hence, an understanding of the adsorption process of copolymers onto oxide surfaces modified by silane coupling agents should aide material processing.

In this study, we report on the adsorption behavior of diblock copolymers onto chemically modified surfaces. The block copolymers used consist of relatively short poly(ethylene oxide) (PEO) blocks and much longer polystyrene (PS) blocks. On polar surfaces, the PEO preferentially adsorbs to the surface, whereas the PS block remains dangling in solution. Surface energetics are varied by treating the surface with a series of silane coupling agents. Adsorption takes place from toluene, a good solvent, onto different surfaces. Fourier Transform Infrared spectroscopy (FTIR) is used to investigate the nature of the chemical structure on the surface. Preliminary work in developing a methodology to obtain quantitative information from the FTIR spectroscopy is also presented.

EXPERIMENTAL SECTION

The copolymers used in this study were obtained from Polymer Laboratories (Amherst, MA) and have the characteristics shown in Table 1. For these samples, both regimes of symmetry are covered (i.e. copolymers with $\beta < N_A^{0.5}$ lie in the so called symmetric to moderately symmetric regime and copolymers with $\beta > N_A^{0.5}$ lie in the highly asymmetric regime). All of the polymer samples have polydispersity indices (M_w/M_N) less than 1.15.

Material	β	$N_A^{0.5}$	PDI
PS(115k)-PEO(25k)	1.29	23.8	1.07
PS(85k)-PEO(23k)	1.12	22.9	1.07
PS(1.7k)-PEO(0.3k)	1.59	2.6	1.08
PS(145k)-PEO(2k)	7.05	6.59	1.09
PS(359k)-PEO(2k)	12.58	6.41	1.14
PS(707k)-PEO(4k)	12.58	9.36	1.1
PS(64k)-PEO(0.5k)	12.58	2.71	1.15
PS(5.8k)-PEO(0.3k)	3.33	2.48	1.14

Table 1: Material characteristics of the copolymers studied.

The silicon wafers were obtained from Silicon Source Inc. (Phoenix) and treated as described previously.[2] The film thickness of the oxide layer was independently measured using ellipsometry prior to further treatment. The silane coupling agents used were obtained from Dow Corning Co. (Midland, MI). The three coupling agents employed in order to give different surface energetics were Z-6020® (Diamino functionality), Z-6040® (Epoxide functionality) and Z-6075® (Vinyl functionality). The method of application of the silane coupling agent to the wafer has been described by Plueddemann et al.[9] After application, the thickness of the silane film was independently measured using ellipsometry. The average thickness of the epoxide

186

films was determined to be 14.0 ± 3.0 Å, the amine films to be 22.0 ± 3.0 Å and the vinyl films to be 13 ± 3.0 Å. HPLC grade toluene (Malinckrodt Inc.) was used after filtering three times through 0.2 micron Whatman filters. The adsorption experiments were all conducted at solution concentrations of 1.00 ± 0.01 mg/ml and the temperature was controlled at 25.0 ± 0.1°C. Low angle laser light scattering (Wyatt Technologies DAWN B) was used to ensure that there was no formation of micelles at the concentrations used in the experiments. A specially modified rotating analyzer ellipsometer (Gaertner Scientific) was used to measure the adsorbed amounts.[10] A Bio-Rad FTS-40 FTIR spectrometer with a narrow-band-pass mercury cadmium telluride (MCT) detector was used to obtain the spectra of the films. The spectra were collected in transmission using at least 512 scans at a resolution of 2 cm^{-1}. The native wafer is subtracted out to obtain the spectra of the film.

The relationship of the measured ellipsometric angles (ψ and Δ) to the film parameters of a multilayer stack is given by:

$$e^{i\Delta} \tan \psi = \frac{R_p}{R_s} = F(n_k, d_k) \tag{1}$$

where n_k and d_k represent the indices of refraction and the thicknesses of each layer present (denoted by subscript k). Measurement of the two independent quantities, ψ and Δ, allows for the solution of two unknowns, a layer thickness, d_1, and a refractive index, n_1. In this study the adsorbed layer thicknesses and refractive indices are determined assuming a homogeneous layer for the thin films. The adsorbed amount of copolymer proves insensitive to the model assumed.[2] The adsorbed amount is calculated from:

$$A = d_1 c_1 = d_1 (n_1 - n_0) / (dn/dc)_0 \tag{2}$$

where n_1 represents the refractive index of the adsorbed layer and d_1 its thickness, n_0 represents the refractive index of the copolymer solution and $(dn/dc)_0$ is the specific refractive index.

Knowing the adsorbed amount, the grafting density, σ, is calculated from Equation 3.

$$\sigma \, (\text{chains}/\text{nm}^2) = \frac{A(\text{mg}/\text{m}^2)}{M_w(\text{mg}/\text{mol})} N_{AV} \, (\text{chains}/\text{mol}) \times 10^{-18}(\text{m}^2/\text{nm}^2) \tag{3}$$

Another important variable in the scaling description of copolymer adsorption is the asymmetry ratio, β, given by:

$$\beta = a'(N_B/N_A)^{0.6} \tag{4}$$

where a' is the ratio of the size of a single nonadsorbing block segment to a single adsorbing block segment and is taken as 0.87 for PS-PEO block copolymer.

In FTIR spectroscopy, the integrated area of the C-H antisymmetric stretch (2920 cm^{-1}) can be used to characterize the film on the surface. The calibration procedure involves the gravimmetric determination of the mass of the polystyrene on spun-coated wafers. In FTIR transmission of thin films on a substrate, a sine wave interference pattern is generated (see Figure 4 below). The thickness of the cast film can be determined by the relationship:

$$d = (1/2n\Delta v) \tag{5}$$

187

where **d** is the thickness of the film, **n**, its refractive index and Δv is the spacing between the maxima of the interference fringes in wavenumbers.

RESULTS AND DISCUSSION

Results from the study are seen in Figure 1, which shows that the grafting density of the symmetric to moderately symmetric diblocks scale with the reciprocal of the head size ($\sigma \propto 1/N_A$). This appears to be true for the different surfaces studied. (i.e. the scaling behavior appears to be similar for the amine, epoxide and vinyl surfaces.) Note that as N_A becomes larger, the adsorbed amounts converge to similar values.

For highly asymmetric diblocks, the surface density scales with the reciprocal of the square of the asymmetry ratio ($\sigma \propto 1/\beta^2$) as shown in Figure 2. This is again true for all the different surfaces studied. Thus, the scaling laws proposed by Marques and Joanny for diblocks in the symmetric to moderately symmetric regime as well as in the highly asymmetric regime are apparently obeyed on all the surfaces. It is noted that as $1/\beta^2$ becomes smaller that the adsorbed amounts converge to similar values. This is to be expected because as β becomes large, it is the excluded volume interactions between the nonadsorbed blocks of the copolymer molecules which govern the surface coverage.

Figure 3 demonstrates the kinetic behavior of one of the diblocks (PS(145k)-PEO(2k)) on the different surfaces. It is seen that as the strength of surface interaction increases, as measured by a greater adsorbed amount, that equilibration takes longer. That is, in moving from strong bonding to weak bonding, the system equilibrates much faster.
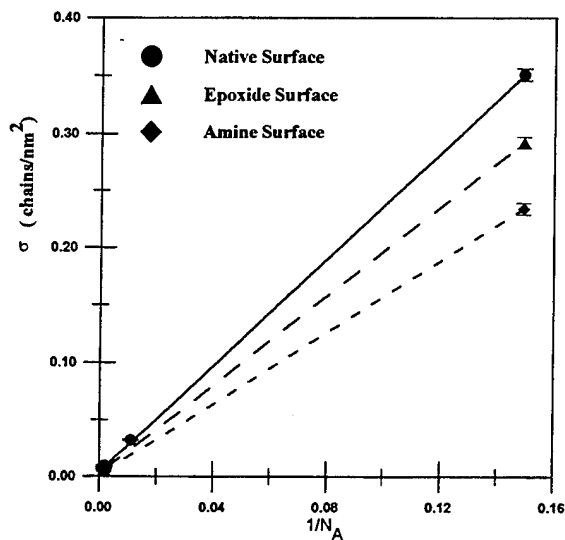

Figure 1: Scaling behavior for symmetric to moderately symmetric diblocks
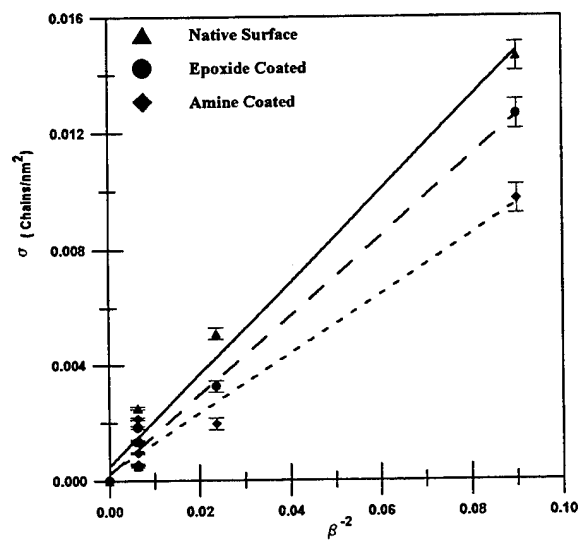($\beta < N_A^{0.5}$) on Native (●), Epoxide (▲) and Amine (◆)
surfaces

Figure 2: Scaling behavior for highly asymmetric polymers ($\beta > N_A^{0.5}$) on Native (▲), Epoxide (●) and Amine (◆) surfaces
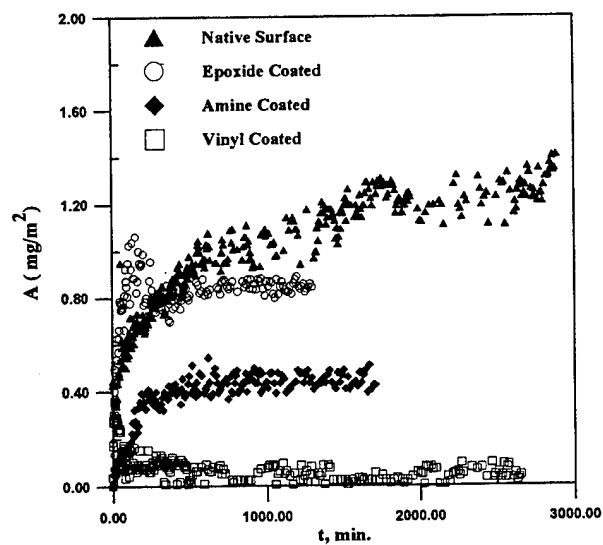

Figure 3: Adsorption kinetics for diblock PS(145k)-PEO(2k) on native (▲), epoxide (O) amine (◆) and vinyl (□) surfaces.

A typical FTIR transmission spectrum for a thick polystyrene film on a silicon wafer is shown in Figure 4. From the interference fringes seen in the thick films, we can directly determine the thickness of the PS film using Equation 5. However for thin films, it is difficult to obtain measurable interference. In this case, the film thickness may be measured indirectly.[11] A calibration curve of the film thickness determined using Equation 5 against the corresponding integrated areas of the C-H stretch is shown in the inset of Figure 4 . The relationship is linear and hence can be extrapolated to thin films if performed with high enough precision. For one of the diblocks (PS(145k)-PEO(2k)), the magnified spectrum in the C-H stretch region is shown in Figure 5. For the above diblock, the thickness of the diblock film is determined by FTIR to be 148.0 ± 3.0 Å. This contrasts with the thickness for the copolymer film determined directly using ellipsometry, which is 100.0 ± 5.0 Å. Also, a curve of the integrated area, in absorbance units, of the C-H stretch against the mass of PS on the surface can be generated. The mass of PS on the wafer can be determined gravimetrically by the difference in dry wafer weights before and after the spin coating process. A calibration of this nature would permit the determination of the amount of polymer adsorbed onto the surface directly.

CONCLUSIONS

The present experimental study lends itself to some interesting conclusions regarding the use of coupling agents at the polymer-inorganic interface. First, in terms of maximizing the surface coverage of the block copolymers it is apparent that changes in copolymer architecture are more important than the acheivable surface energetics modifications. It is to be noted, however, that the twin-handle of varying copolymer architecture and surface energetics allows a rather detailed control of copolymer grafting density. Coupling agents can therefore be used to modify chain grafting densities without changing copolymer architecture.

The diblock materials are found to obey the scaling laws proposed by Marques and Joanny for each of the different surfaces studied (i.e. native oxide surface, the epoxide surface and the diamino surface). In the symmetric to moderately symmetric regime the grafting density scales with the reciprocal of the head block size ($\sigma \propto 1/N_A$) and in the highly asymmetric regime, the grafting density scales with the reciprocal of the square of the asymmetry ratio ($\sigma \propto 1/\beta^2$). However as $1/\beta^2$ decreases, the adsorbed amounts approach the same value. This is on account of the fact that as the copolymer becomes highly asymmetric, the surface coverage is dictated only by the excluded volume interactions of the nonadsorbing blocks and hence surface chemistry is less important. A similar argument may be made at the extreme of the tail regime in which we have moderately symmetric or symmetric copolymers with large adsorbing block sizes. For these copolymers, it is the size of the adsorbing block which dictates the surface coverage. Successful usage of coupling agents to modify the properties of the diblock copolymer - inorganic interface is thus predicated on the appropriate selection of chain architecture.

Figure 3 illustrates that the strength of surface interactions plays an important role in the kinetics of the adsorption process. As the strength of surface interaction decreases, the equilibration time for the adsorption process also decreases. Highly interacting systems, such as the native oxide surface are known to possess long-lived non-equilibrium states.[12,13] This aides in understanding the time required to synthesize the polymer-ceramic interface which is an important component in the pre-processing stages of ceramic manufacture.
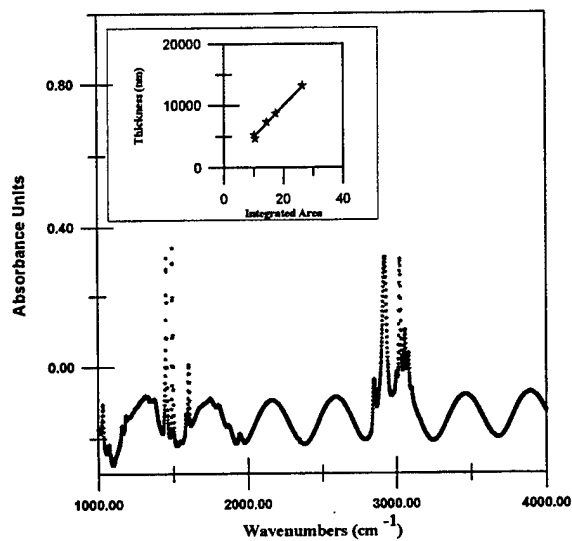
Figure 4: Typical FTIR spectrum for a thick polystyrene film and calibration curve for integrated area of C-H stretch and thickness of PS film (Inset).
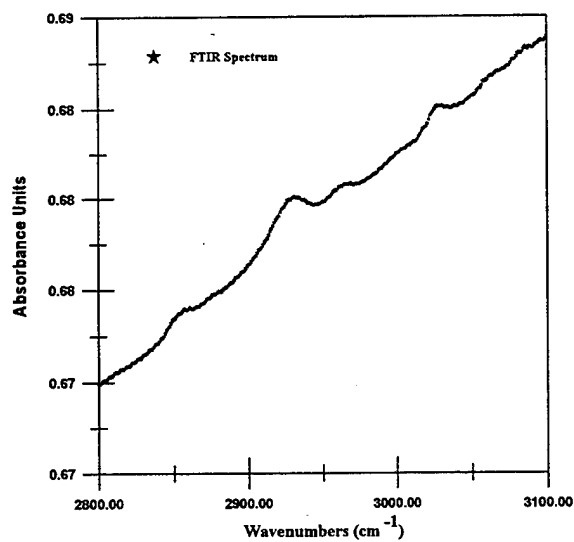

Figure 5 : FTIR spectrum of the diblock PS(145k)-PEO(2k) in the region of the C-H stretch.

191

It is also demonstrated through Figure 4 that it is possible to use FTIR spectroscopy to determine the thickness as well as equilibrium adsorbed amount of polymer on the surface. For a thin polymer film, the integrated area of the C-H stretch correlates with the thickness of the polymer film on the surface.

Hence , we have elucidated the effect of specific surface interactions on the structure and dynamics of the formation process of the polymer-ceramic interface. This is important since it involves the formation of the "green body" and understanding the structure and kinetics of this process would help in optimizing material charaterictics.

ACKNOWLEDGMENTS

REFERENCES

(1)   Bohlein-Mauss, J.; Sigmund, W.; Wegner, G. et al. *Adv. Mater.*, **4**, 973, 1992
(2)   Motschmann, H.; Stamm, M.; Toprackcioglu, C. *Macromolecules*, **24**,3681, 1991
(3)   Halperin, A.; Tirrell, M.; Lodge, T.P. *Adv. Poly. Sci.*, **100**, 31, 1992
(4)   Marques, C.M.; Joanny, J.F. *Macromolecules*, **22**, 1454, 1989
(5)   Guzonas, D.A.; Boils, D.; Tripp, C.P.; Hair, M.L. *Macromolecules*, **25**, 2434, 1992
(6)   Pai-Panandiker, R.S.; Dorgan, J.R. *Macromolecules*, In Press (June 1995)
(7)   Dorgan, J.R.; Stamm, M.; Toprackcioglu, C. et al *Macromolecules*, **26**, 5321,1992
(8)   Stamm, M.; Dorgan, J.R. *Coll. and Surf.*, **86**, 143, 1994
(9)   Plueddemann, E.P. *27th Annual SPI Technical Conference*, Paper 21-B (1972)
(10)   Pai-Panandiker, R.S.; Dorgan, J.R. *Rev. Sci. Instr.*, **66**, 1112, 1995
(11)   Culler, S.R.; Mckenzie, M.T.; Fina, L.J.; Ishida, H.; Koenig, J.L *Appl Spec*, **38**, 791, 1984
(12)   Chakraborty, A.K.; Adriani, P.M. *Macromolecules*, **25**, 2470, 1992
(13)   Chakraborty, A.K.; Adriani, P.M. *J. Chem. Phys.*, **98**, 4263, 1993

Part VII

Surface Preparation

REACTIONS OF DEFINED OXIDIZED CARBON FIBER SURFACES WITH MODEL COMPOUNDS AND POLYURETHANE ELASTOMERS

CHARLES U. PITTMAN, JR., STEVEN D. GARDNER, GUOREN HE, LICHANG WANG, ZHIHONG WU, C. SINGAMSETTY, BIAHUA WU AND GLYN BOOTH
Departments of Chemistry and Chemical Engineering, Mississippi State University, Mississippi State, MS 39762

ABSTRACT

Ex-PAN carbon fiber surfaces, oxidized to varying degrees by HNO_3, have been characterized by NaOH, dye and HCl uptake, ion scattering spectroscopy (ISS), and angle-resolved X-ray photoelectron spectroscopy (ARXPS). Subsequent treatments with tetraethylenepentamine to introduce amino groups or epichlorohydrin to introduce epoxy groups have been thoroughly characterized. The efficiency of using these surface functions to bond polymers onto fiber surfaces has been investigated using model anhydrides and isocyanates (for amines) and diols and diamines (for epoxides). The fraction of surface-bound groups which react drops with an increase in molecular size of the species being grafted. Crosslinked elastomeric polyurethane layers with designed modulus values and thicknesses have been bonded to these fibers. Composites have been prepared (epoxy matrices). The impact strengths and interlaminar shear strengths (ILSS) were studied as a function of the interphase modulus and thickness. Impact strengths increased (even at 500-1500 Å thicknesses). ILSS values depend on interphase modulus.

INTRODUCTION

Poor bonding at the fiber/matrix interface degrades the properties of composite materials. Improvements in this bonding increases the interlaminar shear strength (ILSS) but, most often, decreases the impact strength.[1-3] Impact strength and toughness can be increased by adding a second dispersed rubbery phase to the matrix.[4,5] Several theoretical studies proposed inserting a thin elastomeric layer at the fiber/matrix interface (a concentric interphase layer coated on the fiber) to improve fracture toughness and impact strength.[6-10]

Carbon fibers have been coated with thermoplastic polymers to serve as interphases using dip coating,[11,12] interfacial polycondensation[13] and electropolymerization.[14-17] Block copolymers containing polyisoprene and styrene/maleic anhydride segments were coated on carbon fibers by filament winding.[18] Thin polyimide[19] and polyamide[20] coated carbon fibers have been used in epoxy matrix composites. However, the strength of the fiber/interphase bond or the interphase matrix bond has not been specifically addressed or chemically designed in these studies. Strong interface/fiber adhesion is required to achieve high ILSS.

Unlike previous studies using polymeric interphases, we have reported[21-23] the first studies where carbon fibers have been specifically functionalized with -OH, -COOH, and amino groups to react with interphases and the quantity of these functions were determined. Then crosslinked elastomeric polyurethane interphase layers of defined thicknesses and elastic moduli were bonded to these carbon fiber surfaces followed by construction of carbon fiber epoxy matrix composites containing these elastomeric interphase layers.[21-23] These systems exhibited

195

higher impact strengths than identical composites without elastomeric interphases and, in some cases, no loss of ILSS occurred.[21,22] The defined functionalization of carbon fibers with -OH, -COOH, amino, and epoxy[24] groups will be summarized here together with their reaction efficiency at the surface with model compounds.[24,25] Also, the effect of defined elastomeric interphase layers on impact strength (IS) and ILSS will be discussed.

RESULTS

Oxidation and Binding Amino Groups. Ex-PAN based carbon fibers (Celion G30-500, from BASF, Inc. and Thornel T300 from Amoco, Inc.) were oxidized in 70% wt. nitric acid at 115 °C for varying times. These oxidations greatly increased the surface quantity of acidic phenolic hydroxyl and carboxylic acid functions. Acidic surface functions were quantitatively determined by NaOH uptake experiments. HCl uptake was used to follow amount of basic functions on the fiber (e.g., pyridine type nitrogen, etc.). Next these HNO_3-oxidized fibers were treated at 190-200 °C with tetraethylenepentamine (TEPA) to bind amino groups to the surface. TEPA forms amide functions with the carboxyl groups. Loop structures can also form (see Scheme 1). The quantity of acid groups (see Table I) increased from 3.6 μeq/g (as-received) to 49 μeq/g (after 90 min of oxidation). The quantity of surface basic groups was below 0.5 μeq/g until after TEPA treatment. The amino group surface concentrations for TEPA-treated fibers were much higher, ranging from 4 μeq/g for as-received fibers to 55 μeq/g for fibers which had been oxidized 90 min.

Phenolic hydroxyls can't react with TEPA and they remain on the surface. Some of the carboxylic acid groups are likely to be unreacted. In related studies[23] oxidized fiber surfaces were treated with $SOCl_2$ (forming very reactive -COCl groups) and then with TEPA. All carboxyl groups were converted to amides. The remaining acidic functions were phenolic hydroxyls. They constituted 35-40% of the acid groups introduced on HNO_3 oxidation (-COOH groups 65-60%). Combining this information with (1) the decrease in acid groups (Table I) and (2) the increase in amino groups during the reaction with TEPA gave a ratio (amine added: COOH consumed) ≈ 2.6. Thus, about 37% of the grafted TEPAs are looped.

Table I. Surface Functions Introduced on Carbon Fibers Upon HNO_3 Oxidation (70% wt., 115 °C) and TEPA Treatment (190-200 °C)

HNO_3 Oxidation Time (min)	0	20	40	60	90
Initial Acid Groups (μeq/g)	3.6	13	19	34	49
Initial Basic Groups (μeq/g)	0.2	0.3	0	0.4	0.1
Acid Groups after TEPA Treatment (μeq/g)	3.3	4.8	7.2	16	22
Basic Groups after TEPA Treatment (μeq/g)	4	16	27	39	55

[a]Since it is increasingly difficult to add successive protons to grafted TEPA amino sites (due to the build up of charge-charge repulsion) correction factors were carefully derived from experiments with the reaction products of TEPA and phenyl isocyanate. The detailed reasoning and experiments are presented elsewhere.[22] Correction factors of 1.113 and 1.212 are required for adding a third and fourth proton, respectively, during titration to a -CONH-CH_2CH_2NHCH$_2$CH$_2$NHCH$_2$CH$_2$NH-CH$_2$CH$_2$NH$_2$ fragment.

Scheme 1
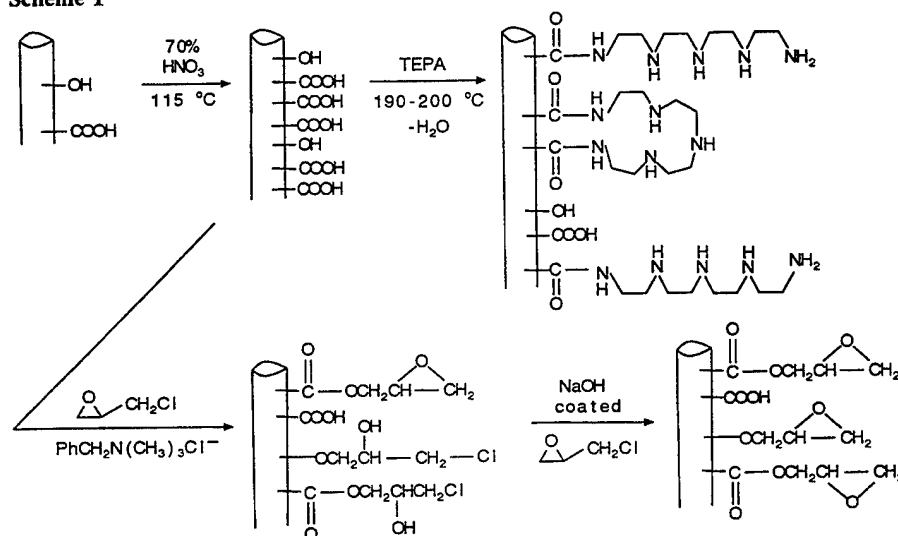
**Binding Epoxide Groups.** Epoxide functions were successfully bound onto HNO_3-oxidized fibers by a two stage process (Scheme 1). First, epichlorohydrin was reacted in the presence of benzyltrimethylammonium chloride to form surface bound α-chloropylene glycol. Then NaOH-promoted ring closure in epichlorohydrin under anhydrous conditions formed the corresponding surface-bound glycidyl esters and ethers over a several day period. NaOH was coated on fibers from step 1 and then the fibers were refluxed in epichlorohydrin. More than 50% of the acidic functions (on fibers starting with 60 μeq/g of acid groups) were converted to glycidyl groups without any polymer formed. A maximum of about 34 μeq/g of epoxy functions were introduced.[25] As the surface acid group concentration increased the efficiency (% of acid groups grafted) of epoxide grafting decreased. The first reliable noninterfering method to quantitatively analyze epoxy groups on carbon fiber surfaces was developed using HBr ring-opening and a bromide selective electrode.[25] Until now carbon fiber surface epoxidation had been unsuccessful. The previous literature as well as several unsuccessful routes in our lab have been discussed.[25]

Reaction of Oxidized Carbon Fibers with Model Isocyanates. Thornel T300 carbon fibers were oxidized in 70% HNO_3 for 60 min at 115 °C. The resulting fibers, having 61.5 μeq/g of acidic groups, were reacted for 3 h at 80 °C in xylene, chlorobenzene and DMF with: 1,6-diisocyanatohexane (mwt. 168), a tetraethyleneglycol oligomer capped with TDI, mwt. 920 (PET-95D) and with a prepolymer tetraethyleneglycol oligomer terminated with isophorone diisocyanate (XAPC-722, mwt. 1444). The terminal isocyanate groups were capped as urethanes by treatment with ethanol. The grafting efficiencies (G_e, % of acidic surface functions which reacted with the isocyanates) decreased sharply as the size of the diisocyanate increased. G_e values fit: $G_e = KM^a$ where M = mol. wt., K = 2750, a = -0.812. Furthermore, the grafting efficiency was highest in DMF. Apparently, the larger molecules shield other surface functions. Isocyanates form urethanes when reacted with phenolic hydroxyls and amides (via loss of CO_2) when reacted with carboxyl groups.

Diisocyanatohexane   Mwt. 168 G_e = 18% (xylene); 37% (chlorobenzene); 40% (DMF)
PET-95D   Mwt. 920 G_e = 9.6% (DMF)
XAPC-722   Mwt. 1444 G_e = 3.7% (xylene); 6.3% (chlorobenzene); 7.5% (DMF)
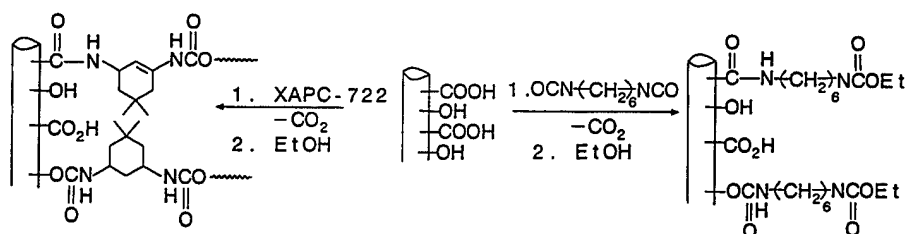
Celion G30-500 fibers were reacted with neat phenylisocyanate at 90 °C after oxidation for various times in HNO_3. The grafting efficiencies were about 30% as the surface acid group concentration on the fibers was varied from 12.5 to 47.1 μeq/g (see Table II).

Table II. Consumption of Acidic Surface Functions on Oxidized
Celion G30-500 Fibers by Phenylisocyanate at 90 °C

HNO_3 Oxidation Time (min)	20	40	60	90
Initial Acidic Groups	12.5	22.7	32.6	47.1
Acidic Groups After PhNCO	8.7	15.0	23.1	31.7
Grafting Efficiency G_e (%)	30	34	29	33

Grafting Acetic Anhydride and Phenylisocyanate to Surface-Bound Amines. Celion G30-500 fibers, grafted with TEPA, had surface amino concentrations from 4.7-45.5 μeq/g. They were reacted in neat acetic anhydride (75 °C, 3 h) and neat phenyl isocyanate (90 °C, 3 h) followed by washing and soxhlet extraction in acetone (3 h). The grafting efficiencies ranged from 50-64% for phenylisocyanate and 49-69% for acetic anhydride.

Starting Amine Concentration (μeq/g)   4.7   18.7   31.3   45.5
G_e (Phenyl Isocyanate) (%)   51   64   50   54
G_e (Acetic Anhydride) (%)   49   69   51   63

Reactions of Surface-Bound Amino Groups with Epoxy Systems of Varying Molecular Weights. TEPA-treated Celion G30-500 fibers were reacted at 80 °C for 19 h with four model epoxides in xylene with phenol as the catalyst: (a) styrene oxide (mwt. 120), (b) EPON 828 (mwt. 378), (c) EPON 834 (mwt. 500) and EPON 1001 (mwt. 1000). The grafting efficiencies of the epoxy models dropped sharply as molecular weight (size) increased (Table III). The values of G_e for epoxy grafting fit the equation: $G_e = K \times M^a$, where K and a were constants and M = mol. wt. (e.g., plots of log G_e versus log M were linear) K = 25700, a = -1.256.

ARXPS/ISS Surface Characterization of Nitric-Acid Treated Carbon Fibers. ARXPS show the surfaces of as-received BASF (Celion G30-500) carbon fibers are appreciably oxidized. The primary carbon/oxygen functionality is C-OH (63% of total oxidized carbon species). Nitric-acid oxidation increases the O/C concentration ratio from 24% (as-received) to 33% (90-min exposure to HNO_3 at 115 °C). The ratio of (carbonyl+carboxyl) groups to

hydroxyl groups increases from 0.52 to 1.3 over this range of HNO_3 oxidations. ISS reveals significant sodium and calcium concentrations on the as-received fibers. After exposure to HNO_3 (60 min, 115 °C), the outermost atomic layers are comprised only of carbon, oxygen, and nitrogen.

Table III. Grafting Epoxy Model Systems to TEPA-Treated Carbon Fibers.
Surface Grafting Efficiencies Vs. Molecular Weight

Model Reactant	Mol. Wt.	Initial Amine Functions (μeq/g)	Amt. Grafted μmol/g	G_e (%)
Styrene Oxide	120	46	31.6	68.7
EPON 828	378	46	6.9	15.0
EPON 834	500	46	3.6	7.8
EPON 1001	1000	46	2.5	5.3

Composites Containing Elastomeric Polyurethane (PU) Interphases. Continuous fiber EPON 830 matrix composites (14 plys) were made from carbon fibers coated with cured polyurethane interphase layers from 500 to 2500 Å thick. The V_f=56%. The ILSSs were measured by three-point bending (ASTM D2344-67) and Izod impact strengths (IS) by ASTM D256-72. Three PU resins were selected with varying stiffness: PU 504/317 (E=138MPa, elongation 29%), PU 504 (E = 7.9 MPa, elongation 290%) and PU 722 (E = 0.5 MPa, elongation 900%). **When the interphases were constructed on TEPA-treated fibers the impact strengths of the fibers increased markedly relative to identical composites without these interphases.** The IS values increased by 1.5 times (PU 504/317), 1.4 times (PU 504) and 2.2 times (PU 722). **Remarkably, most of the increase in IS was achieved with interphase thicknesses of only 1000 to 1500 Å!**

The stiffer interphases (PUs 504/317 and 504) gave little or no decrease in the composites' ILSS. For 504/317 the ILSS were unchanged versus composites with no interphase while those with 504 had ILSS values that were 90-95% of composites with no interphase.

REFERENCES

1. L. T. Drzal, M. J. Rich, M. F. Koenig and P. F. Lloyd, *J. Adhesion*, **16**, 133 (1983).

2. B. D. Agarwal and L. J. Broutman, *Analysis and Performance of Fiber Composites* (John Wiley & Sons, New York, 1980), p. 33.

3. R. V. Subramanian and A. S. Crasto, *Polym. Composites*, **7**, 201 (1986).

4. J. F. Gerard, *Polym. Eng. Sci.*, **28** (9), 568 (1988).

5. J. N. Syltan and F. J. McGarry, *Polym. Eng. Sci.*, **13**, 29 (1979).

6. V. A. Matonis and M. C. Small, *Polym. Eng. Sci.*, **9** (2), 90 (1969).

7. L. J. Broutman and B. D. Agarwal, *Polym. Eng. Sci.*, **14**, 581 (1974).

8. S. D. Gardner, C. U. Pittman, Jr. and R. M. Hackett, *J. Comp. Mat.*, **27** (8), 830 (1993).

9. S. D. Gardner, C. U. Pittman, Jr. and R. M. Hackett, *Comp. Sci. Technol.*, **46**, 307 (1993).

10. B. Y. Low, S. D. Gardner, C. U. Pittman, Jr. and R. M. Hackett, *Comp. Sci. Technol.*, **52**, 589 (1994).

11. J. R. Dauksys, *J. Adhesion*, **5**, 211 (1973).

12. L. D. Tryson and J. L. Kardos, *36th Ann. Conf. on Reinforced Plastic Comp. Inst. SPI*, *2-E* (1981), p. 1.

13. J. H. Crammer, G. C. Tesoro and D. R. Uhlmann, *Ind. Eng. Chem. Proc. Res. Dev.*, **21**, 185 (1982).

14. R. V. Subramanian and A. S. Crasto, *Polym. Composites*, **7**, 201 (1986); S. Dajardin, et al., *J. Mater. Sci.*, **21**, 4342 (1986).

15. J. P. Bell, J. Chang, H. W. Rhee and R. Joseph, *Polym. Composites*, **8**, 46 (1987); H. W. Rhee and J. P. Bell, ibid., **12**, 213 (1991).

16. J. Chang, J. P. Bell and R. Joseph, *SAMPE Quarterly*, **18** (3), (1987).

17. A. S. Wimolkiatisak and J. P. Bell, *J. Appl. Polym. Sci.*, **46**, 1899 (1992) and *Polym. Composites*, **10**, 162 (1989); J. Chang, J. P. Bell and S. Shkolnik, *J. Appl. Polym. Sci.*, **34**, 2015 (1987).

18. J. F. Gerard, *Polym. Eng. Sci.*, **28** (9), 568 (1988).

19. M. Kodama, I. Karino and J. Kobayashi, *J. Appl. Polym. Sci.*, **33**, 361 (1987).

20. T. Skourlis, T. Duvis and C. D. Papaspyrides, *Composites Sci. Technol.*, **48**, 119 (1993).

21. C. U. Pittman, Jr., G. R. He, B. Wu, L. Wang, S. D. Gardner, Proceedings of the First International Conference on Composite Engineering (ICCE/1), D. Hui, Editor, Aug. 28-31 (1994), New Orleans, LA, pp. 403-404 and The Fifth International Conference on Composite Interfaces (ICCI-V). Molecular Interactions and Structure, Ishida, Ed., June 20-23 (1994), Chalmers University of Technology, Göteborg, Sweden

22. G. R. He, PhD Thesis, Mississippi State University, 1994.

23. Wei Li, MS Thesis, Mississippi State University, 1995.

24. Z. Wu, MS Thesis, Mississippi State University, 1994.

25. Z. Wu, C. U. Pittman, Jr. and S. D. Gardner, *Carbon*, in press (1995); *ibid*, submitted (1995).

TAILORING THE STRUCTURE OF POLYMER BRUSHES THROUGH COPOLYMER ARCHITECTURE

DILIP GERSAPPE, MICHAEL FASOLKA, RAFEL ISRAELS AND ANNA C. BALAZS
Materials Science and Engineering Department, University of Pittsburgh, Pittsburgh, PA. 15261.

ABSTRACT

Polymers tethered by one end onto a solid surface are referred to as polymer "brushes". We consider brushes composed of copolymers that contain both A and B monomers. The A monomers are compatible with the surrounding solvent, while the B sites are solvent-incompatible. The solvent incompatibility causes the B sites to associate into domains or clusters within the layer. We use Monte Carlo computer simulations and self-consistent field calculations to determine the effect of copolymer architecture on the structure of the polymer brush. In particular, we alter the copolymer sequence distribution (the arrangement of the A and B monomers along the length of the chain) and determine how both the vertical and lateral morphology of the brush are effected by these variations. The results provide guidelines for controlling the size and shape of the B domains, and consequently, the morphology of the tethered layer.

INTRODUCTION

A polymer "brush" consists of a dense layer of chains that are anchored by one end onto a solid surface. The behavior of brushes has come under considerable scrutiny in the last several years [1]. Interest in these systems stems from the fact that the tethered chains can be used to control the properties of the underlying substrate. For example, tethering chains onto a non-reactive surface can facilitate the adsorption of a subsequent layer or coating. The brush, sandwiched between the solid surface and the outer coating, acts as a "primer" or glue between the two layers. To take full advantage of these surface-modifying properties, we must enhance our understanding of how the composition of the tethered chains affects characteristics of the brush.

In this paper, we probe the effects of chain composition by examining brushes that contain different AB copolymers. The A sites are considered to be compatible with the surrounding solvent, while the B sites are solvent-incompatible. The solvent incompatibility drives the B sites to undergo a mutual attraction. We will refer to these interacting sites as "stickers". (The A sites, on the other hand, are non-interacting.) We first determine the behavior of brushes where the B sites, or stickers, are located just at the tops of the chains [2,3]. We then investigate brushes where the stickers are distributed along the length of the tethered polymers [4]. Specifically, in the first study we use Monte Carlo computer simulations to model the behavior of self-avoiding, grafted polymers that contain attractive sites on the free ends [2]. As we demonstrate below, the mutual attraction between these ends causes the chains to aggregate into clusters. However, the interaction not only alters the structure, but also enhances certain properties of the layer. In particular, the attraction effectively "pulls" the ends out of the bulk of the brush: now, all the ends lie exposed near or at the top of the layer. (In the absence of this interaction, the ends lie dispersed and buried within the brush.) Consequently, they can readily react with subsequent polymer chains or an additional coating. Thus, adding the attractive end-groups provides an effective means of improving the adhesive properties of the layer.

In the second investigation, we combine Monte Carlo simulations and numerical self-consistent field (SCF) lattice calculations to determine the properties of brushes in which the stickers (and non-interacting sites) are distributed along the length of the each chain [4]. Here, we alter the sequence distribution in these AB copolymers to determine how both the vertical and lateral morphology of the brush are affected by such variations. The results provide guidelines for controlling the size and shape of the B domains, and consequently, the morphology of the tethered layer.

THE MODELS

In our Monte Carlo simulations [2], we consider systems of monodisperse, grafted copolymers. The chains are modeled as self-avoiding random walks on a three dimensional, cubic lattice. Each chain is anchored at one end to the $Z = 1$ plane, which represents the surface of a solid substrate. We use the bond fluctuation model [5,6] to simulate the motion of the polymers. We introduced an attractive interaction, Δ, between the sticker sites. This parameter exerts an effect through the Metropolis algorithm [7]: movements that reduce the energy of the system are accepted with unit probability and movements that increase the energy of the system are weighted by a Boltzmann factor.

The size of the lattice in our simulations was 64 x 64 x 156 sites, the largest dimension being along the Z direction. Periodic boundary conditions were imposed in the X and Y directions, while the Z direction was bounded by impenetrable hard walls at $Z = 1$ (the grafting surface) and $Z = 156$. The system was equilibrated by running the simulation for at least 2×10^5 Monte Carlo steps, where each Monte Carlo step involved $N_{chain} \times (N_{beads})^3$ attempted moves. (The parameter N_{chain} refers to the number of chains in the system and N_{beads} refers to the number of sites or beads on each chain.) The chain length was 36 segments for all the simulations. In the first part of the study, the stickers are located on the free ends of the chains and the number of these terminal stickers is varied. The results were averaged over three to five independent runs for each system.

In the second part of the study, we use these Monte Carlo simulations and self-consistent field theory to determine the effect of copolymer sequence distribution. Our self-consistent field method is based on that developed by Scheutjens and Fleer [8], which in turn is based on a Flory-Huggins approach, combining Markov chain statistics with a mean-field approximation. The equations in this model are solved numerically and self-consistently. The self-consistent potential is a function of the polymer segment density distribution and the Flory-Huggins interaction parameters. The effect of randomness on the properties of copolymers was first incorporated into the SCF model by van Lent and Scheutjens [9]. Here, each monomer has a finite probability of being either an A or B site. Thus, their model introduces an annealed randomness, where the ensemble of sequence distributions in the system is allowed to fluctuate. Consequently, it is difficult to isolate the effect of systematically varying the sequence distribution through this model.

We adopt a different approach to specifying the randomness of the chains [4]. We consider each polymer as a separate molecule and fix its sequence distribution at the start of the calculation. This models a quenched or frozen randomness, where each chain retains its sequence distribution throughout the calculation. For all the SCF results presented in this paper, each system involved specifying the sequence distribution of 2500 individual chains and all the results were averaged over five different realizations of these systems. In addition, the Flory-Huggins χ parameter characterizing the A-B interaction was fixed at $\chi_{AB} = 1.0$. The B-solvent interaction was described by setting $\chi_{BS} = 1.0$, while the A-solvent interaction was given by

χ_{AS} = 0.0. The calculation was performed for a chain length of 100 units, keeping the grafting density fixed at 15%.

In both the Monte Carlo and SCF calculations, the sequence distribution of each chain is set as follows. We let the variables P_A and P_B denote the fraction of A and B monomers in the molecule, respectively. Given a site A on the chain, the conditional probability that the next site is a B monomer is given by the parameter $P_{A \to B}$. We define an order parameter, f, through the following equation [10]:

$$P_A\, P_{A \to B} = (P_A P_B)^{1/2}\, f \qquad\qquad (1)$$

where f lies between 0 and 1. For all these calculations, we chose $P_A = P_B = 0.5$. In this case, $f \to 0$ corresponds to a diblock copolymer, f = 0.5 represents a purely random chain and f = 1 corresponds to an alternating chain.

RESULTS AND DISCUSSION: STICKERS LOCATED AT FREE ENDS

Effect of the number of terminal stickers

The structure of the grafted layer depends on the interplay of a number of variables, such as the number of stickers, the grafting density, the chain length and the attractive energy between the stickers. In this paper, we probe the effect of the first two parameters. (The effects of chain length and sticker attraction in the case where the grafted chains contain a single terminal sticker is described in reference 3.) We start by determining the effect of the number of terminal stickers on the morphology of the layer. In particular, we studied systems that had 3, 5 and 9 functional groups on the free end of each chain. The grafting density (the number of chains per unit area of grafting surface) was fixed at 12%, or a total of 122 tethered chains. The interaction energy between the stickers was set equal to -1.2 kT.

We calculated ρ (z), the density profiles of all the monomers in the brush as a function of Z. The density profiles are calculated by counting the total number of monomers present in a particular plane in the Z direction. This sum is then normalized by setting $\Sigma \rho$ (z_i) = 1, where i designates the specific plane. The density profiles for the various examples are shown in Figure 1, where we also plotted the curve for the case of no stickers.

In these plots, the oscillatory behavior near Z = 1 arises from our choice of the bond fluctuation algorithm to model the grafted layer and has been observed in other simulations of polymer brushes using this technique [11]. The region 5 < Z < 30 represents the bulk of the brush, while the Z > 30 domain represents the top of the layer. The density profiles for the 3, 5, and 9 sticker polymers show strikingly different characteristics. The 3 sticker system exhibits a density profile that is identical to the unperturbed, no sticker case. Relative to the 3 sticker example, the density profile for the 5 sticker case shows an enhancement in the polymer density near the top of the layer. When there are 9 stickers on the ends of the chains, the density profile in the bulk region remains fairly constant, but lies lower than the corresponding values for the 3 and 5 sticker cases. There is, however, a significant peak near the top of this brush.

The origin of the relatively high polymer concentrations near the top of the layer in the 5 and 9 sticker scenarios can be understood by examining Figure 2, which displays the density profiles for just the sticker sites. As can be seen, the ends with 5 and 9 stickers are confined to a narrow region of Z, which lies near or at the top of the layer. On the other hand, the density profile for the ends with 3 stickers is effectively spread over the entire range of Z values. Thus,

the distinct features in Figure 1 are due to the localization of the end sites at the top of the layer in the instances of 5 and 9 sticky ends.
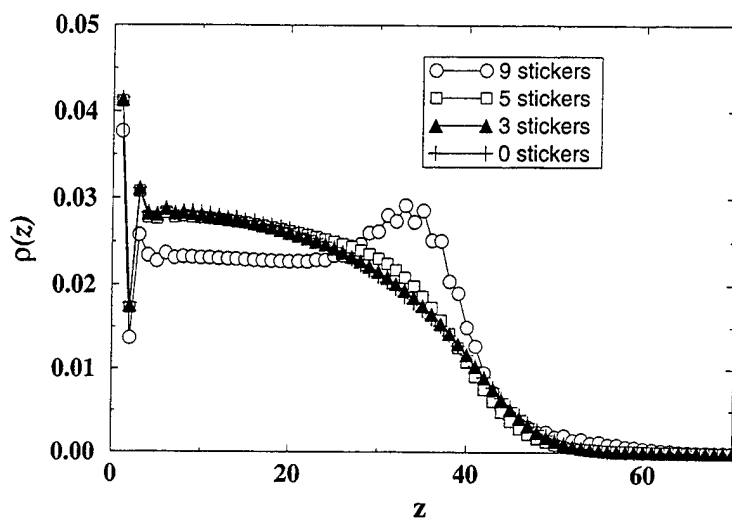
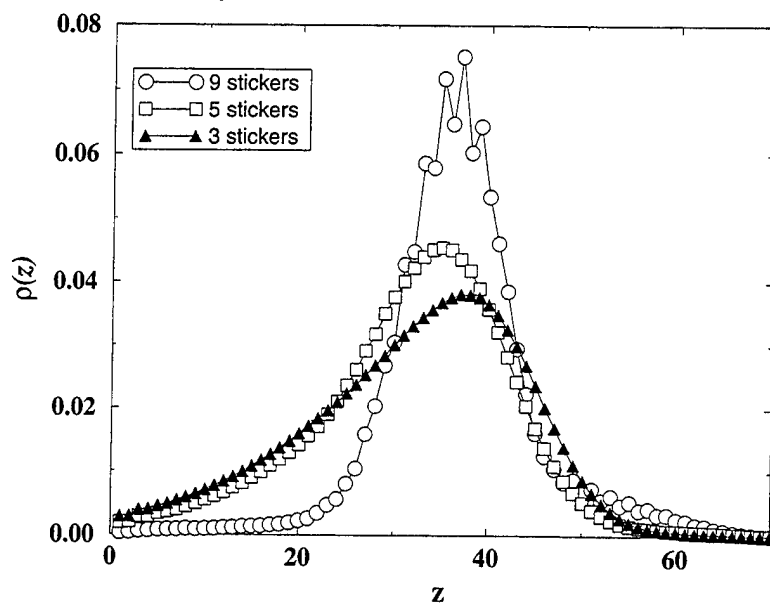Fig. 1 Normalized density profiles for all the monomers in the brush.

Fig.2 Normalized density profiles for just the sticker sites.

The graphical output from the simulation reveals that the ends are not only localized at the top of the layer, but the stickers are also aggregated into distinct clusters [2]. In the case of 3 stickers, there are no signs of clustering. Clustering begins to occur in the case of 5 stickers, while the 9 sticker example shows the most pronounced cluster formation.

Of particular interest is determining how the average height of the layer is affected by the presence of the stickers. The average layer height is calculated as the first moment of the density profile. The 9 sticker case displays the greatest layer height [2]. This phenomenon can be understood by referring to the density profiles in Figure 1. Due to the formation of the clusters in the 9 sticker example, the polymer density is depleted within the bulk of the brush and enhanced near the top of the layer. In effect, the mutual attraction between the stickers pulls the ends out of the lower depths and draws them to the outer surface. Thus, there is an enhanced contribution from polymer segments that lie in the $Z > 30$ range, with a commensurate decrease in contributions from the $Z < 30$ region. Consequently, there is an increase in the average layer height in the case that displays the most pronounced clustering.

Effect of Grafting Density

Another parameter that controls the structure of the layer is the grafting density. As the grafting density is decreased, the chains are less stretched and the height of the brush decreases. Variations in grafting density should also exhibit a pronounced effect on the morphology of the clusters that are formed. To investigate this phenomena, we fixed the number of stickers at 9 (where we know that clustering occurs) and varied the grafting density of the brush. Grafting densities of 12%, 8% and 5% were analyzed. Figure 3 shows the density profiles ρ (z) of all the monomers in the brush for these three grafting densities. As indicated by the pronounced peaks at the top of the layers, clusters form in all these systems. However, the height at which the clusters are located decreases as the grafting density is decreased. In other words, the clusters form closer to the surface at the lower grafting densities.
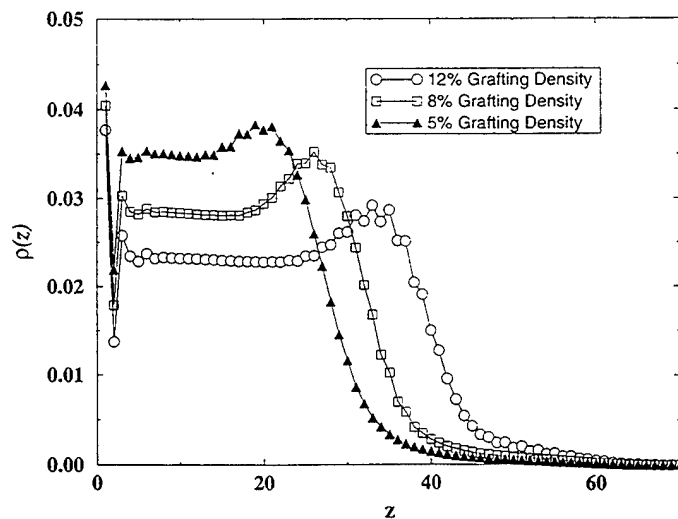

Fig.3   Normalized density profiles for all the monomers in the brush for the three grafting densities: 12%, 8% and 5%.

The variations in grafting density also affect the lateral spacing between the clusters. We found that the clusters lie further apart at lower grafting densities. Decreasing the grafting density increases the average distance between the polymer chains. As the distance between the polymers is increased, the chains must undergo considerable lateral stretching in order for the stickers to associate. As a result, the clusters lie at lower heights and are more spread out. We also observed that the average layer height decreases with the decrease in grafting density.

STICKERS LOCATED THROUGHOUT CHAINS

Effect of Varying the Sequence Distribution

In order to study the effect of sequence distribution on the properties of polymer brushes, we ran the simulations for three particular realizations of the order parameter f: f = 0.1, 0.5 and 1.0. The first case (f = 0.1) corresponds to a polymer brush composed of "blocky" copolymers, the second (f = 0.5) to a brush consisting of purely random copolymers and in the third case, the brush is made up of alternating copolymers.

We first discuss the results obtained from our Monte Carlo simulations, where the surface coverage was fixed at 15% (corresponding to N_{chain} = 153). In Figure 4, we plot the normalized density profiles for the solvophobic component of the brush. The plot clearly shows an enhancement of the solvophobic component density, $\rho_B(z)$, near the grafting surface. This indicates a "layering" transition, but the reason for this behavior is, at first glance, not entirely obvious. As the placement of the monomers along the chain length is random, there should be no preferential plane (in the Z direction) along which clustering occurs.
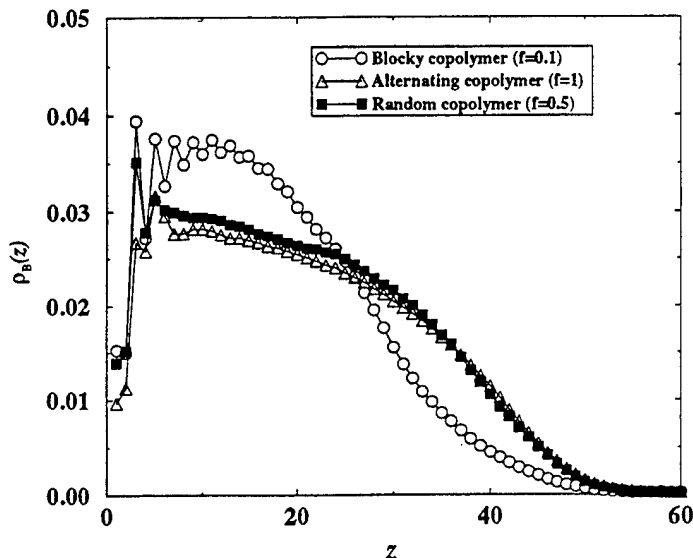
Fig. 4 Normalized density profiles for the solvophobic component. Results obtained from the Monte Carlo simulations.

We believe that this "layering" is a result of chemical heterogeneities that stem from the statistical manner in which we add A and B monomers while growing the copolymers. As a result, the brush is composed of some A-rich polymers and some B-rich polymers, even though the overall composition of the brush is symmetric (equal numbers of A and B monomers). Consequently, when the system is exposed to a selective solvent, the B rich copolymers contract to avoid the solvent. This results in an enhancement of the B monomers near the grafting surface. This effect is most pronounced in the blocky copolymer brush as finite size effects are strongest here. For the random and the alternating brush, the block length (which scales as 1/f) is too small to cause any noticeable aggregation in the Z direction. We note that these compositional fluctuations are always present for finite length polymers and disappear only in the limit of infinitely long chains [12].

The overall density profile of the brush, however, should be independent of f as the brush is compositionally symmetric. This is shown in Figure 5 where the total density profiles (for the A and the B monomers) are plotted for the three values of f. (The slight enhancement of density for the blocky copolymer brush arises from the statistical fluctuation described above.)
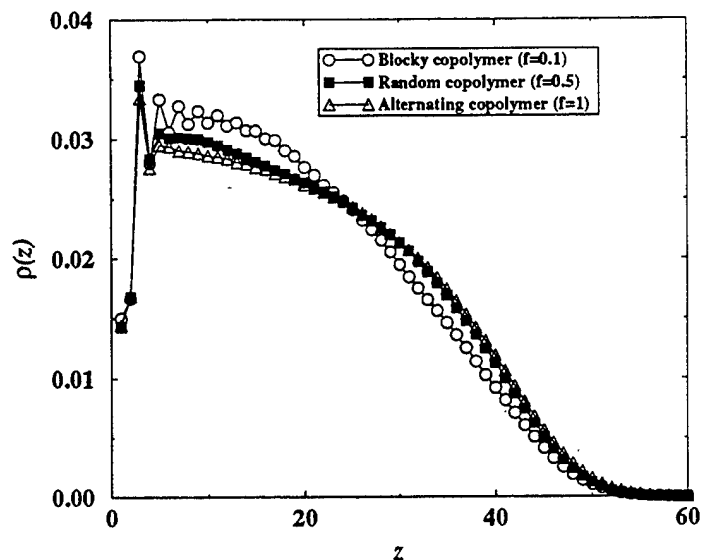
Fig.5   Normalized density profiles for the entire brush. Results obtained from the Monte Carlo simulations.

To check our Monte Carlo result, the overall density profile of the brush in the Z direction was calculated by the SCF method and is plotted in Figure 6. The density profiles for the three f values are now identical, reflecting the compositional symmetry in our system. However, there is still a "layering" effect present in this calculation as the B monomers segregate to the surface (Figure 7). This indicates that the "layering" transition is not an artifact of the Monte Carlo simulations.
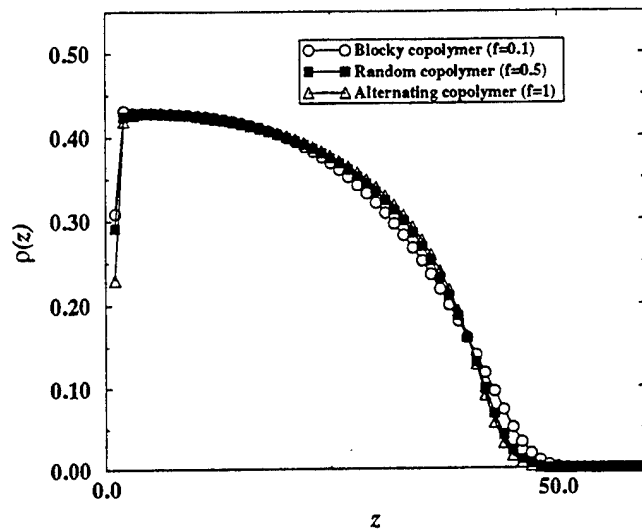

Fig. 6 Normalized density profiles for the entire brush. Results obtained from the SCF calculations.
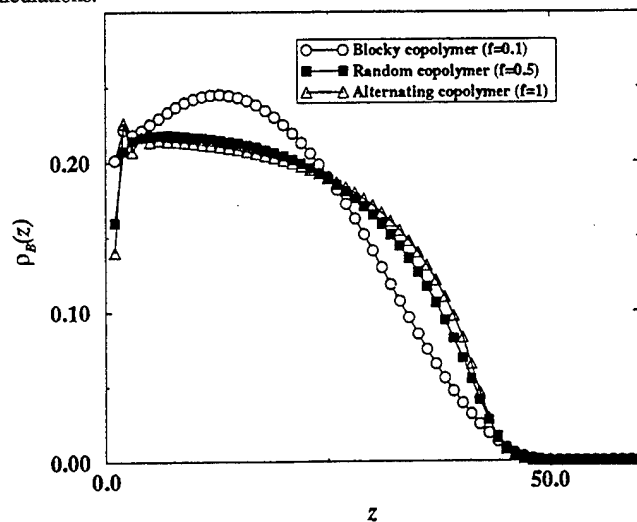
Fig.7 Normalized density profiles for the solvophobic component. Results obtained from the SCF calculations.

To investigate the formation of lateral structures in the polymer brush we define an order parameter following the treatment of Lai [13]:

$$\Psi(x,y) = <\rho_A(x,y) - \rho_B(x,y)> , \qquad (2)$$

where ρ_A is the number of A sites in the Z direction for each point (x,y) and similarly, ρ_B is the number of B sites in this direction. The angular brackets denote an ensemble average in the Monte Carlo simulation. The order parameter, $\Psi(x,y)$, for the three values of f is plotted in Figures 8(a)-(c). The darker regions in these plots denote the B-rich domains, while the lighter areas are the A-rich regions. The variations in the order parameter are clearly evident from these plots. The block copolymer brush shows the largest variations, with large, clearly defined domains of B monomers existing in the system. This behavior is reminiscent of the rippling phase seen in the grafted, incompatible homopolymers [13,14]. The fluctuations in the order parameter are reduced for the random copolymer brush and disappear for the alternating copolymer brush.

(A)

(B)

(C)
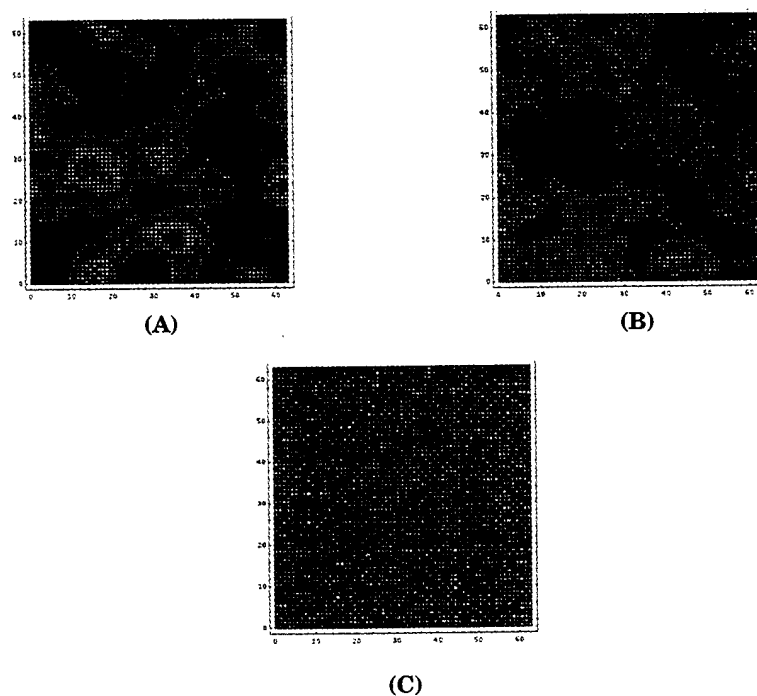
Fig. 8   Plots of the two dimensional order parameter, $\Psi(x,y)$. In (a) f = 0.1, in (b), f = 0.5 and in (c), f = 1.0. The darker regions are the B-rich areas, while the A-rich areas are the lighter regions.

In order to quantify these fluctuations, it is necessary to determine a characteristic length for the B domains. Unfortunately, finite size effects limit our ability to accurately extract these values from our simulations. In spite of this limitation, it can be clearly seen that the copolymer sequence distribution controls both the size and the distribution of these B-rich domains (Figs. 8(a) -(c)).

CONCLUSIONS

In conclusion, we showed how the presence of attractive end-groups can drive grafted chains to aggregate into clusters and thereby, alter the structure of polymer brushes. Using computer simulations, we demonstrated how the structure of the layer can be tailored by varying the number of functional groups (or the block length of stickers) and the grafting density.

The findings presented here show qualitative agreement with recent results by Li and Balazs [3]. They developed a Hamiltonian for grafted polymers that contain a single sticker at the end of each chain. Through the model, they varied the length of the chain and the sticker-sticker attraction. When the attraction between these end-groups was sufficiently strong to overcome the stretching energy of the chains, the stickers aggregated into finite clusters, with the chain ends localized near the top of the layer. Thus, both models point to the ability of the sticker sites to control the lateral and surface properties of the brush.

We note that the formation of clusters within polymer brushes was also predicted to occur when the layer is immersed in a sufficiently poor solvent [15-18]. Here, the chains associate into local bundles to minimize polymer-solvent contact. This behavior alters the lateral properties of the grafted layer, however, the distribution of chain ends in the poor solvent case is much broader [15,19] than presented here or in reference 3.

There are significant advantages to having the majority of the end-groups lie near the top of the layer (as seen in Fig. 3). Specifically, this structure can enhance the adhesive or wetting and lubricating properties of the surface. Thus, our results can provide guidelines for fabricating coatings and films with these enhanced characteristics.

We also examined the case where the stickers, or solvophobic B sites, are distributed along the length of the chains. By combining SCF calculations and Monte Carlo simulations, we could visualize both the vertical and lateral structure of the brush. Our findings show that the overall morphology of the brush is dependent on the sequence distribution of the component copolymers. These results provide guidelines for controlling the size and shape of the B domains, and consequently, tailoring the brush for specific applications.

ACKNOWLEDGEMENTS

REFERENCES

1.   S. T. Milner, Science **251**, 905 (1991).

2. D. Gersappe, M. Fasolka, A. C. Balazs and S. H. Jacobson, J. Chem. Phys **100**, 1970 (1994).
3. W. Li and A.C. Balazs, Molecular Simulations **13**, 257 (1994).
4. D. Gersappe, M. Fasolka, R. Israels and A. C. Balazs, submitted, Macromolecules.
5. I. Carmesin and K. Kremer, Macromolecules **21**, 2819 (1988).
6. H.P. Deutsch and K. Binder, J. Chem. Phys. **94**, 2294 (1991).
7. N. Metropolis , A.W. Rosenbluth, M.N. Rosenbluth, A.H. Teller, and E. Teller, J. Chem. Phys. **21**, 1087 (1953).
8. G. Fleer, M. A. Cohen Stuart, J. M. H. M. Scheutjens, T. Cosgrove and B. Vincent, Polymers at Interfaces, (Chapman and Hall, London, 1993).
9 . B. van Lent and J. M. H. M. Scheutjens, J. Phys. Chem. **94**, 5033 (1990)
10. A. C. Balazs, I. C. Sanchez, I. R. Epstein, F.E. Karasz and W.J. MacKnight, Macromolecules **18**, 2188 (1985); C. Yeung, A. C. Balazs and D. Jasnow, Macromolecules **25**, 1357 (1992).
11. P. Lai and K. Binder, J. Chem. Phys. **95**, 9288 (1991).
12. A. R. Nesarikar, M. Olvera de la Cruz and B. Crist, J. Chem. Phys. **98**, 7385 (1993).
13. P. Y. Lai, J. Chem. Phys **100**, 3351 (1994).
14. J. F. Marko and T. A. Witten, Macromolecules **25**, 296 (1992); G. Brown, A. Chakrabarti and J. F. Marko, Europhys. Lett. **25**, 239 (1994).
15. P. Lai and K. Binder, J. Chem. Phys. **97**, 586 (1992).
16. C. Yeung, A.C. Balazs and D. Jasnow, Macromolecules **26**, 1914 (1993).
17. K. Huang and A.C. Balazs, Macromolecules **26**, 4736 (1993).
18. G. Grest and M. Murat, Macromolecules **26**, 3108 (1993).
19. R. Israels and A.C. Balazs, preliminary results from self-consistent field calculations on end grafted chains with stickers.

POLYMER BRUSH-LINED MEMBRANES FOR FLOW AND FILTRATION CONTROL

EDITH M. SEVICK*, FRANK A. BRUCE*, AND DAVID R.M. WILLIAMS**
*Department of Chemical Engineering, University of Colorado, Boulder CO 80309-0424
**Department of Applied Mathematics, Research School of Physical Sciences and Engineering, Australian National University, Canberra AUSTRALIA.

ABSTRACT

We describe the flow and filtration control imparted to membranes through the adsorption of polymer brushes onto the interior pores. The brushes exhibit a negative Poisson's ratio, i.e. they swell under shear, and as a result behave as sensors and valves controlling the flow and filtration through the pore. The valve-behavior of brushes adsorbed onto cylindrical pores displays the same constant discharge control but also exhibits a critical shear rate for brush swelling.

I. INTRODUCTION

The control of liquid flow is accomplished conventionally by a system of sensors and valves: the sensors measure the flow and the valves are adjusted if this flow is not the desired set point. Recently, Sevick & Williams [1] proposed a novel microvalve which does not involve any movable parts or any external feedback control loop. The microvalve consists of a conduit lined with a polymer brush, i.e., a collection of end-grafted polymers absorbed onto the conduit surface, Figure 1. The polymers are grafted so densely that they overlap strongly and are forced to stretch away from the surface forming an elastic layer. Recent experiment [2,3] and theory [4,5] demonstrated that a polymer brush has a negative Poisson's ratio, i.e. it swells under an applied shearing force, and that there is little flow penetration into the brush [6]. The valve-like response of two sandwiched brushes to an applied pressure drop was shown theoretically and can be simply explained as follows. An applied pressure differential results in laminar flow which imposes a shear stress on the brush, causing brush expansion. This brush swelling reduces the cross-sectional area for solvent flow, and thereby readjusts the prevailing shear stress. Both the shearing force and the brush swelling are determined self-consistently, resulting in a non-linear pressure-discharge relation.
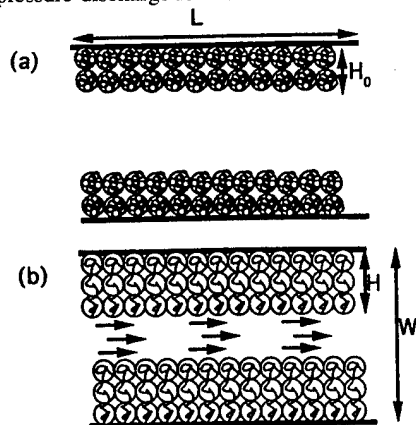

FIGURE 1: (A) The good-solvent planar brush microvalve. The planar polymer brushes, each of height H_0, are grafted to opposing planes of length L, width Z, and separation W << Z. (B) When a good solvent flows across the planes, the brushes swell to a height $H > H_0$. The flow penetrates the brushes only weakly so that the cross sectional area for flow is reduced. The brush swelling produces a closing of the flow area and a dramatic reduction in discharge results.

To clearly demonstrate this, consider two opposing brushes where the grafting planes are separated by W and lined with polymer brushes of height H. The fluid penetrates only weakly into the brushes and consequently the pressure-driven flow is laminar and through a channel of effective height W-2H

$$Q = \frac{\Delta P}{L} Z(W - 2H)^3 / (12\eta) \qquad (1)$$

where Q is discharge or volumetric flow rate, LxZ is the dimension of the grafting planes, η is the solvent viscosity and ΔP is the pressure drop. The novel feature of this assembly is that H is a function of the pressure drop; this is particularly important as the discharge depends upon the third power of (W-2H). Hence, even a weak dependence of H on ΔP provides a strong non-linear ΔP dependence on the discharge.

This expandable brush lining might be an attractive agent for modifying membranes to achieve specific flow and filtration properties. By adsorbing brushes into the interior pore walls, each pore becomes dynamic, responding to pressure fluctuations and providing microvalve action. Depending upon the grafting density and polymer chain length, the brush response in the pores will limit or maintain the flux through the membrane despite an increasing applied pressure. Moreover, the effective pore size depends upon the applied pressure drop, allowing the filtration properties of the membrane to change with the flow rate. This flow and filtration control is the subject of this proceedings; however, other brush effects are also envisioned. For example, a polymer brush adsorbed on the exterior, downstream surface forms a directional valve or diode [7]. The brush spills over the pore aperture, forming a gating valve. Downstream flow is impeded until a critical pressure is achieved, and upstream flow is blocked.

In this proceedings, we describe flow and filtration properties of brush-lined membranes. In the following section, we review the single, planar brush-valve and in Section III we extend this analysis to cylindrical pores. In Section IV we consider briefly the role of pressure drop upon filtration properties and how this is role is modified by a distribution in the membrane pore size.

II. MICROVALVE CONTROL OF A PLANAR BRUSH

In this section we review briefly the description of the planar brush-valve behavior, originally detailed in Sevick & Williams. Based upon the previous equilibrium arguments, we find an equilibrium expression for the brush height as a function of shearing force acting at the brush surface. However, in the brush-valve, the shearing force is NOT a direct or controllable variable, but instead depends upon the applied pressure drop. We construct a continuum mechanical expression describing the dependence of the surface shearing force upon the applied pressure drop for any given brush height. Solving the equilibrium and mechanical expressions simultaneously with Equation (1) provides a simple prediction for the discharge as a function of applied pressure drop. This is detailed in the remainder of this section.

Each tethered chain in a brush can be pictured as a connected sequence of blobs [8]. The blobs are of radius $\xi = R_F^{5/2} / L^{3/2}$ where R_F is the Flory radius and L is the end-to-end distance of the chain. Within each blob the monomers are locally correlated as in a Flory chain. For

214

distances larger than the blob size, the blobs act as hard spheres. The number of blobs per chain is given by $N_b = (L/R_F)^{5/2}$. The brush is an assembly of chains end-grafted onto the grafting plane with density $1/d^2$ where d is the distance between grafting points. The grafting density is assumed to be large, i.e. the chains overlap. When the brush assembly is sheared, the free-chain-ends are displaced distance X in the x direction, the chain is tilted, and the end-to-end distance L is increased. The number of blobs per chain, N_b increases with L further enhancing the excluded volume interaction between blobs. As a consequence the brush will swell: the height of the brush changes from H_O to H. This is the mechanism for brush swelling proposed by Barrat [3]. To analyze the expected degree of swelling and chain tilt with applied shear, the free energy of a chain in the brush assembly can be expressed [1,3] as

$$F_{chain} = \frac{1}{2}kT\frac{L^2}{N_b\xi^2} + kT\xi^3 N_b^2 \upsilon^{-1} - F_\parallel X \qquad (2)$$

where the volume per chain is $\upsilon = d^2 H$. The first term represents the stretching penalty of a Gaussian chain of blobs [9] that opposes brush swelling and shear, the second term is the excluded volume interactions amongst blobs that promote brush swelling, and the final term is the work performed by the shearing force $F_\parallel$ which tilts the chains, displacing the free chain-end distance X in the x direction. Here H_o is the unsheared brush height $H_o = (2/5)^{1/3} d^{-2/3} R_F^{5/3}$.

We now construct the equilibrium and continuum mechanical equations necessary for predicting microvalve behavior. Minimizing the free energy under shear yields two equations, $\partial F/\partial\varepsilon = 0$ and $\partial F/\partial\Delta = 0$, where $\varepsilon = X/H_0$ and $\Delta = H/H_0$ describe x-displacement and swelling under shear. These two equations are combined to give an explicit equilibrium relation between the dimensionless shearing force, $f = F_\parallel\xi_0/kT$, and swelling Δ [1]

$$f = \frac{5}{2}\Delta^{-3/2}(\Delta^3 - 1)^{1/2}(2 - \Delta^3)^{-3/4} \qquad (3)$$

which has the form shown by filled circles in Figure (2). This is the equilibrium relationship describing the brush height for an applied shearing force. The mechanical equation, relates the shearing force acting
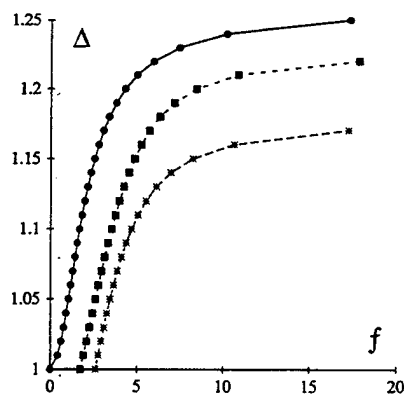

FIGURE 2: The brush swelling, $\Delta = H/H_o$, versus the dimensionless shear force per chain, $f = F_\parallel\xi_0/kT$, according to the Barrat mechanism [3] for planar grafting plane (solid line with filled circles) and for concave grafting surface with $H_o/R = 0.78$ (filled squares) and $H_o/R = 0.80$ (asterisks). At very large forces, the planar brush height grows to a maximum of 125% of the unsheared brush height. The maximum brush swelling decreases with increasing H_o/R.

at the elastic brush surface to the applied pressure drop and is next derived. As shown in [5] the flux through the brushes is insignificant in comparison to the discharge through the brush-free portion of the conduit. Nevertheless, the pressure-driven flow through the brush will place a shearing force along the contour of the chains. We sum the shear acting along the chain contour in approximate manner, assume that force is wholly localized at the tip of the chain, and is equal to $F_{||}$. The pressure within the root and bulk of the brush, i.e. all but the tip-blob, has a force $P'(H-\xi)\xi^2$ where P' is dP/dL. In the tip region, the velocity gradients are important and the force is $\xi^2\sigma = \xi^2\eta\left|\dfrac{dv}{dy}\right| = \dfrac{1}{2}\xi^2(W-2H)P'$. The total force, assumed localized at the tip is then,

$$F_{||} = \frac{1}{2}WP'\xi^2 \tag{4}$$

where ξ, varies with the swelling, Δ, according to

$$\frac{\xi}{\xi_0} = \Delta^{-3/2}\left(2-\Delta^3\right)^{3/4} \tag{5}$$

and is much smaller than W. Since there is a reduction of blob size with brush expansion and shear, the shearing force required to maintain the expanded brush height is reduced. Equations (4) and (5) form the mechanical relation between f and Δ [1] which, taken together with the equilibrium f vs. Δ relation, Equation (3), provide the necessary information to construct dimensionless discharge, q, versus dimensionless pressure, p, descriptions. The q vs. p behavior depends upon $\beta = W/H_0$, the ratio of the conduit size to the no-shear brush height, and is given by filled circles in Figure (3). For very small planar brushes, the pressure discharge behavior is nearly identical to that of conduits without a polymer liner, Figure (3a). Planar brushes which penetrate significantly into the conduit demonstrate a discharge or volumetric flux that is constant over order of magnitude changes in pressure drop, Figure (3b). Planar brushes which fill over 80% into the conduit will exhibit cut-off valve behavior, Figure (3c).

The dimensionless pressure $p = \dfrac{1}{2}WP'\xi_0^3 / kT$ is an important parameter in valve design.

The term kT/ξ_0^3 is the osmotic pressure in the brush [8] and also the elastic modulus of the brush [10]. As the interesting valve behavior occurs for values of p on the order of 1, (Figure 3), the operating range of P' must be roughly $kT/\left(W\xi_0^3\right)$. In other words, the valve effects occur when the applied force per unit area of the brush equals the osmotic pressure [1]. Loosely grafted brushes are "soft", i.e., they have large blob sizes ξ_0, small moduli, and are sensitive to small fluctuations in pressure. In contrast, more densely grafted brushes have smaller blob sizes, larger elastic moduli, and consequently, do not respond as dramatically to pressure fluctuations. The appropriate pressure gradient $P' = kT/\left(W\xi_0^3\right)$ is clearly very sensitive to the blob size ξ_0, and hence to the grafting density. To examine some numerical examples we take $W \sim \xi_0$, so $P' = kT/\xi_0^4$. For a weakly grafted brush $\xi_0 \sim 1000$ Å and $P' \sim 4 \times 10^7$ Pa/m $\sim 10^2$ atm/m. For a membrane of thickness 1000Å this corresponds to a pressure drop of 10^{-5} atm. However, for a more densely grafted brush with blob size $\xi_0 = 100$ Å and again with $L = 1000$ Å, the pressure drop is much larger, 0.1 atm.
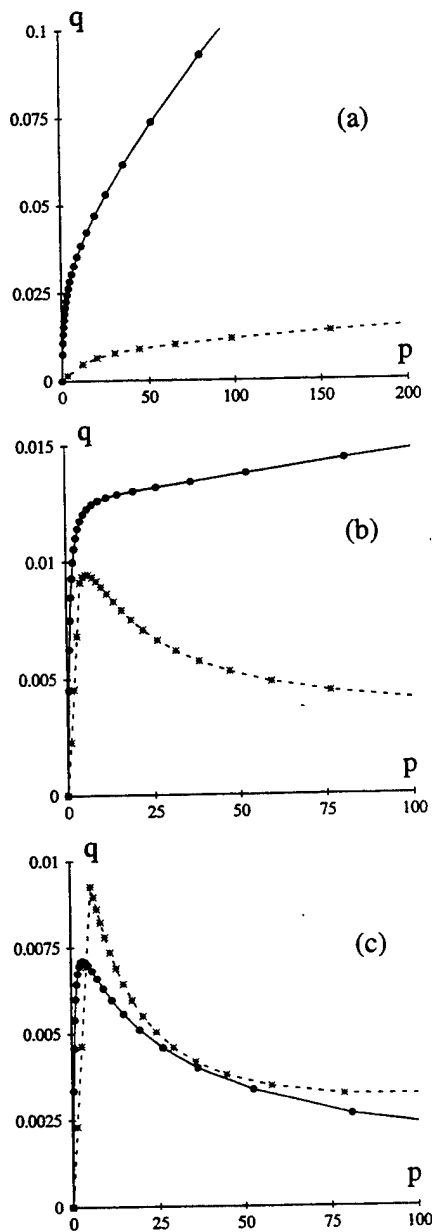
FIGURE 3: The dimensionless discharge q versus the dimensionless pressure p for values of $\beta = H_0/(W/2)$ for planar brush (filled circles) and $\beta = H_0/R$ for cylindrical brushes (asterisks) for various flow regimes. Expressions for p and q are below.

(a): $\beta = 0.74$. The cross sectional area for flow is initially large. At low pressures the height of the brush is not changed significantly by the flow. The discharge is thus proportional to the pressure. At higher pressures, the force on the planar brush is large and it expands to its maximum height of $2^{1/3}H_0$ but the cross sectional area for flow is large and the discharge is again proportional to the pressure. In contrast, the cylindrical brush swells to reduce the cross sectional area sufficiently to render an almost constant and lower discharge. Its maximum swelling is less than that of the planar brush. (b): $\beta = 0.78$. The cross sectional area for flow is reduced from (a). The discharge in the planar brush valve grows initially and levels off to a nearly constant discharge. In comparison, the cylindrical brush valve does not swell with initial increase in pressure until a critical pressure is achieved beyond which swelling occurs. Increased pressure further swells the brush, decreasing the flux.

(c): $\beta = 0.80$. The planar brush exhibits cut-off behavior, i.e., the brush swells continually as pressure is increased from 0. The flux increases until a critical pressure beyond which the swelling dramatically reduces the cross sectional area for flow and hence the discharge. In contrast, the cylindrical valve does not swell as pressure is increased from 0 and flow is standard poiseuille flow. At a critical pressure, the discharge is maximum and the brush begins to swell, reducing the cross sectional area for flow and the discharge. At larger pressures, the increase in discharge with pressure and the decrease in cross sectional area balance in such a way that discharge is nearly constant.

PLANAR BRUSH-VALVES $\qquad q = 6Q\eta\xi_0^3 / \left(kTW^2Z\right) \qquad p = WP'\xi_0^3 / (2kT)$

CYLINDRICAL BRUSH-VALVES $\qquad q = 16Q\eta\xi_0^3 / \left(\pi kTR^3\right) \qquad p = DP'\xi_0^3 / (kT)$

217

III. MICROVALVE CONTROL OF BRUSHES ADSORBED ON CONCAVE SURFACE

The microvalve behavior of a polymer brush adsorbed onto the interior wall of a cylindrical conduit should differ from that of the planar brush-valve in two ways. Firstly , the discharge, Q, through a cylindrical pore depends pore dimension, radius R, to the fourth power, rather than the third power. As such the cylindrical brush-valve should be even *more* sensitive to pressure fluctuations than the planar brush-valve of the previous section. This is easily seen through comparison of Equation (1) with that of discharge through cylindrical conduit:

$$Q = \frac{\Delta P}{L} \pi (R - H)^4 / (8\eta) \tag{6}$$

Again, since brush height, H, varies with the shearing stress or applied pressure drop, the discharge Q is nonlinear in ΔP. Secondly, we might expect that the elastic moduli of a cylindrical brush is larger than that of a planar brush with the same grafting density, and hence the cylindrical brush-valve is *less* sensitive to small pressure fluctuations. In the spirit of the Alexander -deGennes model where each chain is stretched equivalently and the ends of the chain are located at the tip of the brush, the volume per grafted chain is smaller for convex grafting surfaces than for planar ones. Consequently, the larger excluded volume interactions enhance chain stretching, resulting in larger brush heights. This result is available from the free energy expression, Equation (2), where the volume per unit chain, υ is now $\left(H - H^2 / 2R\right)d^2$ and H_0/R, the ratio of brush height to pore radius, is the curvature factor. The blob size varies along the chain, being largest at the grafting root and smallest at the crowded brush tips. However, for simplicity we complete our brush description using an average blob size ξ_0 and ξ, with no-shear and under shear, respectively. The no-shear brush height, H_0, is found from minimization of the free energy with respect to the chain's end-to-end distance or brush height:

$$H_0 = (2/5)^{1/3} d^{-2/3} R_F^{5/3} \left[\frac{1 - 3H_0 / 2R}{(1 - H_0 / 2R)^2} \right]^{1/3} . \tag{7}$$

Thus, larger curvature factors provide more highly stretched chains, smaller blob sizes, larger elastic moduli, and brush-valves that are less sensitive to small pressure fluctuations.

To compare the sensitivity of the cylindrical and planar brush valves, we construct the equilibrium and mechanical expressions that are analogous to Equations (3) and (4). The height of the brush under shear is found from minimization of the free energy with respect to ε and Δ and provides an equilibrium f vs. Δ relationship in the form of two equations which reduce to the planar brush-valve case in the limit $H_0/R \rightarrow 0$. The brush height as a function of applied shearing force is shown in Figure (2) for a cylindrical brush for $\beta = H_0/R = 0.78$ (squares) and 0.80 (asterisks). Note that with cylindrical brushes, the larger the no-shear brush height, the smaller the maximum stretching. More importantly, with larger brushes there exists a critical shearing force required for the onset of brush swelling. It is interesting to note that Klein's surface force measurements exhibited a critical shearing force [2]. The mechanical f vs. Δ

218

relation is found by summing the shearing force acting along the contour of the chain and assuming that it is wholly localized at the tip. The shearing force acting upon chain root and bulk is identical to that found in the planar geometry; however, the shear acting on the tips

differs: $\sigma = \eta \left| \dfrac{\partial v_x}{\partial r} \right| = \eta \dfrac{\partial}{\partial r} \left(\dfrac{P'}{4\eta} \left(R^2 - r^2 \right) \right)$. The total shearing force localized at the brush tip is

$$F_{\parallel} = \frac{1}{2} P' (R + H) \xi^2 \tag{8}$$

As the blob size ξ decreases with swelling, the shearing force required to sustain brush swelling decreases. If the brush height is comparable to the pore dimension, then the shearing force is larger in the cylindrical case than that required in the planar brush case. This is expected as the blobs decrease in size from root to tip and consequently, the brush is more "stiff" requiring larger shearing force to affect and maintain expansion.

Combining the equilibrium f vs. ΔP, Figure 2, the continuum mechanical expression, Equation (8), and Equation (6) provides dimensionless discharge versus pressures predictions. Figure (3) shows p vs. q for three different brush heights, $\beta = 0.74, 0.78,$ and 0.80 where the planar brush exhibits linear, constant-discharge, and cut-off valve behavior and the cylindrical brush exhibits nearly constant-discharge after a critical pressure beyond which valve effects occur.

IV. FILTRATION CONTROL OF MEMBRANE WITH PORE SIZE DISTRIBUTION

Membrane pores are unlikely to be uniform in size and instead possess a distribution of pore sizes. By adsorbing polymer brush and applying a pressure drop, the "effective" pore size distribution will vary as a function of pressure drop. For example, upon adsorption of a chain of a given size, the smallest pores will have very small channels for flow which will decrease dramatically with shear (see Figure 3c). At the same time, larger pores will be relatively unaffected (Figure 3a) while intermediate pores will show constant discharge behavior over a range of pressure drops (Figure 3b). In this way, the filtration behavior of the brush-lined membrane is "dynamic", behaving as different membranes by simply varying the pressure drop across the membrane. Currently, one of us (FAB) is constructing discharge and effective "porosity" descriptions of membranes with various pore size distributions and with constant grafting density. It should be noted that grafting density of physi-sorbed chains may vary from pore to pore, depending upon the pore curvature. There exists no theory nor experimental results which detail this.

V. CONCLUSIONS

In this proceedings, we have reviewed our description of planar brush valves, extended the description to cylindrical pores and discussed briefly how these predictions will impact the flow and filtration control of membranes with adsorbed polymer brushes. These descriptions were prompted by recent surface force measurements made by Klein [2] which were interpreted in terms of negative Poisson's ratio of polymer brushes. Several theories explaining this behavior have been put forth, including our extension to a novel application, polymer brush microvalves.

In order to construct microvalves, these descriptions must be demonstrated experimentally. To this end we have initiated measurements of discharge versus pressure drop across PVP-PS lined track-etched polycarbonate membranes. However, additional studies are needed. First, brush swelling under shear must be demonstrated directly using ellipsometry or neutron scattering. Secondly, we must understand and quantify the brush adsorption on the membrane surface; for example, how is grafting density affected by pore size for different chain architectures, i.e. for block copolymers with different anchor block size? These experiments are necessary for verifying and constructing brush-lined membranes with flow and filtration control.

REFERENCES

[1] Sevick and D.R.M. Williams, *Macromolecules* **27**, 5285 (1994).
[2] J. Klein, D. Perahia, and S. Warburg, *Nature* **352**, 143 (1991).
[3] J. Klein, *Pure Appl.Chem.* **64**, 1577 (1992).
[4] J.-L. Barrat, *Macromolecules* **25**, 832 (1992).
[5] V. Kumaran, *Macromolecules* **26**, 2464 (1993).
[6] J. Klein, Y. Kamiyama, H. Yoshizawa, J.N. Israelachvili, G.H. Fredrickson, P. Pincus, L.J. Fetters, *Macromolecules* **26**, 5552 (1993).
[7] E.M. Sevick and D.R.M. Williams, Advances in Porous Materials, MRS Symposium, in press.
[8] P.G. deGennes, *Scaling Concepts in Polymer Physics* (Cornell University Press: Ithaca NY 1979).
[9] P. Pincus, *Macromolecules* **9**, 386 (1976).
[10] (a) G.H. Fredrickson, A. Ajdari, L. Leibler, and J.-P. Carton, *Macromolecules* **25**, 282 (1992). (b) D.R.M. Williams, *Macromolecules* **26**, 5096 (1993). (c) S.A. Safran and J. Klein, *J.Phys.Paris II* **3**, 794 (1993).

Scanning conduction microscopy: a method of probing abrasion of insulating thin films on conducting substrates

J. T. Dickinson[*] and K. W. Hipps[**]
[*]Department of Physics
[**]Department of Chemistry
Washington State University, Pullman, WA 99164-2814

ABSTRACT

The use of Scanning Force Microscopy (SFM) to probe wear processes at interfaces is of considerable interest. We present here a simple modification of the SFM which allows us to make highly spatially resolved measurements of conductivity changes produced by abrasion of thin insulating films on metal substrates. The technique is demonstrated on fluorocarbon polymer thin films deposited on stainless steel substrates.

INTRODUCTION

The scanning force microscope (SFM) is a useful tool for examining the consequences of tribological wear, particularly on inherently flat surfaces such as single crystals. However, on moderately rough surfaces, changes in topography due to tribological loading are often difficult to interpret in terms of wear processes. We have examined the wear of an important class of coatings, namely fluorocarbon thin films deposited on stainless steel, using a simple modification of standard SFM techniques. Metal-coated silicon nitride tips are used to probe current flow between the tip and the conducting substrate. Simultaneous topography and conduction images are acquired. During wear (performed outside of the SFM), localized thinning of the film and exposure of bare metal are easily and unambiguously detected by this method on size scales less than 50 nm. We describe the technique[1] and present results on two types of fluorocarbon thin films. This technique is similar in spirit to the use of combined STM/SFM imaging[2], and spatially resolved potentiometry used recently to image potentials of metallic structures on integrated circuits.[3] Point-by-point measurements of semiconductor conductivity have also been made using an SFM with conducting tips in efforts to probe semiconductor doping profiles,[4] and to provide spatially controlled potentiometry for thin-film structures.[5]

EXPERIMENTAL

Film topography was characterized with a Digital Instruments Nanoscope III scanning force microscope (SFM) operated in the contact mode. SFM scans were acquired at scan sizes ranging from 200×200 nm^2 to 100×100 μm^2 and at tip velocities from 0.2 to 200 μm/s. A simple modification of the SFM allowed simultaneous, spatially resolved measurements of film conductivity. A schematic of the experimental arrangement is shown in Fig. 1. Scanning conduction microscopy (SCM) measurements were made using commercial triangular Si$_3$N$_4$ SFM tips (115 μm from tip to base)[6] that were sputter coated with 300 Å of Au or Ag at room temperature. Both sides of the cantilever were coated to minimize cantilever deflection due to stresses in the metal coating. The SFM was operated in the contact mode, using a nearly constant compressive force, typically 30-60 nN. Assuming a tip radius of 50 nm, the pressure applied by the tip is about 20 MPa, well below the yield stress of most materials. Forces were determined from the measured displacements and quoted force constants for the commercial cantilever beams used in this experiment. The sample was mounted on double stick tape to insulate it from ground. Electrical contact to the conductive cantilever was made through the substrate. The circuit was completed by a 30-μm wire spot welded to the conducting cantilever clamp.
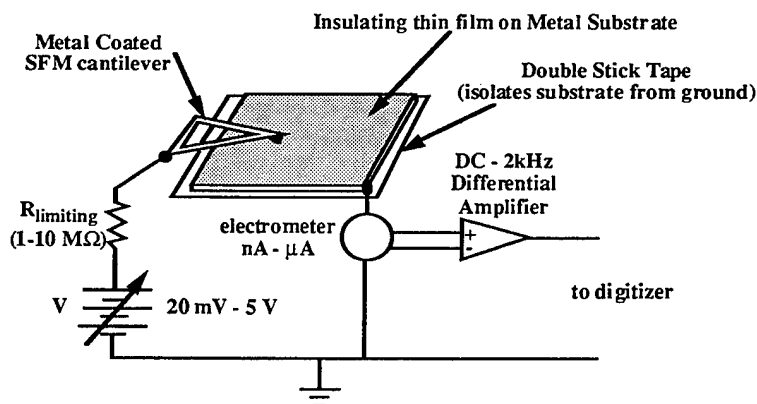
Fig. 1. Schematic diagram of scanning conduction experimental arrangement.

Current measurements were performed with a Keithley 602 electrometer whose output was amplified with a Tektronix 3A9 differential amplifier. The amplifier output was digitized in phase with the acquisition of the SFM image, providing a SCM image that corresponded to the topographical image acquired simultaneously. For improved time resolution, current measurements were occasionally acquired at higher sampling rates during individual scans with a LeCroy 6810 digitizer. A bias voltage (typically, 1 volt) was applied to the sample through a limiting resistor ($R_{limiting}$, typically 1-10 MΩ) to prevent current-induced damage to the metal coating of the SFM tip when metal-to-metal contact was made. When the SFM tip is over a region where the polymer film is thick, the effective tip-to-substrate resistance is high (>10^{12} Ω) and little current flows through the circuit. When the tip crosses a bare region of the substrate, the tip-to-substrate resistance falls to low values (< 10^5 Ω) and the resistance of the circuit is approximately equal to that of the limiting resistor. Regions of intermediate conductivity are also evident. A typical SCM image is a 3-dimensional plot of the current magnitude vs position.

The useful lifetimes of the conducting tips were limited by wear of the metal coating and ranged from 10-30 scans. High currents (> μA) associated with low limiting resistances or high bias voltages, however, dramatically shortened tip lifetimes. Both positive and negative bias voltages produced nearly equal currents with no apparent nonlinearities, suggesting ohmic conduction. Little effort was made to electrically shield the sample; pickup or perhaps ground loops generated small but detectable modulations in the current signal which are visible in the images presented here.

Samples of polytetrafluoroethylene (PTFE) coated stainless steel were prepared in our laboratory by laser ablation deposition.[7-9] PTFE films, ~200 nm thick, were produced by focusing the output of a Lambda Physik EMG 203 MSC laser operating at 248 nm (KrF) through a quartz window onto a PTFE substrate (Goodfellow Chemicals) mounted in vacuum at a pressure of 10^{-4} Pa. The laser was operated at a pulse repetition rate of 10 Hz and a fluence of 4 J/cm^2 per pulse. The ablation products were collected on a stainless steel substrate held at 340 °C. TEM and XRD analysis confirmed that the resulting 300-nm thick films were semi-crystalline PTFE. Stainless steel exposed by wear processes would be oxide coated.

Film abrasion was performed by manually drawing a cotton swab dampened with acetone across the surface. The applied normal force was approximately 2 N over a nominal contact area of 3 mm^2. Although not well controlled, the wear produced by successive linear strokes was indeed cumulative and served as a simple means to demonstrate the technique.

RESULTS AND DISCUSSION

Figures 2(a)-2(e) show 10×10 μm^2 SCM images of a PTFE film on stainless steel prior to and following varying amounts of abrasion. The scans were acquired at a tip velocity of 20 $\mu m/s$ with a 100-mV bias voltage applied through a 10 MΩ limiting resistance; a full-scale reading on the electrometer corresponds to 10 nA. As shown in Fig. 2(a), the nonabraded films are basically insulating. Sampling several regions of the film, we typically observed one or two submicron-sized regions of enhanced conductivity [similar to the small region in the foreground of Fig. 2(a)] in approximately 20% of the scans. These features were reproducible upon repeated scans. The large area of no current indicates that there is no evidence of noise due to discharges that might be generated by contact electrification.[10-12] Spatial resolution, as determined by the smallest patches of conductivity on otherwise non-conducting films, is as small as 20 nm. We suspect that this resolution is significantly influenced by the structure of the conducting patch (steep changes in conductivity) and the morphology of the conducting coating at the tip (i.e., perhaps only a limited portion of the tip is participating). One would expect that small modulations in conductivity would result in much lower resolution.

Figure 2(b) shows a typical SCM scan after a small amount of abrasion (5 strokes of the swab). Some conduction through the film is evident in the SCM scan. All of the conduction zones shown show currents well below the value for tip-to-bare metal contact (10 nA). The total area of the conduction zones (regions exhibiting currents above the noise level) corresponds to 0.6% of the scanned area.

Further abrasion (a total of 8 strokes) increases the area of the conduction zones, as shown in Fig. 2(c). The total area of conduction zones is now 2% of the scanned area. A few of the conduction zones display full scale current readings (10 nA) but most display intermediate values. All of the conduction zones in Fig. 2(c) are a micron across or less, with the majority being much smaller.

Additional abrasion (a total of 16 strokes) further increases the fractional area of the conduction zones, as shown in Fig. 2(d); the conduction zones now occupy approximately 6% of the surface. Most of the conduction zones still display less than full scale current readings.

Wiping the surface with the cotton swab 50 times produces large conduction zones, as shown in Fig. 2(e). Much of the surface now displays full-scale current readings. About 30% of a random sample of 10×10 μm^2 scans on this surface showed large, highly conducting patches. The remainder of the scans displayed large numbers of small, highly conducting regions over most of the scan, similar to the upper third of Fig. 2(e).

SFM topographs acquired simultaneously with these particular SCM scans generally showed little correlation with the regions of conduction. The surface relief actually dropped progressively with abrasion, perhaps due to the removal of particulates (a common problem with thin films grown by pulsed laser deposition). In Fig. 2(f) we show the SFM topograph corresponding to the SCM scan of Fig. 2(e); the highly conducting zone appears to be in a region which tends to be elevated.

Because our abrasion was not well controlled, quantitative analysis of the data is not particularly meaningful. Nevertheless, the fraction of the scanned area occupied by conduction zones is a clean, monotonically increasing function of the "extent of abrasion" (number of strokes). The conducting area fraction increased rapidly over the first several strokes, and subsequently displayed a slower increase proportional to the square of the number of strokes. An improved abrasion apparatus under construction will allow for controlled wear under more technologically interesting conditions.

The influence of the bias voltage on conduction was examined over a range of 10-1000 mV. Basically, the images remain invariant when the current scales are normalized. Over this limited range of tip bias, the measured current is a linear function of bias. Higher biases allowed for the detection of intermediate conducting regions that were in the noise at lower bias voltages. Typical resistances of the tip + film in these intermediate conductivity regions were 10-30 MΩ. Conduction occurred with both plus and minus bias voltages.

The current at a fixed position can be examined as the tip approaches and leaves the surface. Figure 3 shows simultaneous force (a) and current (b) measurements as the tip approaches a region of intermediate conductivity on an abraded PTFE film (275 mV tip bias;
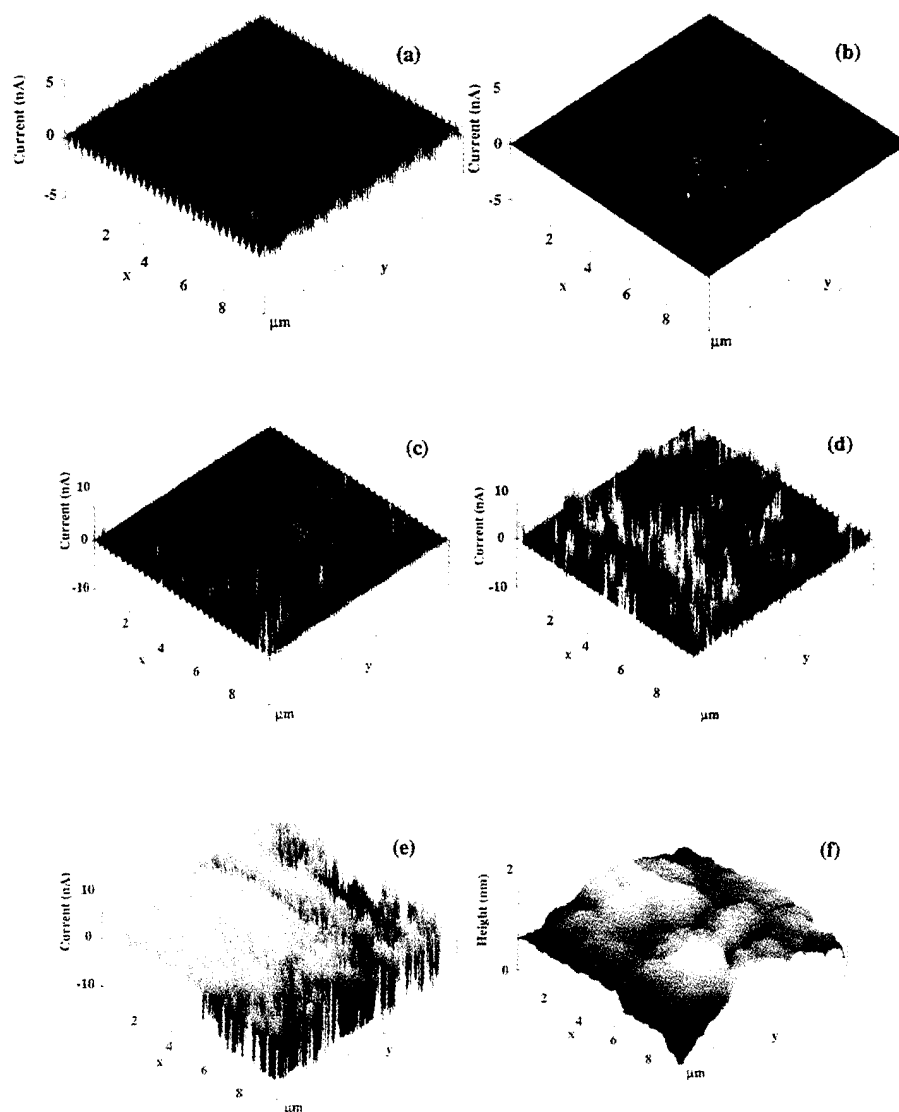
Fig. 2. (a) Scanning Conduction Microscope (SCM) scan of a non-abraded PTFE coated stainless steel sample; (b) SCM scan of the same PTFE film after the light abrasion (5 strokes) (c) SCM scan after a total of 8 strokes; (d) SCM scan after a total of 16 strokes; (e) SCM scan after a total of 50 strokes; (f) SFM topographic scan corresponding to (e).
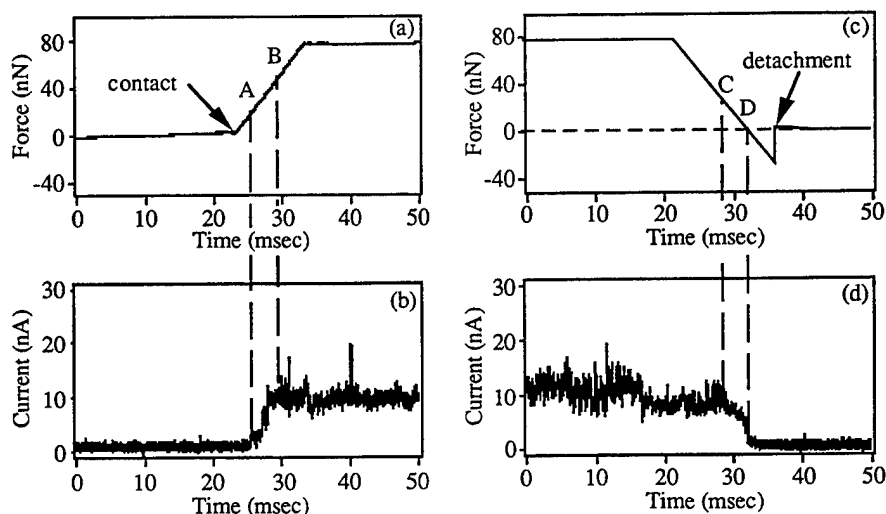
Fig. 3. Simultaneous force and current measurements during tip approach and contact [(a) force, (b) current] and withdrawal and detachment [(c) force and (d) current] on a region of intermediate conduction.

full scale current corresponds to 100 nA). Note that (1) the onset of measurable current (labeled A) occurs after contact when the force has reached ~15 nN; (2) the current continues to rise as the force increases (A to B), but then (3) stops rising at B, at a force of ~50 nN, even though the force continues to increase. Force (c) and current (d) measurements made as the tip is withdrawn are shown in Figs. 3(c) and 3(d). The current does not start to drop until C, when the force has dropped to ~25 nN, and decreases continuously until the force is very nearly zero (D). Note that adhesion produces an attractive force between the tip and surface as tip is withdrawn further; nevertheless, no current is observed after D even though there is obviously a connection between the tip and surface up to the instant of detachment. This physical connection could be due to direct polymer-tip adhesion, perhaps dominated by electrostatic forces.[12]

On high current patches ("metal-to-metal"), slightly higher forces were often required to produce measurable currents, with onsets at ~20 nN; maximum currents were reached at forces of ~65 nN. During tip retraction the current begins to drop at ~60 nN and reaches zero at ~55 nN. Even higher adhesive forces were observed in the final stages of tip withdrawal from the high conductivity regions, again implying continued physical contact *without* measurable current. This higher adhesion may be due to an intervening water layer (which would have poor conductivity), consistent with the hydrophilic nature of an oxidized metal surface.

With slight differences due to the hysteresis during make vs break, the force dependence of the current is nearly the same for these two regions, which display different levels of conduction. However, the current fluctuations were noticeably higher for the intermediate currents. We suggest that this is due to the conduction through thinned polymer, generally involving a hopping mechanism, which would tend to be "noisier".[13] Conduction from the tip to the stainless steel may also be complex, but definitely displays lower amplitude fluctuations.

Numerous efforts are currently under way to produce stable conducting cantilevers which would facilitate SCM studies, e.g., by Thomson and Moreland.[14] Coatings employing higher cohesive energy metals such as W and Rh may provide more durable, longer-lasting tips, with greater tolerance for higher contact forces and higher currents. Doped diamond tips, if

sufficiently conducting, could be very robust and allow a variety of material systems to be studied. In principle, diamond tips would allow for the study of nm-scale wear of very hard coatings on metals and semiconductors.

SUMMARY

Sputter deposited metal coatings on commercial Si_3N_4 tips offer sufficient conductivity to allow SCM imaging and thereby provide a spatial probe of wear. Scans of undamaged polymer films normally showed no detectable conductivity with applied forces up to 100 nN, although some scans revealed small patches of conductivity. Thinned regions produced by wear exhibited intermediate conduction, and exposed, "bare" metal with high conductivity was readily detected. Damage accumulation with increased tribological loading was readily apparent in the evolution of these features. In some cases, useful correlations can be made between simultaneously acquired AFM topography and SCM scans. The high spatial resolution observed in the conduction scans is probably due to the nature of the damaged surface (e.g., exposure of very small, conductive regions to the metal substrate), and perhaps only limited portions of the tip participate in the current path. Compressive forces of at least ~20 nN were required to establish significant conductivity in both the low and high conductivity regions. A plateau in current occurred at applied compressive forces of about 60 nN. Upon retraction of the tip from the surface, measurable hysteresis in the current was observed, probably due to contact maintained by adhesive forces. Scanning at higher compressive forces and/or applied bias produced measurable conductivity in larger areas without any obvious change in topography.

ACKNOWLEDGMENTS

REFERENCES

1. J. T. Dickinson, L. C. Jensen, K. H. Siek, and K. W. Hipps, to appear in Rev. Sci. Instrum. 66 (1995).
2. L. A. Wenzler, T. Han, R. S. Bryner, and T. P. Beebe, Rev. Sci. Instrum. 65, 85 (1994).
3. M. Anders, M. Mück, and C. Heiden, J. Vac. Sci. Technol. A 8, 394 (1990).
4. J. Snauwaert, L. Hellemans, I. Czech, T. Clarysse, W. Vandervorst, and M. Pawlik, J. Vac. Sci. Technol. B 12(1), 304 (1994).
5. M. Anders, M. Mueck, and C. Heiden, J. Vac. Sci. Technol. A 8, 394 (1990).
6. Digital Instruments, Inc., Santa Barbara, CA
7. Graciela B. Blanchet and S. Ishmat Shah, Appl. Phys. Lett. 62 1026 (1993).
8. G. B. Blanchet, C. R. Fincher, Jr., C. L. Jackson, S. I. Shah, and K. H. Gardner, Science 262, 719 (1993).
9. Wenbiao Jiang, M. G. Norton, Lancy Tsung, and J. T. Dickinson, J. Mater. Res. 10, 1038 (1995).
10. Sunkyo Lee, L. C. Jensen, S. C. Langford, and J. T. Dickinson, J. Adhesion Sci. Technol. 9, 1 (1995).
11. L. Scudiero, J. T. Dickinson, L. C. Jensen, and S. C. Langford, J. Adhesion Sci. Technol. 9, 27 (1995).
12. R. G. Horn and D. T. Smith, Science 256, 362 (1992).
13. J. T. Dickinson, S. C. Langford, and L. C. Jensen, J. Mater. Res. 8, 2921 (1993).
14. R. E. Thomson and J. Moreland, "Development of highly conductive cantilevers for atomic force microscopy point contact measurements," to be submitted.

THE MORPHOLOGY OF POLYTETRAFLUOROETHYLENE (PTFE) THIN FILMS FORMED BY PULSED-LASER DEPOSITION

M. GRANT NORTON*, WENBIAO JIANG*, AND J. THOMAS DICKINSON**
* Department of Mechanical and Materials Engineering and
** Department of Physics, Washington State University, Pullman, WA 99164

ABSTRACT

Thin films of polytetrafluoroethylene have been formed by the pulsed-laser deposition technique. The structure of the films was found to be dependent upon the substrate temperature during deposition. At substrate temperatures from room temperature to 200°C the films were determined, by transmission electron microscopy and X-ray diffraction techniques, to be amorphous. Films formed at higher substrate temperatures were found to contain both amorphous and crystalline components. The data for the crystalline component is consistent with it being highly ordered with the long helical molecular chains aligned parallel to the film-substrate interface plane. The maximum amount of crystalline material occurred when the substrate temperature was close to the melting temperature of the polymer.

INTRODUCTION

Most applications for polymeric materials have been based on bulk forms of the material. The possibility of depositing thin films of polymers is of interest and novel methods for polymer film deposition are important because many polymers with desirable physical properties, e.g., high-temperature durability, are intractable. Such polymers cannot be processed by conventional solution or thermal techniques, and hence are not available as thin coatings. The applications for polymer films are driven, in part, by the electronics industry because of the desire for miniaturization and the integration with other materials and technologies. For these applications a dry processing method is often required. Many techniques have been used for the deposition of thin films of polymeric materials and several examples are given in Table I.

The first reported use of the pulsed-laser deposition (PLD) technique for the formation of polymer films was by Hansen and Robitaille [1] and we believe that this technique has considerable potential in this area. PLD utilizes the material ablated from a target as the source of deposited material. Several groups have demonstrated that laser pulses in the UV part of the electromagnetic spectrum can be used to ablate and etch away the surface layers of a polymer [e.g., 2-6]. However, it is only fairly recently that efforts have been directed towards the synthesis of polymeric materials in thin-film form using the PLD technique.

In studies of the formation of polytetrafluoroethylene (PTFE) films via plasma-assisted polymerization it has been demonstrated that the presence of radical and ionic species was a necessary requirement for polymerization. The species that have been proposed as major reactive participants include: CF, CF_2, CF_3, CF_3^+, $C_3F_5^+$, F, and C. Several groups studying the laser ablation of polymers have identified the presence of these and other species, in addition to the monomer, emitted as a result of UV laser irradiation of PTFE targets [e.g., 5,6,7]. Thus, laser irradiation of PTFE produces all the essential species for polymerization and film growth, although not necessarily in the optimum proportions. The successful use of the PLD technique for the formation of PTFE films was first reported by Blanchet and Shah [8]. In this present article, the morphology of laser-deposited PTFE films is reported.

Table I. Deposition Techniques for Polymer Films

Polymer	Deposition Method	Reference
polyaniline	vacuum evaporation	9
methylmethacrylate-tetramethyltin	plasma polymerization	10
polythiophene	electrochemical polymerization	11
epoxy-amine	chemical vapor deposition	12
polymethylmethacrylate	photodecomposition	13
polytetrafluoroethylene	pulsed-laser deposition	8,14
poly(p-phenylene)	vacuum evaporation	15
polytetrafluoroethylene	ion beam sputtering	16
polytetrafluoroethylene	rf sputtering	17
polyphenelyne sulphide	pulsed-laser deposition	18

EXPERIMENTAL

The experimental details of the deposition process used in our laboratory have been reported in detail elsewhere [14]. Briefly, the PTFE films were formed by focusing a Lambda Physik EMG203 excimer laser operating on KrF ($\lambda = 248$ nm) onto a 1.0-mm-thick PTFE target supplied by Goodfellow Corporation. The laser fluence was varied between 3 and 9 J/cm^2, the pulse duration was 20 ns, and the pulse repetition rate was 30 Hz. The films were deposited in vacuum (base pressure 10^{-6} - 10^{-7} Torr) onto either glass microscope slides, 3-mm-diameter carbon-coated copper grids, single crystal NaCl, or single crystal KBr. The latter were used for characterization of the films by infra-red (IR) spectroscopy. The carbon-coated copper grids and the NaCl substrates were used to facilitate fabrication of samples for examination using transmission electron microscopy (TEM): thin films deposited onto NaCl were floated off in deionized water and collected on a copper grid. Films were deposited onto glass substrates for characterization using X-ray diffraction (XRD).

The substrates were mechanically clamped onto the stainless steel plate of a small resistive heater and were positioned parallel to the target. The distance between the target surface and the substrate was ~ 5 cm. The temperature of the substrate heater was monitored by a thermocouple embedded into the heater block at a position just behind the substrate. All the temperatures reported here are those of the substrate heater as measured by the thermocouple. It should be noted that the actual substrate temperature may be lower than that of the substrate heater. If it is assumed that the only thermal losses are radiative from the surface of the substrate, the actual substrate temperature, at a measured value of 350°C, has been calculated to be ~10°C lower.

RESULTS AND DISCUSSION

XRD patterns recorded from the target material showed several peaks consistent with the polycrystalline nature of bulk PTFE. XRD patterns recorded from PTFE films deposited onto glass substrates at a heater temperature of 350°C exhibited a single sharp peak at a 2θ value of 18.09°, implying diffraction from the {100} planes of PTFE, which have a spacing of 0.490 nm. Crystalline PTFE has a hexagonal unit cell at 25°C with lattice parameters a = 0.566 nm and c = 1.95 nm [19]. The crystal lattice consists of the periodic arrangement of the long axes of the helical molecular chain repeat units. The repeat unit for the hexagonal modification is 15 CF$_2$ groups. The presence of a single peak in XRD patterns recorded from the films indicates that the crystalline regions are oriented with the long helical chains of the PTFE molecule parallel to the

film-substrate interface plane. XRD patterns recorded from PTFE films deposited on substrates heated to ≤ 200°C showed no sharp diffraction maxima.

A qualitative examination of the degree of crystallinity of the laser-deposited PTFE films, as determined by the intensity of the (100) peaks in the XRD pattern, found that it varied with the substrate temperature used during deposition. From the plot shown in Figure 1 it can be seen that the maximum amount of crystalline material occurs at a heater temperature of 350°C. For the data shown in Fig. 1 the films were all of an equivalent thickness.
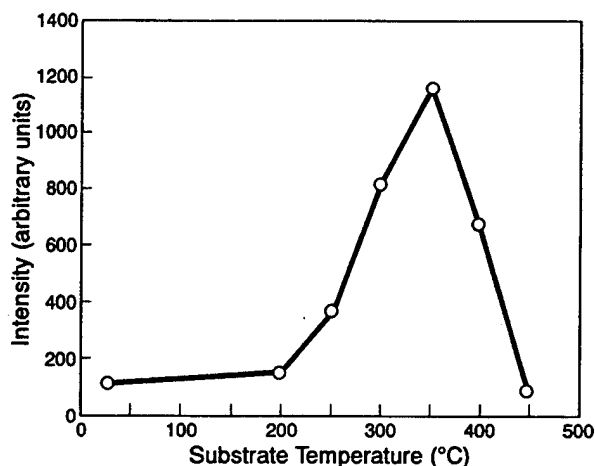
Figure 1. Change in intensity of the (100) peak as a function of substrate heater temperature during film deposition.

Electron diffraction patterns recorded from thin PTFE films deposited onto NaCl substrates confirmed that films formed on substrates heated to ≤ 200°C were amorphous. The diffraction patterns showed two broad diffuse rings as illustrated in Figure 2(a). Electron diffraction patterns recorded from films deposited onto NaCl substrates heated to 350°C showed a series of discrete rings, as shown in Figure 2(b), indicating that these films contained a crystalline phase arranged in a random ("polycrystalline") manner.

It is suggested that the reason why the crystallinity of the films changes with the substrate temperature during deposition, is that at substrate temperatures close to the melting point of PTFE there may be sufficient molecular mobility to allow orientation of the molecular chains into a crystalline configuration. It has been observed that crystallization of PTFE granules heated on NaCl substrates was enhanced at temperatures very near the melting temperature [20]. The ability to change the amount of crystalline material in the laser-deposited PTFE films by modifying the substrate temperature may have a significant impact on the applications of these films.

TEM images of thin PTFE films deposited using a laser fluence of 3J/cm^2 at a heater temperature of 350°C indicated that the films contained both amorphous and crystalline regions. Two types of crystalline region were observed: small (~ 5 nm diameter) crystallites and larger crystalline regions ~ 60 nm in diameter. Both types of crystalline region were found to occur within an individual film. Figures 3 and 4 show high resolution electron micrographs of the smaller and larger crystalline regions, respectively. The long-range crystalline perfection of these

regions can be clearly seen in the high resolution images. The plane spacing in both images was measured to be 0.283 nm. This spacing corresponds to that of the $\{\bar{1}20\}$-type planes in the hexagonal PTFE crystal structure.
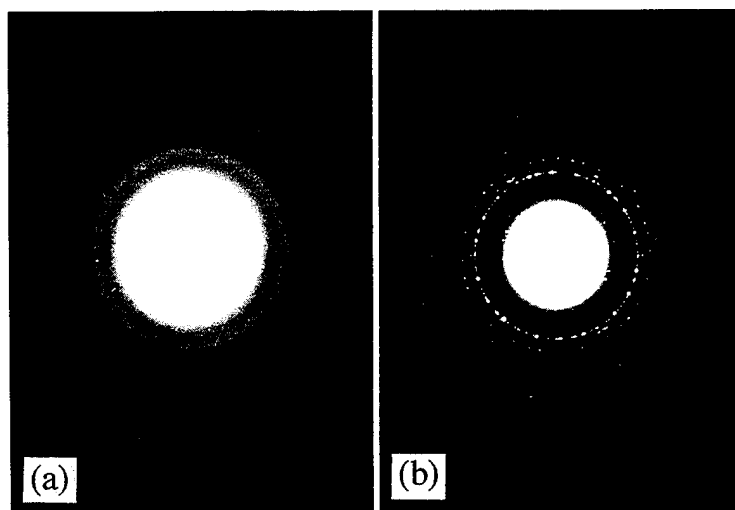
Figure 2. Electron diffraction patterns recorded from thin PTFE films deposited onto NaCl substrates heated to (a) 200°C and (b) 350°C. (Note: different camera constants were used for the two patterns.)
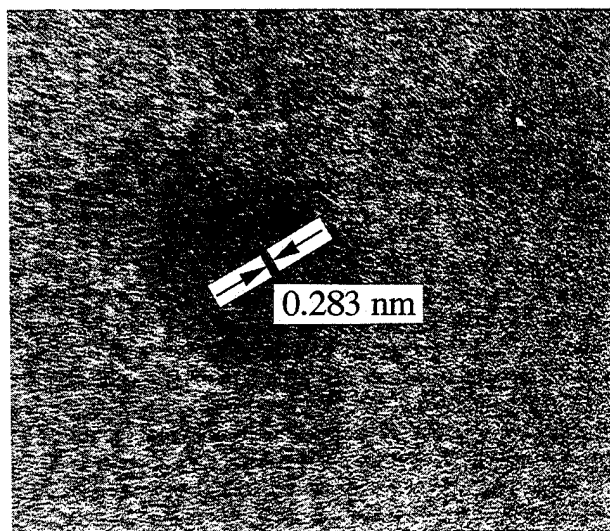
Figure 3. High resolution electron micrograph of a small crystalline inclusion in a PTFE film.
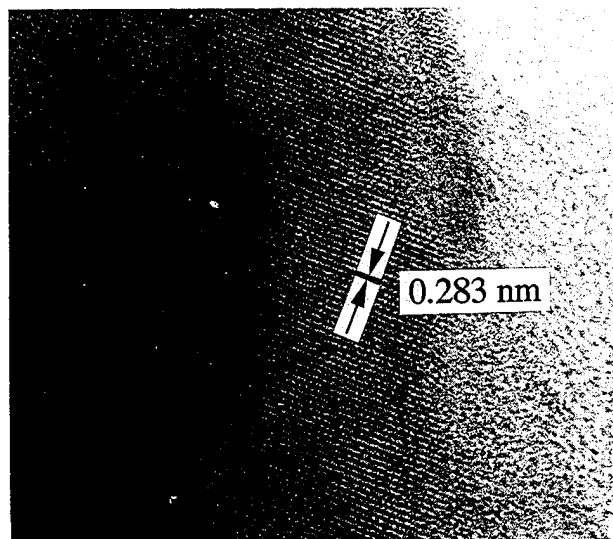
Figure 4. High resolution electron micrograph of part of a large crystalline region.
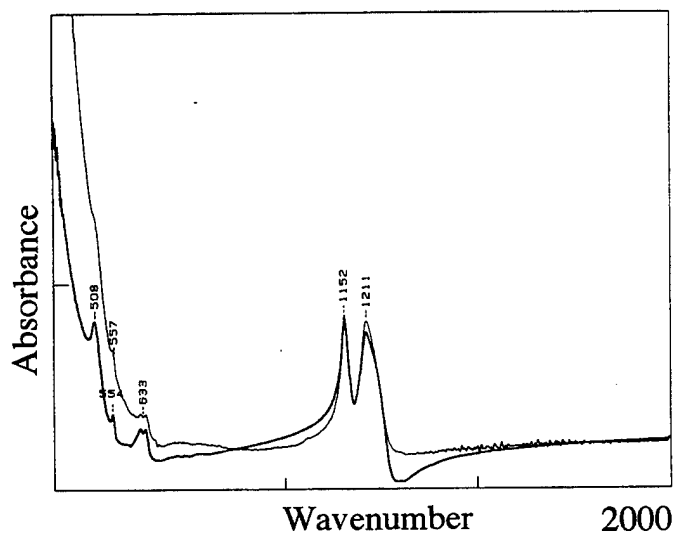
Figure 5. FTIR spectra recorded from PTFE films deposited onto KBr disks at 200°C (light line) and 350°C (dark line).

Selected-area electron diffraction (SAED) patterns recorded from the crystalline region shown in Fig. 4 showed only discrete reflections indicating the mono-crystalline nature of the inclusions [14]. All the reflections could be indexed as arising from PTFE. The presence of the

{00*l*}-type reflections in the electron diffraction patterns is consistent with the long molecular chains lying in the film-substrate interface plane and supports the earlier observation that the crystalline component in these films is highly textured.

Some preliminary results from *in situ* heating experiments performed on the amorphous films in the TEM indicated that the amorphous phase was stable up to temperatures of 280°C; the maximum temperature used in this present study. Further studies in this area are in progress.

Transmission IR spectra recorded from laser-deposited films on KBr substrates showed the chemical similarity between the amorphous and semi-crystalline variants of the PTFE films produced in this study. The spectra showed two strong absorption peaks at 1211 cm^{-1} and 1152 cm^{-1} which correspond to the asymmetrical and symmetrical CF_2 stretching modes. Also resolved were the PTFE rocking and bending modes at 508 and 554 cm^{-1} and the CF_2 wagging and chain stretching modes at 625 and 639 cm^{-1}.

CONCLUSION

In conclusion, thin PTFE films have been formed by pulsed-laser deposition. The films were found to consist of a mixture of amorphous and crystalline components—the relative proportions of which depended upon the substrate temperature during deposition. XRD and TEM studies have shown that the crystalline component of the films is highly ordered with the molecular chains lying parallel to the film-substrate interface plane. Films formed at substrate temperatures ≤ 200°C appear to be amorphous.

REFERENCES

1. S.G. Hansen and T.E. Robitaille, Appl. Phys. Lett. **52**, 81 (1988)
2. P.M. Goodwin and C.E. Otis, J. Appl. Phys. **69**, 2584 (1991)
3. B.J. Garrison and R. Srinivasan, J. Appl. Phys. **57**, 2909 (1985)
4. S.V. Babu, G.C. D'Couto, and F.D. Egitto, J. Appl. Phys. **72**, 692 (1992)
5. J.T. Dickinson, J.-J. Shin, W. Jiang, and M.G. Norton, J. Appl. Phys. **74**, 4729 (1993)
6. J.T. Dickinson, J.-J. Shin, W. Jiang, and M.G. Norton, Nucl. Instrum. and Methods **B91**, 672 (1994)
7. G.B. Blanchet, C.R. Fincher, Jr., C.L. Jackson, S.I. Shah, and K.H. Gardner, Science **262**, 719 (1993)
8. G.B. Blanchet and S.I. Shah, Appl. Phys. Lett. **62**, 1026 (1993)
9. S.C.K. Misra, M.K. Ram, S.S. Pandey, B.D. Malhotra, and S. Chandra, Appl. Phys. Lett. **61**, 1219 (1992)
10. M. Hori, S. Hattori, T. Yoneda, and S. Morita, J. Vac. Sci. Technol. **B4**, 500 (1986)
11. B.D. Malhotra, N. Kumar, and S. Chandra, Prog. Polym. Sci. **12**, 179 (1986)
12. S. Tatsuura, W. Sotoyama, and T. Yoshimura, Appl. Phys. Lett. **60**, 1661 (1992)
13. S. Deshmukh and E.W. Rothe, J. Appl. Phys. **66**, 1370 (1989)
14. W. Jiang, M.G. Norton, L. Tsung, and J.T. Dickinson, J. Mater. Res. **10**, 1038 (1995)
15. T. Asakura and N. Toshima, Jpn. J. Appl. Phys. **33**, 3558 (1994)
16. J.S. Sovey, J. Vac. Sci. Technol. **16**, 813 (1979)
17. L. Holland, H. Bierman, and S.M. Ojha, Thin Solid Films **35**, L19 (1976)
18. S. Kale, M. Swaminathan, and S.B. Ogale, Thin Solid Films **206**, 161 (1991)
19. E.S. Clark and L.T. Muus, Z. Kristall. B **117**, 119 (1962)
20. S. Yamaguchi and M. Tsuji, J. Mater. Res. **8**, 2942 (1993)

ELECTROPLATING OF FLUOROPOLYMERS USING ECR PLASMA DEPOSITED TiN AS INTERLAYER

A. WEBER, A. DIETZ, R. PÖCKELMANN AND C.-P. KLAGES
Fraunhofer-Institute for Surface Engineering and Thin Films,
Bienroder Weg 54 E, D-38108 Braunschweig, F.R.G.

ABSTRACT

A novel low temperature process for titanium nitride (TiN) deposition by means of an electron cyclotron resonance (ECR) plasma CVD process was applied to poly(tetrafluoro-ethylene) (PTFE). The organometallic compound tetrakis(dimethylamido)titanium (TDMAT) introduced into the downstream region of a nitrogen ECR plasma was used as a precursor for TiN deposition at 100°C.

The thin TiN films (thickness 15-30 nm) act as interlayers to activate the electroless deposition of copper followed by an electroplating process. Prior to the deposition of the interlayer, the samples were treated on a biased susceptor with argon ions to enhance the adhesion of the TiN interlayer. This metallization procedure avoids the use of toxic and pollutive etching agents and yields adherent copper layers on PTFE.

The maximum adhesion of the metal film on PTFE was established to be 13 N/mm^2. As shown by atomic force microscopy (AFM), TiN grains were formed on the fluoropolymer surface. Film composition was investigated by secondary ionization mass spectrometry (SIMS).

INTRODUCTION

Fluoropolymers are of great interest in the electronic industry due to their merits like low dielectric constants, low dissipation factors, high thermal stability, and high chemical resistance. The low surface energy of fluoropolymers and their chemical inertness leads to tremendous difficulties regarding the metallization of such polymers [1]. Thus, a surface modification of fluoropolymers is required to improve the adhesion [2]. Hazardous and pollutive etching agents like sodium naphtalenide or sodium in liquid ammonia, are necessary to activate the poly(tetrafluoroethylene) PTFE surface before metallization by electroplating [3]. These treatments lead to the removal of fluorine leaving unsaturated sites

like C=C or C≡C which can be oxidized to provide a higher surface energy for the subsequent metallization step.

Besides these conventional chemical surface treatments some work is done regarding non-equilibrium plasmas, ion beams, and radiation interactions with PTFE surfaces. Enhanced copper-PTFE adhesion was achieved by presputtering treatment prior to the sputtering of copper [4]. The presputtering with Ar^+ ions lead to an increase of the surface roughness. The same effect was also observed at x-ray damaged PTFE [5] and bombarding the PTFE surface with Xe atoms in the keV range. The latter method leads to the formation of PTFE filaments on the surface.

Haag and Suhr [7] reported on improved adhesion of electroplated copper on plasma etched PTFE. Prior to the electroplating, a thin metallic layer was deposited employing a plasma enhanced chemical vapor deposition (PECVD) process. Organometallic compounds of Pd, Pt, Au and Cu were used in this process.

We report here about the application of a novel low temperature titanium nitride (TiN) deposition process [8] as pretreatment for a subsequent electroplating process.

EXPERIMENTAL DETAILS

Depositions were carried out using an ASTeX HPM/M ECR source mounted on a reaction vessel equipped with a substrate holder which is connected to a radio frequency (13.56 MHz) generator. A detailed description of the experimental set up was published previously [8]. The PTFE substrate (5x5 cm^2, thickness 1 mm, purchased from Goodfellow) was placed four inches below the ECR source flange. To achieve a smooth fluoro-polymer surface for SIMS investigations Teflon®AF (DuPont) coated silicon was used as the substrate. A flow of 15 sccm [standard cm^3 min^{-1}] nitrogen, regulated by a mass flow controller, was introduced through the ECR cavity while tetrakis(dimethylamido)titanium (TDMAT) vapor was introduced through a gas ring into the downstream region between the plasma cavity and the susceptor. The TDMAT (purchased from Solvay Germany) was kept in a double glass wall container to allow precise temperature control. The temperature was thermostatically maintained at 25°C to produce a flow of 2.5 sccm. The microwave power (MW) was set to 400 W and thepressure was 0.1 Pa. No external heating of the graphite susceptor was applied. The substrate temperature rose after a process time of 20 minutes to 100°C.

Prior to the deposition of TiN, the substrates were treated with an ECR argon plasma using 15 sccm Ar and a MW power of 400 W. The samples were biased to -100 V for this treatment by connecting the susceptor with a radio frequency (rf) generator operating at 13.56 MHz.

After the deposition of the thin TiN film, the teflon substrates were electroless coated with 150 nm copper. The copper bath consists of an aqueous basic copper sulfate ($CuSO_4$)

solution (50 mmol/l) and formaldehyde as reduction agent. This copper film was enhanced to a thickness of 20 μm by electroplating using an acidic copper electrolyte (1 mol/l $CuSO_4$) and a current density of 10 mA/cm^2.

The adhesion was checked by the scotch tape test and a z-axis pull-out test [9]. In this test a progressive load was applied to a piston stuck on the copper surface until the sample failed. The joint was prepared with an epoxy resin at 100°C.

AFM investigations were performed with a commercial ambient AFM device using silicon nitride pyramidal tips with a tip radius of 50 nm, tracking forces of about 150 nN, and a scan frequency of 2 Hz. Root mean square (RMS) roughness measurements were taken after linear background substraction and substraction of the long range roughness from 3x3 μm^2 images.

RESULTS AND DISCUSSION

Figure 1 represents a scanning electron micrograph of a PTFE sample electroplated with copper. In Figure 2 the influence of an argon plasma pretreatment on the surface roughness and the adhesion strength of the electroplated copper is plotted. The argon plasma pretreatment leads to an increase of the adhesion strength. This effect can be explained by the increasing roughness of the PTFE substrates due to the bombardment with Ar$^+$ ions [4]. Samples without argon plasma pretreatment had already failed the scotch tape test. The failure of the metal/fluoropolymer joint always occured at the TiN/PTFE interface. An influence of the interlayer thickness on the adhesion strength could not be found. The measured adhesion force of the electroplated copper of 13 N/mm^2 is in the range found by Na/NH$_3$ treated PTFE [10]. At a pretreatment time above 10 min the surface roughness decreases, this is presumably caused by the increase of the surface temperature of the PTFE sample on the susceptor. The increase of the surface temperature leads presumably to the formation of volatile C_xF_y species. These species act as monomers for the redeposition of a thin plasma polymerized fluorocarbon layer which inhibits the progress of the surface roughness.
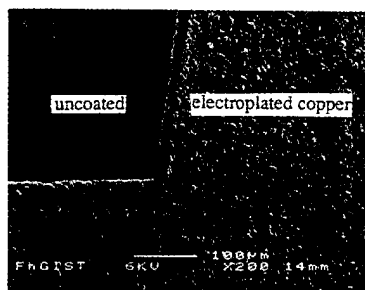
Fig. 1: SEM of PTFE surface electroplated with 20 μm copper after electroless deposition of copper.

Figure 3 reveals the influence of the substrate material and the deposition time on the sheet resistance. Due to the increasing film thickness the surface resistance decreases in a linear fashion. The deposition rate on SiO$_2$ is fairly low and was measured to
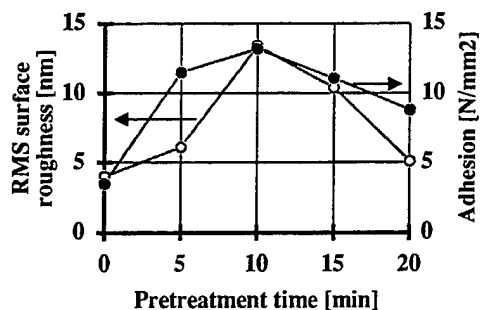
Fig. 2: Influence of an argon plasma pretreatment (15 sccm Ar, HF bias -100 V, MW power 400 W, TiN deposition time 20 min) on the surface roughness and the adhesion strength of electroplated copper on PTFE
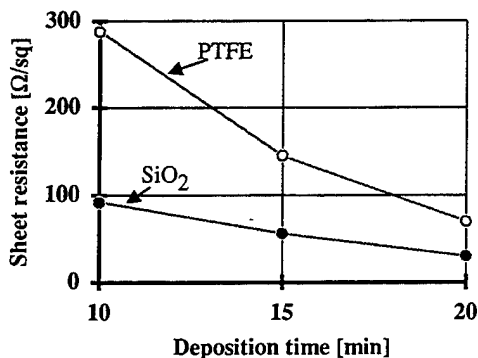
Fig. 3: Sheet resistance of TiN interlayer on PTFE and SiO_2 vs. deposition time

be 1.5 nm/min . Figures 4 a-d represent the surface morphology of an untreated PTFE, an argon plasma pretreated PTFE, a TiN coated PTFE sample, and an TiN coated SiO_2 substrate, respectively. The argon plasma pretreated sample in Figure 4b indicates in comparison to Fig. 4a the formation of small islands on the surface which cause the enhanced adhesion of the TiN interlayer. The TiN on SiO_2 (Figure 4 d) exhibit well shaped small crystallites whereas unpronounced crystallites were grown on PTFE (Figure 4c). The observed differences in the crystallite morphology and the sheet resistance indicate that the growth of TiN on PTFE is strongly influenced by the fluoropolymer. SIMS measurements were performed using Teflon AF coated silicon as substrates. A 15 nm thick TiN layer corresponding to a deposition time of 10 minutes revealed a composition of $Ti_{1.0}N_{1.12}C_{0.75}O_{0.12}F_{0.33}$, indicating a high impurity content of carbon and fluorine.
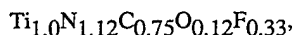
The etch rate of PTFE immersed in an ECR nitrogen downstream plasma was determined to be 80-90 nm/min using the described experimental parameter set. The ability of the ECR nitrogen plasma to etch PTFE leads to the formation of volatile $C_xF_yN_z$ species which are presumably redeposited as plasma polymers. This explains the high contents of carbon and fluorine in this thin, grey colored interlayer and the higher sheet resistance compared to films on an SiO_2 substrate. With increasing deposition time the sheet resistances on PTFE tend towards the numbers measured on SiO_2 as illustrated in Figure 3. The progressing growth of the TiN interlayer suppresses the plasma etching of PTFE. This interlayer
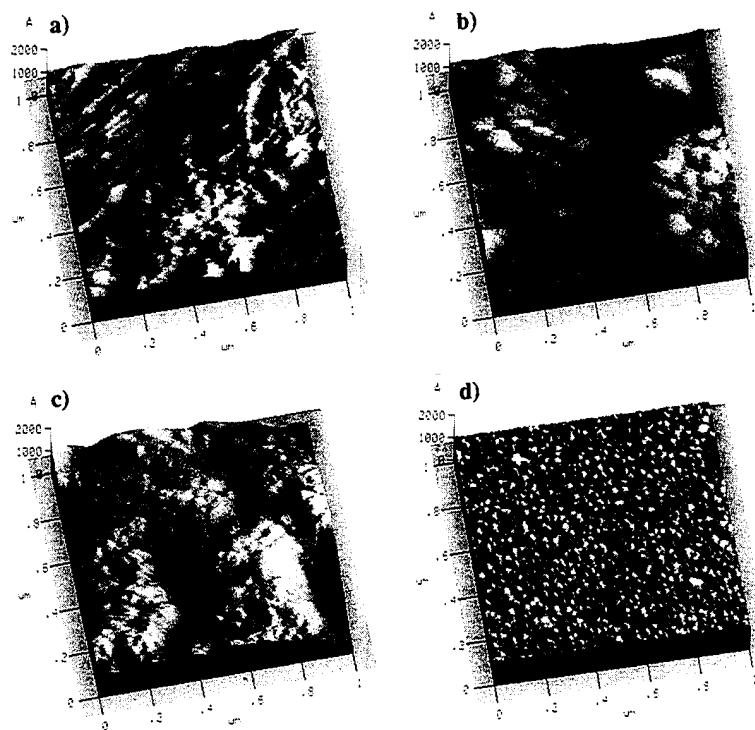
Fig. 4: AFM images (1x1 μm^2) of untreated PTFE (a), PTFE pretreated with Ar plasma, -100 V rf bias, time 10 min (b), subsequently TiN coated (deposition time 20 min) PTFE surface (c), and TiN (deposition time 20 min) on SiO_2 (d)

activates the electroless deposition of copper using formaldehyde as the reducing agent in a copper bath. That means that no further activation with palladium, as necessary in today's electroplating of plastics, is required. A summary of the applied process steps is illustrated in Figure 5.

CONCLUSIONS

Thin TiN films deposited on fluoropolymers in a low temperature plasma enhanced process can be used as interlayers for the electroplating of copper. To achieve an adherent metallization a pretreatment with argon ions at a substrate potential of -100 V is required. The ion bombardment increases the surface roughness leading to an enhanced adhesion of the interlayer. The thin interlayer, with a thickness of 15-30 nm, activates the deposition of electroless copper. A subsequent electroplating process yields a copper coating with an adhesion

I. ECR argon plasma treatment
10 min, rf bias -100 V

PTFE

II. ECR plasma deposition of
TiN interlayer (10-20 min)

PTFE

III. Electroless copper deposition
150 nm Cu, 30 min

PTFE

IV. Electroplating of copper
20 μm Cu, 10 mA/cm^2
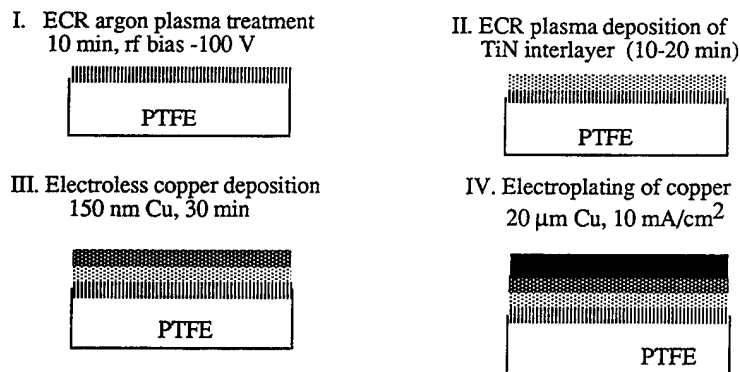
PTFE

Fig. 5: Overview of the used process steps for the metallization of PTFE

force of 13 N/mm^2. The described combination of the plasma based pretreatment steps followed by an electroplating process is a promising approach to avoid pollutive and hazardous reducing agents used in today´s metallization of fluoropolymers.

ACKNOWLEDGMENT

REFERENCES

1. P. K. Wu, G.-R. Yang, X. F. Ma, and T.-M. Lu, Appl. Phys. Lett. **65**, 508 (1994)
2. E. Sacher, Progress in Surface Science **47**, 273 (1994)
3. L. M. Siperko, and R. R. Thomas, J. Adhesion Sci. Technol. **3**, 157 (1989)
4. C.-A. Chang, Appl. Phys. **51**, 1236 (1987)
5. D. R. Wheeler and S. V. Pepper, J. Vac. Sci. Technol. **20**, 442 (1982)
6. R. Michael and D. Stulik, J. Vac Sci. Technol. A **4**, 1861 (1986)
7. C. Haag and H. Suhr, Appl. Phys. A **47**, 199 (1988)
8. A. Weber, R. Nikulski, C.-P. Klages, M. E. Gross, W. L. Brown, E. Dons, and R. M. Charatan, J. Electrochem. Soc. **141**, 849 (1994)
9. F. Garbassi, M. Morra, E. Occhiello, Polymer Surfaces (John Wiley & Sons, New York, 1994), p. 341
10. H. Schonhorn and F. W. Ryan, J. Adhesion **1**, 43 (1969)

METAL DEPOSITION ON LASER MODIFIED TEFLON SURFACES

STEFAN LÄTSCH*, HIROYUKI HIRAOKA** AND JOACHIM BARGON*
*Department of Physical and Theoretical Chemistry, University of Bonn, Wegelerstr. 12, D 53115 Bonn, Germany
**Department of Chemistry, Hong Kong University of Science and Technology, Clearwater Bay, Kowloon, Hong Kong

ABSTRACT

Cu, Ni, and Au were deposited with defined patterns and good adhesion by electroless plating, e-beam evaporation, and sputtering onto Teflon (polytetrafluoroethylene, PTFE), Teflon ET (PTFE-co-ethylene), Teflon FEP (PTFE-co-hexafluoropropylene) and Teflon PFA (PTFE-co-perfluoroalkoxy vinyl ether) surfaces. The polymers had been irradiated in a tetramethyl - ammonium hydoxide solution (TMAH) by a Nd:YAG laser at 266 nm and by an excimer laser at 248 nm prior to the metal deposition process. Both, the treated and virgin polymer surfaces were characterized by x-ray photoelectron spectroscopy (XPS), secondary ion mass spectroscopy (SIMS) and Micro-Raman spectroscopy. The increased metal to polymer adhesion at the interface was found to be due to chemical changes and is in the order $Ni > Cu \cong Au$.

INTRODUCTION

Fluoropolymers possess a variety of exceptional properties such as a low dielectric constant, high resistivity, low coefficient of friction and high thermal and chemical stability. Metallization of such fluorinated polymers offers new applications in the area of electronic packaging, if satisfactory adhesion can be obtained. Poly(tetrafluoroethylene) (PTFE), better known under its trade names Teflon™ (DuPont) or Hostaflon™ (HOECHST), has a dielectric constant (ε) of approximately 2.1. This is considerably lower than the dielectric constant of a-Si ($\varepsilon \cong 4.0$), which is used as a standard material in the microelectronic industry. The high electrical conductivity of Cu lines plated on a Teflon sheet can result in the development of very fast circuit boards with relatively little capacitive coupling. However, the chemical inertness of PTFE is responsible for its poor adhesion to metals. Numerous surface modifications have been reported to obtain improved results. Chemical etching [1,2], ion bombardment [3-5], plasma exposure [6], x-ray and laser irradiation [7-9] have been used to increase the surface wettability and, hence, to improve the adhesion of the deposited metal film.

Combinations of physical and chemical surface modifications were reported by Okoshi et al. [10]. The PTFE surface became hydrophilic after exposure to an ArF (193 nm) excimer laser in a diborane/ammonia gas atmosphere. Niino and Yabe used anhydrous hydrazine gas to modify fluorinated polymers with ArF excimer laser irradiation [11]. These processes require either a high vacuum or toxic gas handling.

We have developed a new method for depositing Cu, Ni, and Au on fluorinated polymer surfaces in large areas or imagewise by exposing the polymer surfaces in aqueous TMAH solution to a KrF excimer laser or to the 4th harmonic of a Nd:YAG laser. Conventional electroless plating processes follow the activation step. Also, e-beam and sputtering induced metal deposition have been investigated. In the present paper, emphasis has been put on the analysis of the polymer surface using x-ray photoelectron spectroscopy (XPS) as well as static and time of

239

flight secondary ion mass spectroscopy (SSIMS, TOF SIMS). These methods provided information on the chemical modifications of the surface which are responsible for the better adhesion at the metal/polymer interface.

EXPERIMENTAL

Sample preparation and irradiation

PTFE, FEP, PFA and ETFE were obtained from HOECHST as 150 μm and 300 μm thin films and were used as received. Irradiation of the samples was carried out using a pulsed Nd:YAG laser (Spectra Physics, GCR3 series) in TEM$_{00}$ mode at 266 nm, or alternatively with an excimer laser (Lambda Physik, EMG 202 MSC) at 248 nm. The polymer sheet was mounted in a quartz cell covered with a thin fused silica window. The cell itself was filled with aqueous tetramethylammonium hydroxide solution (25%, Riedel de Haën) and positioned on a XYZ translating stage. All three axes were driven by computer-controlled high-resolution stepper motors with a speed ranging from 0.005 to 0.5 mm/s. Fused silica lenses and UV mirrors were used to guide, expand and focus the laser beam. Laser irradiation was conducted with an incident beam perpendicular to the surface of the polymer films. Throughout the entire time of the irradiation, the fluence was constantly monitored and ranged between 50 mJ/cm^2 and 120 mJ/cm^2. The samples were exposed to a total of 100 - 9000 laser shots at a repetition rate of 1 - 10 Hz.

Microstructuring was achieved by placing a stainless steel mask in direct contact with the polymer sheet. Both, mask and polymer sheet were then exposed in solution as described above.

Metal deposition

Electroless Cu, Ni, and Au plating was used to metallize the microstructured fluoropolymer samples. Detailed descriptions for metal plating bath compositions can be found elsewhere and were applied as cited [12-14]. E-beam evaporation and sputtering methods were also used. The e-beam evaporation system (Denton, DV-SJ/20C) was used for the deposition of Cu and Ni films onto the treated fluoropolymer surfaces. E-beam evaporation of the metal films was carried out at a pressure of 1x10^{-6} Torr. The thickness of the metal deposited was controlled by time and a profiler. Gold was sputtered by 1 keV Ar$^+$ ion bombardment at 4x10^{-6} Torr. The growth of the film thickness was monitored using a quartz crystal microbalance.

Sample characterization

XPS, SSIMS and TOF SIMS data were aquired on a Perkin Elmer (PHI 5500/ 5600/7200) surface analysis system. XPS experiments were performed using Al Kα radiation (1486.6 eV). The spectra were aligned on the F(1s) peak to account for surface charging. An initial survey sweep was done at a pass energy of 93.6 eV. Detailed multi-plexed analysis of the C 1s and F 1s photoelectrons was done at a pass energy of 23.5 eV. Ion bombardment for SSIMS was accomplished using Xe$^+$ primary ions at 4 keV. TOF SIMS data were aquired with Cs$^+$ primary ion bombardment. Static analysis conditions were assured by ion fluences not higher than 8 x 10^{11} ions/cm^2. Additional spectroscopic data were obtained by Micro-Raman spectroscopy (Renishaw).

Surface morphologies were investigated with a cold field emission SEM (JEOL) at 0.5 to

2 kV to minimize charging effects. Atomic force microscopy (Topometrix) was used to scan the virgin and irradiated polymer surfaces to get qualitative data concerning the surface roughness. The receding and advancing water contact angles were measured at 25°C and 50- 60% relative humidity using a goniometer (Ramé-Hart).

RESULTS AND DISCUSSION

Laser irradiation of all four fluoropolymers in TMAH solution (TMAH) resulted in increased hydrophilicity of the polymer surface. Contact angle measurements showed that irradiation of PTFE with a Nd:YAG laser (266 nm) at 100 mJ/cm^2 and 10 Hz resulted in a decrease of the contact angle from 100° to 40°. after 1500 shots. The decreased contact angle results from to improved hydrophilicity. Longer exposure did not result in higher hydrophilicity of the PTFE surface. FEP, PFA and ETFE irradiated under the same conditions resulted in smaller changes of the contact angle. The values ranged from 100°. for the virgin polymer to 60° to 70°. for the exposed fluoropolymers.

Characteristic peaks for C 1s and F 1s peaks are detected on the virgin polymer surface. The atomic ratio of fluorine to carbon was 1.98, close to the expected value of 2.0. Oxygen detection from surface contamination was negligibly small. XPS spectra of PTFE exposed in TMAH solution reveal the appearance of the N 1s and O 1s peaks in correlation with exposure time. After 300 to 1800 shots with 100 mJ/cm^2 the intensity of the carbon C 1s peak increased gradually as well as the O 1s and N 1s peak intensities. However, the surface modification and formation of hydrophilic groups in the polymer backbone were also accompanied by defluorination as indicated by a decreased F 1s peak. Figure 1 shows the C 1s spectrum of PTFE exposed to 1500 shots at 266 nm, 100 mJ/cm^2 and 10 Hz in TMAH solution. Five peaks can be fit and are assigned to graphitic carbon at 284.6 eV, -CHF-CF$_2$-, -C-OH, and -C-NH$_2$ at 286 eV, -CF$_2$-O- and -C=O at 287.5 eV, -CF$_2$-CHF- and -CF at 289.5 eV and -CF$_2$ at 292 eV. Nd:YAG and Excimer laser exposure of PTFE at 266 nm and 248 nm, both at 100 mJ/cm^2 and 10 Hz, produced the same change of the surface composition. It should be added that none or little
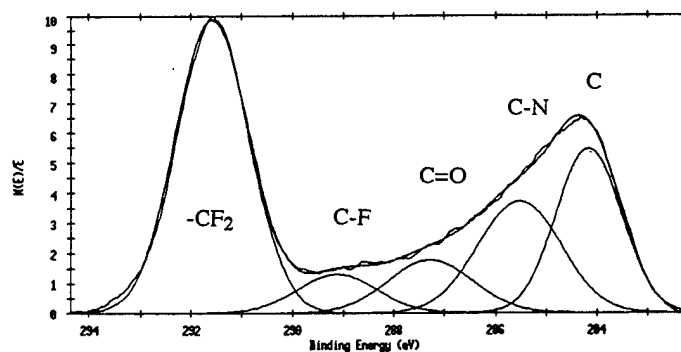
Fig.1: XPS C 1s spectrum of PTFE irradiated in tetramethylammonium hydroxide solution

coloring of the PTFE surface was observed during the first 1200 shots although good metal adhesion was already obtained after 900 laser shots.

Applying the same conditions, the XPS survey and C 1s spectra of FEP and PFA gave similar results. However, the degree of surface modification deviated from the PTFE results. In accordance with the change of contact angles, both fluoropolymers showed smaller O 1s and N 1s peak intensities and a degree of defluorination for FEP and PFA similar to PTFE. Exposure of ETFE at 10 Hz and 100 mJ/cm^2 resulted in strong graphitization. Although the survey spectra show an increased oxygen peak intensity, no nitrogen peaks could be detected. Curve fits of the C 1s spectra reveal increased peaks at 284.6 eV due to graphitic carbon and at 286 eV due to $\underline{C}$HF-CF$_2$- and -$\underline{C}$-OH groups. The peak at 292 eV of exposed ETFE was reduced by two third compared to the original peak of the virgin polymer.

With SSIMS and TOF SIMS, spectra were taken of both virgin and exposed fluoropolymer samples as shown in figure 2. The virgin PTFE spectrum displayed characteristic peaks at m/z = 12 for C$^+$, m/z = 31 for CF$^+$, m/z = 69 for CF$_3$$^+$, m/z = 74 for C$_3F_2$$^+$, and m/z =
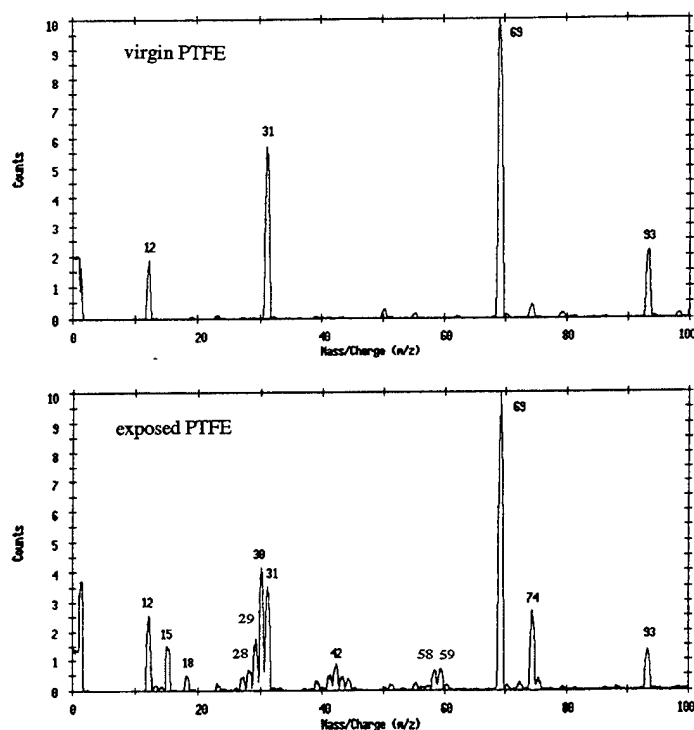
Fig. 2: SSIMS Spectra of virgin and exposed PTFE

93 for C$_3$F$_3$$^+$. Larger fragments with m/z = 131, 143, 155, and 181 were present as well and attributed to C$_3$F$_5$$^+$, C$_4F_5$$^+$, C$_5F_5$$^+$, and C$_5F_7$$^+$. SSIMS and TOF SIMS spectra of PTFE exposed to 1200 shots at 266 nm, 100 mJ/cm^2 at 10 Hz showed additional peaks at m/z = 28 for CH$_2$N$^+$, m/z = 29 for CHO$^+$, and m/z = 30 for CH$_4$N$^+$. Further peaks were detected at m/z = 42 for C$_2$H$_4$N$^+$ or C$_2$H$_2$O$^+$. Peaks at m/z = 58 were assigned to C$_3$H$_8$N$^+$ and at m/z = 59 to C$_3$H$_4$F$^+$. Although the peak intensities are smaller than the characteristic PTFE peaks, they lead to the assumption that the polymer was partly reduced during the laser treatment and that

hydrophilic groups were induced into the polymer backbone.

SSIMS spectra of FEP and PFA indicated that both polymers were defluorinated and partially carbonized as is evident by an increased m/z = 12 peak intensity. No peaks for other surface modification were detected. Carbonization of ETFE surfaces was already very strong after 300 shots at 100 mJ/cm^2 and 10 Hz. SSIMS spectra showed inreased peak intensities for m/z = 12 for C$^+$ and m/z = 27 for C$_2$H$_3^+$. No characteristic peaks for aromatic fragments were detected for increased unsaturation.

AFM and cold field emission SEM were used to investigate the contribution of surface roughness to the metal/polymer adhesion. Figure 3 shows SEM micrographs of virgin PTFE and FEP as well as PTFE and FEP exposed in TMAH solution for 1200 shots at 266 nm, 10 Hz and
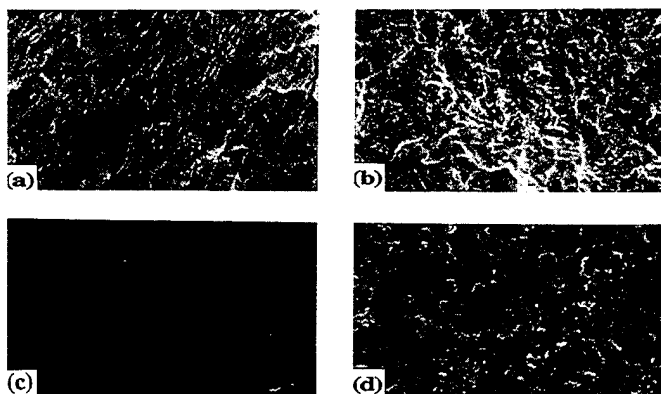
Fig. 3: SEM micrographs of virgin (a) and exposed (b) PTFE and virgin (c)
and exposed (d) FEP. —— = 1 μm in (a) - (d).

100 mJ/cm^2. Laser irradiation of PTFE in TMAH at fluences of up to 100 mJ/cm^2 increased the surface roughness without producing holes or craters on the surface even in large scale. The pictures of FEP are characteristic for PFA and ETFE as well. The virgin FEP surfaces show almost no irregularities. However, on the exposed polymer surface spots of carbonized polymer can be seen. In case of exposed ETFE these spots are ten to hundred times larger than those on FEP and PFA surfaces. Micro-Raman spectra confirmed via a characteristic peak at 1600 cm^{-1} that the dark spots stem from fluoropolymer regions degraded to amorphous carbon. The polymer surface between the amorphous carbon spots were free of any graphitization. Surface roughness was increased for all three polymers by two to five times. The maximum height of the surfaces are 0.3 μm.

On the basis of these results we deposited metal films on the imagewise modified fluoropolymer surface. Figure 4 shows a copper pattern on PTFE deposited by electroless plating. Very strong adhesion was obtained for PTFE compared to FEP, PFA and ETFE. Scotch tape tests applied to metal films on PTFE could not remove the deposited Cu, Ni, and Au even after several applications. In general, adhesion of Ni was found to be stronger than that of Au and Cu. Metal films deposited by e-beam and sputtering methods resulted in slightly stronger adhesion compared to the films deposited by electroless plating. However, it can be assumed that this difference is due to the grainy nature of the films deposited by electroless plating methods.
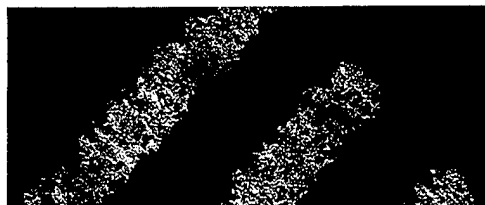
Fig. 4: Copper pattern on PTFE deposited by electroless plating. ———— = 100 μm.

CONCLUSION

The interactions between the tetramethylammonium hydroxide solution (TMAH) and the fluoropolymers under UV - laser irradiation lead to increased hydrophilicity. As demonstrated with XPS and SIMS, the effect especially on PTFE is not purely of a physical nature, but also due to chemical changes on the surface. It can be assumed that hydroxy and amino groups were induced into the polymer backbone, thus, increasing the metal/ polymer adhesion at the interface. Although showing amplified hydrophilicity, FEP, PFA and ETFE were mainly defluorinated and partially carbonized under laser irradiation in TMAH.

Selective area metallization was possible by using a photographic contact mask during exposure of the fluoropolymers in solution. This method could be used for direct patterning of fluoropolymers, especially for PTFE.

REFERENCES

1. H. Schonhorn and F.W. Ryan, J. Adhesion, 1, 43 (1969)
2. D.M. Brewis, R.H. Dahm and M.B. Konieezko, Angew. Makromol. Chem. 43, 191 (1975)
3. P. Bodö and J.E. Sundgren, J. Appl. Phys. 60, 1161 (1986)
4. C.A. Chang, J.E.E. Baglin, A.G. Schrott and K.C. Lin, Appl. Phys. Lett., 51, 103 (1987)
   C.A. Chang, Appl. Phys. Lett., 51, 1236 (1987)
5. B.J.Tan, M. Fessehaie and S.L. Suib, Langmuir, 9, 740 (1993)
6. S.L. Kaplan, E.S. Lopata and J. Smith, Surface and Interface Analysis, 20, 331 (1993)
7. D.R. Wheeler and S.V. Pepper, J. Vac. Sci. Technol., 20 (3), 442 (1982)
8. W.L. Perry, K.M. Chi, T. Kodas, M. Hampden-Smith and R. Rye, Appl. Surf. Sci., 69, 94 (1992)
9. W. Jiang, M.G. Norton and J.T. Dickinson, Mat. Res. Symp. Proc., 304, 97 (1993)
   J.T. Dickinson, J.J. Shin, W. Jiang and M.G. Norton, J. Appl. Phys., 74 (7), 472 (1993)
10. M. Okoshi, M. Murahara and K. Toyoda, Mater. Res. Soc. Symp. Proc., 201, 451 (1991)
11. H. Niino and A. Yabe, Appl. Phys. Lett., 63 (25), 3527 (1993)
12. H. Niino and Y. Yabe, Appl. Surf. Sc., 69, 1-6 (1993)
13. L.L. Gruss and F. Pearlstein, Plating and Surface Finishing, 70 (2), 47 (1983)
14. Y. Okinaka, Plating, 58, 914 (1970)

REMOVAL OF POLY(DIMETHYLSILOXANE) CONTAMINATION FROM SILICON SURFACES WITH UV/OZONE TREATMENT

F.D. EGITTO, L.J. MATIENZO, J. SPALIK, AND S.J. FUERNISS
IBM Corporation, Microelectronics Division, Endicott, NY 13760.

ABSTRACT

UV/ozone cleaning is known to be effective for removing thin organic contaminants, but removal of silicon containing contaminants is questionable. Organo-silicon contaminants, e.g., silicones, can result from a variety of integrated circuit chip and electronic packaging fabrication processes. In this investigation, films of poly(dimethylsiloxane) (PDMS) on silicon substrates, with and without a gold coating, have been used to simulate such contamination up to a thickness of 50 nm. Although treatment consistently reduced the advancing DI water contact angle, in some cases from a value greater than 100° to a value less than 5°, the hydrophilic nature of the treated surfaces was not due to complete contaminant removal, i.e., a significant amount of modified contaminant remained on the surface. High resolution x-ray photoelectron spectroscopy (XPS) in the Si $2p$ region suggest that O-Si-C bonds in the siloxane, observed prior to treatment, are converted to SiO_x, where x is between 1.6 and 2. The time required to reduce the contact angle to a minimum value was greater for the thicker PDMS film samples. Deflection testing was used to evaluate the adhesion of an epoxy-based adhesive to intentionally-contaminated silicon chips, before and after UV/ozone treatment. Although PDMS contamination induced loss of adhesion between the chip and the adhesive, complete conversion to silicon oxides by UV/ozone treatment of contaminants having a thickness of 5.0 nm has been demonstrated to restore adhesion to a value equivalent to that of uncontaminated silicon chip surfaces.

INTRODUCTION

Delamination of integrated circuit (IC) chips from polymer-based encapsulants and adhesives during accelerated reliability testing can result from contamination of the chip during device fabrication processes and wafer dicing. For example, residues of poly(dimethylsiloxane) (PDMS), a release agent on some dicing tapes, may be transferred to the chips. Removal of such contaminants is imperative to assure reliably bonded interfaces [1].

Among the techniques that can be employed for removal of organic contaminants are plasma [2] and laser [3,4] processes. Plasmas used for this application are ionized gases at reduced pressures. Oxygen plasmas are most commonly used for cleaning of organics. Decomposition of organic materials is initiated by reaction with atomic oxygen from the plasma followed by desorption of volatile by-products. Organic removal can also be accomplished by exposure to laser radiation, particularly at wavelengths in the ultraviolet (UV) region where most polymers are capable of absorbing radiation. Absorption is followed by polymer decomposition [3]. Both of these techniques utilize equipment that can require an appreciable capital investment. An alternative approach that utilizes reactive oxygen and UV radiation is UV/ozone cleaning. The apparatus for this technique is quite modest, usually consisting of a UV source, e.g., a low-pressure mercury vapor lamp, and a chamber to house the UV source and the sample(s). Cleaning is almost always performed in air at atmospheric pressure. In comparison with plasma

245

and laser systems, UV/ozone cleaning equipment is relatively inexpensive. An overview addressing UV/ozone cleaning technology and its applications has been given by Vig [5].

The low pressure mercury vapor lamp with a quartz envelope emits strongly at two wavelengths, 184.9 nm and 253.7 nm. Oxygen molecules absorb strongly at 184.9 nm and dissociate to form atomic oxygen [5] that reacts with O_2 to form ozone. Ozone strongly absorbs at 253.7 nm and dissociates to form O_2 and atomic oxygen. Both atomic oxygen and ozone can react readily with organic materials [6] forming polymer radicals. Absorption of UV radiation, if existent, can also lead to formation of polymer radicals, excited molecules, or, if the organic material's ionization potential is low enough, ions. Ultimately, the organic radicals react with atomic oxygen, molecular oxygen, or ozone to form low molecular weight, volatile fragments, like CO_2 and H_2O, that desorb from the surface. UV/ozone cleaning processes are known to be effective for contaminants that are not too thick and its effectiveness is also limited to some types of organic materials, while removal of organo-silicon compounds is questionable.

The effectiveness of a cleaning process can be evaluated by functional testing (e.g., adhesion measurements), chemical surface analysis (e.g., x-ray photoelectron spectroscopy [XPS]) and determination of changes in surface wetting (e.g., by contact angle measurements). Of course, functional tests are the most important measurement of the cleaning process, but these do not reveal whether the surface has been cleaned or simply modified, nor do they reveal the type of modification obtained. On the other hand, chemical analysis of the treated surface may indicate the type and degree of modification, but cannot always be correlated with adhesion. In addition, with most techniques of surface analysis, it is difficult to distinguish between silicon in the contaminant and elemental silicon or silicon oxides in the underlying substrate. Contact angle measurements, the simplest of the techniques listed for evaluation of cleaning processes, can quantitatively reveal surface modification with monolayer sensitivity. The rate of reduction of contact angle with UV/ozone cleaning has been used to characterize the level of organic contamination on IC chips [1]. However, the wettability of a surface is not necessarily indicative of cleanliness, nor is it a predictor of good adhesion. Wetting and adhesion depend not only on surface contamination, but also on surface chemical composition (relative concentrations of atomic species), chemical bonding environments (e.g., oxidation and oxidation states), and roughness. In addition, the presence of a weak boundary layer layer that does not adhere well to the bulk material, even though hydrophilic in nature, will typically exhibit poor practical adhesion to deposited materials. This paper reports on the effectiveness of UV/ozone cleaning in removing silicon-containing contaminants and the effect of the cleaning process on adhesion between IC chips and epoxy-based adhesives.

EXPERIMENTAL

Experiments were performed in a Uvocs, Inc., model T0606B UV/ozone cleaning system. The UV source is a 6" X 6" low-pressure mercury vapor grid lamp with a quartz envelope. Samples were placed 5.7 mm from the lamp envelope.

Films of PDMS were spin-coated from solution onto gold-coated silicon wafers (polished) having a diameter of 125 mm, using a Headway Research Inc. model EC101D-R485 photo-resist spinner. Spin speed was 4000 rpm for 30 seconds. Solutions were prepared by diluting Huls Petrarch Systems PDMS, silanol terminated (MW = 4200), with Burdick and Jackson high purity grade tetrahydrofuran (THF). Thickness of the PDMS film was controlled by varying the concentration, by volume, of the PDMS in the THF solvent. Concentrations in THF included 0.05, 0.1, 0.2, 0.4, 0.6 and 2.0%. After spinning, films were dried by allowing the solvent to evaporate in air. Silicon wafers having a crystalline orientation of (100) were used so that smaller

pieces of reproducible size and shape could be obtained by cleaving along orthogonal planes. Unless otherwise indicated, samples used for experiments with deposited contaminants were about 1.0 cm square. Gold films on the silicon wafers had been vapor-deposited to a thickness of 78 nm. The gold barrier between the silicon wafer and the contaminant film allowed differentiation between the silicon in the contaminant and the silicon in the wafer during chemical analyses. Thin contaminant coatings were invisible to the unaided eye. Since both the thin contaminant films and the gold scratch easily, marks visible in the gold layer indicated areas of damage to the invisible contaminant coatings, so that these areas could be avoided during analyses. The gold surface also served as a reference layer for determining the thickness of PDMS films obtained from solutions having various concentrations in THF using Rutherford backscattering spectroscopy (RBS). The effects of UV/ozone treatment on the PDMS films were found to be more reproducible when the gold was cleaned for ten minutes in the UV/ozone chamber prior to spin-coating. Samples for adhesion testing were prepared by dipping IC chips into a 0.2% solution of PDMS in THF and drying in air. The chips were then bonded to a plate of nickel-plated copper using an epoxy-based adhesive.

Advancing DI water contact angles on treated and untreated samples were measured with a Rame-Hart, Inc., model A-100 goniometer with optical protractor, using a sessile drop technique and drop volumes between 1 μl and 2 μl. For samples exposed to UV/ozone treatment, measurements were made immediately following treatment. Contact angles were recorded within 30 seconds from initial application of the drop. Since the PDMS thickness was uniform over the entire wafer to which it was applied, separate samples were used for each data point. Results obtained in this manner were found to be very consistent and reproducible.

XPS analysis was performed in a PHI-5500 Multiprobe spectrometer equipped with a hemispherical analyzer using non-monochromatized AlK_α rays for excitation. Survey and high-resolution spectra were collected with pass energies of 158 and 11.8 eV, respectively. Binding energies were referenced to the hydrocarbon peak at 284.6 eV. High-resolution XPS spectra in the C 1s and Si 2p regions were used to determine the contributions due to different chemical environments, and to follow them as a function of UV/ozone treatment.

The RBS instrument used for measurement of PDMS film thickness consisted of a tandem accelerator to produce a He^{2+} ion beam of 2.1 MeV. The typical geometry of this apparatus has been described elsewhere [7]. The thickness of PDMS films deposited at known concentrations (from 0.4 to 2.0%) in THF was estimated by the relative shift of the underlying gold layer, calculated using spectral simulation described by Doolittle [8]. Thickness at concentrations less than 0.4% were interpolated (including a data point at zero thickness for a concentration of zero percent).

Adhesion of chips to the adhesive was measured using a deflection testing method. A force is applied at a controlled speed normal to and on the reverse side of a thin metallic plate to which the chip has been bonded. The plate is supported at its edges allowing it to deflect. The maximum force required to initiate separation is an indication of the adhesion at that interface.

RESULTS AND DISCUSSION

PDMS film thicknesses, measured using RBS, are shown as a function of the polymer's concentration in THF in Figure 1. The relationship between concentration and thickness is linear. The extrapolated value of thickness at 0.1% is near 2.5 nm.

Samples were positioned such that the surface was 5.7 mm from the lamp and located within 2.5 cm of the geometrical center of the lamp. The rate of PDMS modification is proportional to the thickness of the contaminant as shown in Figure 2. The hydrophilic

nature of the treated surfaces is not necessarily indicative of complete PDMS removal. Although removal of contaminants will typically result in reduced contact angles, modification (like oxidation) of the contaminant films can have a similar effect, since oxidation of most polymer surfaces tends to increase the surface free energy. Mechanisms leading to reductions in contact angles for samples with different thicknesses of PDMS contamination have been inferred from results of XPS analyses and will be discussed in more detail below.

Data are also shown for the as-received gold surface containing only adventitious contamination, or contamination that might result from the metallization process. Rate of reduction in contact angles for gold-coated samples washed in THF (not shown here) were nearly identical to that exhibited for as-received gold-coated samples, indicating that the solvent does not contribute to wafer contamination or cleaning rates.

Atomic compositions obtained from XPS survey spectra are shown for the surfaces of the as-received gold, and for samples of PDMS having 2.5 nm thickness, before and after exposure to UV/ozone treatment for 10 minutes, in Table I. The gold surface exhibits some level of adventitious carbon and oxygen. In fact, contact angles on UV/ozone-cleaned gold surfaces have been observed to increase from 2° to 20° after sitting in air for 10 minutes following UV/ozone cleaning of the gold. The appearance of gold on the 2.5 nm thick PDMS-coated sample is consistent with the sampling depth of XPS, typically 3 to 5 nm. The concentration of carbon decreases following UV/ozone treatment, however a large increase is observed in the level of oxygen. Silicon is still detected. The signal due to gold does not increase significantly with treatment. These results suggest that although the UV/ozone treatment reduced the contact angle from a value greater than 100° to a value less than 5°, a significant amount of modified contaminant remains on the surface.

High resolution XPS spectra in the Si $2p$ region are shown for PDMS samples before and after ten minute UV/ozone exposure in Figure 3. The peak at 102.4 eV, observed prior to treatment, can be attributed to O-Si-C bonds in the siloxane and the peak at 103.8 eV, observed following treatment, corresponds to SiO_x, where x is between 1.6 and 2 [9]. For a thin PDMS film treated to a minimum contact angle, all of the silicon that remains on the surface is converted to an oxide. Because of the relative concentrations of silicon and oxygen shown in Table I, it appears that some oxygen must also be associated with carbon residues. UV/ozone treatment does not completely remove PDMS, but modifies the film considerably.
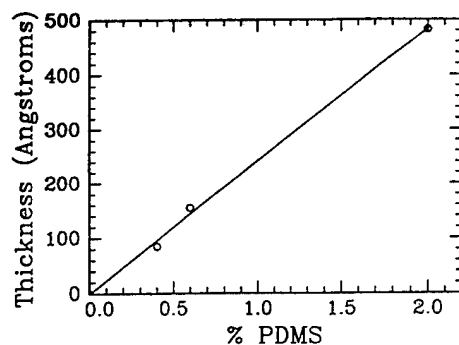
Figure 1. Thicknesses of PDMS, obtained using RBS, as a function of concentration in THF.
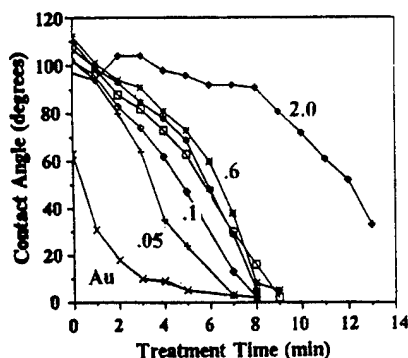
Figure 2. Contact angles for PDMS films of various thickness (concentration in THF) and as-received gold.

Table I. Atomic percent compositions of selected test surfaces.

Sample	C	O	Au	Si
As-received Au	25.9	13.1	61.0	0
2.5 nm PDMS, untreated	48.5	28.6	10.2	12.7
2.5 nm PDMS, 10 minute treatment	25.7	51.8	12.0	10.5

Table II. Deflection test peak force values (Newtons) for adhesion
between intentionally-contaminated IC chips and adhesive.

Sample	No UV/Ozone	10 Min. UV/Ozone
Uncontaminated Chip	65	67
PDMS-Contaminated Chip (1)	20	61
PDMS-Contaminated Chip (2)	23	72

Conversion of organo-silicon materials to silicon oxides is a phenomenon that is well documented for exposure to oxygen plasma environments [1,10,11]. In particular, polysiloxanes have been known as negative e-beam resists since the early 1970s [10]. Oxygen reactive ion etching of silicon-containing polymers results in an initial thickness loss and a gradual slowing of polymer erosion until etching ceases. During etching, it is believed that silicon-containing monomer diffuses to the polymer surface where it is converted to SiO_2 and functions as an increasingly effective etching barrier [2].

Several IC chips were coated by dipping into solutions of 0.2% PDMS in THF. Of these, several received UV/ozone treatment. Samples were then bonded to nickel-plated copper plates and deflection testing was performed to measure the adhesion between the chip and the bonding adhesive. Samples that had not been coated with PDMS were also tested. Results are shown in Table II. PDMS contamination induced loss of adhesion between the chip and the adhesive. UV/ozone treatment restored adhesion to a value equivalent to that obtained for samples without contaminant. Hence, even though the contaminant was not removed, thorough conversion to oxides restored adhesion.
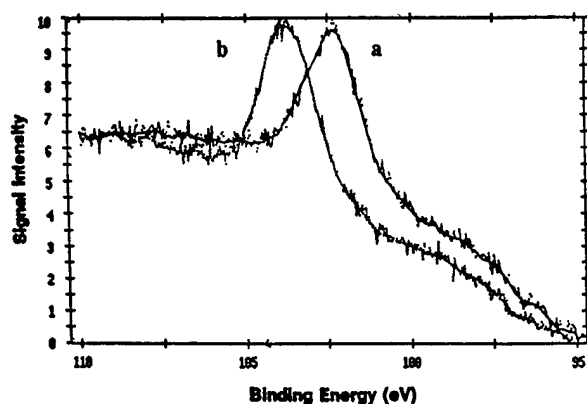
Figure 3. High resolution XPS spectra in the Si 2p region for PDMS samples before (a) and after ten minutes of UV/ozone exposure (b).

249

CONCLUSIONS

UV/ozone cleaning has been shown to be effective in restoring adhesion between contaminated IC chips and an epoxy-based adhesive. Although complete removal of silicon-containing contamination was not possible, adhesion improvement was observed for films on which the organo-silicon contaminant is completely converted to silicon oxides and the original thickness of the contaminant was on the order of 5.0 nm.

ACKNOWLEDGEMENTS

REFERENCES

1. G.S. Ganesan, G. Lewis, and H.M. Berg, Int. J. Microcircuits Electron. Packag., **17** (2), 152 (1994).

2. F.D. Egitto, V.Vukanovic, and G.N. Taylor, in Plasma Deposition, Treatment, and Etching of Polymers, edited by R. d'Agostino, (Academic Press, Inc., San Diego, CA, 1990), pp. 321-422, and references therein.

3. R. Srinivasan and B. Braren, in Lasers in Polymer Science and Technology: Applications, Volume III, edited by J.-P. Fouassier and J.F. Rabek, (CRC Press, Inc. Boca Raton, FL, 1990), pp. 133-179.

4. H.K. Park, C.P. Grigoropoulos, W.P. Leung, and A.C. Tam, IEEE Trans. Compon. Packag. Manuf. Technol. A, **17**, 631 (1994).

5. J.R. Vig, in Treatise on Clean Surface Technology, edited by K.L. Mittal, (Plenum Press, New York, 1987), pp. 1-26.

6. J.F. Rabek, in Comprehensive Chemical Kinetics: Volume 14, Degradation of Polymers, edited by C.H. Bamford and C.F.H. Tipper, (Elsevier Scientific Publishing Company, Amsterdam, The Netherlands, 1975), pp. 423-538.

7. P.F. Green, C.J. Palmstrom, J.W. Mayer, and E.J. Kramer, Macromolecules, **18**, 501 (1985).

8. L.R. Doolittle, Nucl. Instrum. Methods, **B9**, 344 (1985).

9. J. Li, J.W. Mayer, L.J. Matienzo, and F. Emmi, Mater. Chem. Phys., **32** (4), 390 (1992).

10. E.D. Roberts, J. Electrochem. Soc., **120**, 1716 (1973).

11. M.J. Owen and P.J. Smith, J. Adhes. Sci. Technol., **8** (10), 1063 (1994).

AUTHOR INDEX

SUBJECT INDEX